TECHNISCHE UNIVERSITÄT DRESDEN

Technical University Dresden

Faculty of Environmental Sciences

Dissertation title:

Terrestrial vegetation–water interactions in observations and models

Dissertation to obtain the academic degree

Doctor rerum naturalium (Dr.rer.nat.)

Submitted by:

Wantong Li, M.Sc.

Born on 20. 07. 1995, Chuzhou, China

1. Reviewer: JProf. Dr. Matthias Forkel, TU Dresden
2. Reviewer: Prof. Dr. AJ (Ryan) Teuling, Wageningen University, The Netherlands
3. Reviewer: Prof. Dr. Benjamin Stocker, University of Bern, Switzerland

Defense date: 05.06.2023

Note on the commencement of the doctoral procedure

1. I hereby assure that I have produced the present work without inadmissible help from third parties and without aids other than those stated; ideas taken directly or indirectly from external sources are identified as such.

2. When selecting and evaluating the material and also when producing the manuscript, I have received support from the following persons: René Orth, Matthias Forkel, Mirco Migliavacca

3. No further persons were involved in the intellectual production of the present work. In particular, I have not received help from a commercial doctoral adviser. No third parties have received monetary benefits from me, either directly or indirectly, for work relating to the content of the presented dissertation.

4. The work has not previously been presented in the same or a similar format to another examination body in Germany or abroad, nor has it - unless it is a cumulative dissertation - been published. 5. If this concerns a cumulative dissertation in accordance with §10 Section 2, I assure compliance with the conditions specified there.

6. I confirm that I acknowledge the doctoral regulations of the Faculty of Environmental Sciences of the Technische Universität Dresden.

.....
Location, date

.....
Doctoral student’s signature

Declaration of conformity:

I hereby confirm the accordance of this copy with the original dissertation on the topic:

“Terrestrial vegetation-water interactions in observations and models”

.....

Location, date

.....

Signature (first name surname)

Contents

Summary 7

Zusammenfassung 11

1 Introduction 15

1.1 Motivation 16

1.2 Terrestrial vegetation and its relationship with water supply 18

1.2.1 Vegetation functioning 18

1.2.2 Hydro-meteorological drivers of evaporation and vegetation productivity 19

1.2.3 Vegetation structure and physiology 21

1.3 Terrestrial water cycle and its relationship with vegetation 24

1.3.1 Water balance 24

1.3.2 Vegetation regulating the water cycle 26

1.3.3 The relevance of vegetation on hydrological extremes 27

1.4 Advances in observations and models 30

1.4.1 Spaceborne remote sensing 30

1.4.2 Data-driven and physical-based models 34

1.5 Research questions and thesis outline 37

1.5.1 What is the relationship between vegetation productivity and water supply? 37

1.5.2 Can vegetation regulate hydrological extremes? 38

1.5.3 Can land surface models capture vegetation-water interplay? 40

1.5.4 Thesis outline 40

2 Global vegetation controls using multi-layer soil moisture 41

2.1 Introduction 42

2.2 Data and methods 43

2.3 Results and discussion 45

2.4 Conclusions 53

2.A Appendix 54

3 Widespread increasing vegetation sensitivity to soil moisture 70

3.1 Introduction 71

3.2 Data and methods 72

3.3 Results and discussion 78

3.4 Conclusions 85

3.A Appendix 86

4 The drought effect on vegetation physiology inferred from space *101*
4.1 Introduction 102
4.2 Data and methods 104
4.3 Results and discussion 111
4.4 Conclusions 122
4.A Appendix 123
5 Drought propagation into the terrestrial water cycle *136*
5.1 Introduction 137
5.2 Data and methods 139
5.3 Results and discussion 145
5.4 Conclusions 155
5.A Appendix 157
6 Drivers of high river flows in European near-natural catchments *171*
6.1 Introduction 172
6.2 Data and methods 173
6.3 Results and discussion 179
6.4 Conclusion 184
6.A Appendix 186
7 Synthesis *193*
7.1 What is the relationship between vegetation productivity and water supply? 194
7.2 Can vegetation regulate hydrological extremes? 197
7.3 Can land surface models capture the observed vegetation-water interplay? 199
7.4 Limitations 200
7.4.1 Difficulties in predicting SIF in tropical regions 200
7.4.2 Observing terrestrial photosynthesis and evaporation 201
7.4.3 Methods related to variable importance quantification 202
7.5 Outlook 202
7.5.1 Vegetation sensitivity to soil moisture and its implications 203
7.5.2 Vegetation functioning and related structure and physiology 203
7.5.3 Extreme events: floods and drought 204
References *206*
Statement of authorship contributions *238*

Acknowledgements..... 239

Curriculum Vitae.....241

Scientific publications..... 242

IMPRS certificate..... 244

Summary

Background: In the context of global climate change, vegetation is particularly relevant as it can take up anthropogenic CO_2 emissions and regulate water and energy cycling. While previous research provided valuable insights into long-term changes in vegetation greenness and in terms of the vegetation response to increasing temperature and atmospheric CO_2, vegetation-water interactions are still not fully understood. In fact, root-zone soil moisture dynamics have a fundamental influence on modulating vegetation greenness and productivity. Nevertheless, neither the sensitivity of vegetation productivity to soil water supply nor the vegetation functional response (i.e., photosynthesis and transpiration) to soil drought episodes have been fully resolved at the global scale. Missing global observations of vegetation functioning and terrestrial water variability are bottlenecks, and statistical tools for analyzing large and multi-stream data are poorly exploited, preventing a better understanding of global vegetation water response.

At the same time, a better knowledge of the vegetation response to the water supply in turn advances the understanding of the terrestrial water cycle. Hydrological extremes are damaging infrastructure and can affect human well-being, and have been reported to become more frequent and intense in many regions around the world. While a consensus exists regarding the importance of meteorological drivers for regulating the water cycle and related extreme events, the role of vegetation dynamics and characteristics is understudied. Its greater consideration in hydrological studies offers the potential to more accurately understand the processes driving hydrological extremes. Thereby, a better understanding on vegetation-water interactions in terms of vegetation water sensitivity and vegetation feedbacks on climate extremes can advance the accuracy of land surface modelling which is essential to improve climate projections.

Thanks to recent developments in Earth observations and in the applicability of powerful statistical analyses tools, investigating global vegetation-water interactions is now possible with unprecedented accuracy. In this context, this thesis builds particularly on (i) novel data products such as Sun-induced chlorophyll fluorescence or global gridded soil moisture and evapotranspiration products obtained from upscaling station measurements with machine learning algorithms, (ii) longer records and updated processing of established data products such as leaf area index and terrestrial water storage, and (iii) the development of explainable machine learning methods which can efficiently derived information from multivariate data streams, and are furthermore implemented and readily applicable in ecohydrological studies. With these datasets and tools, this thesis revisits the sensitivity of global vegetation to soil water supply across space and time.

Research objectives: The overarching goal of this thesis is to assess the vegetation response to soil water dynamics across the globe by applying data-driven statistical approaches, to study the relevance of vegetation dynamics for hydrological extreme events, and to evaluate the respective performance of land surface models. To achieve this overarching goal, three research questions (RQ) are posed:

RQ 1: What is the relationship between vegetation productivity and soil water supply?

While global water and energy controls on vegetation dynamics have been studied thoroughly, the sensitivity of vegetation productivity to water-related variables across space, time, and soil depth is largely unknown. In Chapter 2, the sensitivity of vegetation productivity to soil moisture from different soil layers has been quantified and differentiated using random forests in conjunction with the SHapley Additive exPlanations method. Chapter 3 quantifies the vegetation sensitivity to soil moisture for observation-based data and land surface models in different time periods, and detects related sensitivity trends. At the same time, the large-scale vegetation drought response carries information on ecosystem vulnerability and resilience to water limitation. Chapter 4 isolates the physiological vegetation drought response by disentangling signals of vegetation structural changes from overall vegetation variability from multiple remote sensing data streams.

RQ 2: Can vegetation regulate hydrological extremes?

The second question targets at understanding the role of vegetation for regulating hydrological extremes at large spatial scales. Chapters 5 and 6 focus on the effects of vegetation on droughts and floods, respectively, in addition to that of hydro-meteorological drivers. Chapter 5 aims at understanding the propagation of rainfall deficits into evaporation and runoff fluxes across the globe, and shows that this is modulated to some extent by the vegetation next to other drivers such as climate, topography and human activities. Chapter 6 studies the importance of vegetation-related drivers such as leaf area index and evaporation in regulating high river flows in European near-natural catchments. Spatial variations in the relevance of precipitation for inducing such high flows are modulated by the tree cover fraction. Thereby, spatiotemporal vegetation dynamics are complementing hydrological flood generation mechanisms.

RQ 3: Can land surface models capture the observed large-scale vegetation-water interplay?

The third question is addressed in Chapters 3 and 5 by comparing the vegetation-soil-moisture interplay derived from observation-based data streams with that from land surface models from the TRENDY ensemble. Chapter 3 evaluates to which extent land surface models can reproduce the global sensitivity of vegetation to soil moisture across soil layers as well as respective sensitivity trends across past decades. Chapter 5 diagnoses the accuracy of the evaporation and runoff response to drought across the globe as simulated by land surface models, and explores potential poorly represented biophysical processes that induce biases in the modelled drought responses of surface water fluxes.

Key results

RQ 1: Root-zone soil moisture is the predominant driver of vegetation productivity in more than half of the global study area, and vegetation is more sensitive to deeper-layer soil moisture in arid regions as well as in grass- and shrub-dominant regions (Chapter 2). Vegetation sensitivity to soil moisture is non-stationary across

time with overall increasing trends during the past 36 years in many semi-arid and arid regions due to decreasing trends in precipitation (Chapter 3). Dry ecosystems across the globe also exhibit severe physiological stress during soil moisture drought, reflected in decreases in light use efficiency and stomatal conductance (Chapter 4).

RQ 2: Vegetation plays an essential role in modulating drought and high river flows through two main pathways: (i) its effects on transpiration and leaf area across time, and (ii) its variation across space with different dominant vegetation types. During drought, runoff reductions are driven by increases of evaporation (note that vegetation transpiration is the main source of ecosystem evaporation) particularly in boreal and tropical regions with typically high tree cover fractions (Chapter 5). High river flows are mainly driven by hydrological variables such as precipitation, but dynamic evaporation and leaf area index also play a role. Moreover, with higher tree cover fractions the relevance of precipitation in generating high flows increases, potentially related to litterfall (Chapter 6).

RQ 3: Land surface models (LSMs) do not fully capture the observed large-scale vegetation-water interplay. LSMs can partly distinguish water and energy-controlling regimes of vegetation productivity (i.e., leaf area index), while vegetation sensitivity to near- and sub-surface soil moisture is generally overestimated. Increasing trends of vegetation sensitivity to near- and sub-surface soil moisture are also not properly captured by LSMs, related to the misrepresentation of plant water stress (Chapter 3). The vegetation-soil moisture sensitivity is not only overestimated in the case of leaf area index but also for evaporation as another vegetation-related variable. Overestimated long-term relationships between evaporation and soil moisture in turn introduce uncertainties in the simulated drought propagation into evaporation in wet regions across the globe (Chapter 5).

Conclusions:

This thesis takes advantage of state-of-the-art global observation-based data and land surface models as well as of explainable machine learning approaches to better understand the vegetation response to soil water availability across space and time in terms of overall conditions as well as extreme events. The main results emphasize the relevance of root-zone soil moisture in influencing vegetation dynamics in semi-arid and arid regions, and quantify related increases over time in the past three decades. During drought, vegetation dynamics are largely controlled by water stress impacts on vegetation physiology. Vegetation in turn affects the hydrological cycle in the case of droughts and floods. Depending on climate and vegetation characteristics, vegetation can mitigate or aggravate these extremes. The presented results of land surface model simulations demonstrate uncertainties in capturing observed large-scale vegetation-water interactions. This is associated with misrepresented responses of vegetation-related variables to soil moisture deficits which might be due to an insufficient consideration of g biophysical and biogeochemical processes such as root growth and water infiltration. This thesis provides a better understanding of processes underlying vegetation-water interactions,

and this can inform more accurate predictions of terrestrial carbon and water cycling under continuing climate change.

Zusammenfassung

Hintergrund: Im Zusammenhang mit dem globalen Klimawandel ist die Vegetation besonders wichtig, da sie die anthropogenen CO_2-Emissionen aufnehmen und den Wasser- und Energiekreislauf regulieren kann. Während frühere Forschungsarbeiten wertvolle Einblicke in langfristige Veränderungen des Grüns der Vegetation und in Bezug auf die Reaktion der Vegetation auf steigende Temperaturen und atmosphärisches CO_2 lieferten, sind die Wechselwirkungen zwischen Vegetation und Wasser noch immer nicht vollständig verstanden. Tatsächlich hat die Dynamik der Bodenfeuchte in der Wurzelzone einen grundlegenden Einfluss auf die Veränderung des Grüns und die Produktivität der Vegetation. Dennoch sind weder die die Empfindlichkeit der Vegetationsproduktivität gegenüber der Bodenwasserversorgung noch die funktionelle Reaktion der Vegetation (d. h. Photosynthese und Transpiration) auf Bodentrockenheitsepisoden auf globaler Ebene vollständig geklärt worden. Forschungsengpässe sind fehlende globale Beobachtungen von Vegetationsfunktion und Bodenwasservariabilität. Außerdem werden die statistischen Instrumente für die Analyse umfangreicher und vielschichtiger Daten nur unzureichend genutzt, was ein besseres Verständnis der globalen Reaktion der Vegetation auf Wasser verhindert.

Gleichzeitig trägt eine bessere Kenntnis der Reaktion der Vegetation auf die Wasserversorgung zu einem besseren Verständnis des terrestrischen Wasserkreislaufs bei. Hydrologische Extremereignisse schädigen die Infrastruktur, können das menschliche Wohlergehen beeinträchtigen und treten Berichten zufolge in vielen Regionen der Welt immer häufiger und intensiver auf. Während ein Konsens über die Bedeutung meteorologischer Faktoren für die Regulierung des Wasserkreislaufs und der damit verbundenen Extremereignisse besteht, ist die Rolle der Vegetationsdynamik und -eigenschaften noch nicht ausreichend erforscht. Ihre stärkere Berücksichtigung in hydrologischen Studien bietet das Potenzial, die Prozesse, die hydrologische Extreme antreiben, genauer zu verstehen. Dadurch kann ein besseres Verständnis der Wechselwirkungen zwischen Vegetation und Wasser im Hinblick auf die Wasserempfindlichkeit der Vegetation und die Rückkopplung der Vegetation auf Klimaextreme die Genauigkeit der Landoberflächenmodellierung verbessern, was für die Verbesserung der Klimaprojektionen unerlässlich ist.

Dank der jüngsten Entwicklungen im Bereich der Erdbeobachtung und der Anwendbarkeit leistungsfähiger statistischer Analysewerkzeuge ist es nun möglich, globale Wechselwirkungen zwischen Vegetation und Wasser mit noch nie dagewesener Genauigkeit zu untersuchen. In diesem Zusammenhang stützt sich diese Arbeit insbesondere auf (i) neuartige Datenprodukte wie sonneninduzierte Chlorophyllfluoreszenz oder globale Bodenfeuchte und Evapotranspiration, die aus der Hochskalierung von Stationsmessungen mit Algorithmen des maschinellen Lernens gewonnen wurden, (ii) längere Aufzeichnungen und aktualisierte Aufbereitungen etablierter Datenprodukte wie Blattflächenindex und terrestrische Wasserspeicherung und (iii) die Entwicklung erklärbarer Methoden des maschinellen Lernens, mit denen Informationen effizient aus multivariaten Datenströmen abgeleitet werden können und die darüber hinaus leicht implementier- und in

ökohydrologischen Studien anwendbar sind. Basierend auf diesen Datensätzen und Werkzeugen, wird in dieser Arbeit die Empfindlichkeit der globalen Vegetation gegenüber der Bodenwasserversorgung über Raum und Zeit hinweg neu untersucht.

Forschungsziele: Das übergeordnete Ziel dieser Arbeit besteht darin, die weltweite Reaktion der Vegetation auf die Bodenwasserdynamik mit Hilfe datengestützter statistischer Ansätze zu untersuchen, die Bedeutung der Vegetationsdynamik für hydrologische Extremereignisse abzuschätzen und die entsprechende Leistung von Landoberflächenmodellen zu bewerten. Um dieses übergeordnete Ziel zu erreichen, werden drei Forschungsfragen (RQ) gestellt:

Frage 1: Welche Beziehung besteht zwischen der Produktivität der Vegetation und der Bodenwasserversorgung?

Während Wasser und Energie als globale Steuergrößen von Vegetationsdynamik gründlich untersucht wurde, ist die Empfindlichkeit der Vegetationsproduktivität gegenüber wasserbezogenen Variablen über Raum, Zeit und Bodentiefe hinweg weitgehend unbekannt. In Kapitel 2 wurde die Empfindlichkeit der Vegetationsproduktivität gegenüber der Bodenfeuchte in verschiedenen Bodentiefen mit Hilfe von Random Forests (deutsch: Zufallswald) in Verbindung mit der SHapley Additive exPlanations Methode quantifiziert und differenziert. In Kapitel 3 wird die Empfindlichkeit der Vegetation gegenüber der Bodenfeuchte mit beobachtungsbasierten Daten und Landoberflächenmodelle in verschiedenen Zeiträumen quantifiziert und damit verbundene Empfindlichkeitstrends ermittelt. Gleichzeitig liefert die großräumige Reaktion der Vegetation auf Trockenheit Informationen über die Anfälligkeit und Widerstandsfähigkeit von Ökosystemen gegenüber Wasserlimitierung. In Kapitel 4 grenzt die physiologische Reaktion der Vegetation auf Trockenheit ein, indem Signale der strukturellen Vegetationsveränderung von der Gesamtvariabilität der Vegetation aus mehreren Fernerkundungsdatenströmen isoliert werden.

RQ 2: Kann die Vegetation hydrologische Extreme regulieren?

Die zweite Frage zielt darauf ab, die Rolle der Vegetation bei der Regulierung von hydrologischen Extremen auf großen räumlichen Skalen zu verstehen. Kapitel 5 und 6 befassen sich jeweils mit den Auswirkungen der Vegetation auf Dürren bzw. Überschwemmungen, zusätzlich zu den Auswirkungen von hydro-meteorologischen Treibern. Kapitel 5 zielt darauf ab, weltweit Fortpflanzung von Niederschlagsdefiziten in Verdunstungs- und Abflussströme zu verstehen, und zeigt, dass dies zum Teil von der Vegetation beeinflusst wird, neben anderen Faktoren wie Klima, Topographie und menschlichen Aktivitäten. Kapitel 6 untersucht die Bedeutung vegetationsbezogener Treiber wie Blattflächenindex und Verdunstung bei der Regulierung hoher Abflüsse in naturnahen europäischen Einzugsgebieten. Der Anteil der Baumbedeckung moduliert die räumliche Variationen in Bezug auf die Rolle des Niederschlags für die Auslösung solch hoher Abflüsse.

Dadurch ergänzen räumlich-zeitliche Vegetationsdynamiken die hydrologischen Mechanismen der Hochwasserentstehung.

Frage 3: Können Landoberflächenmodelle das beobachtete großräumige Zusammenspiel von Vegetation und Wasser erfassen?

Die dritte Frage wird in den Kapiteln 3 und 5 behandelt, indem die Wechselwirkung zwischen Vegetation und Bodenfeuchte aus beobachtungsbasierten Datenströmen, mit den jeweiligen Wechselwirkungen in Landoberflächenmodellen aus dem TRENDY-Ensemble verglichen wird. In Kapitel 3 wird bewertet, inwieweit Landoberflächenmodelle die globale Empfindlichkeit der Vegetation gegenüber der Bodenfeuchte in den verschiedenen Bodentiefen sowie die jeweiligen Trends in den vergangenen Jahrzehnten reproduzieren können. In Kapitel 5 wird die Genauigkeit der globalen, von Landoberflächenmodellen simulierten, Verdunstungs- und Abflussreaktionen auf Dürre diagnostisch ausgewertet, und potenziell schlecht abgebildete biophysikalische Prozesse untersucht, die zu Verzerrungen in den modellierten Reaktionen der Oberflächenwasserflüsse auf Dürre führen.

Wichtigste Ergebnisse

RQ 1: Die Bodenfeuchtigkeit in der Wurzelzone ist in mehr als der Hälfte des globalen Untersuchungsgebiets der vorherrschende Antriebsfaktor für die Produktivität der Vegetation, und die Vegetation reagiert empfindlicher auf die Feuchtigkeit in tieferen Bodenschichten in trockenen Regionen, sowie in Regionen, in denen Gräser und Sträucher dominieren (Kapitel 2). Die Empfindlichkeit der Vegetation gegenüber der Bodenfeuchte ist zeitlich nicht stationär, mit insgesamt steigenden Trends in vielen semi-ariden und ariden Regionen aufgrund abnehmender Niederschläge im Laufe der letzten 36 Jahren (Kapitel 3). In trockenen Ökosystemen auf der ganzen Welt kommt es bei Trockenheit auch zu schwerem physiologischem Stress, der sich in einem Rückgang der Lichtnutzungseffizienz und der stomatären Leitfähigkeit zeigt (Kapitel 4).

RQ 2: Die Vegetation spielt eine wesentliche Rolle bei der Regulierung von Trockenheit und hohen Abflüssen durch zwei wesentliche Pfade: (i) ihre Auswirkungen auf die Transpiration und die Blattfläche im Zeitverlauf und (ii) ihre räumliche Variation mit verschiedenen dominanten Vegetationstypen. Während einer Dürre wird die Verringerung des Abflusses durch eine erhöhte Verdunstung angetrieben (wobei zu beachten ist, dass die Transpiration der Vegetation die Hauptquelle für die Verdunstung des Ökosystems ist), insbesondere in borealen und tropischen Regionen mit typischerweise hohen Baumbedeckungsanteilen (Kapitel 5). Hohe Abflüsse werden hauptsächlich durch hydrologische Variablen wie Niederschlag angetrieben, aber auch die dynamische Verdunstung und der Blattflächenindex spielen eine Rolle. Darüber hinaus nimmt die Bedeutung des Niederschlags bei der Erzeugung hoher Abflüsse mit höherem Baumbewuchs zu, was möglicherweise mit dem Streufall zusammenhängt (Kapitel 6).

RQ 3: Landoberflächenmodelle (LSM) erfassen das beobachtete großräumige Zusammenspiel von Vegetation und Wasser nicht vollständig. LSMs können teilweise zwischen wasser- und energiesteuernden Regimen der Vegetationsproduktivität (d. h. Blattflächenindex) unterscheiden, während die Empfindlichkeit der Vegetation gegenüber oberflächennaher und tieferer Bodenfeuchte im Allgemeinen überschätzt wird. Zunehmende Trends in der Empfindlichkeit der Vegetation gegenüber oberflächennaher und tieferer Bodenfeuchte werden auch durch LSM nicht richtig erfasst, was mit der falschen Darstellung des Wasserstresses der Pflanzen zusammenhängt (Kapitel 3). Die Empfindlichkeit der Vegetation gegenüber der Bodenfeuchte wird nicht nur beim Blattflächenindex, sondern auch bei der Verdunstung als einer weiteren vegetationsbezogenen Variable überschätzt. Die langfristig überschätzte Beziehungen zwischen Verdunstung und Bodenfeuchte führen wiederum zu Unsicherheiten bei der simulierten Fortpflanzung von Trockenheit in die Verdunstung in feuchten Regionen weltweit (Kapitel 5).

Schlussfolgerungen:

Diese Arbeit nutzt modernste globale Beobachtungsdaten und Landoberflächenmodelle sowie Ansätze des erklärenden maschinellen Lernens, um die Reaktion der Vegetation auf die Wasserverfügbarkeit des Bodens in Raum und Zeit besser zu verstehen, und zwar sowohl im Hinblick auf allgemeine Bedingungen als auch auf extreme Ereignisse. Die Hauptergebnisse unterstreichen die Bedeutung der Bodenfeuchte in der Wurzelzone für die Vegetationsdynamik in semiariden und ariden Regionen und quantifizieren deren Zunahme in den letzten drei Jahrzehnten. Während einer Dürre wird die Vegetationsdynamik weitgehend durch die Auswirkungen von Wasserstress auf die Vegetationsphysiologie gesteuert. Die Vegetation wiederum beeinflusst den Wasserkreislauf bei Dürren und Überschwemmungen. Je nach Klima- und Vegetationsmerkmalen kann die Vegetation diese Extreme abmildern oder verschlimmern. Die vorgestellten Ergebnisse von Landoberflächenmodellsimulationen zeigen Unsicherheiten bei der Erfassung der beobachteten großräumigen Wechselwirkungen zwischen Vegetation und Wasser. Dies steht im Zusammenhang mit falsch dargestellten Reaktionen vegetationsbezogener Variablen auf Bodenfeuchtedefizite, die auf eine unzureichende Berücksichtigung biophysikalischer und biogeochemischer Prozesse wie Wurzelwachstum und Wasserinfiltration zurückzuführen sein könnten. Diese Arbeit liefert ein besseres Verständnis der Prozesse, die den Wechselwirkungen zwischen Vegetation und Wasser zugrunde liegen, und dies kann zu genaueren Vorhersagen des terrestrischen Kohlenstoff- und Wasserkreislaufs bei anhaltendem Klimawandel führen.

1 Introduction

Terrestrial vegetation-water interactions address questions related to but not limited to two disciplines: ecology and hydrology, so called ecohydrology. Ecology is defined as the study of interactions of organisms with biotic processes and abiotic environment. Vegetation is implicated in essentially every part of ecology as it is the beginning of the terrestrial food chains, and the dynamics of vegetation productivity and biomass affect the global carbon cycle and land-atmosphere moisture and heat exchanges. Hydrology studies the processes that include the movement of water from the subsurface to the land surface and atmosphere, and from the surface to the subsurface inversely. The key components of the terrestrial water cycle such as soil moisture, evaporation, and runoff are tightly linked with and affect terrestrial vegetation, climate, ecosystem services, and human society. Terrestrial vegetation-water interactions involve many processes regulating carbon, water, energy, and nutrient cycling. In this thesis, using data driven approaches, I focused on unravelling the interaction between the global- and continental-scale water cycle and vegetation functioning to better understand: (i) drivers of vegetation productivity and greenness with a special focus of root-zone soil moisture taken up by vegetation, and (ii) extreme events in the water cycle by illustrating the vegetation relevance for the drought influence into evaporation and runoff and for the generation of high river flows.

1.1 Motivation

In the context of global climate change due to increased greenhouse gases, vegetation is a particularly relevant topic because it modulates carbon, water and energy cycles (Monteith and Unsworth 2013). The response of terrestrial vegetation to global warming and increasing atmospheric CO_2 has been found non-stationary across space and time (Piao et al. 2017; Wang et al. 2020; Wang et al. 2014). Water supply is also important for vegetation growth, and soil moisture is one of the most essential water supplies (Miguez-Macho and Fan 2021). The relationship between vegetation productivity and soil moisture availability is still understudied due to the previous lack of consistent global data on soil moisture. Climate change involves increases of soil moisture drought's intensity and frequency in many regions over the last decades, and climate projections suggest an intensification of these changes (Dai, Zhao, and Chen 2018; IPCC 2021). Therefore, there is an urgent need to understand how and to what extent vegetation could react to changes in soil moisture across the globe and if there has been any change in its response during the last decades.

Previous studies have illustrated the relevance of the water cycle for global vegetation and the resulting carbon cycle, especially for dry ecosystems (Humphrey et al. 2018; Jiao et al. 2021; Liu et al. 2020). But there are still critical knowledge gaps such as spatiotemporal vegetation sensitivity to soil moisture globally and during the last decades: site-level studies revealed the differentiated sensitivity of vegetation to soil moisture at different depths, due to the interaction between near-surface and sub-surface soil moisture dynamics and root distribution (A et al., 2019; Seneviratne et al. 2010; Fan et al., 2017). However, this important aspect has not been explored globally yet, mainly due to a lack of consistent global soil moisture data at different depths. Addressing associated questions could provide a better understanding of the terrestrial vegetation dynamics and its water-driving processes. Over recent years, the growing suite of spaceborne remote sensing and ever-improving land surface models present an opportunity to better address these questions with over thirty-year estimates of vegetation greenness and soil moisture (Jiao, Wang, and McCabe 2021). In the thesis, I exploited new satellite data products, and process-based and statistical models to advance the understanding of vegetation-water interactions beyond the previous knowledge.

Spaceborne remote sensing observes vegetation greenness from the optical reflectance, which contributes a crucial share of productivity dynamics (Seddon et al. 2016; Tucker et al. 2005). Nevertheless, when focusing on short-term vegetation productivity during severe stress conditions e.g., soil moisture drought, greenness indices to represent vegetation productivity could underestimate drought influence (He et al. 2022; Stocker et al. 2019; Morton et al. 2014; Saleska et al. 2007). Instead, newly-launched satellite sensors measuring e.g., sun-induced fluorescence can better capture the efficiency of light absorption through photosynthesis and hence vegetation productivity (Doughty et al. 2019; Magney et al. 2019). Also, the new developments in microwave remote sensing could open new opportunities for monitoring vegetation drought response, biomass dynamics, and observed diurnal signals could infer plant hydraulics (Konings et al., 2022). Taking advantage of new observation opportunities, vegetation functioning and physiology variations can be quantified globally

to benchmark respective land system models and promote the understanding of vegetation responses to soil moisture drought.

Not only soil moisture influences vegetation growth, vegetation characteristics can also regulate soil moisture through evaporation, rainfall interception and runoff (Budyko 1974; Scheffer et al. 2005; Seneviratne et al. 2010). Studies about evaporation and runoff partitioning using the Budyko framework illustrated the importance of fractional vegetation cover (Chen et al. 2022; Zhou et al. 2015), while the application of vegetation relevance to extreme events e.g. drought propagation is relatively few (Orth and Destouni 2018; Van Loon 2015). Further, not only the total fraction of vegetation cover and vegetation functional properties could modulate drought propagation. For example, vegetation stomatal closure in drought-sensitive vegetation can reduce transpiration to prevent desiccation and mitigate drought consequences on the subsurface (Konings, Williams, and Gentine 2017), while some other types of vegetation increase transpiration and aggravate the short-term sub-surface water depletion (Zhao et al. 2022). Therefore, a better understanding of the propagation of drought into the water cycle is needed for the sake of the efficient implementation of the existing management options in the form of irrigation, dam operations, and restrictions on water consumption.

Not only shortage of water but also water excess can potentially damage vegetation functioning. Another type of hydrological extreme, the flood, is also one of the most damaging natural hazards, and high river flows can lead to flooding which may have severe socio-economic and environmental impacts (Kundzewicz and Kaczmarek 2000). Similar to the potential relevance of vegetation on drought propagation, the generation of high river flows is likely also modulated by vegetation dynamics or vegetation-formed catchment characteristics but with different biophysical processes such as interception capacity. Previous studies demonstrated precipitation as a predominant driver that generates high river flows or floods. In contrast, other drivers, including snowmelt and soil moisture could jointly regulate high river flows next to precipitation (Berghuijs et al. 2019). It is thus fundamental to understand a more comprehensive generating process of high river flows by accounting for the relevance of vegetation which can advance the respective model development (Brunner et al. 2021).

The structure of Chapter 1 is the following: In Section 1.2, I provide some background on terrestrial vegetation and its relationship with soil moisture; In Section 1.3, I introduce the terrestrial water cycle and its relationship with vegetation; In Section 1.4, I discuss recent technical advances in vegetation-water interactions. In Section 1.5, I outline main research questions and an overview of the next chapters.

1.2 Terrestrial vegetation and its relationship with water supply

1.2.1 Vegetation functioning

Vegetation regulating the carbon cycle

The global carbon cycle binds together terrestrial ecosystems, the atmosphere, oceans, and soil organic matter. However, atmospheric CO_2 has increased dramatically due to humans' fossil fuel emissions and land use changes, resulting in global climate change (Friedlingstein et al. 2022). Terrestrial vegetation can potentially mitigate the increasing rate of atmospheric CO_2 concentrations and feedback to climate. Generally, terrestrial vegetation absorbs 123 ± 8 SD petagrams of carbon per year through photosynthesis (Beer et al. 2010). About half of absorbed carbon is soon released to the atmosphere by plant respiration. The remains (net primary production) are stored as vegetation biomass, later transferred into the soil due to vegetation senescence, disturbance, mortality, or released by fire (Janzen 2004).

Vegetation photosynthesis, which is also referred to as gross primary production (GPP), is the process of absorbing light energy by green leaves and producing carbohydrates from CO_2 and water. And to do so, stomata open for CO_2 uptake and water is lost as transpiration. Hence, carbon sequestration through vegetation ties energy and water exchanges together (Bonan 2010). The simplified chemical reaction of photosynthesis can be described as:

$$CO_2 + H_2O + light \rightarrow carbohydrate + O_2 + H_2O \quad (1.1)$$

The actual reaction at the leaf level is more complex and related to three biochemical processes: light reactions to convert light energy into chemical energy, dark reactions to fix CO_2 into carbohydrates, and the diffusion process that stomata open to allow CO_2 to diffuse into the leaf. To mechanistically model leaf photosynthesis, Collatz, Ribas-Carbo, and Berry (1992) and Farquhar, von Caemmerer, and Berry (1980) firstly develop biochemical models using constraint functions on carboxylation to estimate photosynthesis by CO_2, and enzyme activities and the electron transport rate which depend mostly on temperature and radiation. Larger spatial scale applications are limited due to e.g., the extrapolating ability of local parameterisations (Anav et al. 2015). Remote sensing is then applied to derive large-scale parameterisations of vegetation photosynthesis which will be introduced in Section 1.4.1.

Vegetation regulating the energy and water cycles

Not all wavelengths of light energy can be absorbed for the usage of vegetation photosynthesis. Only photosynthetically active radiation (PAR) with wavelengths between 0.4 and 0.7 μm can be absorbed by foliar pigments such as chlorophyll and carotenoid. Thus, to monitor large-scale photosynthesis or GPP, a common light use efficiency model defines GPP as the absorbed PAR and the efficiency of each vegetation type to

convert light absorbed into the biochemical energy (e.g., carbohydrates and structure) through photosynthesis (Field 1991; Monteith 1977):

$$GPP = PAR \times fPAR \times \varepsilon \quad (1.2)$$

where *fPAR* denotes the fraction of PAR absorbed by the canopy, and *PAR* multiplying *fPAR* denotes the *APAR*, which is absorbed PAR. ε (gC MJ^{-1}) is the photosynthetic efficiency and is determined by the vegetation type, environmental stresses such as water supply, light, and temperature (Bao et al. 2022; Turner et al. 2003; Medlyn et al. 2002). For estimating large-scale GPP, remote sensing provides the critical inputs for this approach (more details can be found in Section 1.4.1).

When a plant absorbs light energy, it also requires water uptake from the root-zone soil moisture or the precipitation to do photosynthesis. At the same time of doing photosynthesis, the water flowing through vegetation experiences a phase change from liquid water to water vapor via transpiration. Transpiration at the leaf level can be calculated by stomatal conductance and the difference between intercellular and atmospheric vapor pressure divided by the total atmospheric pressure (Ehleringer, Hall, and Farquhar 1993). According to Fick's law, vapor pressure deficit (VPD) is often used to calculate total atmospheric pressure. As plant stomata has evolved a physiological compromise between CO_2 uptake and water loss as a result of evolutionary history, previous studies described first approaches that link stomatal conductance with photosynthesis to calculate transpiration (Collatz, Ribas-Carbo, and Berry 1992; Collatz et al. 1991; Ball et al. 1987).

Transpiration generally accounts for 61% ± 15% SD of the total land evaporation (Schlesinger and Jasechko 2014; Miralles et al., 2016), which is also commonly called as evapotranspiration to emphasize plant transpiration (Miralles et al. 2020; Hereafter I constantly use evaporation for the total land evaporation). The remaining contributions of evaporation are from soil evaporation, interception loss, and evaporation from water bodies, snow- and ice-covered surfaces (Schlesinger and Jasechko 2014). Site-level evaporation can be directly measured by the eddy covariance technique. The methodologies for monitoring evaporation are more mature than monitoring transpiration (Nelson et al. 2020; Zhou et al. 2016) and evaporation is an essential part of the surface energy balance. For this purpose, apart from a major focus on vegetation productivity, this thesis mainly discusses evaporation in vegetation-covered regions rather than transpiration. Nevertheless, large-scale evaporation can only be estimated by combining satellite remote sensing and physiological (or water or energy balance) models (with details in Section 1.4.1).

1.2.2 Hydro-meteorological drivers of evaporation and vegetation productivity

Drivers of evaporation

Two distinct climate regimes have been commonly recognized to characterize land surface evaporation: a wetter regime where evaporation is unresponsive to soil moisture increases and a drier regime where soil moisture increases induce evaporation increases (Budyko 1974; Eagleson 1978; Koster, Schubert, and Suarez 2009; Seneviratne et al. 2010). Evaporation in the wetter regime is thus energy (i.e., temperature and radiation) controlled whereas in the drier regime is water controlled e.g., soil moisture control (Gentine et al. 2019; Denissen et al. 2020). Evaporation and vegetation productivity are modulated by plant stomatal regulation and leaf area, so they share similar environmental drivers (Gentine et al. 2019). The concept of energy-water regimes can also be transferred to classify the controls of vegetation productivity.

Drivers of vegetation productivity

Long-term changes in vegetation productivity cannot be isolated from changes in atmospheric CO_2 or ocean-atmosphere oscillations (Monteith 1964), while the sub-seasonal to interannual variability of vegetation productivity is more directly regulated by a multitude of hydro-meteorological variables (Bloomfield et al. 2022; Gonsamo, Chen, and Lombardozzi 2016; Linscheid et al. 2020; Nemani et al. 2003; Piao, Wang, Wang, et al. 2020; Stocker et al. 2018). These hydro-meteorological controls on vegetation productivity are mostly non-linear not only in space (Jonard et al. 2022; Stocker et al. 2018) but can also be found in time such as for vegetation sensitivity to temperature (Piao et al. 2017). Main energy-related variables include temperature and solar radiation. Temperature determines the Rubisco activity and the rate of electron transport and limits vegetation productivity in boreal and temperate regions and cold seasons (Bernacchi et al. 2001; Kumarathunge et al. 2019). The estimated global average optimum air temperature is approximately 23 ± 6 ˚C, and the optimum temperature at the ecosystem level is lower than the leaf level due to leaf evaporative cooling. Above a potential optimum temperature, the foliar photosynthesis rate can be impaired (Huang et al. 2019). Incoming shortwave solar radiation benefits vegetation productivity due to a synchronous increase in PAR which regulates electron transport rate (Huang & Xia, 2019; Li et al. 2018), while GPP saturates under very high irradiance and suffers from its associated heat stress (Knohl and Baldocchi 2008). The increase of diffuse radiation show the opposite effect on light use efficiency compared to direct solar radiation, as more light diffuses into deeper canopy layers and relaxes light saturation of sunlit leaves with certain high irradiance (Bao et al. 2022; Knohl and Baldocchi 2008). VPD is calculated by the relative humidity and temperature and is another fundamental driver of vegetation productivity. VPD can be treated as an energy-related variable representing the atmospheric water demand. VPD commonly has a negative influence on GPP, as plants respond to rising atmospheric demand by partly closing stomata to reduce water loss (Fu et al. 2022; Novick et al. 2016); In some tropical forests, VPD promotes vegetation productivity due to increased light use efficiency from new leaf flushing despite the reduction in canopy conductance (Green et al. 2020).

In terms of water-related variables, antecedent precipitation is classically studied in controlling vegetation productivity, as precipitation is the original water input for the land surface, and vegetation productivity is stimulated principally by precipitation in semi-arid and arid areas (Li et al. 2019; Piao et al. 2011, 2020; Xu et

al. 2011). Simultaneous precipitation under cloudy conditions is strongly associated with decreased solar radiation and temperature, and is not an obvious control of vegetation productivity due to underlying confounding effects (Liu et al. 2018). Instead, root-zone soil moisture is the main and a more direct source for vegetation water uptake (Seneviratne et al. 2010; Stocker et al. 2018). Other water sources such as groundwater and bedrock water also influence vegetation activities, but they are more predominant when vegetation is under extremely severe root-zone water stress and has root plasticity to access these deep-water sources (Miguez-Macho and Fan 2021; Mu et al. 2021). But these water sources are harder to be studied at the global scale with only a few observations compared to soil moisture.

Soil moisture controls on vegetation productivity

From the mechanistic point of view, soil moisture dryness can reduce root and hydraulic conductance and hence leaf water potential, and stimulate chemical signals such as abscisic acid in some species, altogether resulting in decreasing stomatal conductance (Buckley 2019). For large-scale soil moisture controls on vegetation, a previous study explored the impact of soil moisture availability on the terrestrial carbon uptake (Green et al. 2019). Soil moisture variability and trends induces carbon flux trends of about two to three gigatons of carbon per year which is a large proportion of the total land carbon sink. A satellite-based study illustrates that soil moisture is the dominant driver of ecosystem production in semi-arid regions (Liu et al. 2020), while another model-based work suggests stronger soil moisture impact on interannual variability of vegetation productivity through some feedback that amplifies atmospheric dryness than the direct soil moisture effect (Humphrey et al. 2021). Studies evaluated the importance of VPD and soil moisture on GPP variability with conflicting results, leaving it an unresolved question of how the ecosystem reacts to soil or atmospheric dryness. Fu et al. (2022) then quantified the response function of tower-measured GPP by accounting for the interactions between VPD and soil moisture. Fu et al. (2022) demonstrates that GPP and related maximum photosynthetic rate have a consistently negative response to VPD, while the GPP response to soil moisture shows a first negative and then positive pattern depending on soil moisture amount. Nevertheless, terrestrial vegetation and its relationship with soil moisture is never a simple question. In fact, this relationship has been revealed to vary consistently in different regions, time periods, temporal scales, or soil layers.

1.2.3 Vegetation structure and physiology

Ecosystem functioning is measured by processes such as photosynthesis or evaporation and their resulting fluxes (Bonan 2010) with details introduced in Section 1.2.1. The emergent behaviour (e.g., fluxes) of terrestrial vegetation ecosystems encompass two main parts: vegetation structure and physiology. Vegetation structure can largely determine a potential functioning, and vegetation physiology determines an actual functioning capacity with additional environmental influence that are listed in Section 1.2.2.

Vegetation structure

Bonan (2010) defined ecosystem structure as measured by the amount of materials such as above-ground biomass, leaf area, and root biomass; From the remote-sensing point of view, vegetation structure can be observed with dynamic changes of different types of foliar cover, biomass, and plant height (Nelson et al. 1988; Zeng et al., 2022). One of the main study objectives of vegetation structure, foliar cover, emerges to be in a long research tradition, not only because it adjusts the magnitude and direction of radiation and matter exchanges between the land surface and the atmosphere, but also because it primarily results in changes in the remote sensing signals in the visible to near-infrared regions (Hobbs, Mooney, and Lulla 1990). To determine the fPAR and light interception, the fraction of leaf area per unit ground, leaf area index (LAI) products have been developed and made globally accessible since the beginning of 1980s (Fang et al. 2019).

LAI influences canopy conductance, the albedo of ecosystems, and aerodynamic roughness, resulting in surface energy partitioning and water flux processes. Williams and Torn 2015 illustrates that evaporative fraction is better correlated with LAI than soil moisture, and the land-atmosphere coupling can be underestimated using only a conventional correlation method between soil moisture and surface evaporative fraction in the Southern Great Plains. Forzieri et al. 2017 uses satellite observations to analyze how LAI regulates the terrestrial energy balance and finds that in boreal zones, increases of LAI contribute to a reduction of surface albedo, whereas in arid regions increases in LAI lead to an evaporative cooling.

Vegetation physiology

Physiological characteristics such as water or light use efficiency or leaf conductance also contribute largely to ecosystem functions. Still, they are hard to observe and understudied at the ecosystem level (Reichstein et al. 2014). Leaf hydraulic conductance is defined as the ratio of the water flow rate to the water potential gradient across the leaf (Sack and Scoffoni 2012). Because of this, ecosystem vegetation physiology can only be quantified as differentiated components of vegetation structure in explaining functioning. As shown in Figure 1.1, vegetation structure largely shifts incoming light's amount and quality for the pigment absorption for the photosynthesis process. At the same time, photosynthesis is also controlled by non-stomatal processes (i.e., metabolic processes) related to physiology such as the rubisco activity and electron transport rate. Vegetation hydraulics is also one of the main physiological regulations on plant transpiration, which involve soil, trunk, branch, and leaf hydraulic conductance in the soil-vegetation-atmosphere continuum (Konings, Williams, and Gentine 2017). When soil is dry and atmospheric demand is high, without early stomatal closure to prevent water loss, leaf and xylem water potential easily declines, leading to a high risk of xylem embolisms. Embolisms block later water refilling from the soil to the leaf during drought recovery periods which can cause plant mortality (McDowell et al. 2008). Different from such unprotected behavior, isohydric vegetation normally has stronger stomatal regulation to prevent xylem embolisms with early decreases of

transpiration but easy recovery and high resilience under drought, if vegetation does not suffer from carbon starvation (Konings and Gentine 2017).

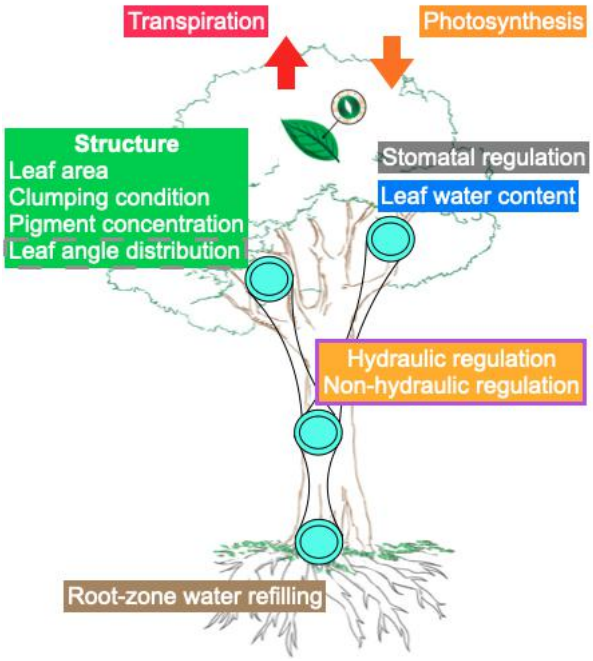

Figure 1.1. Vegetation photosynthesis and transpiration and their related structure and physiology. The figure is from Li et al. 2023, Nature Commun.

Vegetation structure VS. physiology

When comparing vegetation structure and physiology in controlling functions of terrestrial vegetation ecosystems, Migliavacca et al. (2021) quantifies significant proportions of vegetation structure (LAI, nitrogen content in vegetation and vegetation height) in explaining a set of functional properties, and the other two key traits that explain ecosystem functions are related to physiological characteristics i.e. water-use strategies and carbon-use efficiency. Stocker et al. (2019) indicates that using vegetation greenness in representing GPP could underestimate drought influence due to additional soil moisture downregulation on physiological processes. Yearly vegetation greenness and GPP dependency is largely determined by the climate condition of the ecosystem with declined coupling in wet regions (Hu et al. 2022). When focusing on the vegetation feedback to climate, Betts et al. (1997) finds the physiological and structural vegetation feedbacks are contrasting under increases of Anthropogenic CO_2. For example, CO_2 promotes water use efficiency and suppresses transpiration which increases surface sensible heat. On the other hand, CO_2 fertilization effect promotes LAI which increases surface albedo in most cases, and ultimately provides another climate feedback. Nevertheless, the CO_2 effect on vegetation physiology is not yet fully concluded (De Kauwe, Medlyn, and Tissue 2021). Another recent study emphasizing the plant physiological influence on the climate suggests that

maximum leaf gas exchange rate and water flow via the plant hydraulic continuum intensify land-atmosphere coupling (Anderegg et al. 2019).

1.3 Terrestrial water cycle and its relationship with vegetation

1.3.1 Water balance

Terrestrial water balance refers to a simplified expression that the terrestrial water storage (ΔS) is equal to the difference between precipitation (P) input and evaporation (E) output to the atmosphere and runoff (R) output to the ocean:

$$\Delta S = P - E - R \quad (1.3)$$

Note that there are some other water components on the right side of this equation, since not all precipitation reaches the ground surface (Bonan 2010). For example, interception is a part of precipitation that temporarily stores on plant surfaces with a large proportion of it directly evaporating back to the atmosphere. Interception generally occupies approximately 10-20% of annual total precipitation, but it remains one of the most uncertain fluxes lacking long-term observations (Zhong et al. 2022). Some winter precipitation falls as snow which can be intercepted by leaves or branches of plants, and can also be stored on the land surface and often turns to liquid water infiltrated into the soil or recharge the surface streamflow directly when the growing season starts.

Terrestrial water storage

Terrestrial water storage includes surface soil moisture, root-zone soil moisture, groundwater, vegetation water storage, river and lake water, and snow and ice. Terrestrial water storage can be measured by the Gravity Recovery and Climate Experiment (GRACE) satellite mission from the year 2002 by the anomalies of the Earth's gravity field (Wahr et al. 2004) with details in Section 1.4. Soil moisture is a key water state variable which is usually defined as the total amount of water within an unsaturated soil zone (Peng et al. 2017). Surface soil moisture supplies water for vegetation growth, and regulates near-surface temperature through soil evaporation (Seneviratne et al. 2010). Near-surface soil moisture can be detected by microwave remote sensing and coupled tightly with near-surface meteorology, while the sub-surface soil moisture is the water layer that matters predominantly for vegetation-related evaporation and can be estimated by the vertical extrapolation of near-surface soil moisture measurements together with data assimilation techniques (Seneviratne et al. 2010). Data assimilation techniques can benefit from soil moisture observations and other meteorological observations to optimize the parameters of modelling schemes and prediction performance. Soil moisture can be expressed in different units with a common one (m^3/m^3) expressed as the ratio of volume of water and soil (Robock et al. 2000).

Evaporation and runoff

Evaporation is also called the green water, and the blue water is the water in freshwater lakes, rivers and aquifers. Green-water evaporation and blue-water runoff are two main water fluxes in the terrestrial water cycle. Evaporation is fundamental for ecosystem services and food security and can be estimated by considering the natural forcing of energy availability. For example, potential evaporation is estimated by temperature as a surrogate for the amount of energy that evaporates water (Thornthwaite 1948). However, the actual evaporation can be further reduced by soil moisture deficit. The Penman-Monteith equation accounts for this aspect by adding the canopy resistance to express vegetation exerting controls on evaporation. It estimates the actual evaporation by a combination of energy input, atmospheric demand and canopy resistance (Monteith 1964). The Penman-Monteith equation also has limitations e.g., CO_2 effect on vegetation stomata not being included (Lemaitre-Basset, Oudin, and Thirel 2022; Milly and Dunne 2016). Therefore, other approaches to derive terrestrial evaporation by combining Earth observations have been developed which are discussed in Section 1.4.

The other main water flux, runoff, is defined as the amount of water draining from a certain land area and entering a river system. Runoff is also an important water component for human activities such as irrigation and power production, and it encompasses a fast component surface runoff and a slow component subsurface runoff (Kabat 2004). Surface runoff is related to precipitation infiltration capacity which depends on the actual soil moisture and soil texture: if the infiltration capacity is lower than the precipitation rate, the excess water can flow downhill. Subsurface runoff refers to soil water flowing laterally through the soil and discharge to a close channel. In land surface models, surface runoff is estimated based on a parameter of infiltration rate, and subsurface runoff is usually assumed to occur after exceeding the soil holding capacity (Kabat 2004). The Global Streamflow indices and Metadata Archive data from over 35000 stations can be used to upscale global gridded runoff products by combining meteorological inputs and modelling (Do et al. 2018; Ghiggi et al. 2021).

Partitioning of precipitation into evaporation and runoff

The partitioning of runoff and evaporation is essential for understanding the land surface dynamics and associated weather and climate. The Budyko framework by combining the water balance is a typical approach to do the partitioning at basin scale. The original Budyko approach relates the long-term evaporative ratio (a ratio between evaporation and precipitation) to its respective aridity (a ratio between potential evaporation and precipitation) (Budyko 1974). And runoff can be estimated as a function of mean long-term evaporation and precipitation by assuming a negligible water accumulation in a basin (Caracciolo, Pumo, and Viola 2018). The Budyko' s relationship is as following:

$$\frac{E}{P} = 1 + \left(\frac{Ep}{P}\right) - \left(1 + \left(\frac{Ep}{P}\right)^{\omega}\right)^{\frac{1}{\omega}} \quad (1.4)$$

Where evaporation (E) is assumed to be mainly controlled by a water-related variable, precipitation (P), and an energy-related variable, potential evaporation (Ep). The approach has been further improved by taking the influence of climatological and vegetation characteristics into account (Chen et al. 2022; Fu, 1981; Wang et al. 2022). Vegetation is one of the key parameters that control the precipitation partitioning into evaporation and runoff in terms of spatial variations and interannual dynamics (Gan, Liu, and Sun 2021).

1.3.2 Vegetation regulating the water cycle

Indirect vegetation influence on the water cycle

Indirectly, vegetation regulates the entire water cycle by shaping the surface albedo and roughness and transporting moisture to the air for precipitation recycling, and ultimately drives dynamics of soil moisture, evaporation and runoff (Duveiller, Hooker, and Cescatti 2018; Groner et al. 2018; Y. Li et al. 2015). In terms of energy inputs, shifts of vegetation composition and vegetation phenology can lead to changes in land surface albedo and hence available energy that can be used to evaporate soil water (Betts et al. 1997; Cescatti et al. 2012; Duveiller, Hooker, and Cescatti 2018). In terms of water inputs, tree restoration modelling shows that large-scale tree expansion can increase evaporation recycling and thus water availability by about 6% but decrease water availability by about 38% of the global areas with an additional effect of teleconnection to transport moisture to downwind regions (Hoek van Dijke et al. 2022). Moreover, there also exists lagged vegetation feedback on the water cycle. Global warming-induced increases in vegetation greenness in the early growing season can lead to decreases in soil moisture in the later growing season, because large parts of terrestrial water storage are consumed by preceding vegetation activities (Lian et al. 2020).

Direct vegetation influence on the water cycle

Using a causality analysis, Zhang et al. (2022) highlights direct vegetation controls on soil moisture variability. There are over 66% of the terrestrial vegetation areas showing bidirectional controls between soil moisture and vegetation growth; And out of these areas, 12% more areas show an exclusive controlling regime of vegetation on soil moisture dynamics. In fact, vegetation regulates the short-term variation of soil moisture, evaporation and runoff related to two main aspects: vegetation functional processes such as plant water uptake, and vegetation structural processes such as canopy interception and soil infiltration. Schlaepfer et al. (2017) suggests dramatic decreases of deep root-zone soil moisture during the growing season when implementing global climate models, related to increases in vegetation productivity and other physiological adaptation due to shifts in vegetation composition. Through vegetation structural processes, forest types and canopy structural changes result in different proportions of precipitation interception (Kermavnar and Vilhar 2017), and the higher root biomass can increase the rate of soil infiltration which enhances soil moisture availability and reduces surface runoff (Cui et al. 2019).

1.3.3 The relevance of vegetation on hydrological extremes

The result of a warmer and greener world

In the late 1980s, the climate was arguably considered as controlled by two main parts of the planet – the atmosphere and the ocean, while the role of vegetation on regulating climate system dynamics was under debate (Kabat 2004). Until the 2000s, the growing local-to-global observed and modelled evidence suggested terrestrial vegetation as an essential moderator of the climate system, not only a passive recipient of atmosphere-ocean dynamics and climate change (Cox et al. 2000). Related to increasing atmospheric CO_2 and global warming, terrestrial vegetation has shown larger areas of greening trends than browning trends over the last three decades observed by spaceborne remote sensing (Piao, Wang, Park, et al. 2020; Zhu et al. 2016). Global warming and ecosystem greening have multifaceted impacts on the water cycle and climate feedback as shown in Figure 1.2. Among these processes, evaporation trends are essential because it determines the surface energy partition and water transport to the atmosphere for recycling. Ensemble results of remote-sensing and machine-learning models consistently suggest that terrestrial evaporation has a significantly increasing trend by 0.62 mm per year (Pan et al. 2020; Zeng, Peng, and Piao 2018). Increased evaporation is tightly related to vegetation greening trends because the expansion of foliage area promotes plant transpiration and intercepted water evaporation which are partially counteracted by decreases of soil evaporation (Zhang et al. 2016). Multiple lines of evidence show that increases in evaporation and associated extreme precipitation scenarios increase the intensity and frequency of extreme events such as drought and flooding (IPCC 2021; Tabari 2020; Zhou et al. 2019).

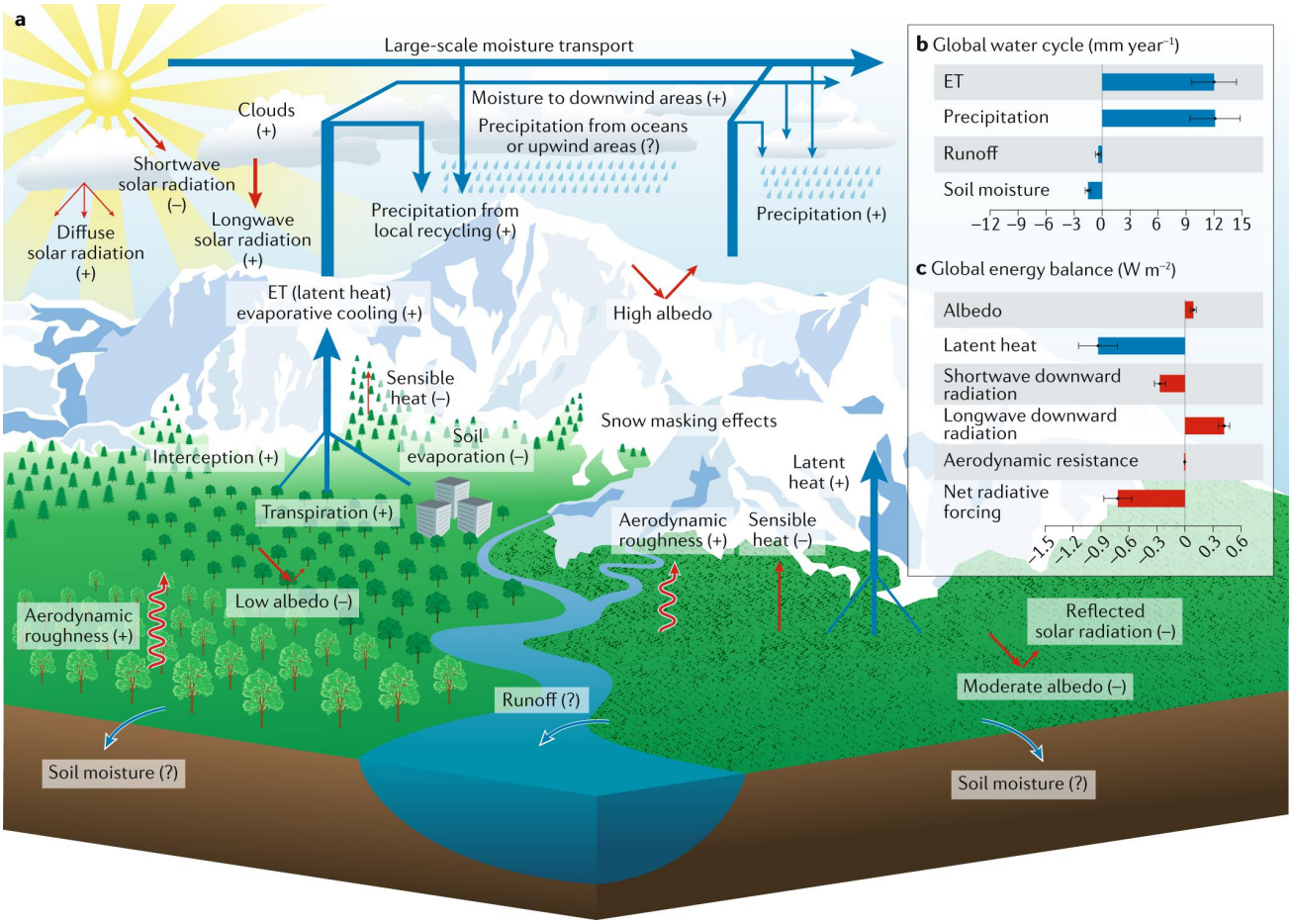

Figure 1.2. Schematic diagram summarizing the surface water cycle and atmospheric processes lead by changes in vegetation greenness (Piao, Wang, Park, et al. 2020). (a) indicates processes related to vegetation greenness and their increasing, decreasing or unknown trends denoted by symbols '-', '+', and '?'. (b) Summarizing changes of key water variables induced by greening such as evaporation increases at around 12 mm per year from 1982 to 2011. (c) Summarizing changes of key energy variables induced by greening with a unit of W/m^2 from 1982 to 2011. The error bars show the standard error of the estimated trends.

Drought

There are many well-known large drought episodes have occurred in recent years, such as the European droughts in 2003 and 2018 (Büntgen et al. 2021; Fink et al. 2004), the 2010 Russian drought (Barriopedro et al. 2011), the 2001–2009 millennium drought in Australia (van Dijk et al. 2013) and the 2012–2014 drought in California (AghaKouchak et al. 2014). Therefore, there is great scientific attention to drought related topics, advancing the understanding of drought causing mechanisms and its impacts (Van Loon, 2015). Key improvements are that the drought cause is not a simple lack of precipitation but can also be related to evaporation (Teuling et al. 2013), and the drought impact is not always unilateral, as some ecosystems suffer from drought, while others benefit from it.

However, there are still knowledge gaps about drought such as soil moisture drought propagation and respective processing speed and magnitudes. Soil moisture drought, defined as a period with abnormal soil moisture deficit and caused mainly by the precipitation deficits and excess evaporation (IPCC 2021). Very low temperatures can also induce winter liquid soil moisture drought, but it is out of the scope of this thesis that relates vegetation regulation on the water cycle. First studies addressing drought propagation were done regionally at the end of last century, and studying drought propagation has been continued with a focus mostly on groundwater or other hydrological components (Eltahir & Yeh, 1999; Peters et al. 2006; Van Loon, 2015; Van Loon, 2013). However, soil moisture determines land evaporation, while the drought propagation result is unclear which can be relevant for the renewable water resource. (Orth and Destouni 2018) firstly focuses on evaporation and runoff flux responses to soil moisture drought, and finds the strong relevance of vegetation greenness increases corresponding to evaporation increases and severe runoff decreases in northern Europe. Since then, a more comprehensive process understanding of drought propagation is needed by considering more multifactorial drivers that potentially determine evaporation-runoff trajectories under drought globally.

High river flows

Floods are expected to intensify under global change in some regions, caused largely by extreme precipitation (Kundzewicz and Kaczmarek 2000; Tabari 2020). Floods have various definitions with common ones such as abnormally high levels in river flows (Brunner et al. 2021). The relative impact e.g., areas of inundations is not included in such definition, while with more extreme thresholds of high river flows, the relative impact is partly correlated (Fischer, Schumann, and Bühler 2021; Zimba et al. 2018). Since precipitation is clearly the predominant driver of high river flows, the controlling regime of proportions of precipitation flowing into rivers is not crystal clear (Berghuijs et al. 2019; Blöschl et al. 2017; Stein, Pianosi, and Woods 2020). Previous studies made efforts to investigate the influence of climate and vegetation characteristics on spatiotemporal flow-generation mechanisms using the Budyko theory, while the understanding of vegetation aspects is not fulfilled compared to the climate aspects (Yang et al. 2021). By transferring two main characteristics of vegetation, functioning and structure, one can expect a better understanding of vegetation controls on precipitation-river flow generating processes and their relevance for extremes. Evaporation is one of the main processes that vegetation mitigates heavy rains in generating high flows when vegetation is water limited; But if vegetation is already under waterlogging, additional water inputs might damage vegetation growth and thus water uptake and aggravate high flows (Page et al. 2020). Vegetation structural changes also regulate high flow generation, since an expansion of canopy instantaneously intercepts some rains which can either reduce the subsurface streamflow, while less plant roots accelerate the surface streamflow due to a decreasing soil infiltration, and ultimately regulate the river flows in modelling studies (Lunka and Patil 2016; Camarena, Wübbelmann, and Förster 2022; Mendes et al. 2021). Therefore, a better understanding of the influence of vegetation and climate on regulating precipitation-generated extreme river flows is needed with more data-driven investigations.

1.4 Advances in observations and models

1.4.1 Spaceborne remote sensing

A better understanding of vegetation

Spaceborne remote sensing observes vegetation dynamics covering multidimensional vegetation functioning and structure, providing numerous opportunities to dig into vegetation performance under a changing climate (see Figure 1.3). Since Rouse et al. (1974) calculated the Normalized Difference Vegetation Index (NDVI) by red and near-infrared bands, NDVI has been commonly used as measuring vegetation greenness. NDVI shares a close relationship with photosynthesis activities, as chlorophylls absorb more red-band radiation and spongy mesophylls reflect more near-infrared radiation (Tucker et al. 1986). NDVI has been widely used as representing fractional PAR, and the simple calculation of NDVI with two bands can help to largely cancel out systematic biases e.g., sensor calibration and bidirectional effects. After that, LAI and fraction of PAR are produced as they are key biophysical variables in vegetation modelling. LAI and fraction of PAR are estimated by combining optical reflectance with radiative transfer models and field calibrations/validations (Myneni et al. 2002; Yan et al. 2016). There are many other vegetation greenness indices developed during the last thirty years for multiple ecological aims; Among them, the near-infrared reflectance of vegetation (NIRv) has been developed to overcome soil-reflectance mixed signals on NDVI by accounting for the proportion of vegetation reflectance (Badgley, Field, and Berry 2017; Dechant et al. 2022). Overall, these mentioned vegetation greenness indices are capable of studying long-term ecological questions since they can be derived from satellites since the 1980s.

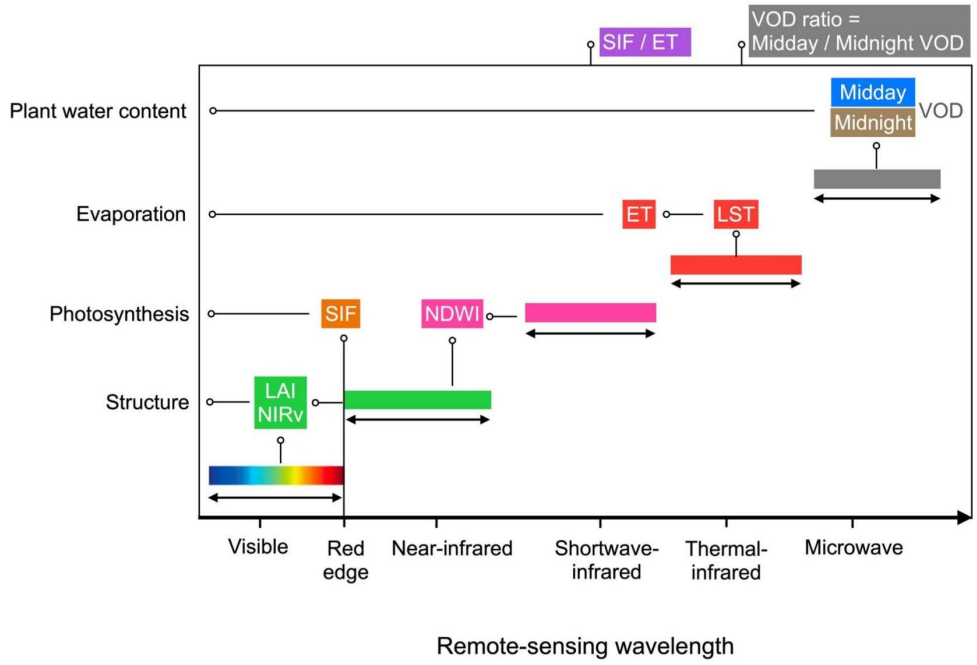

Figure 1.3. Overview of satellite-observed wavelength bands for representing vegetation dynamics. The figure is from Li et al. 2023, Nat. Commun.

Although greenness indices largely represent biophysical and structural properties of vegetation productivity, they have limited abilities to represent functioning under environmental stresses (Zeng et al. 2022), related to a less precise representativeness of light use efficiency in Equation (1.2) in Section 1.2.1. A new possibility called sun-induced chlorophyll fluorescence (SIF) emerges, with a strong positive linear relationship with measured GPP at the canopy or ecosystem level. SIF is a weak electromagnetic signal in the red-edge wavelength emitted by chlorophyll molecules and driven preliminary by absorbed PAR (APAR), and it contains the information of light use efficiency for carbon assimilation (Frankenberg et al. 2011; Joiner et al. 2011; Walther et al. 2019). SIF can be described as:

$$SIF = APAR * LUEf * fesc \quad (1.5)$$

Where *LUEf* is the light use efficiency of fluorescence and can be directly measured by passive or laser-induced active pulse-modulated methods (Coops et al. 2010). *fesc* is the escape probability of fluorescence photons from the canopy.

SIF retrievals require the high quality of satellite equipment, and atmospheric remote sensing specific sensors fit SIF requirements, including the Greenhouse Gases Observing Satellite, the Global Ozone Monitoring Experiment–2, and the Orbiting Carbon Observatory 2 (Guanter et al. 2012; Sun et al. 2018). To study short-term GPP responses to extreme hydro-meteorological conditions, SIF retrieval with coarse temporal resolution from these satellites might be limited by cloud and geometry-related biases (Saleska et al 2007; Morton et al 2014). Alternatively, the TROPOspheric Monitoring Instrument (TROPOMI) onboard the Sentinel-5p satellite

provides near-daily global SIF imagery with 16-day revisiting cycle, but the data are only accessible from 2018 (Magney et al. 2019; Doughty et a., 2019).

Focusing on longer wavelengths, shortwave-infrared band is related to a strong vegetation water absorption but also combined with other effects such as protein, lignin and cellulose content (Zeng et al. 2022). Due to water absorption, soil reflectance normally decreases in the shortwave-infrared band. The normalized difference water index (NDWI) based on the near- and shortwave-infrared bands is used to monitor moisture conditions of the land surface. Compared to NDVI, the NDWI was found to have a slightly better relationship with soil moisture fluctuations, while NDWI's representativeness of vegetation water content is understudied due to the difficulty of partitioning vertical water content from soil and vegetation (Gu et al. 2008; Jackson 2004). Using NDWI to study vegetation water stress, one needs to combine with another vegetation product to identify vegetated areas.

Land surface temperature (LST) from the thermal-infrared remote sensing is mechanistically linked with vegetation evaporative cooling effect (Farella et al. 2022). Spaceborne sun-synchronous orbits such as the Moderate Resolution Imaging Spectroradiometer (MODIS) satellites provide fine spatial-resolution imagery whereas geostationary orbits provide continuous diurnal observations but coarser spatial resolutions (Fisher et al. 2017; Xiao et al. 2021). Some global evaporation products are using LST as one model input due to its biophysical and physiological representations such as (i) the upscaling of eddy covariance-measured evaporation (Jung et al. 2019) and (ii) Surface energy balance based evaporation (Kalma, McVicar, and McCabe 2008). Both ET products contain uncertainties, such as an underperforming of machine-learning approaches in predicting stress conditions in (i), and the imperfect surrogate for aerodynamic resistance which does not account for the advection of sensible heat in (ii) (Mu et al. 2011). There are other methods to estimate evaporation without LST but using other observations. The Penman-monteith approach models MODIS evaporation by combining vegetation greenness indices and meteorological data, but the approach ignores the influence of vegetation physiological changes such as CO_2-induced changes in stomatal regulation; Or the water balance approach is used to calculate evaporation by the difference between global observations of precipitation and GRACE terrestrial water storage, assuming runoff is negligible at a coarse resolution (Zhao et al. 2022).

Vegetation optical depth (VOD) in the microwave remote sensing measures how much vegetation water content attenuates reflected or emitted microwave signals from the soil surface, so that VOD is influenced by above-ground biomass and the water content per unit of biomass (Zhang et al. 2019). Microwave frequencies are capable of observing vegetation irrespective of cloud cover. There are different frequencies of VOD products including L-band, C-band, X-band, and Ku-band VOD from lower to higher frequencies (and from higher to lower wavelengths). VOD with lower frequencies is more sensitive to the entire vegetation (such as leaves, branches and stems). In comparison, VOD with higher frequencies is more sensitive to the upper canopies, depending on the penetration depth (Konings et al. 2021). Note that high-frequency VOD such as

the L-band is sensitive to the radio frequency interference problem and highly influenced regions need to be masked (Konings, et al. 2017; Xu et al. 2022). Commonly used microwave satellite sensors e.g., AMSR-E and SMAP provide day- and night-time observations with every 2-3 day revisiting cycle, but these sensors are sensitive to soil moisture variations with potential confounding influence. The algorithms of VOD retrieval require to separate soil moisture information from vegetation water content which is still a challenge until now. There are some other uncertainties related to current VOD retrieval methods, e.g., they do not consider changes in canopy temperature and thus radiation emitting, and vertical and horizontal variations in canopy water content (Parinussa et al. 2016; Xu et al. 2015). More field campaigns for calibration and validation are urgently needed to improve retrieval methods (Konings et al. 2021). The state-of-the-art ecological applications of VOD products are related to large-scale drought responses of forests (Fan et al. 2019; Yang et al. 2022), live-fuel moisture content and wildfire warning (Forkel et al. 2023; Ma et al. 2021), and vegetation physiological properties (Konings & Gentine, 2017; Zhang et al. 2019).

Soil moisture and terrestrial water storage

At the same time, soil moisture observations have been progressively developed by spaceborne microwave remote sensing. Two types of satellite soil moisture are available: active microwave techniques detect the energy that the land surface reflects after transmitting an energy pulse, whereas passive microwave sensors detect the land surface self-emission (Nichols 2011; Peng et al. 2017). Common soil moisture products such as AMSR-E/Aqua surface soil moisture (LPRM), the Advanced SCATterometer (ASCAT), The Soil Moisture and Ocean Salinity (SMOS), the Climate Change Initiative (CCI), and Soil Moisture Active Passive (SMAP) have been evaluated against each other, validated against in-situ measurements from field campaigns, and are widely used for understanding vegetation dynamics, drought monitoring or model evaluations (Anoop et al. 2017; Dorigo et al. 2017; Ma et al. 2019; Wagner et al. 2013; Wigneron et al. 2021). However, these products can only observe the top layers of the soil down to around 5 cm with exact observed depths depending on the penetration depth of the microwave frequency and the soil wetness (Collow et al. 2012; Dorigo et al. 2017).

The root-zone soil moisture is still not explicitly observed by satellite observations. Still, it can be vertically extrapolated taking advantage of advances in data assimilation as well as continuously updating observations from the remote sensing and in-situ measurements (Peng et al. 2017). Benefitting from satellite observations, soil moisture reanalysis products with root-zone layers such as ERA5-Land, GLEAM, and MERRA-2 have been developed as benchmarks, and can be applied to topics related to vegetation-water interactions (Gelaro et al. 2017; Martens et al. 2017; Muñoz-Sabater et al. 2021). Since the robustness of reanalysis is still questioned due to uncertainties in their model schemes such as assumptions of evaporative rooting depths, in-situ measured soil moisture networks have been comprehensively used in machine-learning algorithms to upscale an independent global gridded soil moisture product (O et al. 2022; O and Orth 2021). Such kind of data-driven soil moisture products also have limited performance when predicting time-series data in data-sparse regions or for extreme climatic conditions. For this, applying GRACE terrestrial water storage (TWS)

provides an additional option of observational evidence of the water availability (Wahr et al. 2004), but TWS dynamics is mixed by groundwater so that the relevance of TWS on vegetation is likely not exceeding root-zone water availability. Also, vegetation normally has shallow roots to reduce the oxygen stress below the water table (Fan et al. 2017).

1.4.2 Data-driven and physical-based models

Data-driven explainable machine learning

Machine learning approaches are increasingly used in ecological and hydrological science, benefitting from rapid and sizable increases in Earth system observations (Reichstein et al. 2019). Since machine learning is data-driven, it does not require biophysical and physiological assumptions, so related datasets are an independent alternative to traditional physical-based modelling (Green et al. 2020; Stocker et al. 2018). Among various machine learning approaches, Random Forests are consistently used in this thesis, because they have shown robust performance in previous applications related to Earth system process understanding (Besnard et al. 2021; Nelson et al. 2020; Nicodemus, 2011; Zhang & Yang, 2020). Random Forests also have advantages such as simple hyperparameterisations, bootstrap aggregating, no assumptions on data distributions, and the ability to account for non-linear relationships between predictor and target variables (Breiman 2001). One ongoing challenge in the field of machine learning is to derive a functional relationship between response variables and predictors, which is often referred as explainable machine learning (Roscher et al. 2020). Recent advances in explainable machine learning can help to derive transferable scientific knowledge from machine learning practice.

In this context, SHapley Additive exPlanations (SHAP) dependence method is capable of isolating marginal contributions of a single predictor variable on the predicted target in a local effect for data subsets, or multiple predictors or effects from all data, and SHAP is commonly for tree-based models (Lundberg & Lee 2017). SHAP is calculated by the weighted average of the prediction difference between a model accounting for or not one predictor variable in all possible combinations and instances of predictor data, and weights are the reciprocal of the number of predictor features that are used in submodels. For details of SHAP algorithm, the reader can refer to (Lundberg and Lee 2017; Molnar 2022). Two main applications for the SHAP method on random forests in this thesis: (i) to understand the relative importance of predictor variables in terms of their contributions to the magnitude of predictions, and (ii) to infer the target variable sensitivity to a certain predictor to address climate sensitivity questions. These applications can essentially benchmark the land surface modelling (Figure 1.4).

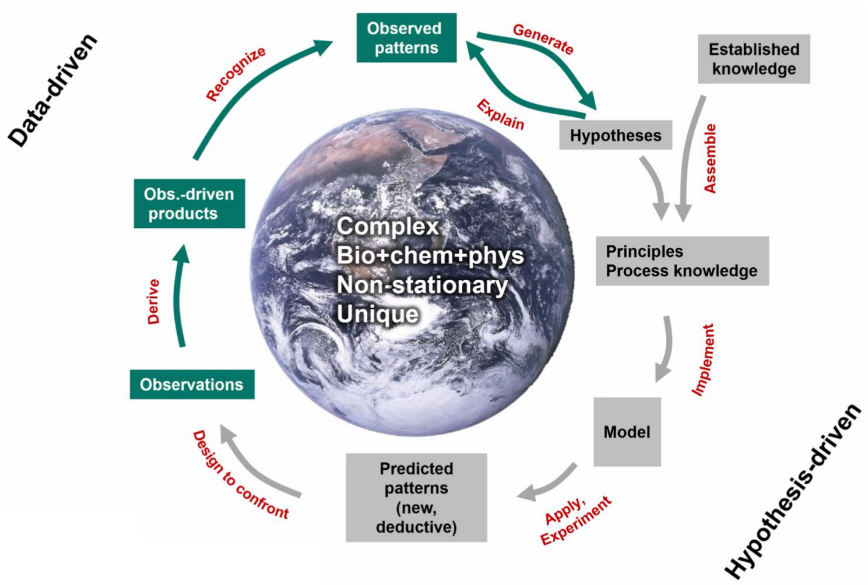

Figure 1.4. Research paradigms: data-driven approaches help to solve remaining puzzles in the Earth system processes. The figure is adapted from presentations from Markus Reichstein and Reichstein et al. (2019).

Physical-based land surface models

Land surface modelling was starting from the second half of last century (Sellers et al. 1997). The vegetation dynamics for the first time was modelled in a way that vegetation can absorb radiation, present a rough surface to enable a vertical mixing of sensible and latent heat, and exchange carbon and water through stomatal conductance. Since then, models began to explicitly incorporate vegetation biophysical and physiological dynamics, such as LAI and stomatal conductance, which can help to regulate hydrological cycle e.g., evaporation and associated climate feedback (Arora 2002). After twenty years of development, land surface models (LSMs) now encompass a broad and complex set of interrelated processes bridging the disciplines of biophysics, hydrology, biogeochemistry, ecology and human and societal science (Fisher & Koven, 2020) (Figure 1.5).

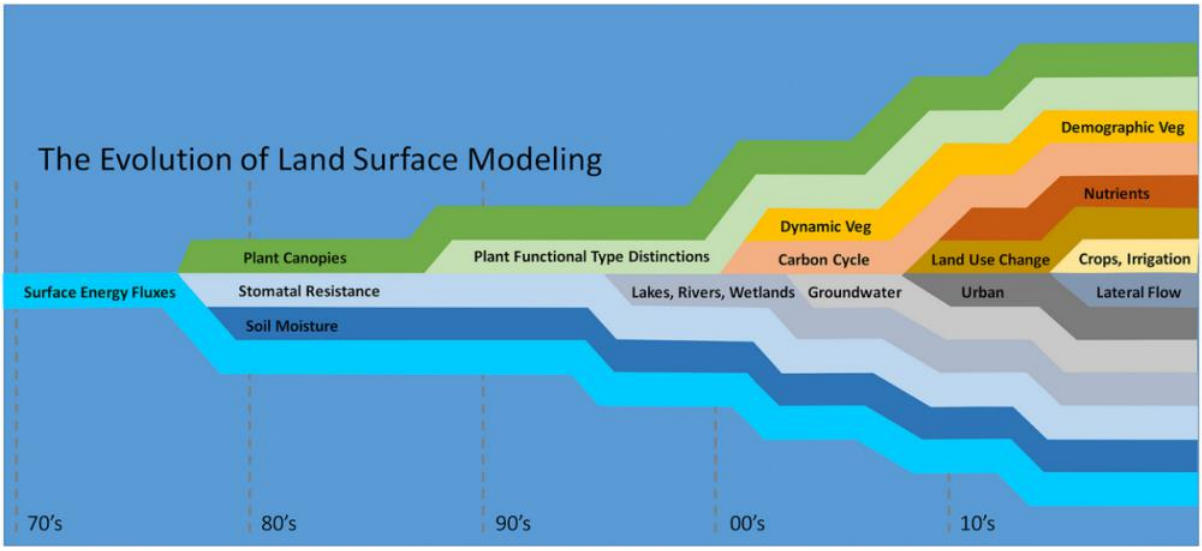

Figure 1.5. Schematic figure of the evolution of land surface models since the 1970s (Fisher & Koven, 2020).

However, the divergence between individual model outputs is still substantial in terms of the long-term carbon cycle responses to global warming (Arora et al. 2020; Rogelj et al. 2022), suggesting an urgent need of constraining terrestrial vegetation-water interactions in the carbon cycle in a better way (Humphrey et al. 2021). The performance of individual models in simulating vegetation functioning and structure depends on their representativeness of biophysical and biochemical processes such as vegetation-soil hydraulics (Trugman et al. 2018; Zhao et al. 2022). Other simplifications in the LSMs such as the strong reliance on plant functional types can also potentially limit model performance because plants can adapt to the local climate (Reichstein et al. 2014). Understanding not only long-term vegetation-water interactions but also their influence on extreme events is also crucially relevant, since climate extremes are projected to be intensified. Using observation-based data and data-driven approaches can better address these questions by understanding the uncertainties of climate projections in Earth system models and further improving models.

1.5 Research questions and thesis outline

The overall objective of this thesis is to better understand terrestrial vegetation-water interactions taking advantage of newly developed observations, models, and analysis approaches. Since now we are able to study more accurate vegetation and water objectives across the globe e.g., photosynthesis, ecosystem evaporation, and soil moisture, there are numerous scientific questions which can either be revisited or addressed for the first time. In this thesis, I would like to mainly discuss questions related to a better understanding of vegetation drivers, drivers of hydrological extremes, and respective model evaluations. Three main research questions are formed:

1. What is the relationship between vegetation productivity and water supply?

2. Can vegetation regulate hydrological extremes?

3. Can land surface models capture the observed vegetation-water interplay?

1.5.1 What is the relationship between vegetation productivity and water supply?

Since water supply is essential for semi-arid vegetation ecosystems, and soil moisture is one of the most accessible water sources, the relationship between vegetation productivity and soil moisture is not fully understood. Specifically, the hydrometeorological controls of vegetation productivity are not explicitly explored due to the lack of consideration of multi-layer soil moisture. Previous studies at large scales often used hand-designed approaches to represent the plant-available water such as lagged precipitation in certain months (Wu et al. 2015), while a more comprehensive investigation of the vertically resolved soil water dynamics has only been studied at the site level (A et al. 2019). Also, there are often linear assumptions when studying vegetation and meteorological drivers (Nemani et al. 2003). **Chapter 2** does not assume a linear relationship, and hypotheses that using multi-layer soil moisture, vegetation water controlling regimes can be better quantified, because shallow and deep soil moisture complement vegetation water uptake when they two decouple with each other. Different regions might show different importance and sensitivity of water controls on vegetation, related to types of climate and vegetation regimes. Due to recent advances of observation-based opportunities such as SIF for vegetation productivity and soil moisture reanalysis data at different depths, **Chapter 2** describes a study using SIF and hydro-meteorological data including multi-layer soil moisture to better understand soil moisture controls on vegetation productivity, and to quantify how climate and vegetation regimes regulate the relative importance of hydro-meteorological drivers on SIF.

As a result of ongoing climate change, soil moisture is declining in many regions (Greve et al. 2014), while it remains unclear how climate change has affected the sensitivity of global vegetation to soil water availability, and if there are potential hotspot regions with high vegetation sensitivity to soil moisture (Jiao et al., 2021; Seddon et al. 2016). Changes in vegetation water sensitivity are related to many processes such as water

limited frequency and durations, plant hydraulic regulation and composition changes (Gampe et al. 2021; Konings, Williams, and Gentine 2017, Carminati and Javaux 2020). There are still knowledge gaps about the global sensitivity of vegetation productivity to soil moisture across three decades as well as temporal changes in the sensitivity. **Chapter 3** assumes a stationary relationship between vegetation productivity and soil moisture as the first step and then exclusively study the potential trends of temporal relationships. The study then hypotheses multiple ecological and climatic drivers that could be spatially relevant on trends of sensitivity. **Chapter 3** uses the longest available satellite-based datasets and overcomes the assumption of a constant relationship between vegetation greenness and soil moisture across time by detecting trends of the sensitivity of vegetation greenness to soil moisture over 36 years. The derived trends are then analyzed in terms of their spatial patterns, to find potential drivers such as trends of precipitation and some other climate variables, as well as ecological characteristics such as vegetation compositions and long-term vegetation sensitivity to soil moisture.

Vegetation functioning is affected by its structure and physiology, whereas large-scale physiological response to soil moisture drought is not fully understood. Previous studies reveal vegetation physiological changes under water stress at the site level, e.g., with reductions in stomatal conductance as well as increases in enzyme activities when temperature is below the optimal threshold (Novick et al. 2016; Fu et al. 2022; Luo and Keenan 2020). However, large-scale physiological response to drought is still the knowledge gap which contributes to the uncertainties of global carbon quantification and climate projections (Stocker et al. 2019; Chen et al. 2022). **Chapter 4** hypothesizes a widespread effect of vegetation physiological response during drought and attributes different physiological changes by variables such as concurrent hydro-meteorological anomalies, overall climate and vegetation regimes, and drought duration. This study presents ecosystem functional responses to drought i.e., vegetation photosynthesis and evaporation, and differentiates structural and physiological components from the total functional responses. This study quantifies the large-scale physiological changes during drought development and recovery periods. It provides a better understanding of hydro-meteorological drivers and land-term land surface characteristics in moderating drought-related vegetation changes. A physical-based model is applied in this study which helps to link remote-sensing-derived changes to non-hydraulic and hydraulic physiological controls. In summary, **Chapters 2, 3, and 4** study the first research question from three perspectives, respectively: (i) explaining vegetation functioning using different soil moisture layers, (ii) quantifying trends in vegetation water sensitivity, and (iii) understanding physiological response to drought stress.

1.5.2 Can vegetation regulate hydrological extremes?

Vegetation structural and functional properties regulate the water cycle as mentioned in Section 1.3, but their separate roles in modulating hydrological extremes are understudied. Since drought and floods are among the most damaging natural hazards, additional knowledge on drought propagation or flood generation can inform a more efficient implementation of government management options. Previous studies focused on drought

propagation into evaporation and runoff across Europe using catchment-measured and modeled data (Orth and Destouni 2018), or focused on the global-scale drought propagation using model-based meteorological and hydrological indices such as the standardised precipitation-evapotranspiration index (Fuentes, Padarian, and Vervoort 2022). However, these data are less benefitted from multi-stream data assimilation and up-to-date algorithms of modelling (e.g., Machine learning), and the role of vegetation regulation on evaporation and runoff fluxes is not explicitly explored, so that a revisit of global drought propagation is worthwhile. Moreover, vegetation types and dynamics can result in evaporation and runoff anomalies (Teuling et al. 2013; O et al. 2022). For example, drought-tolerant vegetation might close their stomata and reduce transpiration, so that drought deficit propagates more into evaporation rather than into runoff, whereas non-sensitive vegetation might maintain transpiration but reducing dramatically regional runoff. There are certain knowledge gaps about the different importance of vegetation on evaporation or runoff when considering a comprehensive suite of other potential hydro-meteorological, climate and vegetation drivers. To address these questions, **Chapter 5** studies speed and magnitudes of global soil moisture drought into the green-water evaporation and the blue-water runoff using global gridded data-driven products. This study considers a comprehensive suite of vegetation, climate, soil, and topography characteristics, and human activities, as well as other relevant water fluxes to better understand their relevance in determining spatial patterns of different drought propagation magnitudes. Eddy-covariance evaporation is applied to support the usefulness of large-scale, upscaled evaporation data.

Major floods are characterized by a combination of hydrological extremes and antecedent basin properties such as the wetness. Different studies based on different catchments identified multifactorial floods or high flow drivers such as precedent precipitation, soil moisture, and snowmelt. However, there are few studies refer to many relevant drivers simultaneously and consider a comprehensive suite of vegetation-related drivers of high flow events. It leaves a knowledge gap in the joint understanding of a variety of observation-based controls of high river flows across continental-scale areas. **Chapter 6** describes a study of understanding generating processes of high river flows in European catchments where multifactorial vegetation and hydro-meteorological data are used to complement the general precipitation-flood generating mechanism. Catchments are selected based on near-natural dynamics of streamflow observations, while they could still include potential changes of land use and river regulation. Different temporal scales (daily, weekly, and monthly) are grouped to study the preceding conditions of vegetation and hydro-meteorological variables preceding high river flows, and different thresholds are used to study high-flow events at different extreme levels. Main drivers are then analyzed according to their relative importance across catchments, and the characteristics of vegetation and topography specific to each catchment are expected to regulate the relative importance of these high flow drivers. Overall, **Chapters 5 and 6** focus on drought and floods, respectively, to better quantify their associations with vegetation next to other hydro-meteorological variables.

1.5.3 Can land surface models capture vegetation-water interplay?

Although many LSMs continuously advance their representations of soil moisture effects on vegetation productivity (Cox, Huntingford, and Harding 1998; Trugman et al. 2018), they might still be limited by existing assumptions due to the complexity in actual processes (Eller et al. 2020; Ukkola et al. 2016). Evaluating model performance in terms of vegetation-water interplay are hence requisite. LAI is readily available as a key prognostic variable from LSMs, and a more accurate representation of LAI response to soil moisture stress requires the differentiation between soil layers (Forzieri et al. 2020; Rogers et al. 2017). Near-surface soil moisture primarily controls soil evaporation and precipitation infiltration and co-varies more with atmospheric conditions, while sub-surface soil moisture is a more relevant plant water source (Li et al. 2021; Miguez-Macho and Fan 2021). **Chapter 3** thus uses LAI and soil moisture from ensembles of LSMs to quantify the global sensitivity of LAI to soil moisture across near-surface and sub-surface soil layers and respective trends in the respective sensitivity. Global LAI sensitivity to soil moisture and its trends from LSMs is then compared with satellite-observation-based data. In addition to LAI, LSMs also simulate evaporation and runoff as these fluxes are essential components of the land energy and water balances, and of land-atmosphere exchanges of energy and water (Pitman 2003). Previous studies have found that the seasonal dynamics of ET are well captured in LSMs, while evaporation variability at the inter-annual scale and during water-stressed conditions is not properly reproduced (Berg and Sheffield 2018; Ukkola et al. 2016; Zhao et al. 2022). **Chapter 5** diagnoses the performance of LSMs in reproducing drought propagation into global evaporation and runoff fluxes, and studies if potential normal-condition biases of vegetation-water interplay in LSMs are associated with misrepresentation of drought propagation into evaporation under drought.

1.5.4 Thesis outline

In **Chapters 2-6**, each chapter presents one study with publication information indicated in each first page. Each study is introduced by following the order of abstract, detailed introduction, data and methods, results and discussion, conclusions, and appendix. **Chapter 7** provides conclusions about the main questions as addressed in **Chapters 2-6**, and limitations and an outlook for future research. References, author contributions, acknowledgements, curriculum vitae, scientific publications (including publications incorporated as thesis chapters and co-authored publications), and IMPRS certificate (including courses and outreach activities) are provided in the end of the thesis.

2 Global vegetation controls using multi-layer soil moisture

Abstract

The productivity of terrestrial vegetation is determined by multiple land surface and atmospheric drivers. Water availability is critical for vegetation productivity, but the role of vertical variability of soil moisture is largely unknown. Here, we analyze dominant controls of global vegetation productivity represented by sun-induced fluorescence and spectral vegetation indices at the half-monthly time scale. We apply random forests to predict vegetation productivity from several hydrometeorological variables including multi-layer soil moisture and quantify the variable importance. Dominant hydrometeorological controls generally vary with latitudes: temperature in higher latitudes, solar radiation in lower latitudes, and root-zone soil moisture in between. We find that including vertically resolved soil moisture allows a better understanding of vegetation productivity and reveals extended water-related control. Deep(er) soil moisture controlling semi-arid grasses and shrubs illustrates underlying deep(er) rooting systems as an adaptation to water limitation. This study highlights the potential to infer sub-surface processes from remote sensing observations.

This chapter is published as:

Li, W., Migliavacca, M., Forkel, M., Walther, S., Reichstein, M. & Orth, R. (2021). Revisiting global vegetation controls using multi-layer soil moisture. Geophysical Research Letters, 48, e2021GL092856. https://doi.org/10.1029/2021GL092856

2.1 Introduction

Terrestrial vegetation couples the global water and carbon cycles between the atmosphere and the land surface. Vegetation productivity is determined by a multitude of hydrometeorological variables (Monteith and Unsworth 2013; Nemani et al. 2003; Piao, Wang, Wang, et al. 2020). The underlying relationships are complex in time and space because of interactions among variables (Cox et al. 2013; Garonna et al. 2018; Pearson et al. 2013) and short-term variations of hydrometeorology potentially influencing ecosystems through nonlinear effects (De Keersmaecker et al. 2015; Fatichi and Ivanov 2014; Paschalis et al. 2015; Reichstein et al. 2013). The hydrometeorological controls of anomalies in global vegetation productivity are still not fully understood at the half-month time scale, because underlying variables were not investigated comprehensively. For example, previous research often used hand-designed approaches to represent the plant-available water (e.g., lagging precipitation in specific months). The knowledge gap contributes to uncertainties in assessing the sensitivity and resilience of ecosystems to different climate drivers (Sakschewski et al. 2016), and in future climate projections (Duveiller, Hooker, and Cescatti 2018; Feng et al. 2014; Novick et al. 2016).

Previous studies investigated dominant hydrometeorological controls of vegetation productivity at a global scale and across different ecosystems (Beer et al. 2010; Jeong et al. 2017; Li and Xiao 2020; Madani et al. 2017; Seddon et al. 2016; Walther et al. 2019; Wu et al. 2015). While these studies and recent gross primary production (GPP) estimates agree that vegetation in (semi-)arid areas is significantly impacted by soil moisture (SM) (Stocker et al. 2018; 2020), a corresponding global analysis including the impact of SM from multiple depths is lacking. Several studies have already highlighted the local relevance of multi-layer SM to ecosystems: root water uptake from deeper soil layers can help mitigate water stress and maintain plant transpiration (Migliavacca et al. 2009; Schulze et al. 1996); A et al. (2019) demonstrated divergent relative importance of surface SM versus deeper SM depending on land cover types; and Schlaepfer et al. (2017) simulated lowered sub-surface SM compared to surface SM which largely impact vegetation dynamics in temperate drylands. This way, distinguishing shallow and deep SM is expected to allow for a more accurate identification of global vegetation controls as the accessibility and availability of water for plants varies in space and time. For this purpose, the state-of-the-art ERA5 reanalysis provides multi-layer SM (Hersbach et al. 2020) that has been successfully applied in hydrometeorological studies (Kolluru, Kolluru, and Konkathi 2020; M. Li, Wu, and Ma 2020; Tarek, Brissette, and Arsenault 2020).

Reliable observation-based global photosynthesis proxies are available for recent years through satellite-derived sun-induced fluorescence (SIF). SIF data are increasingly used to study the relationships between global vegetation productivity and hydrometeorological drivers (Chen et al. 2021; Jiao, Chang, and Wang 2019; M. Li, Wu, and Ma 2020; Wagle et al. 2016; Walther et al. 2019; X. Yang et al. 2015; Zuromski et al. 2018). Besides, spectral vegetation indices and biophysical parameters from multi-spectral satellite instruments are widely used to study drivers of vegetation phenology and productivity (Buermann et al. 2018; Forkel et al. 2015). In this study, we consider SIF alongside two spectral indices (the normalized difference

vegetation index, NDVI, Tucker 1979; and near-infrared reflectance of terrestrial vegetation, NIRv, Badgley et al. 2017), and a comprehensive set of explanatory variables representing energy (temperature; radiation; vapor pressure deficit, VPD) and water availability (precipitation; multi-layer SM) to revisit global photosynthesis and greenness controls.

2.2 Data and methods

2.2.1 Remote sensing proxies of vegetation productivity and greenness

SIF is used as a proxy for variations in photosynthesis because it captures radiation emitted by chlorophyll molecules and is related to photosynthetic activity. We use one of the longest available satellite-derived SIF records which is based on the Global Ozone Monitoring Experiment–2 (GOME-2) instrument and ranges from 2007 to 2018 (Köhler et al. 2015). The raw global SIF observations at daily time scale are filtered to remove data based on (i) high solar zenith angles (>70˚), (ii) large differences to the normal local overpass time (2 p.m-8 a.m in the next day), and (iii) large cloud cover (>50%), as done by Köhler et al. (2015). We note that different levels of cloud filtering of the satellite retrievals yield similar SIF anomalies, such that a cloud cover threshold of 50% is a reasonable compromise between SIF data quality and quantity (Köhler et al. 2015).

To complement the photosynthesis analysis we use NDVI and NIRv as spectral vegetation indices (Huete et al. 2002; Badgley et al. 2017). NIRv is defined as NDVI multiplied by the near-infrared reflectance (Badgley et al. 2017). We obtain red and near-infrared reflectance from the MOD13C1 v006 product (https://lpdaac.usgs.gov/products/mod13c1v006/) in an original 16-day and 0.05˚ resolution. NDVI and NIRv are computed from data with quality flags 0 and 1 representing good and marginal data, thereby ignoring low-quality data.

2.2.2 Hydrometeorological data

We consider a comprehensive selection of energy and water-related variables from the ERA5 reanalysis. This involves the HTESSEL land surface scheme that accounts for spatial variations in soil types and assimilates spaceborne microwave instruments of surface soil moisture (Gianpaolo Balsamo et al. 2009; Hersbach et al. 2020). Even though soil moisture estimates from deeper layers in ERA5 are less constrained by observations, previous studies illustrated the agreement of ERA5 SM data in each layer with independent observations (Albergel et al. 2012; 2013; 2018; Hersbach et al. 2020; Jing, Song, and Zhao 2018; M. Li, Wu, and Ma 2020; L. Liu, Zhang, and Zuo 2014) (see Section 2.A.1 for details). Energy-related variables include temperature at 2-m height (temperature), surface downward solar radiation (solar radiation) and VPD, and the water-related variables are total precipitation (precipitation), SM layer 1 (0-7 cm), layer 2 (7-28 cm), layer 3 (28-100 cm) and layer 4 (100-289 cm). For comparison, we compute total SM by averaging values across the individual

layers weighted by their thickness. It is to note that VPD is related to the relative humidity and temperature. Hence, it is an energy-related variable but represents the demand of the water in the atmosphere.

2.2.3 Climate and Vegetation Regimes

To evaluate the results of our analyses, we compute the aridity index for each grid cell as the ratio between the long-term averages of net radiation (expressed in mm) and precipitation using ERA5 data (Budyko 1974). We distinguish climate regimes using long-term mean temperatures and aridity index. We use fractional vegetation cover data from the AVHRR vegetation continuous fields products (VCF5KYR, https://lpdaac.usgs.gov/products/vcf5kyrv001/) from 2007 to 2016 to classify the fraction of total vegetation cover, and the fraction of tree cover in total vegetation cover (Song et al. 2018).

2.2.4 Data pre-processing

The data pre-processing is illustrated in Appendix Figure 2.A1. All vegetation data and hydrometeorological data are aggregated to 0.5° spatial and half-monthly temporal resolution where SIF is available, and 16-day original NDVI and NIRv are linearly interpolated to half-monthly resolution. The first half-month consists of the first 15 days of the month, and the second half-month consists of the remaining days in the respective month. The study period is limited to 2007-2018 because of the SIF availability. In all SIF-based analyses we focus on data with SIF > 0.5 $mW/m^2/sr/nm$ to filter out sparse or dormant vegetation. This filtering is also applied in the NDVI and NIRv analyses, where additionally negative NDVI and NIRv values are filtered out. Grid cells are only considered in the analysis if more than 15 data points are left after filtering, and if the vegetation cover fraction exceeds 5%. For all target and predictor variables, we obtain half-monthly anomalies by subtracting the mean seasonal cycles determined by averaging values from all years for each of the 24 half-monthly periods between the first half of January and the second half of December. As we focus on relationships at short time scales, we remove long-term trends for each grid cell determined by a locally weighted smoothing filter (Cleveland 1979) with a smoothing span of 0.4. Moreover, this helps to filter out any signal introduced by potential satellite sensor degradation.

2.2.5 Identification of relative importance of hydrometeorological variables

Random forests (RF) is a non-parametric regression-based method requiring no statistical assumptions on predictor and target variables, and is designed to process large amounts of diverse input data (Breiman 2001). With this flexibility it is better placed than traditional statistical methods to detect nonlinear relationships among short-term hydrometeorological variations and vegetation productivity. We also note that our RF analysis can indicate plausible governing processes from emergent relationships, but it by construction does not suggest causality. In this study, all hydrometeorological anomalies are used as predictor variables, and anomalies of SIF and vegetation indices are employed as target variables per each grid cell, respectively (Appendix Figure 2.A1). RF training is done using information from each grid cell and the surrounding grid

cells (forming 3x3 grid cell matrices) to obtain sufficient data. The performance of the RF model is then evaluated by the fraction of explained variance in regression analysis carried out with the linear least-squares using cross-validation (hereafter referred to as R^2; see details in Appendix Section 2.A.2). Grid cells with R^2 lower than or equal to 0 are filtered out. Finally, two experiments are performed with RF models differing in the SM data used: total versus multi-layer SM alongside precipitation, VPD, solar radiation, and temperature.

Permutation importance is one of the most common methods for RF to measure the relative importance of each predictor variable (Lunetta et al. 2004, 20; Nicodemus 2011; F. Zhang and Yang 2020). It is inferred from the difference of error before and after a temporal permutation applied to the particular variable (Cutler, Cutler, and Stevens 2012; Gómez-Ramírez, Ávila-Villanueva, and Fernández-Blázquez 2019). To validate results of permutation importance we employ two more methods and to infer confounding effects we also quantify the sensitivity of SIF response to each predictor variable (see Appendix Section 2.A.2 for variable importance identification methods and sensitivity algorithm).

When considering multiple hydro-meteorological variables, the identification of global vegetation controls is challenged by potential high collinearity (Dormann et al. 2013) between some of the variables. Most previous studies did not consider more than three variables, thereby somewhat circumventing this problem while ignoring potentially important variables (Claessen et al. 2019; Garonna et al. 2018; X. Li and Xiao 2020; Seddon et al. 2016). Though RF are also challenged by the collinearity in the input data, they yield more robust results with noisy training data and have high interpretability (Zhang and Yang 2020), for example by inferring the sign of the sensitivity of vegetation productivity to particular predictor variables. As the computed relationships and their signs are consistent with previous literature and physical expectations (see Section 2.3), we note that RF are applicable in our multi-variate context. Further, collinearity can sometimes be mitigated through a pre-processing of the data by removing long-term trends or the mean seasonal cycle (see Section 2.2.4), as long as the collinearity is mainly driven by them, i.e., trends or seasonal cycles would be similar between variables while shorter-term dynamics are not.

2.3 Results and discussion

2.3.1 Model performance

The spatial patterns of RF model performance are similar between the two experiments using total and multi-layer SM with comparatively high R^2 (> 0.3) in central North America, central Eurasia, southern and eastern Africa, central Asia, and eastern Australia (Figure 2.1). The predictive performance is improved in most regions across the globe when using multi-layer instead of total SM. Vertical SM information improves model performance particularly in semi-arid regions such as Australia, central North America and central Asia (Figure 2.1c, d). In these regions plant rooting systems apparently adapt to compensate for local water deficits

which arise from divergent dynamics of surface and root-zone SM across time and space (Berg, Sheffield, and Milly 2017; Lian et al. 2020; Schlaepfer et al. 2017; Zhang et al. 2016).

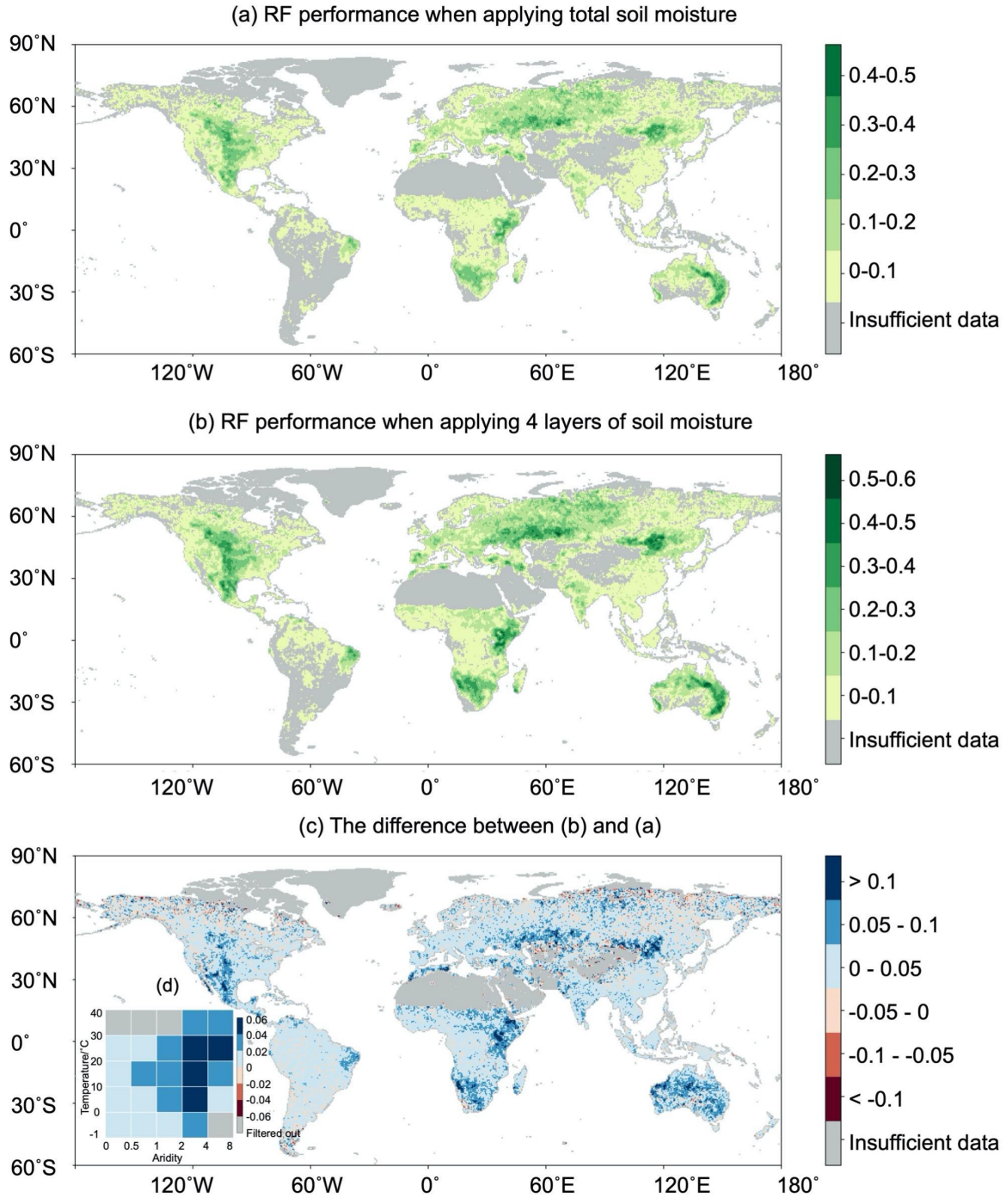

Figure 2.1. RF model performance (R^2) in predicting SIF when using (a) total and (b) multi-layer SM. (c) is the difference between (b) and (a); and (d) summarizes (c) across climate regimes (i.e., temperature and aridity).

Although the performance of SIF prediction is improved with multi-layer SM, the R^2 values are still relatively low, especially in large regions in South America. This relates to a typically significantly decreased model performance in predicting global vegetation productivity for anomalies compared to absolute data and mean seasonal cycles (Kraft et al. 2019). Further, it is related to input data quality where the satellite-based SIF retrievals are strongly impacted by noises in large regions in South America (Joiner et al. 2013; Köhler, Guanter, and Joiner 2015). Furthermore, using relatively coarser GOME2 pixels to derive the SIF data includes more residual cloud contamination than for example the finer-scale MODIS footprints (Joiner et al. 2013). Therefore, our RF models show much better performance in the case of NDVI and NIRv (Appendix Figure 2.A2) compared with SIF. In this context the performance of RF is generally lower in humid regions compared to drier regions, related to increased cloud cover which degrades the quality of the satellite retrievals as previously shown (Kraft et al. 2019; Linscheid et al. 2020). We include regions with weak model performance in the case of SIF for the subsequent analyses, and we believe that our methodology is robust, because (i) our main goal is to rank the relative importance of predictors instead of accurately capturing their dynamics; (ii) we find strongly similar global patterns of main controlling variables across SIF, NIRv and NDVI; and (iii) controlling patterns are largely in line with previous studies (Madani et al. 2017; Nemani et al. 2003; Seddon et al. 2016).

Additionally, we verify that the efficiency of using multi-layer SM in RF is not an artifact of over-fitting (Appendix Figures 2.A3, 2.A4), and we find similar results when using the root fractions in each soil layer as weights in the total SM vertical average computation rather than the layer depths (Appendix Figure 2.A5; root fractions are derived from ERA5 data by following ECMWF, 2020). See section 2.A.3 for uncertainties in vegetation data and model tests in detail.

2.3.2 Main hydrometeorological controls on global vegetation productivity

The global water- vs energy-related controls of vegetation productivity significantly vary between the two experiments involving total and multi-layer SM (Figure 2.2). Overall, in the multi-layer SM analysis (Figure 2.2b) temperature is identified as the main driver of SIF in the higher northern latitudes, solar radiation dominantly controls SIF in tropical regions, and VPD emerges as a main control in parts of the western Amazon forests (Green et al. 2020), eastern North America, northern Eurasia and eastern Asia. In between the tropics and the higher latitudes, where mostly (semi-)arid climate regimes are prevailing, water-related variables play the dominant role. Precipitation and surface SM (0-7 cm in ERA5) control SIF in central India, western Sahel and in central-southern Africa. Root-zone SM (7-28 cm in ERA5) mainly controls SIF in southern North America, southern Europe, and many parts of Eurasia, India and Australia. In general, root-zone SM (7-28 cm in ERA5) emerges as the most relevant water reservoir for vegetation productivity, while deeper SM (28-100 cm in ERA5) is particularly important in the transitional zones and temperate dry regions, such as central North America and southern Europe. To further test the assumption of energy variables misleadingly being detected as the main control where surface SM is the actual main driver due to the

insufficiency of the total SM experiment (energy variables negatively contribute to the variation of SIF), we repeat the analysis from Figure 2.2 while only considering variables with positive contributions to SIF prediction. The result confirms our hypothesis and illustrates that confounding effects can be minimized using multi-layer SM (Appendix Figure 2.A6; Appendix Section 2.A.4).

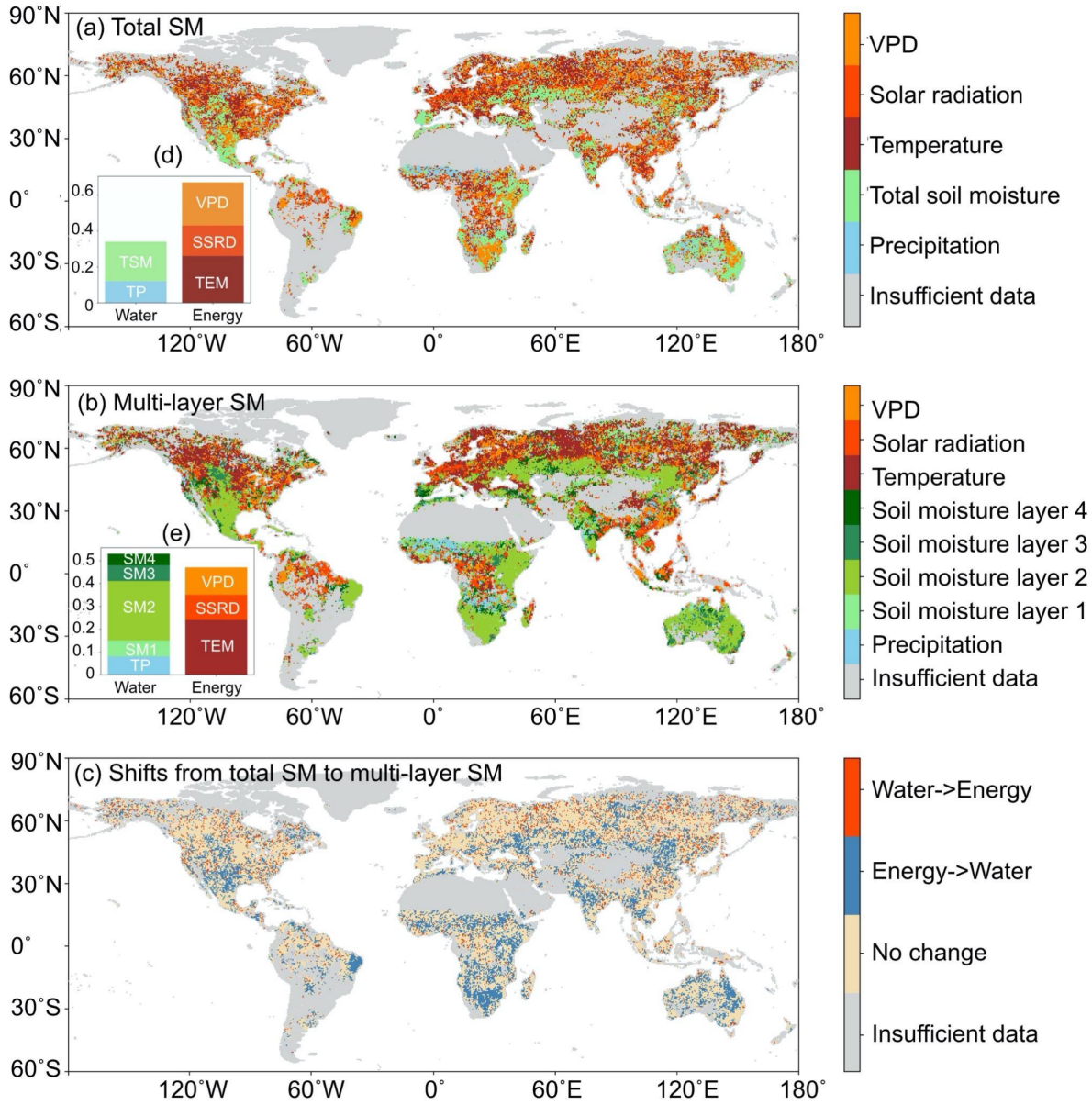

Figure 2.2. Main hydrometeorological controls on SIF using (a) total and (b) multi-layer SM. (c) Shifts between the energy and water controls from (a) to (b). Proportions of the study area where each variable is the most important factor are shown in (d) and (e). TP denotes precipitation; TSM denotes total SM; SM1, 2, 3, 4 denote SM in layers 1, 2, 3, 4 respectively; TEM denotes temperature; SSRD denotes solar radiation; VPD denotes vapor pressure deficit.

Confirming these SIF-based results, we find similar global patterns of the main controlling variables in the case of NIRv and NDVI (Appendix Figure 2.A7), even though they show extended SM-controlled regions. Furthermore, indicating physical meaningfulness of the obtained global patterns, we find that the sensitivities of SIF to the respective diagnosed hydrometeorological main controls are typically strongly positive (Appendix Figure 2.A8). This is also true for precipitation when it is identified as the most important predictor.

Next, we analyze the prevailing main controls across climate and vegetation regimes. Overall, controlling patterns across climate regimes in Figure 3a are in line with first-order constraints for evapotranspiration from Seneviratne et al. 2010, and from Denissen et al. 2020 in a European study. Root-zone SM (7-28 cm in EAR5) is identified as the main control in (semi-)arid regions. In humid regions energy variables are the most relevant, and overall temperature is the most important while solar radiation also plays a role. Solar radiation best explains SIF variability for forests in humid regions, because SIF is mechanistically linked through absorbed photosynthetically active radiation which depends on the variability of the irradiance (Li and Xiao 2020). In extreme warm and dry conditions, precipitation is identified as the dominant control. This could be explained as (usually weak) rainfall would not significantly wet the soil surface because of quick evaporation from warm surfaces (Seneviratne et al. 2010) and soil water repellency after long dry periods (S. Song and Wang 2019). The rain-induced evaporation in turn mitigates atmospheric water stress (high VPD), and thereby contributes to the precipitation control on SIF. In Figure 2.3d-f we show that grasses and shrubs with a low fraction of tree cover are most water-controlled, regions with intermediate tree cover are typically temperature-controlled, and regions with the highest tree cover are mostly radiation-controlled. Energy controls involve a relatively lower vulnerability of tree ecosystems to droughts than other ecosystems (Huang and Xia 2019), as droughts are typically associated with above-average solar radiation and newly developing leaves that can support photosynthesis (Hutyra et al. 2007; Li, Xiao, and He 2018; Orth and Destouni 2018; Wu et al. 2016; Yan et al. 2019). While the NDVI and NIRv analyses overall confirm the SIF results, they show extended water-related controls in arid regions and in tree-grass mixed regimes, consistent with previous findings (Walther et al. 2019). This is more pronounced for NDVI, potentially due to larger confounding effects of background brightness in NDVI as a response to SM changes, while NIRv contains more information about vegetation canopy structure and partly overcomes this issue (Badgley, Field, and Berry 2017; Badgley et al. 2019). Appendix Figure 2.A9 finally investigates jointly the role of fraction of tree cover and aridity and shows that the main hydrometeorological controls change in response to both of them.

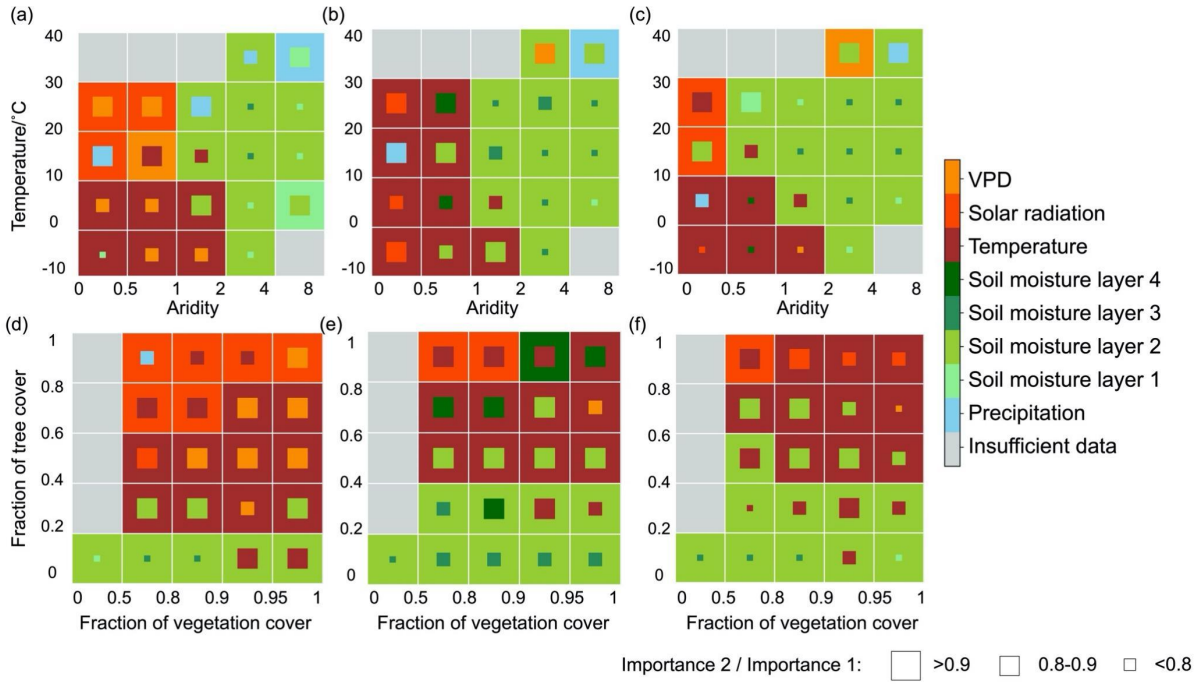

Figure 2.3. Main hydrometeorological controls on (a, d) SIF (b, e) NIRv and (c, f) NDVI across climate and vegetation regimes. The most important variables are indicated by the color of the temperature-aridity and tree -vegetation boxes, respective second most important variables are denoted by the inner square color, where the size indicates the relative importance compared to the most important variable. Temperature-aridity and tree-vegetation boxes containing less than 10 available data (grid cells) are shown in gray. The aridity index and the fraction of vegetation cover are visualized by non-linear sequences following their skewed distributions.

We furthermore analyze variations of hydrometeorological controls between early and late growing seasons. Temperature control can be found in larger regions in the early growing season compared to the later growing season, while the control of SM expanded in the late growing season (Appendix Figures 2.A10, 2.A11) is in line with previous studies (Buermann et al. 2018; Lian et al. 2020; Zhang et al. 2020). Overall, patterns for these two sub-periods do not differ much from the results for the entire growing season (See Appendix Section 2.A.4 for details).

2.3.3. Main water-related controls on global vegetation productivity

Focusing exclusively on water-related first- and second-order controls reveals that the most important soil layer varies across climate-vegetation regimes (Figure 2.4a-c). Shallow (7-28 cm in ERA5) and deep root-zone SM (28-100 cm in ERA5) are the most relevant layers for semi-arid grasses or shrubs, indicating that plants can adapt to water-scarce conditions at the surface with establishing deeper-reaching rooting systems (Fan et al. 2017). This is in line with previous but smaller-scale study from (A et al. 2019); further studies confirm that in dry surface soils in (semi-)arid regions, root plasticity and morphology support water uptake

from deeper soil layers (Schulze et al. 1996), for instance in local Mediterranean grass (Barkaoui et al. 2016), savannas ecosystems (Hoekstra et al. 2014; Nippert and Holdo 2015) or central Brazilian savannas (Oliveira et al. 2005). For even drier climate conditions, shallower soil layers become more relevant (Figure 2.4a-c), probably because intermittent vegetation productivity mostly benefits from rainfed surface SM, or deeper fine roots down to the water table capillary fringe play a role (Fan et al. 2017). Interestingly, towards humid conditions our analysis shows a dominant role of surface SM (0-7 cm in ERA5) and precipitation, while these regions are characterized by high tree cover with expected deep rooting systems. This could be due to frequent precipitation keeping surface soil layers wet such that trees absorb significant fractions of water through the near-surface roots (Li et al. 2007), while the dependence on deeper layers for trees during short droughts is not reflected here. Furthermore, we note that these regions are characterized by first-order energy controls (Figure 2.3) such that the results could also partly be an artifact as precipitation and surface SM are expected to co-vary with the dominant energy variables.

We validate our findings on the relative importance of the different soil layers by comparing them with multiple global rooting-depth products from two perspectives, effective root-zone water uptake and physical maximum rooting depths (Figure 2.4d-i). In general, rooting depths from Fan et al. (2017) and Schenk and Jackson (2009) although from the physical maximum perspective show similar patterns as our results with deepest roots in semi-arid areas and for non-tree vegetation such as grasses and shrubs. Canadell et al. (1996) states that maximum rooting depths of trees, shrubs and grasses can exceed 2 meters, respectively. Our results indicate that grasses and shrubs use their deep roots more often such that we can detect a respective relevance of deep soil moisture reservoirs while trees predominantly use shallow roots as water is often easily accessible in wet surface layers. See Appendix 2.A.5 for data details.

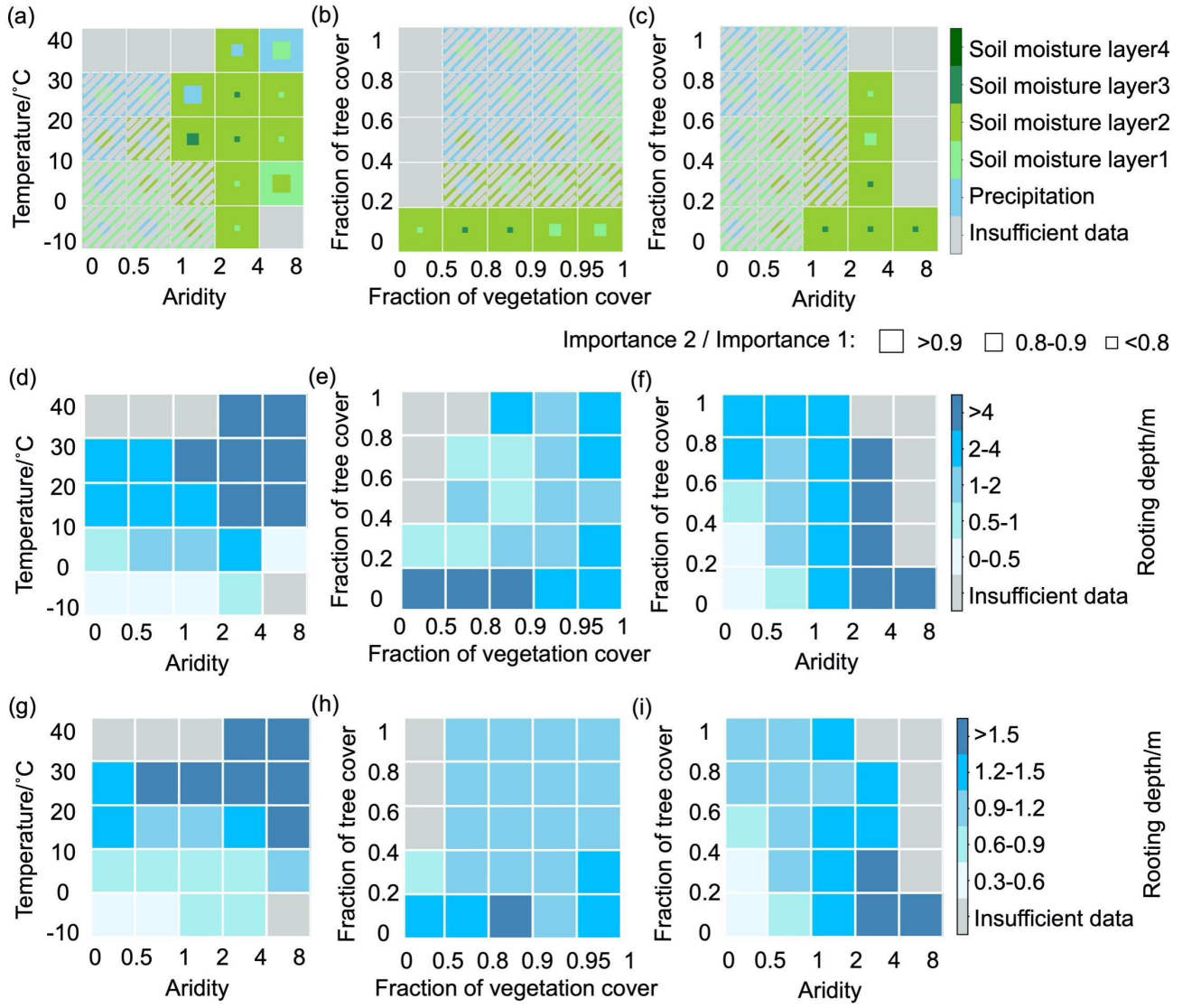

Figure 2.4. (a-c) Main water-related controls on SIF, and distributions of rooting depths from (d-f) (Fan et al. 2017) and (g-i) (Schenk and Jackson 2009) across climate regimes and vegetation characteristics. (a-c) Similar to Figure 2.3 but focusing on SIF and water-related controls only. Dark-gray hatching indicates that an energy variable is identified as the main control on SIF in these boxes in Figure 2.3.

To illustrate the robust importance-based analyses we use: (i) Spearman correlation (Appendix Figure 2.A13) and (ii) SHAP feature importance (Appendix Figure 2.A14) and find similar results. Further, we employ alternative SM products, namely GLEAM, MERRA-2 and SoMo.ml (see data details in Appendix 2.A.5; Appendix Figure 2.A15), all of which lead to similar results as found with the ERA5 SM. We note that using a suite of SM products derived independently with physical models or machine learning approaches highlights that our results are not an artifact of one single SM model. In particular we find across these datasets that generally shallow soil layers are more relevant in humid regimes and deep(er) soil layers are more important in semi-arid areas and for non-tree vegetation such as grasses and shrubs, confirming our previous results, while the layer depths and amounts are different across products and cannot be readily compared. In addition,

we convert multi-layer soil moisture to water potential. Thereby, the water potential is computed as the difference between actual soil moisture and the permanent wilting point which is inferred from the soil texture in each grid cell (ECMWF, 2020). We find similar results indicating no major influence of the considered water availability metric on our results (Appendix Figure 2.A16), as the role of different soil types might be diluted at large spatial scales where usually different soil types coincide in individual grid cells. Furthermore, we acknowledge, however, that our analyses do not consider water storage strategies related to hydraulic traits (Matheny et al. 2015) and irrigation effects.

2.4 Conclusions

This study illustrates that vegetation productivity relies on water from different soil depths while these characteristic depths vary with climate and vegetation types. In particular, we elucidate at the global scale that semi-arid areas and vegetation types such as grasses and shrubs are controlled by comparatively deep layers as they have deep rooting systems. This complexity is not yet sufficiently acknowledged by dynamic global vegetation models (Guimberteau et al. 2018; Schaphoff et al. 2018; Warren et al. 2015) which apply globally constant soil depths, and do not account for deep rooting strategies or potential physical barriers for vertical soil water transport (Sakschewski et al. 2020). This highlights the relevance of our results, and of our approach illustrating that sub-surface soil processes can be inferred with the help of surface-based Earth observations. Further, we compare the hydrometeorological controls of vegetation productivity obtained with different respective proxy metrics. SIF is more strongly related to photosynthesis, compared with NDVI and NIRv, but SIF data are only available for recent years. Our results show that NDVI and NIRv yield similar spatial patterns and largely confirm the SIF-based results. However, we find extended water-related controls in the cases of NDVI and NIRv, especially in temperate wet regimes, probably induced by changes of soil background reflectance as a response to soil moisture changes. Overall, our study contributes to an advanced understanding of the global-scale partitioning of hydrometeorological controls of vegetation productivity by benefitting from the ever-growing suite of global eco-hydrological data streams.

2.A Appendix

This appendix includes the supplementary text and figures of the presented publication.

2.A.1 ERA5 soil moisture evaluation

While the ERA5 soil moisture product is in principle derived with a land surface model and therefore can potentially reflect its shortcomings. The assimilation of observations from spaceborne microwave instruments provides quantitative information for the surface SM, facilitating the retrieval of root-zone SM (Albergel et al. 2012). The model structure and parameterization governing the root-zone soil moisture dynamics has been thoroughly validated against related variables such as runoff or the surface heat fluxes (Balsamo et al. 2015; Gianpaolo Balsamo et al. 2009). Therefore, we chose to use ERA5 multi-layer soil moisture in our analysis, even though it is necessarily less constrained by direct observations and larger uncertainties are expected for deep soil layers than for surface layers (Drusch et al. 2009).

Many studies evaluated soil moisture products from the European Centre for Medium-Range Weather Forecasts (ECMWF) (e.g. ERA5, ERA-Interim) against in-situ observations from global hydrology networks (Albergel et al. 2012; 2013; 2018; Hersbach et al. 2020; Jing, Song, and Zhao 2018; Li, Wu, and Ma 2020; Liu, Zhang, and Zuo 2014). As listed above, most comparisons of reanalysis SM products agreed that ERA-Interim from ECMWF reproduces well the spatial and temporal dynamics, and ERA5 as the newest released product from ECMWF clearly enhances the simulation performance over ERA-Interim by improving the data assimilation from higher resolutions and better understanding the global balance of precipitation and evaporation.

Different layers of SM were also evaluated separately from the top down to 1 meter in many studies. Li, Wu, and Ma (2020) found that ERA5 total SM shows a higher consistency with observations than the other products at the network scale, while MERRA-2 is closer to the observations regarding linear trends. Based on the hydrology network in Australia, Jing, Song, and Zhao (2018) evaluated first three layers in ERA-Interim SM, and concluded that all the evaluated layers of SM can capture temporal features well except for the depth of 28-100 cm in the winter, and the layer of 7-28 cm has higher absolute and temporal accuracy. Albergel et al. (2012) also evaluated the good quality of multi-layer SM from ERA-Interim even over 1 meter.

2.A.2 More details in the Random Forests (RF) modelling

During RF model training, the data are randomly split 63% into training and the remaining into cross-validation when separating between decision trees, because the bootstrap method is used in RF (Leo Breiman 2001; L. Breiman 1996). After training, the performance of the RF model is evaluated at each 3x3 grid cell matrices by computing the R^2 between the modelled and observed target variable for data that was not used for training (out-of-bag data) (L. Breiman 1996).

Permutation importance measures the relative importance of each predictor variable from the difference of errors before and after a temporal permutation applied to the particular variable (Cutler, Cutler, and Stevens 2012; Gómez-Ramírez, Ávila-Villanueva, and Fernández-Blázquez 2019). When RF performs regression, the difference of R^2 instead of errors is calculated, and the permutation importance generally ranges from -1 to 1, but a negative value indicates no efficient information from a predictor. To validate results of permutation importance we employ two more methods: (i) Spearman correlation (Zwillinger and Kokoska 1999) and (ii) SHapley Additive exPlanations (SHAP) feature importance which measures marginal contribution of each predictor to the target variable (Lundberg and Lee 2017; Sundararajan and Najmi 2019).

In addition to the determination of the most relevant hydrometeorological controls we study the sensitivity of the vegetation response to each predictor variable. The sensitivity is determined by the slope from fitted linear quantile (median) regression between the SHAP dependence of a target variable and a predictor variable (similar method was applied by Forkel et al. (2019) using partial dependence plots), as SHAP dependence enables to measure the marginal effect each predictor variable has on the target variable for individual and global explanations (Lundberg and Lee 2017). The magnitude and the sign of sensitivity complement the information in importance identification.

All data-processing and analyses are done with Python 3.7 by using the NumPy 1.16.1 (Oliphant 2006), Statsmodels 0.11.1 (Seabold and Perktold 2010), Scikit-learn 0.22.1 (Pedregosa et al. 2011), Matplotlib (Hunter 2007) and shap 0.35.0 packages (Lundberg and Lee 2017).

2.A.3 Uncertainties in vegetation data and model tests

NDVI can saturate because of red band reflectance in high biomass regions such as the Amazon, as it has been reported in previous studies (Huete 1997; Huete et al. 2002). But a significant linear relationship between tower-based daily mean SIF and GPP has still been found even when NDVI is clearly saturated at high GPP (Yang et al. 2015). In fact, unlike vegetation optical indices, SIF is mechanistically linked to photosynthesis, does not saturate in the tropics, and has been shown to have a near-linear relationship with ecosystem GPP at weekly and monthly scales (Green et al. 2020; Guanter et al. 2012). (Magney et al. 2019) suggested that SIF is less affected by clouds and is not prone to saturate with high leaf area.

Dense canopy has the potential to confound the relationship between SIF and GPP, as the fluorescence escaping probability is associated with canopy structure (Dechant et al. 2020; Fournier et al. 2012; Migliavacca et al. 2017). However, Dechant et al. 2020; Zeng et al. (2019) show that SIF is highly sensitive to canopy structure that underlies, in part, the strong correlation between SIF and GPP, particularly at the seasonal time scale. Besides, previous literature suggests that SIF and GPP could decouple under extreme environmental stresses due to leaf-level photosynthetic regulation (Helm et al. 2020; Wohlfahrt et al. 2018). In our analysis, we consider the full variability range of SIF conditions where extreme conditions only represent

a small fraction of the data. We therefore expect that changing SIF-GPP relationships under extreme conditions do not have a major effect on our analyses.

Further, sun-sensor geometry could also confound SIF-GPP relationship, as Köhler, Guanter, et al. (2018) illustrated geometry effects in Amazon forests. While the differences accounting or not for the observation angle is not that much regarding to the correlation between SIF and GPP (He et al. 2017), and our study is focusing on partitioning global controls on vegetation productivity in global domain using half-month data anomalies, and thereby the influence of observation angles would not conclude to a different pattern of global vegetation controls with consistent main results coming from SIF, NIRv and NDVI.

We perform further RF model experiments to investigate if the added skill in the case of the multi-layer SM is related to the increased number of predictor variables, and therefore an increased flexibility of the model, or to the additional information contained in the individual layers compared with the total SM. First, the experiment of multi-layer RF (4 variables) performs better than the experiment of 5 SM variables, showing that the enhanced performance is not exclusively due to the increased number of variables and hence increased flexibility of the RF model (Appendix Figure 2.A3). We note that the fifth layer is supposed to provide no additional information as a weighted average from the other four predictor variables it is. Second, regionally enhanced performance can be found when replacing total SM with individual layers (Appendix Figure 2.A4), indicating that additional information can be explored by the RF model from SM from individual layers.

2.A.4 Complemented analyses about main hydrometeorological controls on Sun-induced fluorescence (SIF)

Main Hydrometeorological controls on Sun-induced fluorescence (SIF) when only considering positive variable contributions

We repeat the analysis from Figure 2.2 while only considering variables with positive contributions to SIF prediction. The result shows that consistent proportions of water-related controls can be found when using multi-layer SM, while around 4% of the study area is shifted from energy- to water-control in the total SM experiment, confirming potential confounding effects can be minimized using multi-layer SM (Supplementary Figure 2.A6). However, total SM does not provide sufficient information to the RF model to detect water-controlled regions, because confounding effects may mislead main controls identification. For example, energy-related variables can misleadingly be detected as main controls in the total SM experiment in the case that surface soil moisture is the actual main driver: temperature and VPD co-vary with surface soil moisture, while its variations are overshadowed by that of deeper layers in the total SM information.

Main hydrometeorological controls on Sun-induced fluorescence (SIF) in the early and late growing seasons

The main hydrometeorological controls which we determine for the entire growing season may vary from early to later periods. To analyze potential differences, we separate the growing season into two periods, an early period before the first peak of the seasonal cycle of SIF (half-month with the highest SIF across each year) in each grid cell, and a later period including the peak and the time thereafter. In the early growing season, larger regions show temperature control, such as northern Europe, while in the late growing season, the control of root-zone soil moisture (7-28 cm in ERA5) is expanded, such as in central North America and south Europe (Appendix Figure 2.A10). Despite the difference in cloud cover between the early and late growing season periods we find overall similar results but expected increased water controls following the drier conditions (Appendix Figure 2.A10), highlighting that cloud cover likely has no major influence on our results. Elevated evapotranspiration in the early growing season can induce water deficits in the later growing season in previously energy-limited ecosystems, and hence soil moisture plays a more important role in vegetation productivity in the later growing season, especially in the transition zone of climate and vegetation types (Appendix Figure 2.A11; Zhang et al. 2020; Buermann et al. 2018; Lian et al. 2020). Patterns for the whole growing season are generally consistent with these two partitioned periods (Figure 2.3a, d; Appendix Figure 2.A10a). We note, however, that alternative approaches of distinguishing between early and late growing seasons can affect these results, especially for regions with complex growing season timing, even though the main conclusion with the increased water-control is expected to hold.

2.A.5 Additional global soil moisture and rooting-depth products

To further complement our results on the relative importance of vertical SM layers, we include three global model-based products of vegetation rooting depth distributions from (i) (Fan et al. 2017) (https://wci.earth2observe.eu/thredds/catalog/usc/root-depth/catalog.html), (ii) (Schenk and Jackson 2009) (https://daac.ornl.gov/ISLSCP_II/guides/ecosystem_roots_1deg.html), and (iii) from (Yang, Donohue, and McVicar 2016) (effective plant rooting depth, https://data.csiro.au/collections/collection/CI19813).

Rooting depths from Fan et al. 2017 and Schenk & Jackson, 2009 show similar patterns with deepest roots in semi-arid areas and for non-tree vegetation such as grasses and shrubs (Figure 2.4d-i). Less agreement is found with the rooting depths from Yang et al. 2016 (Appendix Figure 2.A12). The former two products were rooting-depth data driven by extrapolation, and the one from (Yang, Donohue, and McVicar 2016) was instead derived by a hydrological model by balancing the trade-offs between carbon costs and the benefits of deep rooting. From a perspective of maximum physical rooting depths modeling, actual effective water uptake may partly diverge inferred by the former two products due to ignored seasonal variability of hydraulic traits in the model framework, while the third one may largely underestimate effective roots in grasses, shrubs and savannas without using deep rooting strategies (Sakschewski et al. 2020).

To validate our findings we also use alternative SM products: (i) MERRA-2 surface and root-zone SM (Gelaro et al. 2017), (ii) GLEAM v3.3 surface and root-zone SM (Martens et al. 2017), and (iii) SoMo.ml with three layers (O. and Orth 2021). Table S1 shows the information of depths for all SM products that we use and classify into surface SM and root-zone SM.

Table 2.A1. Depths and layers for different soil moisture (SM) products

	Surface SM	Root-zone SM
ERA5	Layer 1 (0-7 cm)	Layer 2 (7-28 cm)
		Layer 3 (28-100 cm)
		Layer 4 (100-289 cm)
GLEAM	Layer 1 (0-10 cm)	Layer 2 (10-100 cm)
MERRA-2	Layer 1 (0-5 cm)	Layer 2 (0-100 cm)
SoMo.ml	Layer 1 (0-10 cm)	Layer 2 (10-30 cm)
		Layer 3 (30-50 cm)

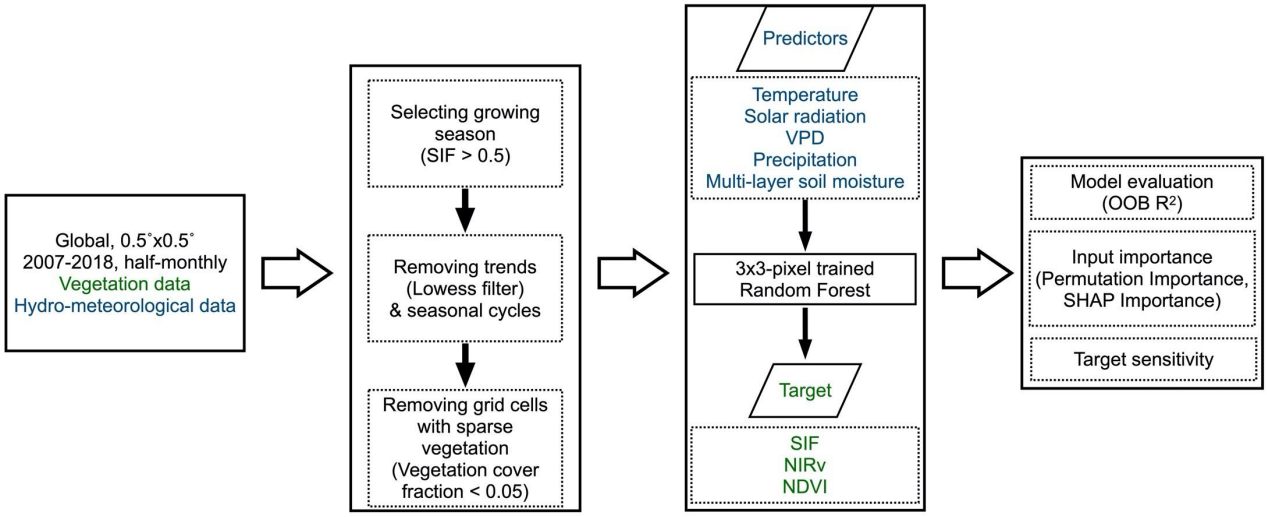

Figure 2.A1. The flowchart of data-processing and data analysis. Details about data-processing can be found in the Data and Methods section. Hydrometeorological data are considered as predictor variables (blue color). Vegetation data relating to different proxies of vegetation productivity (normalized difference vegetation indices, NDVI; near-infrared reflectance vegetation, NIRv; and sun-induced fluorescence, SIF) are the target variable (green color). Three aspects are needed when implementing predictions: Model evaluation by Out-of-bag (OOB) R^2 is conducted to test our methodology. Permutation importance method is used to identify the relative importance of each predictor variable. SHapley Additive exPlanations (SHAP) importance method is also used to confirm the result of Permutation Importance. Target sensitivity is the slope of each linear regression between SHAP dependence and one predictor variable to obtain the sensitivities of target variables (e.g. SIF) to predictor variables (e.g. multi-layer SM).

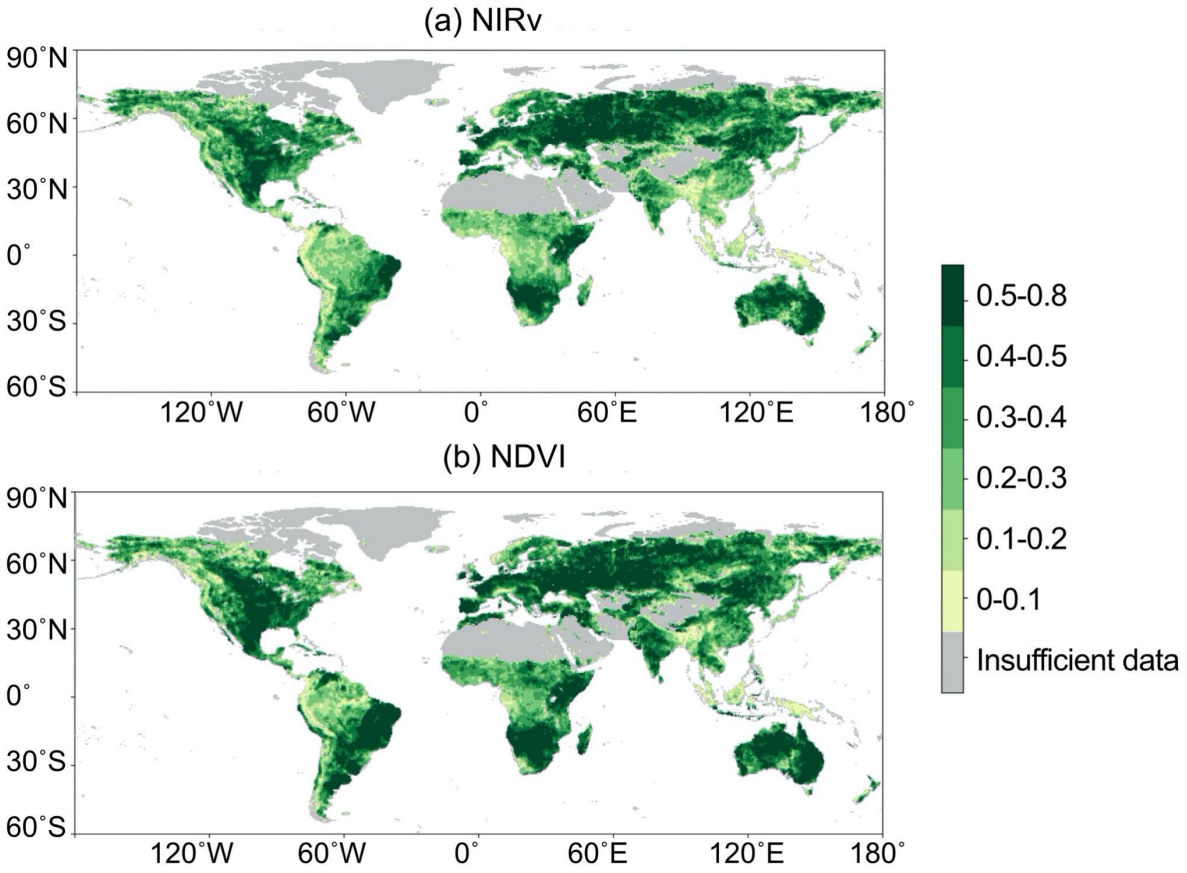

Figure 2.A2. Model performance (R^2) in prediction for (a) NIRv and (b) NDVI in the multi-layer SM (SM layer 1, 2, 3 and 4) experiment.

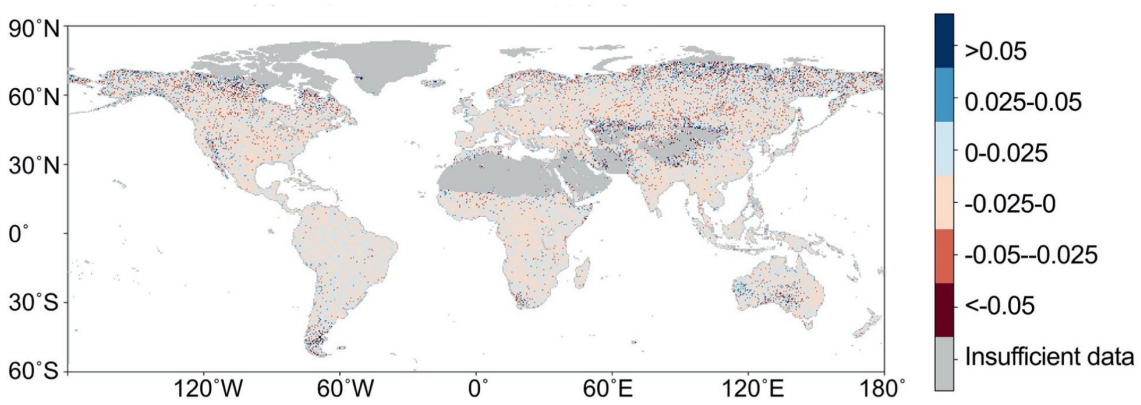

Figure 2.A3. The differences of R^2 in predicting SIF between the experiments with 5 variables of SM (SM layer 1, 2, 3, 4, and total SM) and 4 variables of SM (SM layer 1, 2, 3, and 4) as predictors. The differences in prediction performance using 4 or 5 layers of SM are negligible, indicating that the increase in model performance when using 5 SM layers are not exclusively due to the increased number of variables and hence increased flexibility of the RF model.

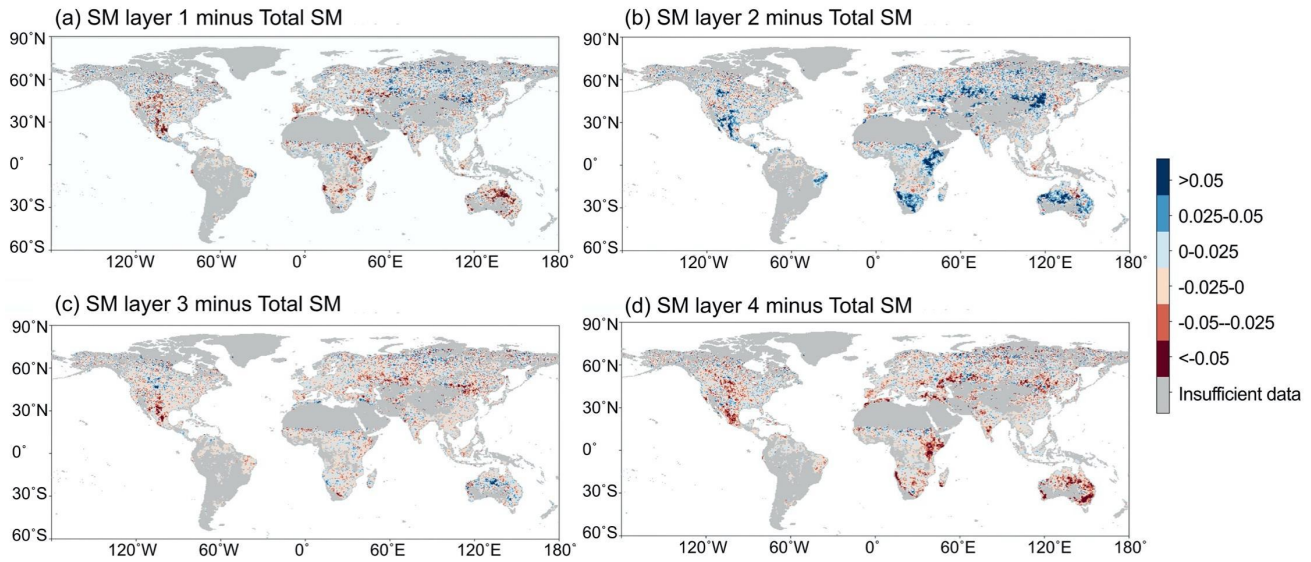

Figure 2.A4. The differences of R^2 in predicting SIF between models including (a) SM layer 1, (b) SM layer 2, (c) SM layer 3, or (d) SM layer 4, with a model including total SM. All the other predictor variables (precipitation, temperature, solar radiation, and VPD) are used in the analyses as predictors. Regions with positive values show that the performance of SIF prediction using one individual SM layer as predictor is better than using total SM as predictor.

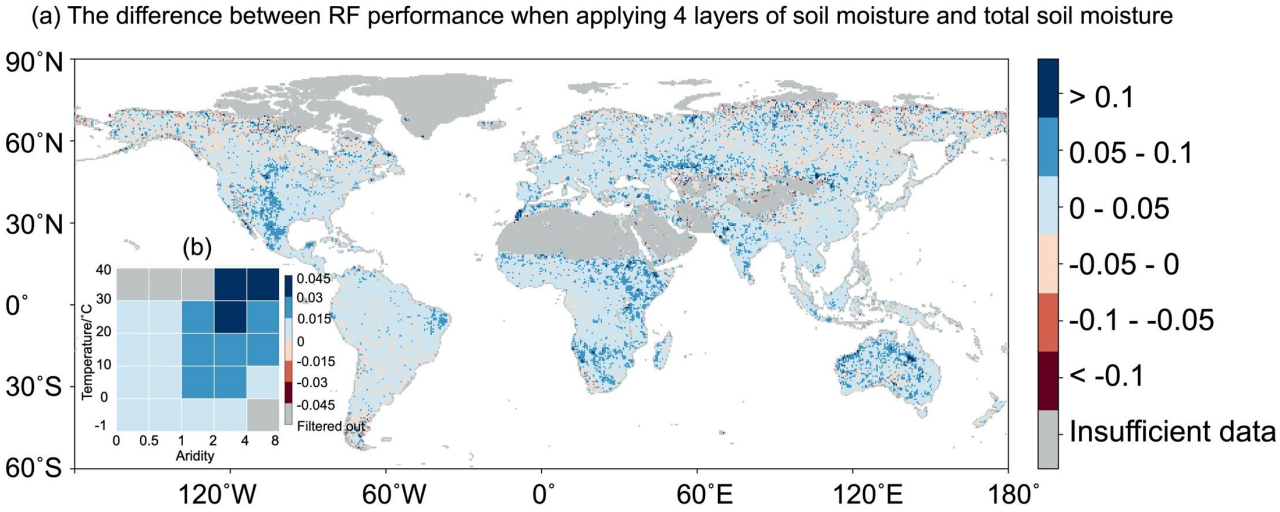

Figure 2.A5. The differences of R^2 in predicting SIF between models including multi-layer soil moisture and total soil moisture, and (b) summarizes differences across climate regimes. Figure S5 a is similar to Figure 1 c but total soil moisture is calculated by 4-layer averages weighted by root fraction per layer from ERA5 scheme.

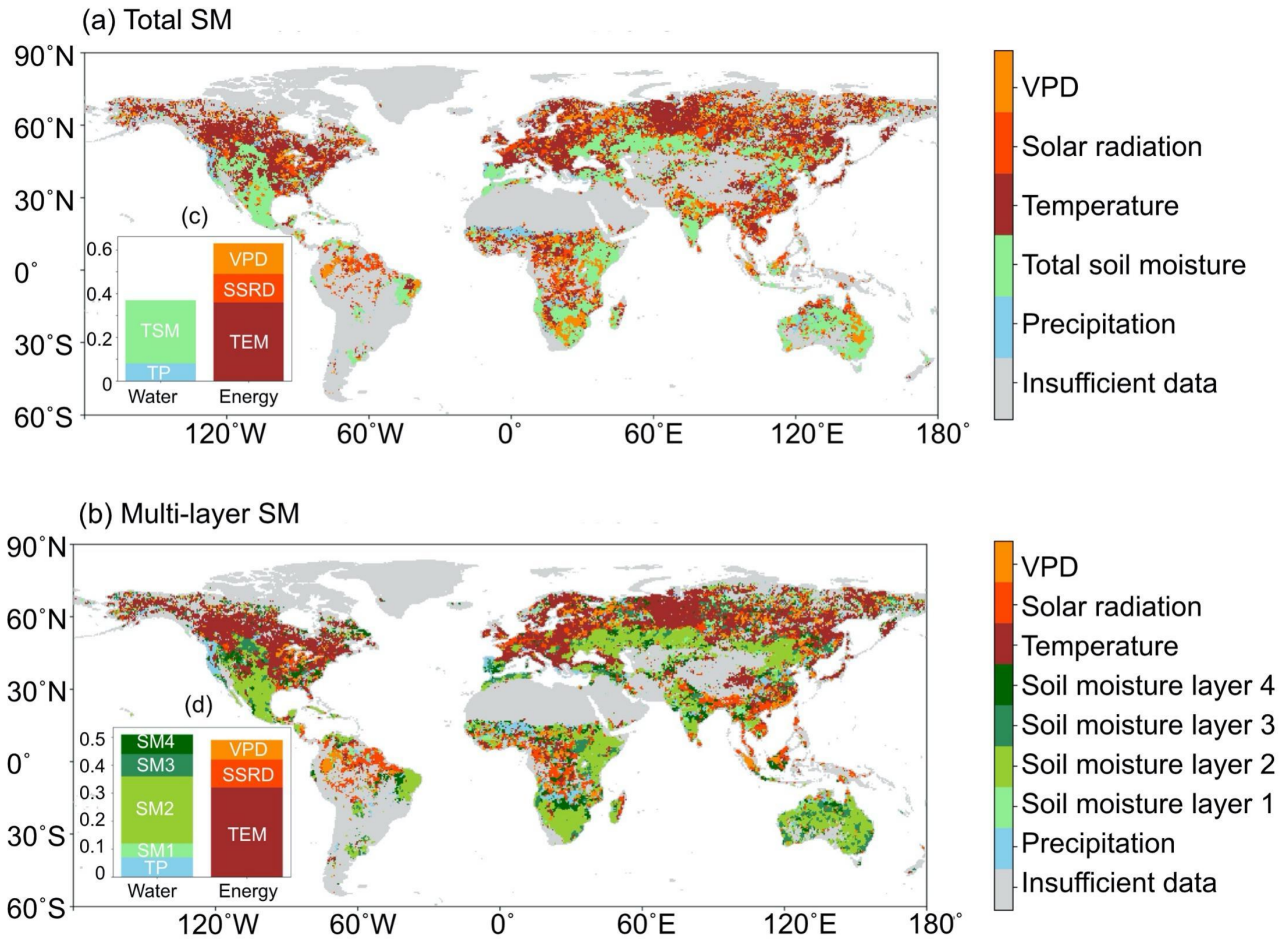

Figure 2.A6. Main hydrometeorological controls on sun-induced fluorescence (SIF) by only considering grid cells and variables with positive contributions using (a) total soil moisture (SM) alongside all other predictor variables, and (b) multi-layer SM alongside all other predictor variables. The figure insets (c and d) representing the proportion of study area where each variable is the most important factor. Figure S5 is similar to Figure 2 but focusing on positive contributions from hydrometeorological variables only.

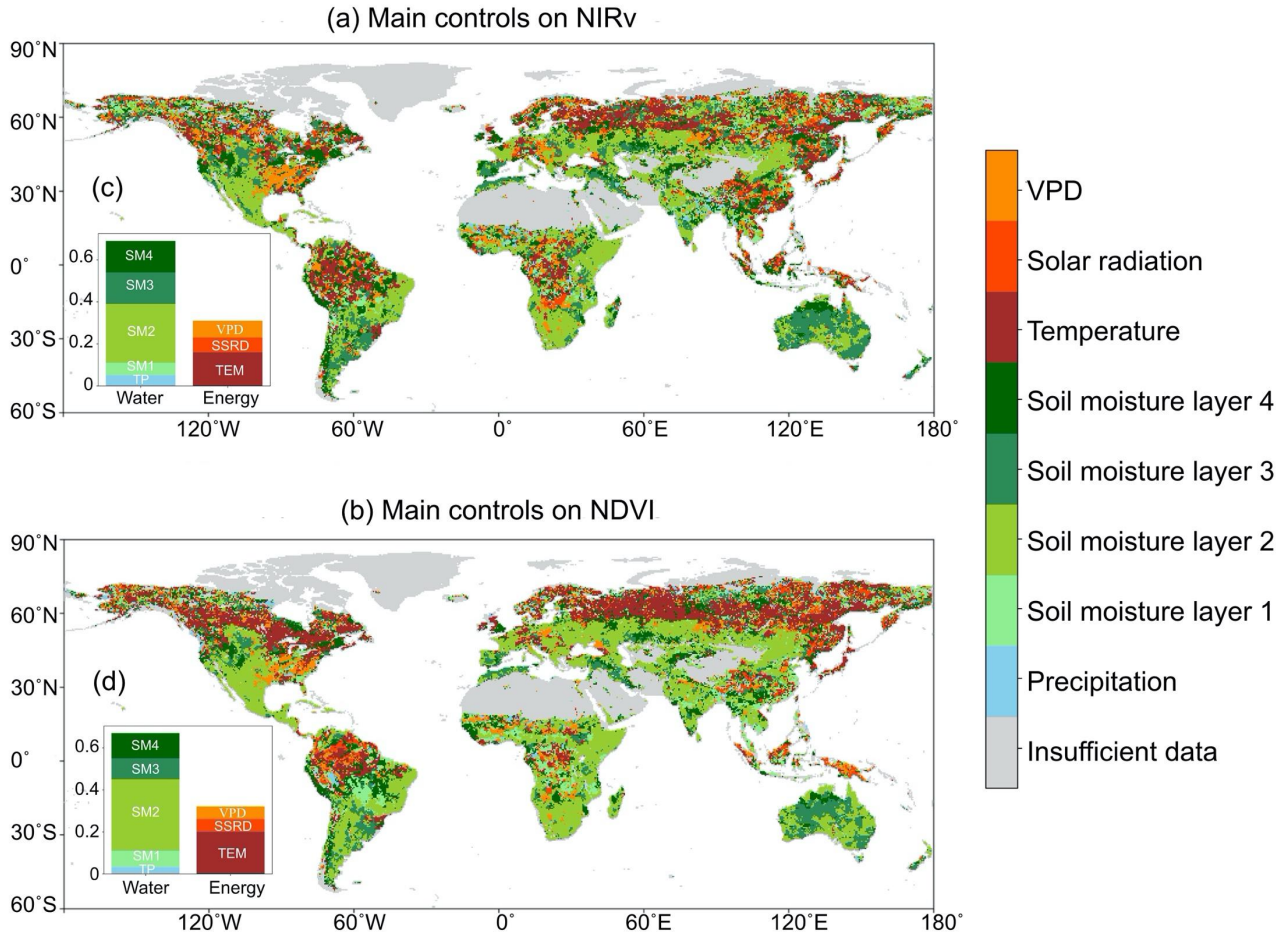

Figure 2.A7. Main hydrometeorological controls on (a) NIRv and (b) NDVI at the global level. The figure insets (c and d) represent the proportion of study area where each variable is the most important factor.

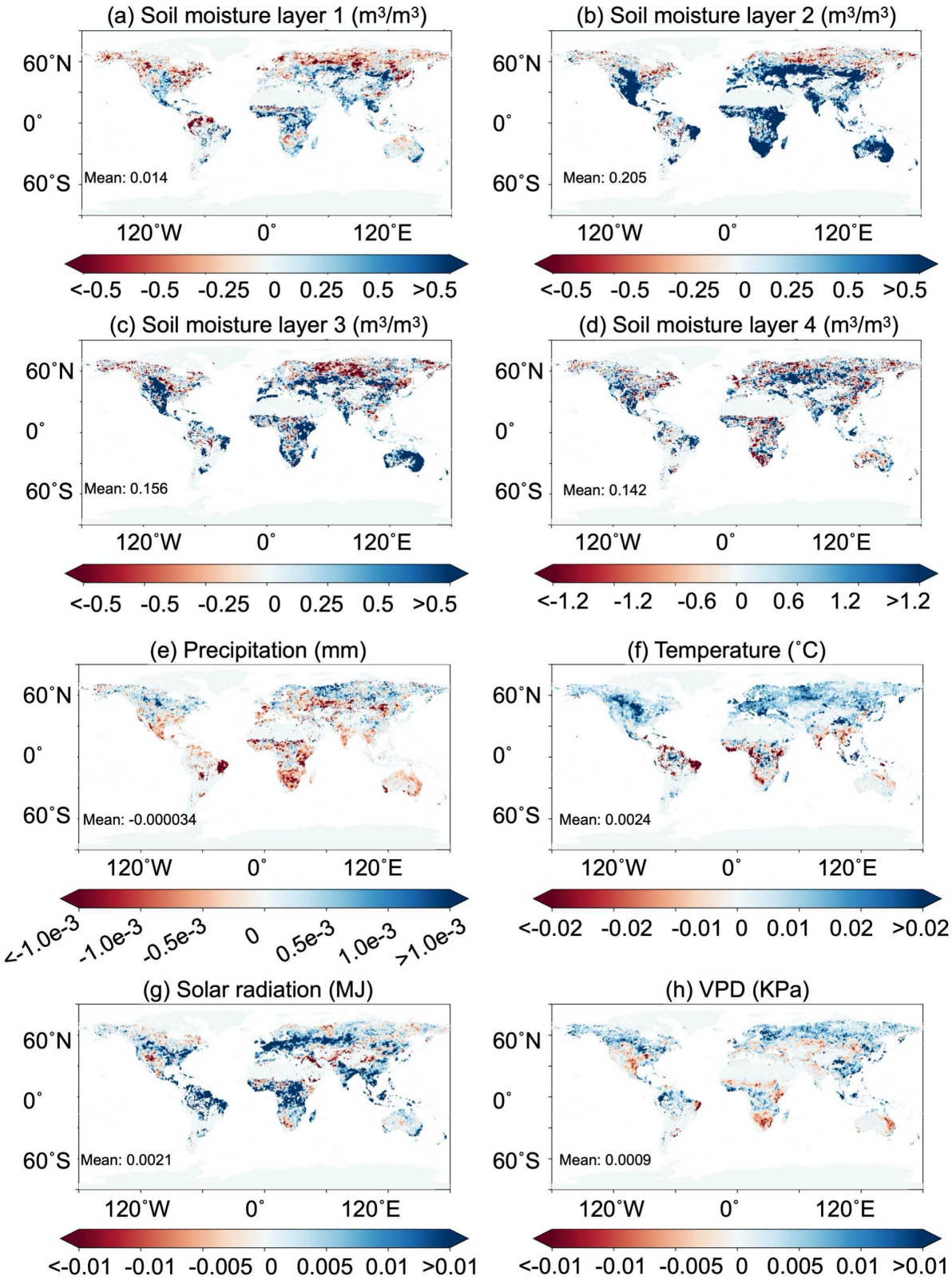

Figure 2.A8. The sensitivities of SIF to hydrometeorological controls at a global scale. Mean values are calculated for all grid-cells in the map except the ones with fractional vegetation cover below 5% and poor performance in SIF prediction (R^2<0).

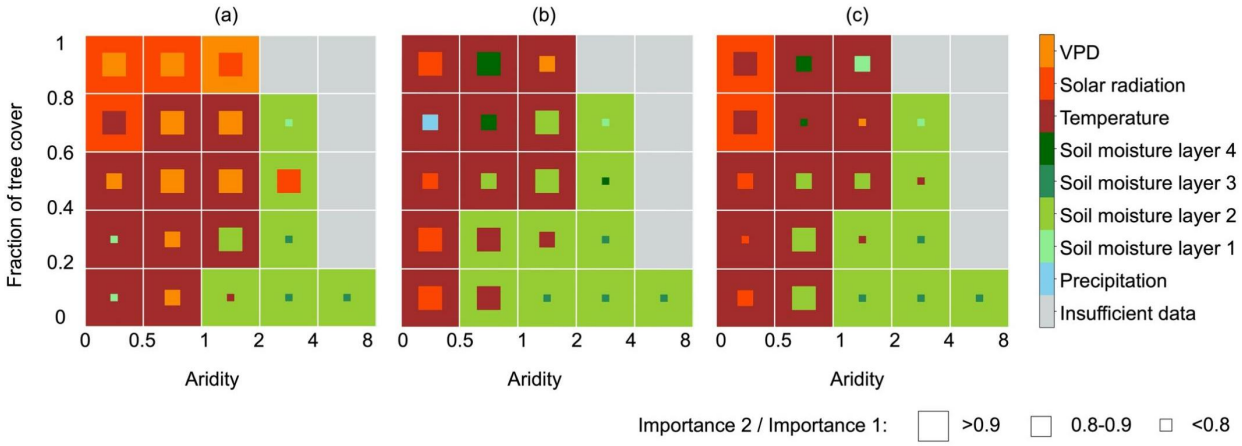

Figure 2.A9. Main hydrometeorological controls on (a) SIF, (b) NIRv, and (c) NDVI across classes of fraction of tree covers and aridity.

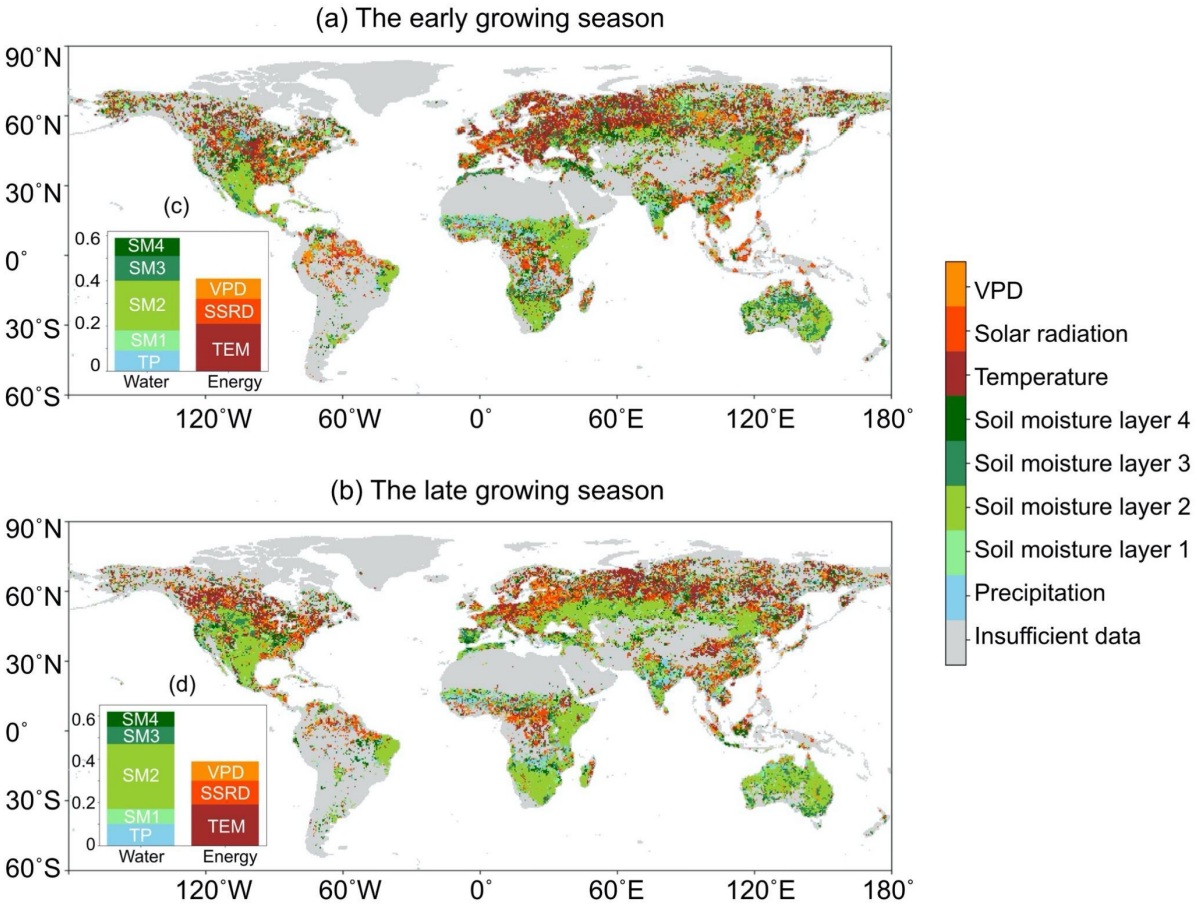

Figure 2.A10. Main hydrometeorological controls on sun-induced fluorescence (SIF) in the (a) early and (b) late growing seasons at the global scale. The figure insets (c and d) represent the proportion of study area where each variable is the most important controlling factor.

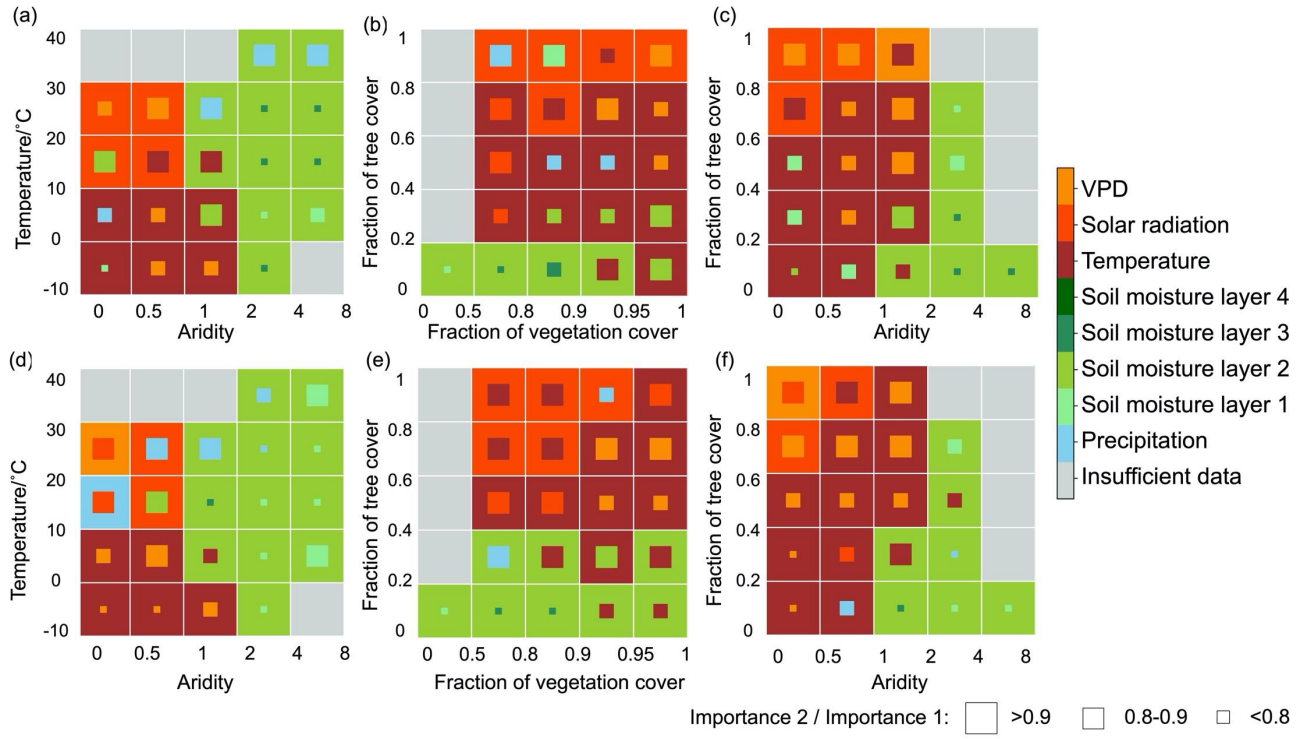

Figure 2.A11. Main hydrometeorological controls on sun-induced fluorescence (SIF) in the (a, b, c) early and (d, e, f) late growing seasons across climate regimes, vegetation characteristics and classes of fraction of tree covers and aridity.

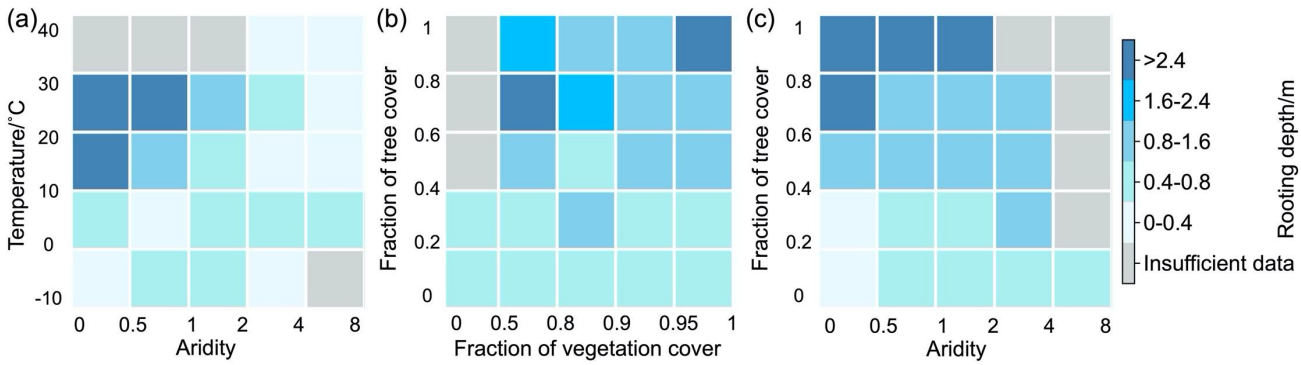

Figure 2.A12. Distributions of rooting depths from Yang et al. 2016 across (a) climate regimes, (b) vegetation characteristics, and (c) classes of fraction of tree covers and aridity.

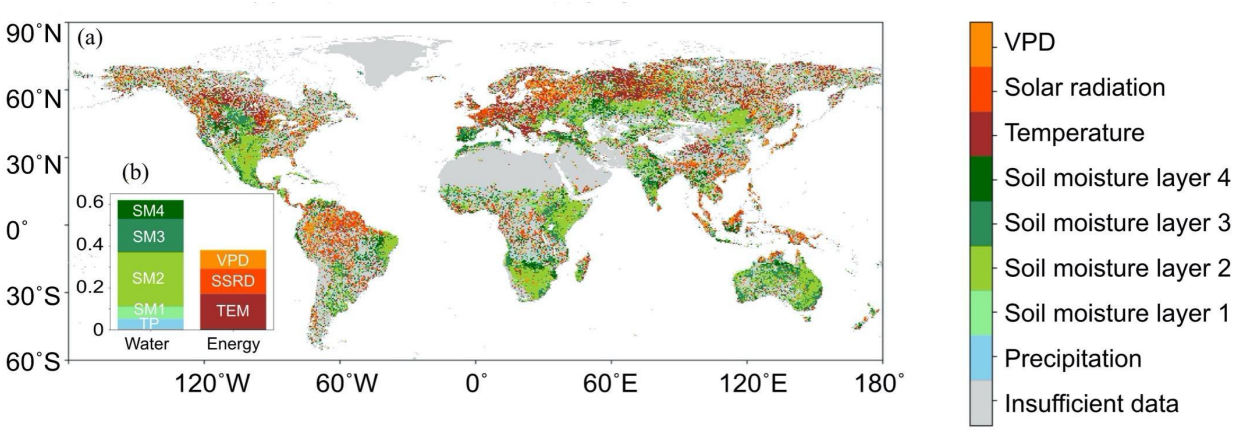

Figure 2.A13. Main hydrometeorological controls on SIF by applying Spearman Correlation (a) in a global scale and (b) with proportion of study area where each variable is the most important factor.

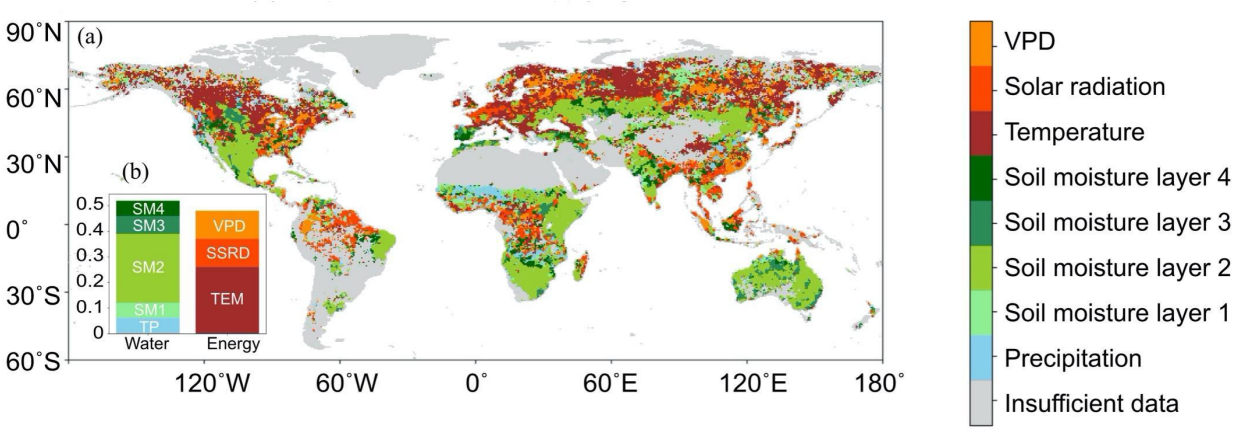

Figure 2.A14. Main hydrometeorological controls on SIF by applying SHAP feature importance method (a) at a global scale and (b) with proportion of study area where each variable is the most important factor.

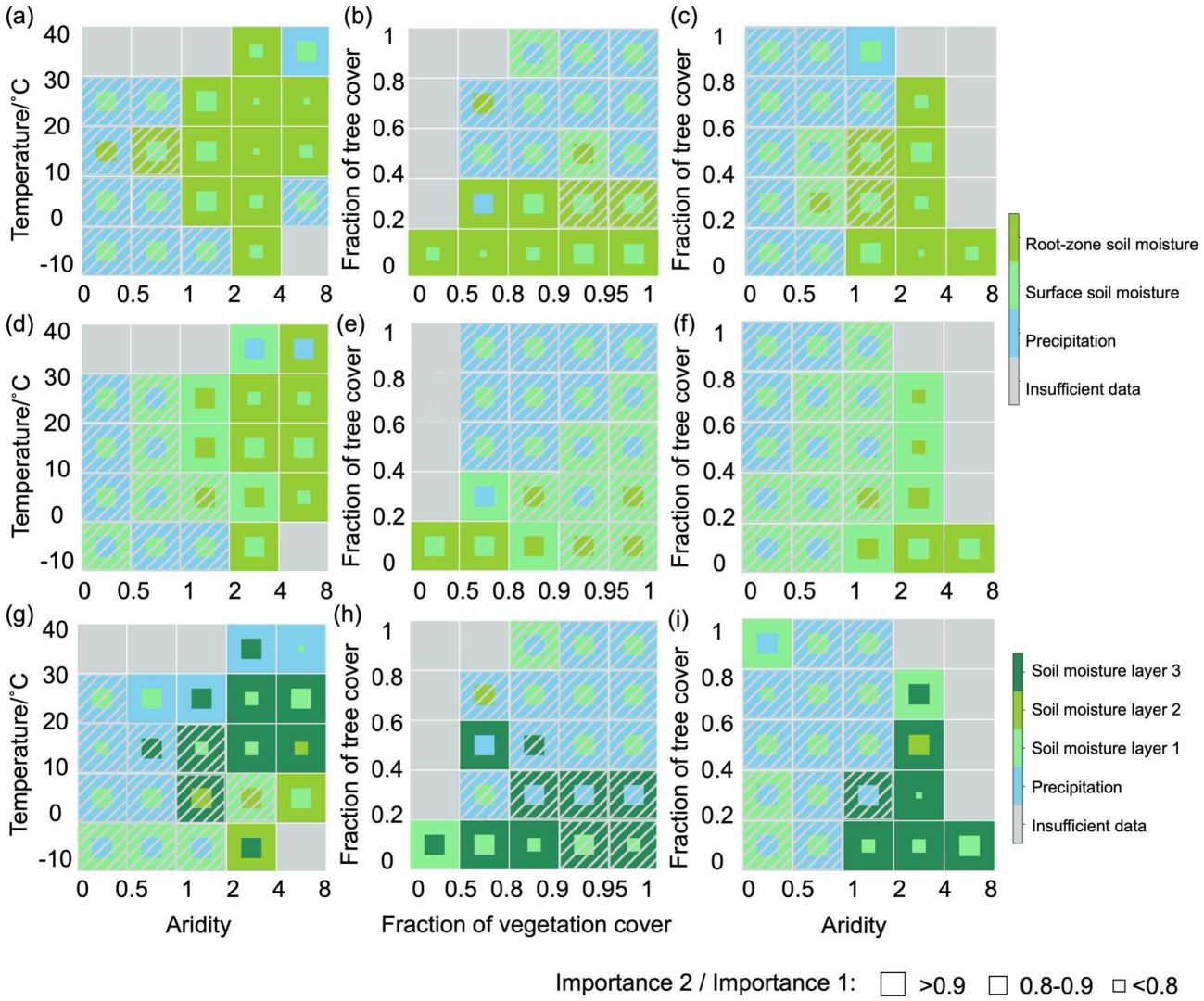

Figure 2.A15. Main water-supply-related controls on SIF by applying (a-c) GLEAM soil moisture, (d-f) MERRA-2 soil moisture and (g-i) SoMo.ml across climate regimes, vegetation characteristics and classes of fraction of tree covers and aridity. Dark-gray hatching indicates that temperature, solar radiation or VPD is identified as the main control on SIF in these boxes.

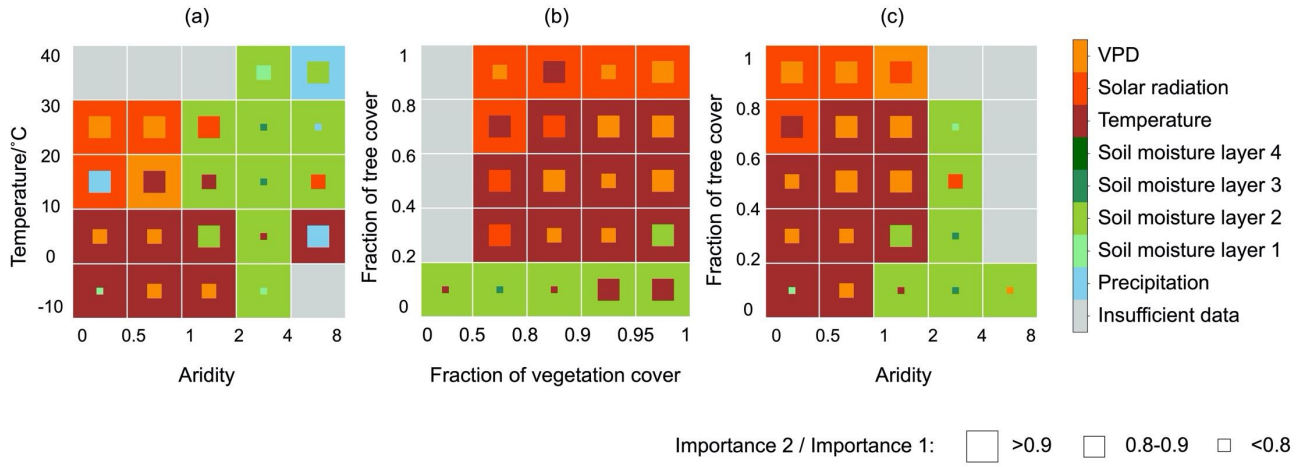

Figure 2.A16. Main hydrometeorological controls on SIF using water potentials across (a) climate regimes, (b) vegetation characteristics, and (c) classes of fraction of tree covers and aridity. Water potentials in the ERA5 scheme are calculated by the differences between actual volumetric soil moisture and volumetric soil moisture in permanent wilting points defined by the soil type per grid cell from the ERA5 scheme.

3 Widespread increasing vegetation sensitivity to soil moisture

Abstract

Global vegetation and associated ecosystem services critically depend on soil moisture availability which has decreased in many regions during the last three decades. While spatial patterns of vegetation sensitivity to global soil water have been recently investigated, long-term changes in vegetation sensitivity to soil water availability are still unclear. Here we assess global vegetation sensitivity to soil moisture during 1982-2017 by applying explainable machine learning with observation-based leaf area index (LAI) and hydro-climate anomaly data. We show that LAI sensitivity to soil moisture significantly increases in many semi-arid and arid regions. LAI sensitivity trends are associated with multiple hydro-climate and ecological variables, as the strongest increasing trends occur in the highest water-sensitive regions with declining precipitation. State-of-the-art land surface models do not reproduce the increasing sensitivity as they misrepresent water-sensitive regions and sensitivity strength. Our sensitivity results imply an increasing ecosystem vulnerability which can lead to exacerbated reductions in vegetation carbon uptake under future intensified drought, consequently amplifying climate change.

This chapter is published as:

Li, W., Migliavacca, M., Forkel, M., Denissen, J., Reichstein, M., Yang, H., Duveiller, G., Weber, U. & Orth, R. (2022). Widespread increasing vegetation sensitivity to soil moisture. Nature Communications, 13, 3959. https://doi.org/10.1038/s41467-022-31667-9

3.1 Introduction

Terrestrial vegetation is a crucial component in modulating the exchange of water, energy, and carbon between the land surface and the atmosphere (Humphrey et al. 2018; Nemani et al. 2003; Seddon et al. 2016). At the same time, vegetation provides multiple essential ecosystem services such as food production and carbon uptake. The latter is critical for mitigating climate change by absorbing human-emitted CO_2 (Canadell et al. 2021). Vegetation requires sufficient energy and nutrients, and also soil moisture availability is essential, particularly in semi-arid regions (Li et al. 2021; Stocker et al. 2018). As a result of ongoing climate change, soil moisture is declining in many regions as a consequence of decreased precipitation and higher evaporative water demand due to increased temperatures (Greve et al. 2014). Related to this, the extent of regions where vegetation is dominantly controlled by the water supply has increased (Jiao et al. 2021), although increasing CO_2 likely alleviates water stress by improving water use efficiency (De Kauwe, Medlyn, and Tissue 2021). Yet, it remains unclear how climate change has affected the sensitivity of global vegetation to soil water availability, and if there are potential hotspot regions with high vegetation sensitivity to soil moisture where vegetation is particularly vulnerable to changes in soil moisture availability. Changes in vegetation water sensitivity relate to multiple processes: (i) soil drying and more frequent droughts can lead to increased sensitivity as water becomes more often limiting for plant activity (Gampe et al. 2021); (ii) plants can regulate water losses through their stomata (at the cost of decreased photosynthesis), which can prevent increased sensitivity to soil moisture through reduced water consumption (Konings, Williams, and Gentine 2017); and (iii) vegetation composition can affect ecosystem water sensitivity, for example, herbaceous and woody plants have different strategies to respond to soil dryness (Carminati and Javaux 2020; Anderegg et al. 2019). Quantifying and understanding the resulting sensitivity patterns and changes thereof are fundamental for inferring ecosystem vulnerability(Seddon et al. 2016), and have important implications for developing land surface models which can then contribute to more accurate predictions of the future terrestrial carbon sink and global climate (Canadell et al. 2021; Green et al. 2019; Humphrey et al. 2021).

The increasing suite of Earth observations, including recent satellite-based vegetation and surface soil moisture products, now present the opportunity to assess the interplay between soil moisture and vegetation globally (Humphrey et al. 2018). In fact, leaf area index (LAI) products and other vegetation indices related to vegetation greenness and productivity can represent long-term global vegetation growth dynamics . They are routinely employed to study land-atmosphere interactions as they are sensitive to soil moisture dynamics, and can diagnose temporal sensitivity to environmental drivers thanks to their relatively higher signal-to-noise ratio than photosynthesis-related indicators such as sun-induced fluorescence (Li et al. 2021). Furthermore, LAI is readily available as a key prognostic variable from land surface models (LSMs) (Forzieri et al. 2020). From a modelling perspective, a more accurate representation of LAI response to soil water stress requires the differentiation between soil layers, as near-surface soil moisture primarily controls soil evaporation and precipitation infiltration and co-varies more with atmospheric conditions (Seneviratne et al. 2010), while sub-

surface soil moisture is a more relevant plant water source (Li et al. 2021; Miguez-Macho and Fan 2021). State-of-the-art soil moisture reanalyses cover multiple layers and allow for comprehensive analyses of the vegetation-water interplay by benefiting from satellite-observed surface soil moisture and in-situ multi-depth soil moisture measurements (Balsamo et al. 2018; Muñoz-Sabater et al. 2021).

Here we investigate the global sensitivity of LAI to soil moisture and sensitivity trends with observation-based data and model simulations between 1982 and 2017. For this purpose, we use an approach of explainable machine learning (Molnar 2022) to study the relationship between LAI and soil moisture anomalies (de-trended and de-seasonalized; Methods: Data pre-processing), which can isolate the effect of soil moisture across layers on LAI from that of the other hydro-climate variables (i.e., air temperature, precipitation, vapor pressure deficit, solar radiation anomalies). Specifically, we employ the Shapley Additive Explanations (SHAP) method in random forest modelling to estimate the sensitivity of LAI to soil moisture ("overall sensitivity" hereafter; Methods: Overall sensitivity; Appendix Figure 3.A1). Next to overall sensitivity, we estimate temporal variations of LAI sensitivity to soil moisture for 3-year-block data and analyze trends in temporal variations of sensitivity (Methods: Trends of sensitivity). We perform cross-validation for the random forest models for both the overall and the 3-year block sensitivities and disregard grid cells in the case of out-of-bag (OOB) $R^2 < 0$. We use five long-term satellite-derived LAI datasets and ERA5-Land soil moisture reanalysis (Muñoz-Sabater et al. 2021), as well as modelled data from offline simulations from 9 TRENDY LSMs. To better understand LAI response to soil moisture across layers and fairly compare respective layers in observations and LSMs, we distinguish between near-surface (0-~10cm) and sub-surface (~10-~100cm) soil moisture for individual products and models (Appendix Table 3.A1). To validate the robustness and uncertainty of observation-based results, we use additional satellite-based vegetation indices (i.e., normalized difference vegetation index, NDVI, and kNDVI (Camps-Valls et al. 2021)) and alternative soil moisture reanalysis products (Methods: Observation-based data). In this study, we explore the sensitivity of global leaf area index to soil moisture by applying explainable machine learning to observation-based datasets. We show that this sensitivity is increasing in many regions of the globe during the last 3 decades, which is not reproduced by land surface models.

3.2 Data and methods

3.2.1 Observation-based data

We use five satellite-based LAI products that cover the period 1982-2017. This allows us to assess the robustness of our results with respect to the underlying differences in post-launch sensor calibration, corrections of orbital shifts and sensor degradation, as well as cloud and atmospheric corrections (YB Liu et al. 2018). In particular, we employ the third generation Global Inventory Modelling and Mapping Studies LAI (GIMMS3g V1) (Zhu et al. 2013), the Land Long Term Data Record LAI (LTDR V5) (Pedelty et al. 2017), the Global Land Surface Satellite LAI (GLASS V40) (Xiao et al. 2016), the Long-term Global Mapping LAI

(GLOBMAP V3) (Liu et al. 2012), and the GEOV2-AVHRR LAI products (https://www.theia-land.fr/wp-content/uploads/2020/11/THEIA-MU-44-0369-CNES-GEOV2-AVHRR-Product-User-Manual-V2.pdf) (Verger, Baret, and Weiss 2020). We note that the individual long-term LAI products used within our LAI ensemble account to different extents for biases such as sensor drifts, resulting in discrepancies in their estimated inter-annual trends and variability. We account for these discrepancies by removing long-term trends and mean seasonal cycles, as well as by confirming that potentially spurious trends in the inter-annual variability of LAI do not strongly influence our inferred LAI sensitivity trends. Furthermore, we find that LAI sensitivity trends from 4 out of 5 individual LAI products are significantly increasing which supports our main results. The exception is GLASS LAI which is known for its considerable differences compared with the other products in terms of trends and variability for pre-MODIS time period (Jiang et al. 2017), likely contributing to its divergent long-term changes in LAI sensitivity (Appendix Figure 3.A15).

To further validate our results, we additionally use GIMMS3g v1 NDVI from 1982 to 2015 as an alternative vegetation index that does not rely on radiative transfer modelling, and similar products based on a different instrument, MODIS: MOD15A2H LAI and MOD13C2 NDVI from 2000 to 2017. Moreover, Kernel NDVI, which uses nonlinear generalization to better monitor vegetation productivity, is retrieved from MOD13C2 NDVI by following (Camps-Valls et al. 2021), using the recommended length-scale parameter of 0.5. MODIS products are selected with good quality flags, thereby ignoring low-quality data. We are not considering alternative vegetation indices or products derived from satellite observations such as sun-induced fluorescence and vegetation optical depth as they usually provide shorter records which are less suitable for long-term trend analysis. More specifically, (i) sun-induced fluorescence has a lower signal-to-noise ratio compared with the employed greenness-related indices5 and (ii) vegetation optical depth is more related to vegetation water content while we aim to focus on productivity and greenness (Liu et al. 2011).

To keep consistency with LSMs-related analyses, we employ CRU-JRA v3.26 meteorological datasets, including temperature, surface downward solar radiation, vapor pressure deficit (VPD), total precipitation (Harris et al. 2014; Kobayashi et al. 2015) (https://www.dropbox.com/sh/nlwz4n4r2k02ovb/AAC7BqTjS8fe4CR2IWWAfnRMa?dl=0). To analyze the water constraint of observational LAI, we use soil moisture from the ERA5-Land reanalysis (Muñoz-Sabater et al. 2021) where we use layer 1 (0-7cm depth) as near-surface soil moisture and the weighted mean of layers 2 (7-28cm) and 3 (28-100cm) as sub-surface soil moisture. This state-of-the-art reanalysis data has been successfully applied to understand vegetation responses to water availability (Li et al. 2021; Walther et al. 2019; Jiao et al. 2021). Soil moisture estimates from deeper layers in ERA5-Land are less constrained by observations, which is also true for its predecessor ERA-Interim/Land. In fact, the latter soil moisture products have been successfully evaluated many times against in-situ observations from global hydrology networks and has also been widely compared with other soil moisture reanalyses (Li, Wu, and Ma 2020; Liu, Zhang, and Zuo 2014; Albergel et al. 2012; 2013; Jing, Song, and Zhao 2018; Albergel et al. 2018).

We consider four additional global soil moisture products to validate our results: (i) the Modern-Era Retrospective analysis for Research and Applications-Version 2 (MERRA-2, 1982-2017) (Gelaro et al. 2017), (ii) the Global Land Evaporation Amsterdam Model (GLEAM v3a, 1982-2017) (Martens et al. 2017); (iii) a machine-learning-based product trained with multi-layer in-situ measurements (SoMo.ml, 2000-2017) (O and Orth 2021); and (iv) the satellite-derived ESA CCI surface soil moisture (1982-2017) (Dorigo et al. 2017). Since the validation of the newly published ERA5-Land soil moisture reanalysis has only recently been done using in-situ measurements during 2010-2018 (Muñoz-Sabater et al. 2021); the usefulness of this product for longer-term analyses as in our study can be deduced from successful long-term validations of related products from the European Centre for Medium-Range Weather Forecasts (ECMWF) (Li, Wu, and Ma 2020; Liu, Zhang, and Zuo 2014) which are based on the same land surface model and similar parameterisations. Additionally, the GLEAM soil moisture reanalysis which we also use is validated against over one thousand in-situ measurements during 1980-2015 (Martens et al. 2017). The global soil moisture product SoMo.ml takes advantage of large numbers of long-term in-situ measurements with machine learning algorithms, such that it can learn the relationship between meteorological input data and resulting soil moisture dynamics. Applying these machine learning algorithms in data sparse regions to obtain a global gridded soil moisture product is a way to transfer knowledge between data-rich and data-poor regions. SoMo.ml is limited by its time coverage from 2000 to 2017 but supports our main results by confirming the global patterns of overall LAI sensitivity and the global patterns of sensitivity trends obtained with ERA5-Land for the same time period (Appendix Figure 3.A13). Similar to the results obtained with the ERA5-Land reanalysis of soil moisture, ESA CCI yields an increasing trends of LAI sensitivity to soil moisture (Appendix Figure 3.A13). The trend based on ESA CCI data seems more pronounced, even though the absolute values of the LAI sensitivity cannot be compared due to different soil moisture units. Given that similar LAI sensitivities to soil moisture are derived with multiple independent soil moisture products, we note that our findings are robust despite the variability between existing soil moisture products.

To account for the potential vegetation responses to deep water sources, we additionally study LAI sensitivity to total water storage data from GRACE (Wahr et al. 2004). GRACE measures the anomalies of the Earth's gravity field that can inform relative changes in the land water storage. Due to its limited observed time period 2003-2017, we only compare the overall LAI sensitivity to total water storage and to sub-surface soil moisture for this time period.

Soil layers considered for near-surface and sub-surface soil moisture are listed in Appendix Table 3.A1. The unit of all considered soil moisture data is converted from m^3/m^3 to mm using the respective layer depths to be consistent with the soil moisture unit used in land surface models; however, this conversion could not be applied for ESA CCI soil moisture since the observation depth differs in time and space depending on the penetration depth of the microwave frequency and the soil wetness, so that the absolute values of LAI sensitivity to soil moisture are not comparable with that of the other products (Wahr et al. 2004).

3.2.2 Model data

To illustrate the performance of LSMs with the aspect of vegetation-soil moisture interplay, we simulate monthly LAI and multi-layer soil moisture during 1982-2017 using 9 models from the TRENDY v7. These models are ISAM, LPX-Bern, CLM5.0, JSBACH, JULES, ORCHIDEE-CNP, LPJ-GUESS, VISIT, and CABLE-POP. Factorial simulations are derived from Scenario 3, which include variable CO2, climate, and land-use changes. To thoroughly study interactions within LSMs and to fairly compare model results with observations, we use the same climate forcing CRU-JRA v2.0 datasets (Harris et al. 2014; Kobayashi et al. 2015) (https://catalogue.ceda.ac.uk/uuid/7f785c0e80aa4df2b39d068ce7351bbb) including temperature, surface downward solar radiation (solar radiation), vapor pressure deficit (VPD; derived from temperature and relative humidity), total precipitation in all observational and LSMs-related analyses. All the data are derived by following the TRENDY-v7 protocol (Le Quéré et al. 2018; Sitch et al. 2015). We manually aggregate the multi-layer soil moisture into near- and sub-surface soil moisture. The near-surface soil moisture in the article refers to the layer approaching 10 cm, while sub-surface soil moisture refers to the layer approaching 100 cm (Appendix Table 3.A1). For LSMs including only 2 layers we leave it as it is. We note that also the observation-based results are subject to uncertainty, in particular related to the soil moisture reanalysis data which can potentially be degraded by imperfect soil and vegetation type representations in the land surface model underlying the reanalysis. But the sub-surface soil moisture reanalysis can benefit from the assimilation of other data streams such as precipitation and radiation, as well as the satellite-based near-surface soil moisture assimilation helps to simulate sub-surface soil moisture through the infiltration process and mitigate model errors.

3.2.3 Auxiliary data

The VCF5KYR fraction of vegetation cover data includes three types of land cover and land use fraction: tree cover, non-tree cover, and bare ground (Song et al. 2018). The global study area is defined by the total vegetation cover (sum of tree and non-tree cover) $\geq$ 5% using 1982 -2016 averages and by the fraction of irrigation cover $\leq$ 10% (Data are collected around 2005; http://www.fao.org/aquastat/en/geospatial-information/global-maps-irrigated-areas/latest-version/) (Siebert et al. 2015). Irrigated or non-vegetated regions are the remaining land areas except the global study area. Non-soil-moisture controlled regions are defined as areas where LAI is not positively sensitive to soil moisture in observations and models. The area fraction in global maps is the number of grid cells weighted by the actual areas according to the geographic coordinates. The VCF5KYR fraction of vegetation cover data is also used to distinguish non-tree cover fraction by the ratio between non-tree cover (e.g., grasses and shrubs) and total vegetation cover as one of the ecological variables reflecting vegetation composition in the attribution analysis.

Climate regimes are applied to analyze global patterns of overall LAI sensitivity, and defined by the aridity index and long-term mean temperature data using ERA5-Land data. The aridity index is calculated as the ratio

of the long-term mean net radiation and unit-converted precipitation (Budyko 1974). Aridity values higher than 1 denote semi-arid regions or dry conditions.

3.2.4 Data pre-processing

We provide a flowchart of data-processing and the sensitivity analysis in Appendix Figure 3.A1. All observational and LSMs data are aggregated to monthly temporal resolution, and 0.5°x0.5˚ spatial resolution, including that a few models are upscaled regarding spatial resolutions. In all experiments and all vegetation and hydro-climate variables, we select growing-season data by temperature>5˚C and ensemble LAI means from the original signals>0.5 to keep a temporal consistency, whereas additionally negative values of vegetation indices are filtered out. Seasonality and long-term trends are removed to obtain the anomaly of every single vegetation and hydro-climate variable by subtracting long-term mean monthly signals and by subtracting a locally weighted smoothing filter (Cleveland 1979) with a smoothing span of 0.4, respectively. In this way, we exclude long-term common trends derived by changes in the equilibrium state, such as long-term successional cycles or human overgrazing. We also largely exclude biases from multi-sensor shifts and focus specifically on short-term vegetation responses to soil moisture anomalies.

3.2.5 Overall sensitivity

Note that overall sensitivity, temporal variations of sensitivity and sensitivity trends are first computed for each observational product (or land surface model) and then averaged across products to obtain more robust multi-product estimates.

We use explainable machine learning (SHapley Additive exPlanations) to study LAI sensitivity to soil moisture availability by disentangling the contribution of (i) near-surface soil moisture to LAI anomalies from the influence of other variables including sub-surface soil moisture and (ii) similarly of sub-surface soil moisture from the influence of other variables including near-surface soil moisture. For this purpose, we first train Random forests models and then apply SHapley Additive exPlanations (SHAP) to isolate the marginal contributions of each predictor on the target variable. Random forests are one of the data-driven machine learning algorithms based on a bootstrap aggregating strategy for improving results stability, and it requires no statistical assumptions on predictors and target variables using sufficient numbers of data (Leo Breiman 2001).

For each LAI product from observational data or LSMs, we treat the LAI anomaly as the target variable and corresponding hydro-climate anomalies as predictors by a common hyperparameter setting optimized by grid-cell level tests (numbers of estimators: 100; maximum features: 30%; random state: 42). We collect all predictors and target data during 1982-2017 from one grid cell and the surrounding grid cells (3x3 shape) to train a model for the core grid cell if more than 50 data points are included. We remove grid cells that have model performance worse than the mean of training data itself using cross-validation out-of-bag score (OOB R^2>0). We note that the rather low threshold (OOB R^2>0) is selected because of a typically significantly

decreased model performance in predicting global vegetation productivity for anomalies compared to time series that include the mean seasonal cycles (Li et al. 2021; Kraft et al. 2022), while it can still be efficiently used to study relationships between predictor variables and targets. Regions with $R^2<0$ are mostly associated with very low LAI variability or frequent human management (Appendix Figure 3.A2), and the increasing thresholds of OOB R^2 do not affect our main conclusions (Appendix Figure 3.A6).

For one trained model, we apply SHAP dependence method to isolate marginal contributions of near-surface (or sub-surface) soil moisture on the LAI anomaly (Lundberg and Lee 2017). We define overall LAI sensitivity as the slope estimated from Theil-sen regression between SHAP dependence for LAI and near-surface (or sub-surface) soil moisture anomalies by assuming that grid cell-level interaction between LAI and soil moisture is nearly linear (W. Li et al. 2021). Overall sensitivity is first computed for each observational LAI product or land surface model before averaging the results to yield more robust multi-product estimates.

Because the sensitivity is inferred by a linear regression, it should not be expected to represent the full interactions between vegetation and soil moisture per grid cell. This method combines the advantages of bootstrap aggregating and non-distribution-assumption by random forest modelling, as well as advantages of global interpretations being consistent with the local explanations in the SHAP algorithm (W. Li et al. 2021; Lundberg and Lee 2017; Besnard et al. 2021), hence strengthening the robustness of the results than using traditional statistical methods.

3.2.6 Trends of sensitivity

Grid cells with negative overall sensitivity or non-significant ($p>=0.1$) results are defined as non-soil-moisture controlled regions, meaning that energy-related variables such as radiation could dominantly control vegetation growth, and the detected dependence on water is likely due to confounding effects. Therefore, we remove these grid cells in the first place of studying changes in vegetation-water relationships. To address temporal variations of LAI sensitivity to near- and sub-surface soil moisture, respectively, we split the data from the entire 1982-2017 analysis period into twelve 3-year blocks (1982-1984, 1985-1987, …, 2015-2017). We train models independently again by 3x3 data points for each core grid cell if more than 15 data points are included, and infer temporal sensitivity by SHAP and Theil-sen regression by further assuming that grid cell-level interaction between LAI and soil moisture within 3-year blocks is nearly linear. We remove grid cells that have model performance worse than the mean of training data itself using cross-validation out-of-bag score and show non-significant ($p>=0.1$) results from Theil-sen regression.

We use the Mann-Kendall's test to detect the trends of changes in LAI sensitivity which does not require data with normal distribution (Hirsch, Slack, and Smith 1982). To confirm the 3-year split would not bias results, we also detect trends of 5-year-block sensitivity and find no significant differences (Appendix Figure 3.A7).

3.2.7 Attribution analysis

To better understand trends of LAI sensitivity to sub-surface soil moisture, we again apply random forests and the SHAP attribution method to predict trends of LAI sensitivity to sub-surface soil moisture (Leo Breiman 2001; Lundberg and Lee 2017). We focus on sub-surface soil moisture in this context as LAI is often more strongly controlled by this layer. Note that at the same time, near-surface soil moisture is still included as a predictor in the random forest model, but the respective sensitivity of LAI is not evaluated. We treat sensitivity trends as the target variable, and multiple hydro-climate and ecological factors from growing seasons as predictors to train a model using global grid cells, and then we employ SHAP values to quantify marginal contributions of each single factor on sensitivity trends and then rank global-relevant variable importance by SHAP importance algorithm (absolute weighted averaged marginal contributions from each predictor variable). After identifying the dominant factors for sensitivity trends (Appendix Figure 3.A9), we present combined impacts from the top two important variables which are precipitation trends and overall sensitivity and elucidate potential mechanisms across grouped ecosystems (Figure 3.4).

3.3 Results and discussion

3.3.1 Global patterns of LAI sensitivity to soil moisture

We analyze the overall sensitivity of LAI to soil moisture across the global land area where we disregard (i) irrigated and (ii) non-vegetated regions (Methods: Auxiliary data), as well as grid cells where (iii) the random forest model does not perform well (OOB $R^2 < 0$) due to scarce vegetation activities or frequent human management (Appendix Figure 3.A2). Observation-based results show that the area fraction of regions with positive LAI sensitivity to near-surface soil moisture is slightly higher than negative sensitivity (Figure 3.1a). Significantly positive sensitivity ($p<0.01$) indicates that increases in near-surface soil moisture enhance LAI dynamics. This is found in (semi-)arid regions such as southern North America, southern Eurasia, eastern and southern South America, Australia, South Africa and eastern Africa. Observed negative sensitivity in many boreal regions indicates that increased near-surface soil moisture tends to suppress LAI, potentially associated with the soil water excess such as waterlogging (Ohta et al. 2014). However, the negative LAI sensitivity to soil moisture is also likely caused by the confounding effects, because energy-related variables such as temperature and radiation have been identified as main controls on LAI in such regions, whereas soil moisture inversely covaries with these variables (Nemani et al. 2003; Seddon et al. 2016). Focusing on sub-surface soil moisture, we find more widespread positive sensitivity (Figure 3.1b), indicating a higher relevance of this moisture reservoir for LAI owing to the higher amount of plant roots exploiting this layer than the shallow near-surface layer (Li et al. 2021; Fan et al. 2017). Meanwhile, the magnitude of LAI sensitivity is higher for the near-surface soil moisture as in this layer there is a relatively high fraction of coarse roots, which allow for more efficient use of soil water for vegetation growth (Fort et al. 2017). Main regional differences between LAI sensitivity to near-surface and sub-surface soil moisture are found in the African pantropics where

temperature, and hence evaporative demand, is comparatively high, and precipitation is comparatively low (M. Huang et al. 2019) such that typically water is evaporated by plants or from surfaces, stimulating vegetation growth before reaching the deeper soil.

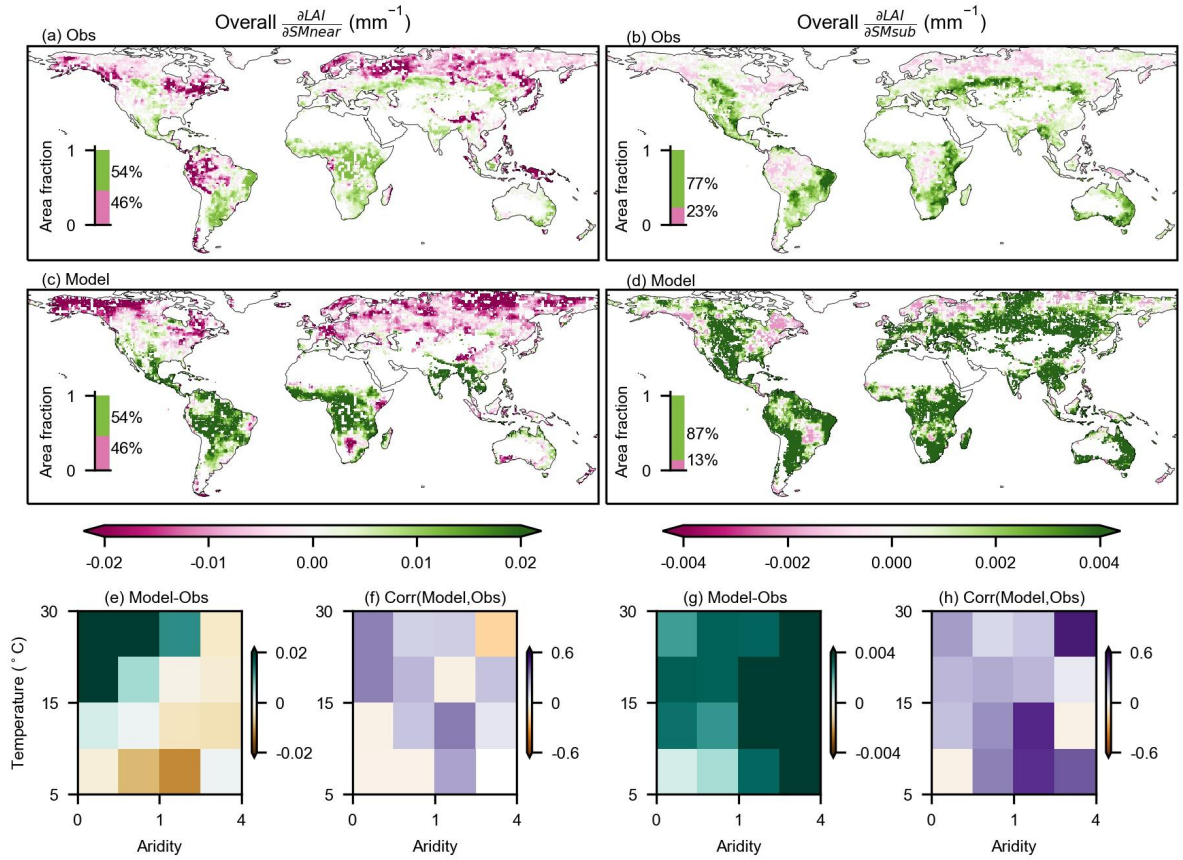

Figure 3.1. Global sensitivity of LAI to soil moisture in the period 1982-2017. (a, b) LAI sensitivity to near-surface ($\frac{\delta LAI}{\delta SMnear}$) and to sub-surface soil moisture ($\frac{\delta LAI}{\delta SMsub}$) from observations (Obs), given as respective ensemble means (Methods: Overall sensitivity). (c, d) Similar to (a, b) but for LSMs (Model). (e, g) Mean differences between observational and model results across climate regimes. (f, h) Spatial coherence between observational and model results inferred by correlation coefficients using sub-regional data across climate regimes. All panels apply the two-sided significance test at the $p<0.01$ level as assessed with Theil-sen regressions for each grid cell, and grid cells which pass the significance test are colored according to the sensitivity values in (a-d). To note that the results are a descriptive measure, as the field significance is not tested.

The global patterns of LAI sensitivity to soil moisture in LSMs partly match the observation-based results (Figure 3.1c-d). Differences exist for near-surface soil moisture where extra-tropical regions in the northern hemisphere and South Africa are not sufficiently reflected in the model results, and for sub-surface soil moisture where the models generally overestimate the positive sensitivity. When grouping the sensitivity

results by the local long-term aridity and temperature conditions, we find that the observed LAI sensitivity changes predominantly along aridity gradients, while the modelled sensitivity tends to respond more strongly to temperature gradients (Appendix Figure 3.A3; see aridity definition from Methods: Auxiliary data). Further comparing the observational with model results, we find overestimated (underestimated) LAI sensitivity in dry and hot (wet and cold) regions in the case of near-surface soil moisture (Figure 3.1e). For sub-surface soil moisture, the strongest overestimation occurs in dry areas, while the bias is lower in wet areas (Figure 3.1g). The spatial sensitivity patterns agree more with observational results in the case of sub-surface soil moisture (Fig, 3.1f-h).

3.3.2 Non-linear relationships between LAI and soil moisture across space

Next, we analyze to which extent the differences between the results from models and observations are related to different response functions of LAI sensitivity to soil moisture. For this purpose, we build upon the relationships between significant LAI sensitivity to available amounts of growing-season soil moisture (Figure 3.2; see Methods: Data pre-processing for growing-season definition). Observation-based results show that LAI sensitivity to soil moisture is typically high for dry conditions and decreases toward wetter conditions for both soil moisture layers. The results exhibit non-linear relationships (Figure 3.2) in line with previous research using site measurements (Stocker et al. 2018). Model-based results are similar in the case of sub-surface soil moisture, even though with a more pronounced sensitivity increase towards dry soil moisture conditions (Rogers et al. 2017). Instead, for the sensitivity to near-surface soil moisture, we find considerable differences between observations and models. However, differences between individual models are substantial for both soil layers (Appendix Figure 3.A4). The mismatch between models and observations and the divergence between models can be related to different representations of the processes occurring in the soil-vegetation continuum and representation of roots profile and water potentials in models, which lead to differences in simulated soil moisture dynamics and soil-vegetation coupling (Arora and Boer 2005; Trugman et al. 2018). Furthermore, soil moisture constraints on carbon allocation, leaf senescence, phenology, or photosynthesis (Rogers et al. 2017; Medlyn et al. 2011) are uncertain and differ between models, as well as the number and depths of soil layers, and their consideration for inferring vegetation water stress (Medlyn et al. 2011; Medlyn, De Kauwe, and Duursma 2016). Vegetation water stress can also be related to atmospheric dryness (vapor pressure deficit) as well as soil dryness, while their relative roles are not fully understood and hence difficult to capture in models (Humphrey et al. 2021). Nevertheless, the difference between the soil moisture amounts of reanalysis and LSMs should be interpreted with caution due to different soil and vegetation types employed in the reanalysis scheme versus that of LSMs (Muñoz-Sabater et al. 2021; Ito and Oikawa 2002).

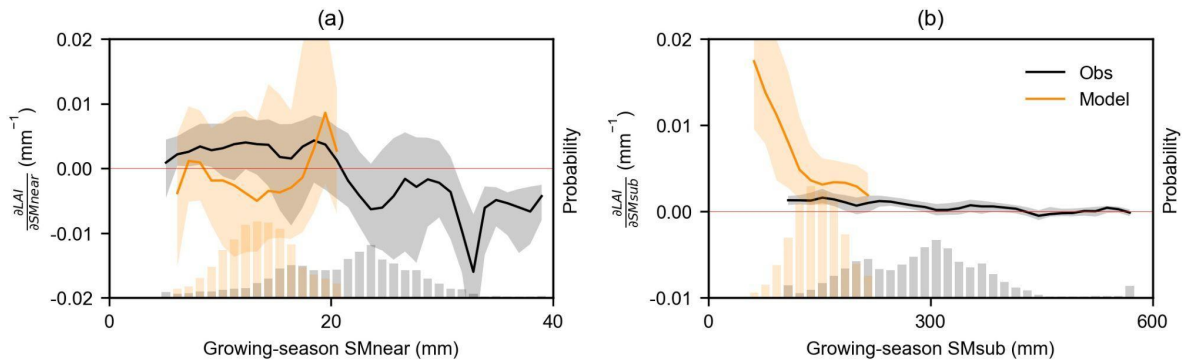

Figure 3.2. Response functions of global LAI sensitivity to soil moisture. (a) Response functions of LAI sensitivity ($\frac{\delta LAI}{\delta SMnear}$) to growing-season mean near-surface soil moisture (growing-season mean SMnear) from observations (Obs) and LSMs (Model). (b) Similar to (a) but for LAI sensitivity to sub-surface soil moisture ($\frac{\delta LAI}{\delta SMsub}$). In (a) and (b), global grid cells show only significant LAI sensitivities to soil moisture are included. Two-sided significance tests are done for each grid cell at the $p<0.01$ level as assessed with Theil-sen regressions. The solid line and shaded areas show the median and interquartile ranges of LAI sensitivity across space. Probability distributions of near-surface soil moisture in observations and models are shown at the bottom of each plot. Results here are based on ensemble-product means, while results from individual products or models are presented in Appendix Figure 3.A4.

3.3.3 Increasing LAI sensitivity to soil moisture

Moving beyond overall LAI sensitivity to soil moisture, we now analyze changes in the 3-year-block sensitivity to study their temporal variability from 1982 to 2017 (Figure 3.3). For this purpose, we only consider soil moisture-controlled regions with significantly positive overall LAI sensitivity to soil moisture in observations and models to mitigate the influence of confounding effects (Figure 3.1). We find significantly increasing trends ($p<0.01$) for observed LAI sensitivity to sub-surface soil moisture after averaging global results (Figure 3.3a). LAI sensitivity increases in ~30% of the study area and mainly occurs in central and southern North America, central Eurasia, India, Australia, eastern Africa, central and eastern South America (Figure 3.3b). By contrast, LAI sensitivity decreases in ~15% of the study area, occurring in central South Africa, the African and Amazon extratropics, Central Europe, eastern and central Asia (Figure 3.3b). Note that Figure 3.3 focuses on sub-surface soil moisture for simplicity while the observed LAI sensitivity to near-surface soil moisture is provided in Appendix Figure 3.A5 also with significantly increasing trends globally. In addition, we validate the robustness of our methodology by (i) testing different thresholds for the random forest model performance as indicated by the OOB R^2 (Appendix Figure 3.A6) and (ii) repeating the analysis with 5-year blocks (Appendix Figure 3.A7; we find similar results in both cases.

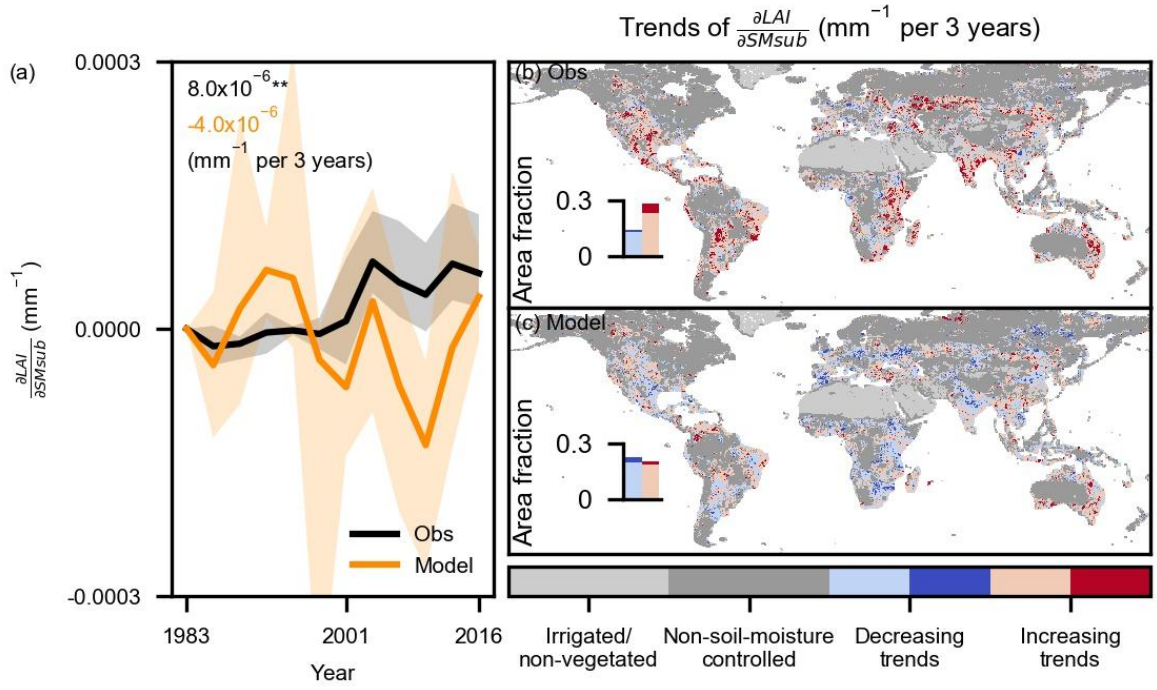

Figure 3.3. Trends of LAI sensitivity to sub-surface soil moisture. (a) Temporal variations of global mean LAI sensitivity to sub-surface soil moisture ($\frac{\delta LAI}{\delta SMsub}$) computed by 3-year blocks between 1982 and 2017. The y-axis denotes the change since 1982 in respective products or models. Solid lines denote the median results from ensemble observations (Obs) and land surface models (Model); Shaded areas denote interquartile ranges of LAI sensitivity from multiple LAI products and models; Text denotes slopes of trends; ** denotes passing the two-sided significance test as assessed with Mann-Kendall at $p<0.01$ (Methods: Sensitivity trends). (b) Trends of LAI sensitivity to sub-surface soil moisture in observations and models using ensemble means. (c) Similar to (b) but for land surface models. Insets indicate the area fraction of decreasing and increasing trends within the global land area, excluding irrigated and non-vegetated regions. Light blue and red colors denote insignificant changes ($p>=0.1$); dark blue and red colors denote significant changes ($p<0.1$). In (b) and (c), two-sided significance tests are done for each grid cell at the $p<0.1$ level as assessed with Mann-Kendall's test. See Methods: Auxiliary data about the determination of irrigated/non-vegetated and non-soil-moisture controlled regions.

By contrast, there is no trend in LAI sensitivity to sub-surface soil moisture in TRENDY model simulations after averaging global results (Figure 3.3a). The spread between the results of individual models is substantial, as indicated by the orange shading. We find similar extents of areas with regionally increasing and decreasing trends, respectively (Figure 3.3c). Furthermore, we confirm similar results when focusing on respective soil moisture-controlled study areas inferred from either observations or models as defined from positive overall LAI sensitivity to soil moisture (Appendix Figure 3.A8).

3.3.4 Attribution of trends of LAI sensitivity to soil moisture

We perform an attribution analysis to understand changes in LAI sensitivity to sub-surface soil moisture. We exclusively focus on sub-surface soil moisture in this context as LAI is often more strongly controlled by soil moisture in this layer, and the observed coupling between LAI and sub-surface soil moisture is captured relatively well by land surface models (Figure 3.2). We explain sensitivity trends inferred from observations by relevant hydro-climate and ecological variables (Jiao et al. 2021; Gampe et al. 2021; Carminati and Javaux 2020; Anderegg et al. 2019)(Methods: Attribution analysis). We find that the observed spatial trend patterns are strongly related to (i) overall LAI sensitivity to sub-surface soil moisture and (ii) inter-annual precipitation trends (Appendix Figure 3.A9). We group the results from Figure 3b with respect to the identified main controls (Figure 3.4a) and find that positive trends in LAI sensitivity to sub-surface soil moisture are strongest for regions with the largest overall sensitivity and the most substantial decrease in precipitation. Areas with high overall sensitivity include large ratios of grasses and shrubs which have strong roots' hydraulic controls but weak stomatal regulation (Konings, Williams, and Gentine 2017; Carminati and Javaux 2020). Small decreases in water supply tend to trigger drastic changes in LAI, reflecting a non-linear vegetation water response (Berdugo et al. 2020). In a few regions, we find increasing LAI sensitivity despite weakly increasing precipitation trends, which relates to increased evaporative demand due to increasing temperatures. Moreover, our results suggest that deeper soil moisture or groundwater can generally not sustain a constant vegetation water sensitivity by compensating for precipitation decreases (Mu et al. 2021). Soil moisture trends also play a role, even though they are less prominent than precipitation trends. This might be related to the higher observational uncertainty in soil moisture (trends) than precipitation (trends) owing to more indirect measurements and heterogeneous soils. Trends in energy-related variables (temperature, radiation, vapor pressure deficit), vegetation composition and changing composition (see Methods: Auxiliary data for non-tree cover) are of secondary importance.

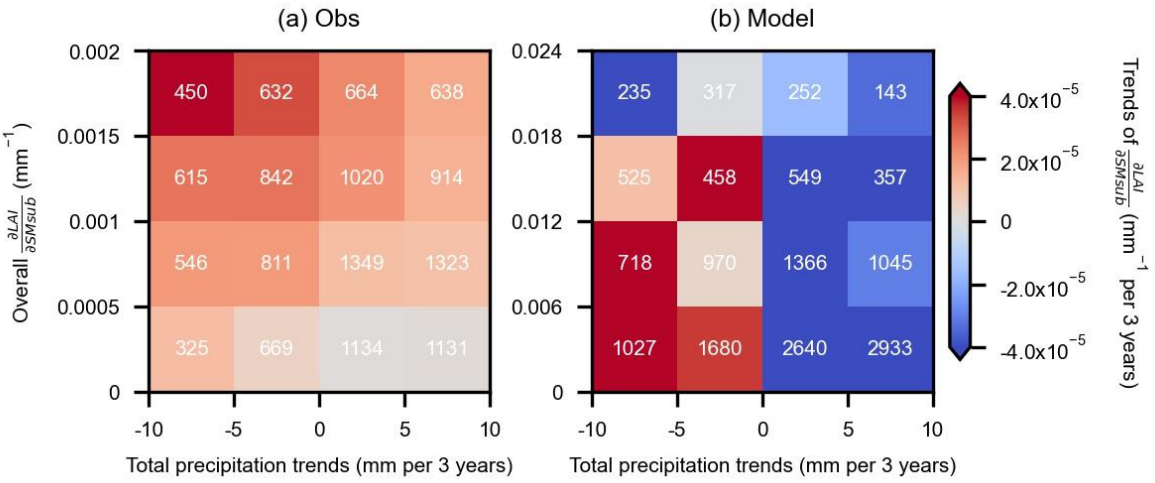

Figure 3.4. Trends of LAI sensitivity to sub-surface soil moisture ($\frac{\delta LAI}{\delta SMsub}$) grouped by precipitation trends and overall sensitivity (Overall $\frac{\delta LAI}{\delta SMsub}$). (a) Colors indicate median values of trends in LAI sensitivity to sub-surface soil moisture (SMsub) in observational ensemble means (Obs) grouped by precipitation trends and overall sensitivity; numbers of grid cells in each group are shown in white. (b) Similar as in (a) but for ensemble means of land surface models (Model).

We also evaluate the model-based spatial patterns of LAI sensitivity trends against the identified main controls (Figure 3.4b). We find that precipitation decreases (increases) lead to increased (decreased) LAI sensitivity to soil moisture, consistent with the observation-based results. The role of overall LAI sensitivity in determining sensitivity trends in models is less clear than in the observations, suggesting that this key deficiency is behind the reason for the poorly modeled trends in LAI sensitivity (Figures 3.1 and 3.2).

Our observed results might be affected by three sources of uncertainty: (i) the satellite-based LAI products used in the analysis regarding their retrieval uncertainties and representativeness of the greenness and vegetation productivity, (ii) uncertainties in the soil moisture reanalysis products which rely on modeling assumptions, can be more pronounced for sub-surface soil moisture, as this layer does not have direct satellite data to assimilate, and (iii) artifacts in the long-term LAI time series derived from the Advanced very high-resolution radiometer (AVHRR) instrument. We address these uncertainties to assess the robustness of our main findings. First, our results show great consistency in the overall sensitivity (Appendix Figure 3.A4) and sensitivity trends (indicated by the gray shading in Figure 3.3a and Appendix Figure 3.A5a) derived from ensemble long-term LAI products. The same analysis conducted on NDVI and kNDVI, alternative vegetation indices related to greenness and vegetation productivity, are consistent with LAI results (Appendix Figure 3.A10). We also find consistency between our results and the ones obtained from Moderate Resolution Imaging Spectroradiometer (MODIS), which is characterized by higher quality but covering a shorter period than AVHRR (Appendix Figure 3.A10). Second, our main results hold when employing different state-of-the-

art soil moisture reanalysis products, which illustrate that our analysis is robust against different designs of model schemes (decreasing sensitivity patterns towards increasing soil moisture in Appendix Figure 3.A4; increasing sensitivity trends in Appendix Figures 3.A11 and 3.A12). Moreover, we perform our analysis with soil moisture datasets that are independent of reanalysis products applying process-based models; One derived with machine learning-based extrapolation of in-situ measurements (SoMo.ml) (O and Orth 2021) shows similar global patterns of overall LAI sensitivity and global patterns of sensitivity trends obtained with ERA-Land for the same time period; And another one derived from satellite observations (ESA CCI soil moisture) (Dorigo et al. 2017) confirms our main findings of significantly increasing global trends of LAI sensitivity to soil moisture (Appendix Figure 3.A13). We further note that other water sources such as deep soil moisture, groundwater and bedrock water can also influence vegetation productivity (Miguez-Macho and Fan 2-21). We account for this by using satellite-observed total terrestrial water storage data from GRACE (Wahr et al. 2004), and find that sub-surface soil moisture reanalysis can largely capture the vegetation response to deep soil water in many regions, and LAI is even more related to the soil moisture reanalysis as it probably reflects more strongly the root-zone water availability (Appendix Figure 3.A14). Third, issues such as sensor drifts in the AVHRR instrument can potentially introduce artifacts in LAI retrievals (Frankenberg et al. 2021; Wang et al. 2021; Tucker et al. 2005; Jiang et al. 2017; Liu et al. 2018). We largely account for potential biases and discrepancies between LAI products by using de-trended and de-seasonalized LAI data (Methods: Data pre-processing). Next to this, we also find that potentially spurious trends in the inter-annual variability of LAI cannot efficiently explain the observed patterns of LAI sensitivity trends (Appendix Figure 3.A9). The consensus of most LAI products in terms of global patterns of increasing trends of LAI sensitivity to soil moisture further supports the robustness of our findings (Appendix Figure 3.A15).

3.4 Conclusions

In conclusion, we show that the sensitivity of LAI to soil moisture has significantly increased in soil water-controlled regions during 1982-2017. This is driven primarily by decreasing water supply (i.e., precipitation) and modulated by LAI sensitivity to water availability. Our study illustrates that understanding changes in the soil moisture-vegetation interplay requires jointly considering changing climate (Jiao et al. 2021; Gampe et al. 2021) and vegetation characteristics (Carminati and Javaux 2020; Anderegg et al. 2019) in the form of overall sensitivity. Our results are derived through explainable machine learning, which can essentially isolate the influence of soil moisture on LAI from that of other relevant drivers, and thereby goes beyond purely correlation-based analyses. Land surface models fail to capture the increasing LAI sensitivity to soil moisture, related to an inaccurate representation of overall LAI sensitivity in terms of spatial patterns and magnitude. Overall, the detected increasing vegetation sensitivity to soil moisture reflects enhanced ecosystem vulnerability to soil dryness. By identifying high and increasing sensitivity regions, our study highlights hotspot areas where decreasing soil moisture trends can induce severe impacts on vegetation and related carbon-climate feedbacks.

3.A Appendix

This appendix includes the supplementary materials of the presented publication.

Table 3.A1. Depths and layers for aggregated near- and sub-surface soil moisture from observation-based products and land surface models. *LPX-Bern applies the two-bucket method which does not define specific depths of two soil layers; *LPJ-GUESS, VISIT and CABLE-POP are not used in averaging results of LSMs-based LAI sensitivity to near-surface soil moisture, due to incompatible value ranges of near-surface soil moisture amount with the other models (Appendix Figure 3.A3).

		Near-surface soil moisture	Sub-surface soil moisture
Reanalyses	ERA5	Layer 1: 0-7 cm	Layer 2-3: 7-100 cm
	GLEAM	Layer 1: 0-10 cm	Layer 2: 10-100 cm
	MERRA-2	Layer 1: 0-5 cm	Layer 2: 5-100 cm
Observation-based	SoMo.ml	Layer 1: 0-10 cm	Layer 2-3: 10-50 cm
Land surface models	ISAM	Layer 1-3: 0-9 cm	Layer 4-7: 9-82.56 cm
	LPX-Bern	Layer 1-4: first bucket*	Layer 5-8: second bucket*
	CLM5.0	Layer 1-2: 0-6 cm	Layer 3-8: 6-92 cm
	JSBACH	Layer 1: 0-6.5 cm	Layer 2-3: 6.5-122.5 cm
	JULES	Layer 1: 0-10 cm	Layer 2-3: 10-100 cm
	ORCHIDEE-CNP	Layer 1-6: 0-9 cm	Layer 7-10: 9-150 cm

LPJ-GUESS	Layer 1: 0-50 cm*	Layer 2: 50-150 cm
VISIT	Layer 1: 0-30 cm*	Layer 2: 30 cm-200 cm
CABLE-POP	Layer 1-2: 0-8 cm*	Layer 3-4: 8-64.3 cm

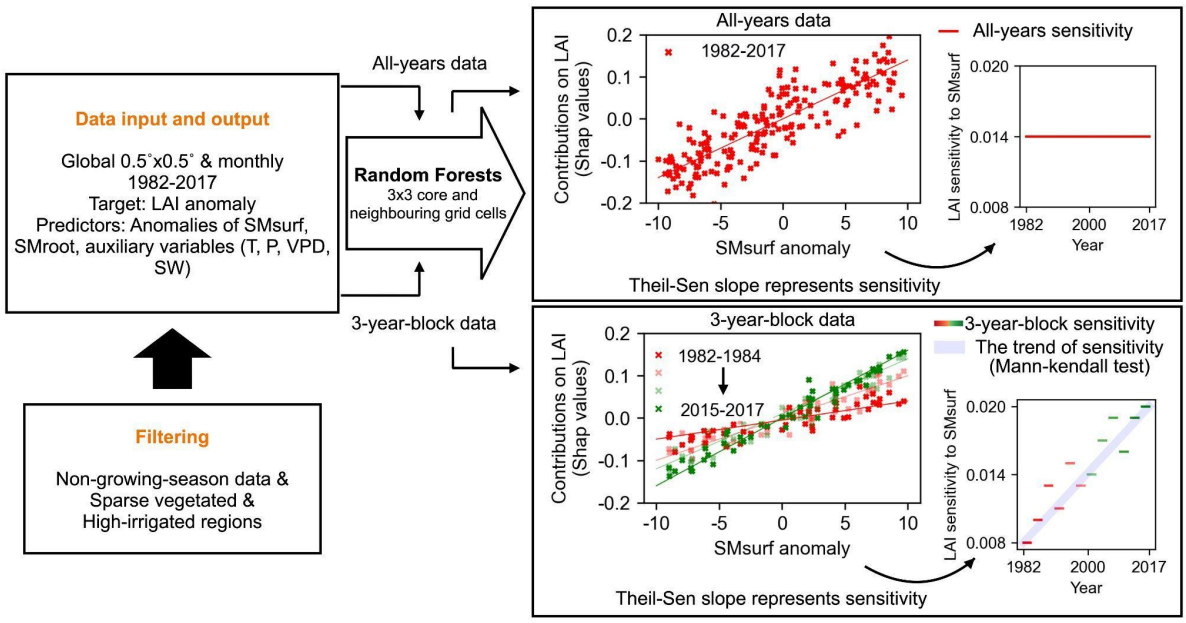

Figure 3.A1. The flowchart of data-processing and sensitivity analysis. Details can be found in Methods: Data -processing, Auxiliary data, Overall sensitivity and Sensitivity trends, respectively. Hydro-climate data anomalies are the predictor variables and LAI anomaly is the target variable. Random forests and SHAP values are used to isolated contributions of near-surface (or sub-surface) soil moisture to LAI for each 3x3 grid cells, and Theil-sen regression is used to estimate the linear sensitivity of LAI to near-surface (or sub-surface) soil moisture from all-years data and 3-year-block data, separately. To note that values of x and y axes in conceptual sub-figures do not have any real meaning. T denotes temperature, P denotes precipitation, VPD denotes vapor pressure deficit, and SW denotes incoming short-wave solar radiation.

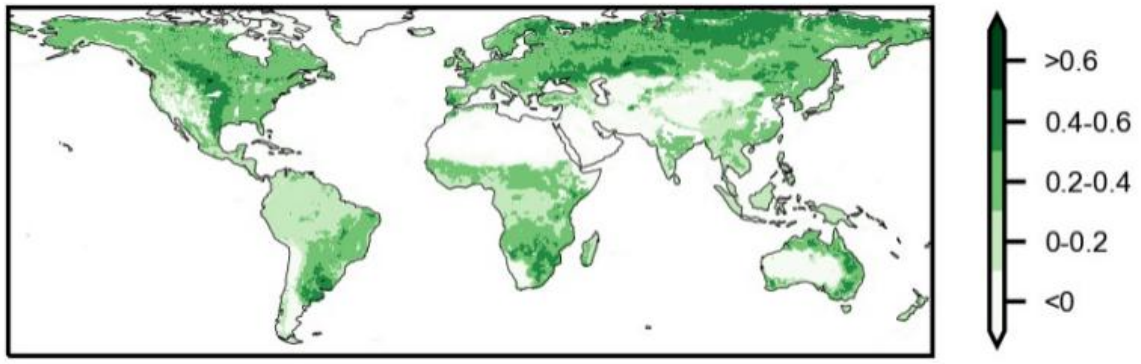

Figure 3.A2. The performance (out-of-bag R^2) of grid cell-based random forest models predicting monthly LAI from hydro-climate anomalies from ERA5-Land during 1982 to 2017. We display the mean R^2 across results from 5 observed LAI products.

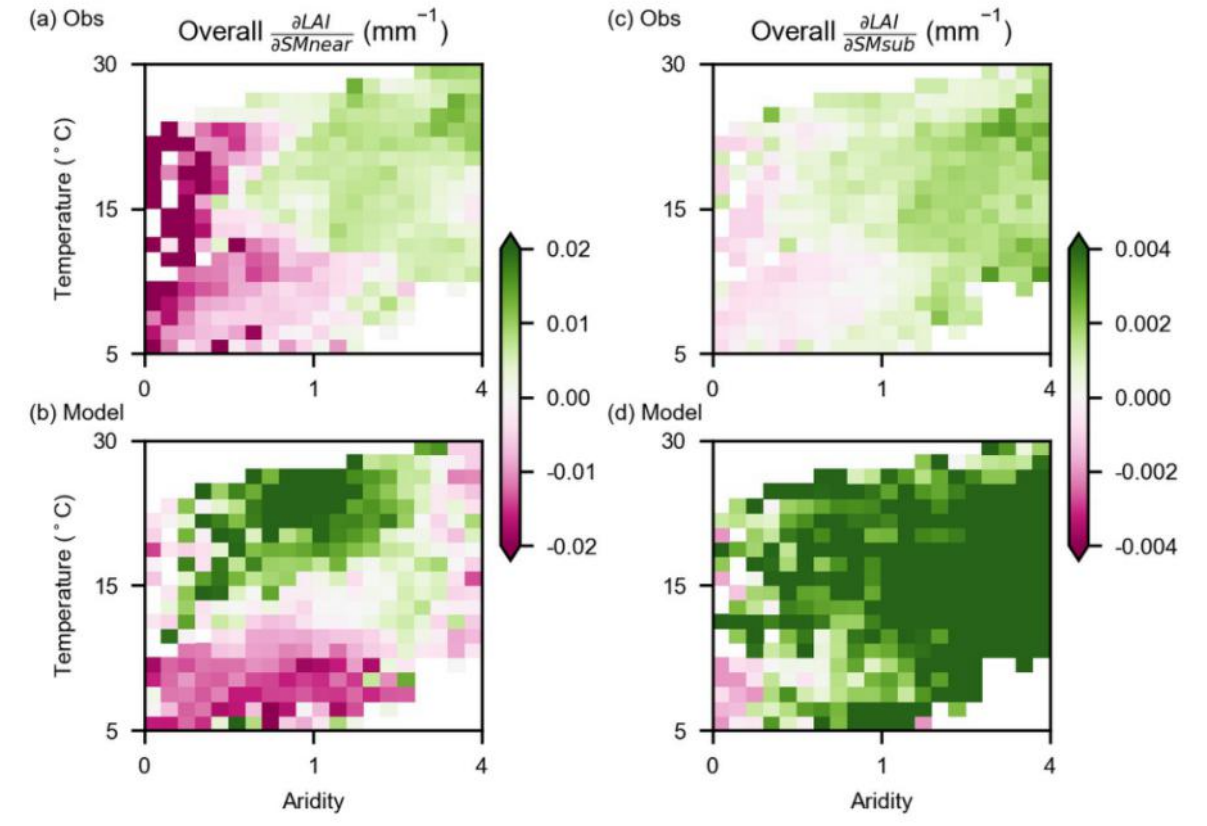

Figure 3.A3. Overall sensitivity of LAI to near-surface soil moisture (Overall $\frac{\delta LAI}{\delta SMnear}$) and sub-surface soil moisture (Overall $\frac{\delta LAI}{\delta SMsub}$) from observations (Obs) and LSMs (Model), given as respective ensemble means across climate regimes. Values higher than 1 in aridity index denote dry conditions (Methods: Auxiliary data).

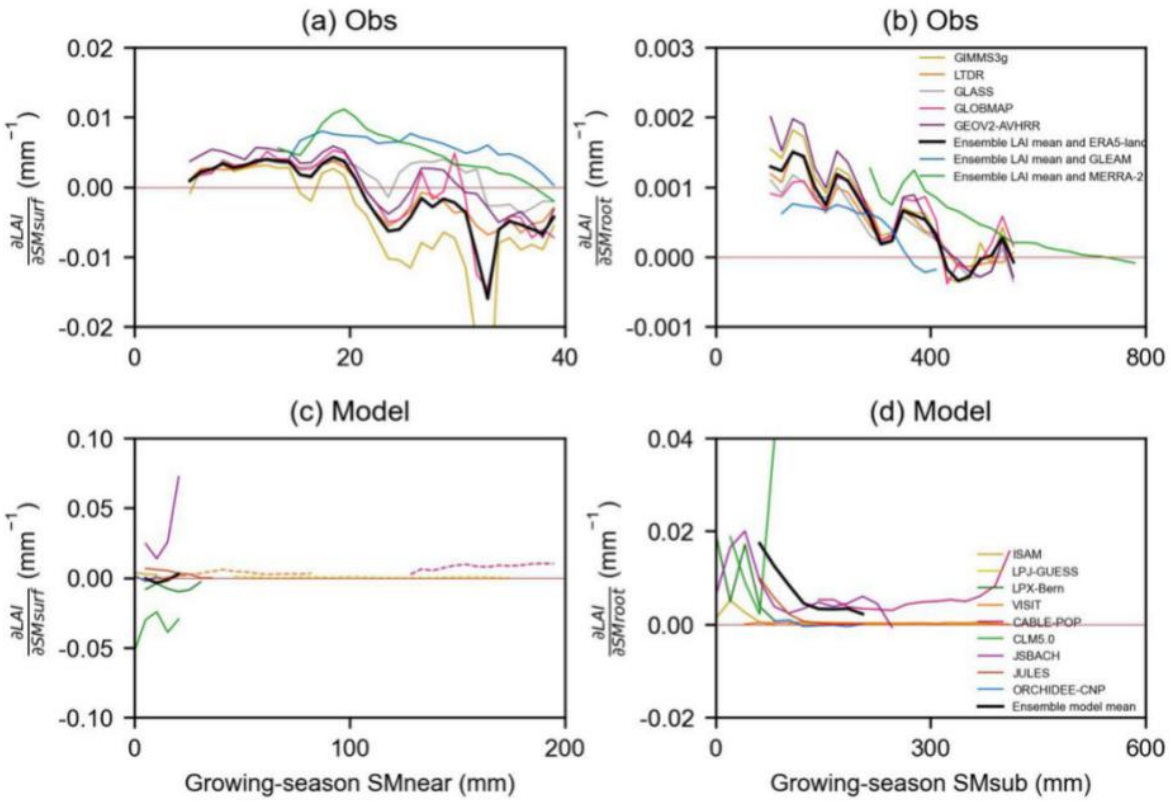

Figure 3.A4. As Figure 3.2 but providing individual response functions of global LAI sensitivity to soil moisture from individual observational and LSMs results. (a) Response functions of LAI sensitivity ($\frac{\delta LAI}{\delta SMnear}$) to growing-season (see Methods: Data pre-processing) mean near-surface soil moisture (SMnear) from observations (Obs) across global grid cells. The black line shows the ensemble means and colored lines show observational results from individual products with visible labels. (b) Similar to (a) but for LAI sensitivity to sub-surface soil moisture ($\frac{\delta LAI}{\delta SMsub}$). (c) and (d) Similar to (a) and (b) but for LSMs results (Model). All panels only include global grid cells with significant LAI sensitivities to soil moisture. To infer significant LAI sensitivities, two-sided significance tests are done for each grid cell at the $p<0.01$ level as assessed with Theil-sen regressions. Single LSMs results not being accounted for averaged results (black lines) due to incompatible value ranges of near-surface soil moisture amounts are marked by dashed lines in (c).

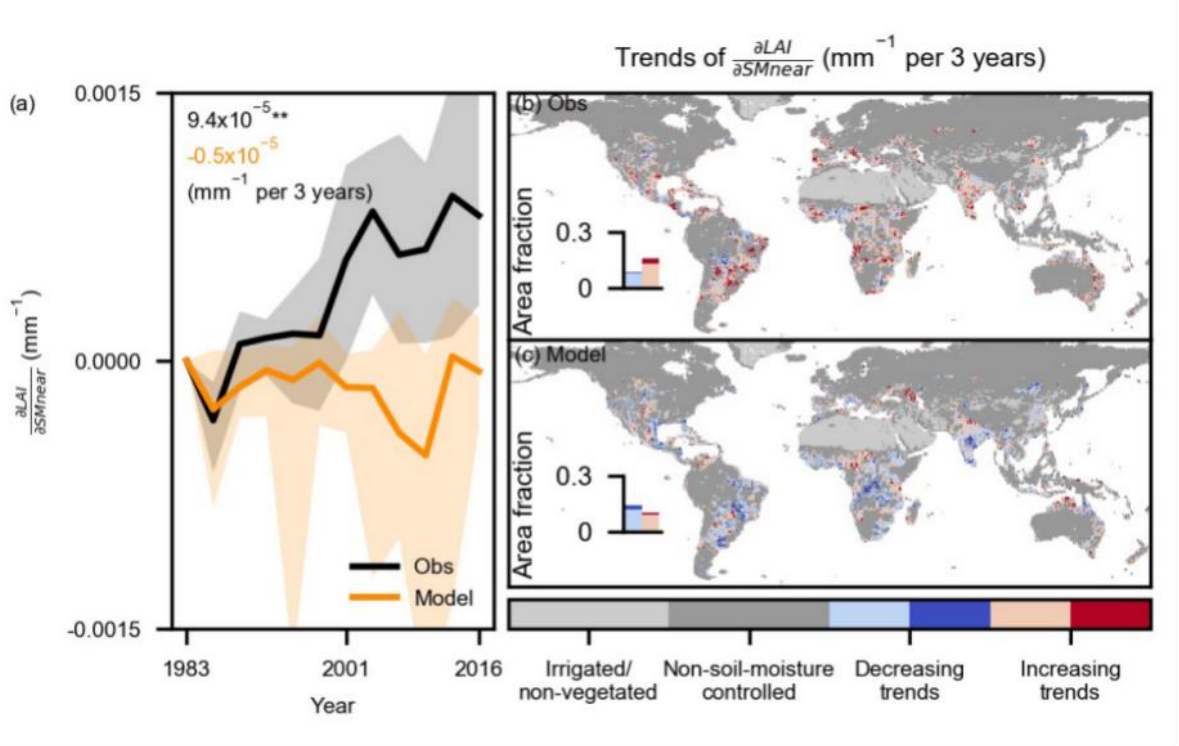

Figure 3.A5. Similar as in Figure 3.3 but for trends in LAI sensitivity to near-surface soil moisture (SMnear). (a) Temporal variations of global mean LAI sensitivity to near-surface soil moisture ($\frac{\delta LAI}{\delta SMnear}$) are computed by 3-year blocks between 1982 and 2017. The y-axis denotes the change since 1982 in respective products or models. Solid lines denote the median results from ensemble observations (Obs) and LSMs (Model); Shaded areas denote interquartile ranges of LAI sensitivity from multiple LAI products and models; Text denotes slopes of trends; ** denotes passing the two-sided significance test as assessed with Mann-Kendall at $p<0.01$, otherwise $p>0.05$ (Methods: Sensitivity trends). (b) Trends of LAI sensitivity to near-surface soil moisture ($\frac{\delta LAI}{\delta SMnear}$) in observations and models using their ensemble means. (c) Similar to (b) but for land surface models. Insets indicate the area fraction of decreasing and increasing trends within the study area. Light blue and red colors denote insignificant changes ($p>=0.1$); dark blue and red colors denote significant changes ($p<0.1$). In (b) and (c), two-sided significance tests are done for each grid cell at the $p<0.1$ level as assessed with Mann-Kendall's test.

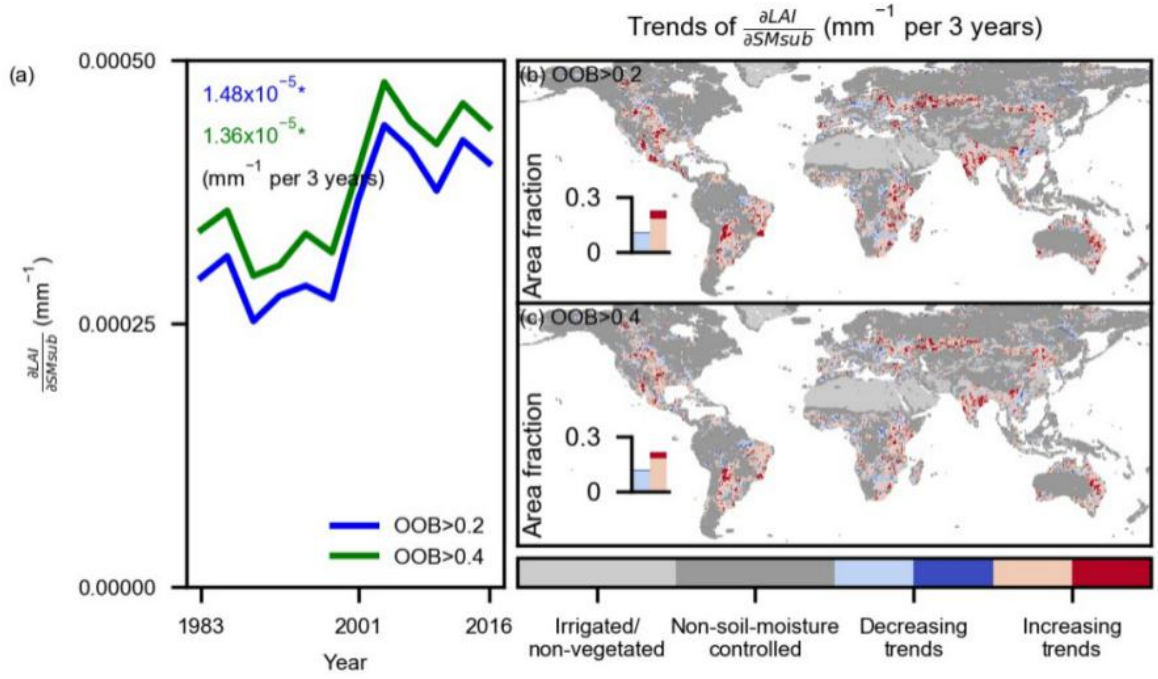

Figure 3.A6. Similar as in Figure 3.3 but for overall and 3-year-block sensitivities derived using different thresholds of cross-validation out-of-bag R2. (a) Temporal variations of global mean LAI sensitivity to sub-surface soil moisture ($\frac{\delta LAI}{\delta SMsub}$) as computed from 3-year blocks between 1982 and 2017. Numbers in the upper left corner denote slopes; * denotes passing the two-sided significance test as assessed with Mann-Kendall at $p<0.05$ (Methods: Sensitivity trends). (b, c) Trends of LAI sensitivity to sub-surface soil moisture (Trends of $\frac{\delta LAI}{\delta SMsub}$). Insets indicate the area fraction of decreasing and increasing trends within the study area. Light blue and red colors denote insignificant changes ($p>=0.1$); dark blue and red colors denote significant changes ($p<0.1$). In (b) and (c), two-sided significance tests are done for each grid cell at the $p<0.1$ level as assessed with Mann-Kendall's test.

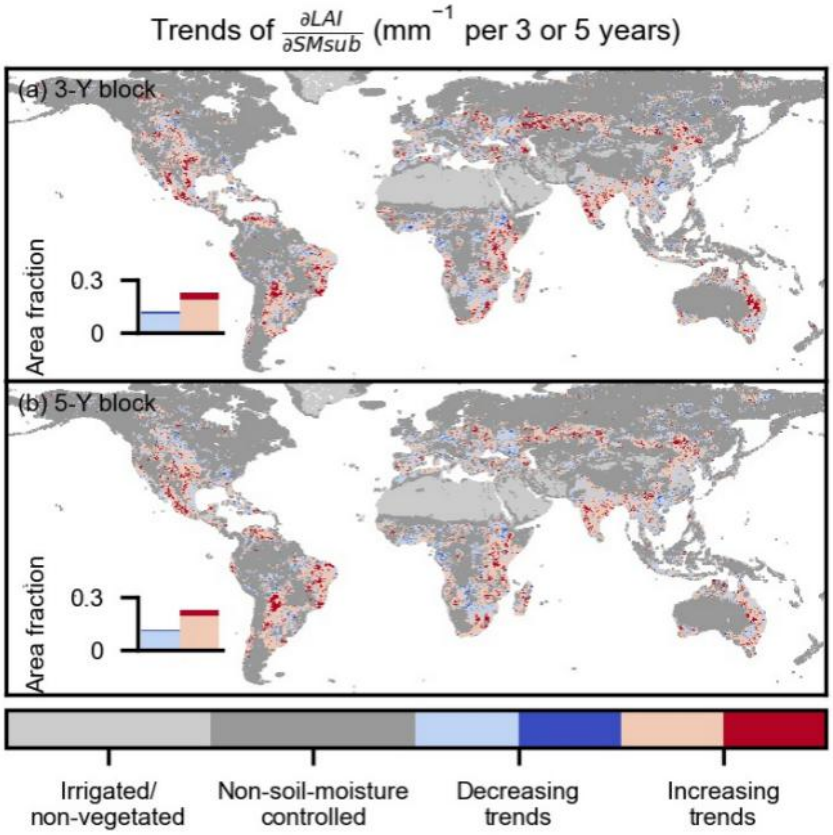

Figure 3.A7. Similar as in Figure 3.3 but for global trends in observed LAI sensitivity to sub-surface soil moisture (Trends of $\frac{\delta LAI}{\delta SMsub}$) inferred by different subsets of data. (a) 3-Y blocks from 1982 to 2017 (1982-1984, 1985-1987, …, 2015-2017) and (b) 5-Y blocks from 1982 to 2016 (1982-1986, 1987-1991, …, 2012-2016). Insets indicate the area fraction of decreasing and increasing trends within the study area. Light blue and red colors denote insignificant changes ($p>=0.1$); dark blue and red colors denote significant changes ($p<0.1$). In (a) and (b), two-sided significance tests are done for each grid cell at the $p<0.1$ level as assessed with Mann-Kendall's test.

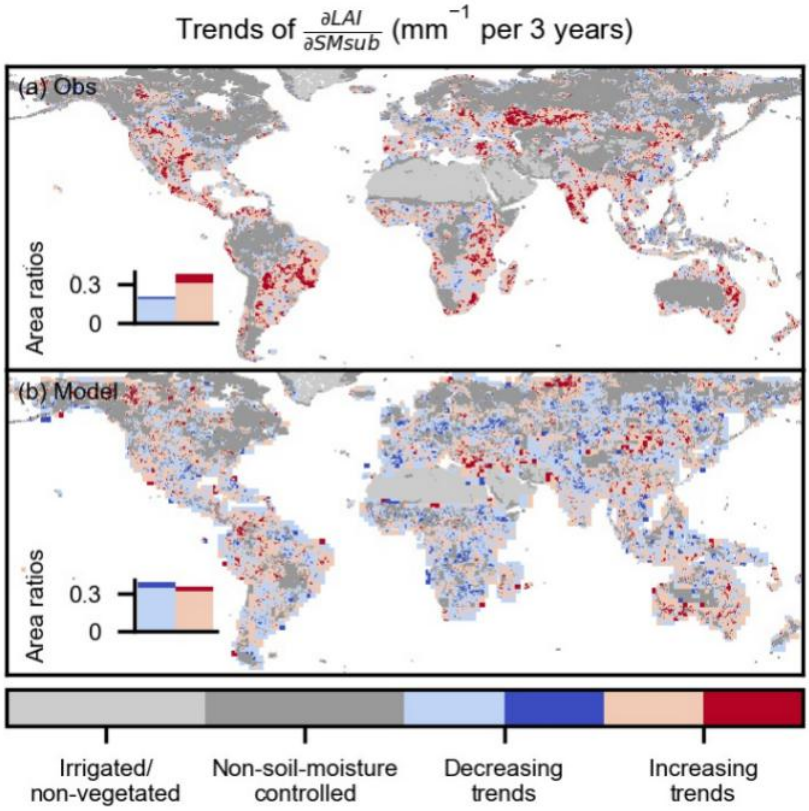

Figure 3.A8. As Figure 3.3 but providing a full version of global trends in LAI sensitivity to sub-surface soil moisture (Trends of $\frac{\delta LAI}{\delta SMsub}$). (a) observed sensitivity trends (Obs) without additional filters by positive overall sensitivity inferred from LSMs. (b) sensitivity trends from LSMs (Model) without additional filters by positive overall sensitivity inferred from observational results. Insets indicate the area fraction of decreasing and increasing trends within the study area. Light blue and red colors denote insignificant changes ($p>=0.1$); dark blue and red colors denote significant changes ($p<0.1$). In (a) and (b), two-sided significance tests are done for each grid cell at the $p<0.1$ level as assessed with Mann-Kendall's test.

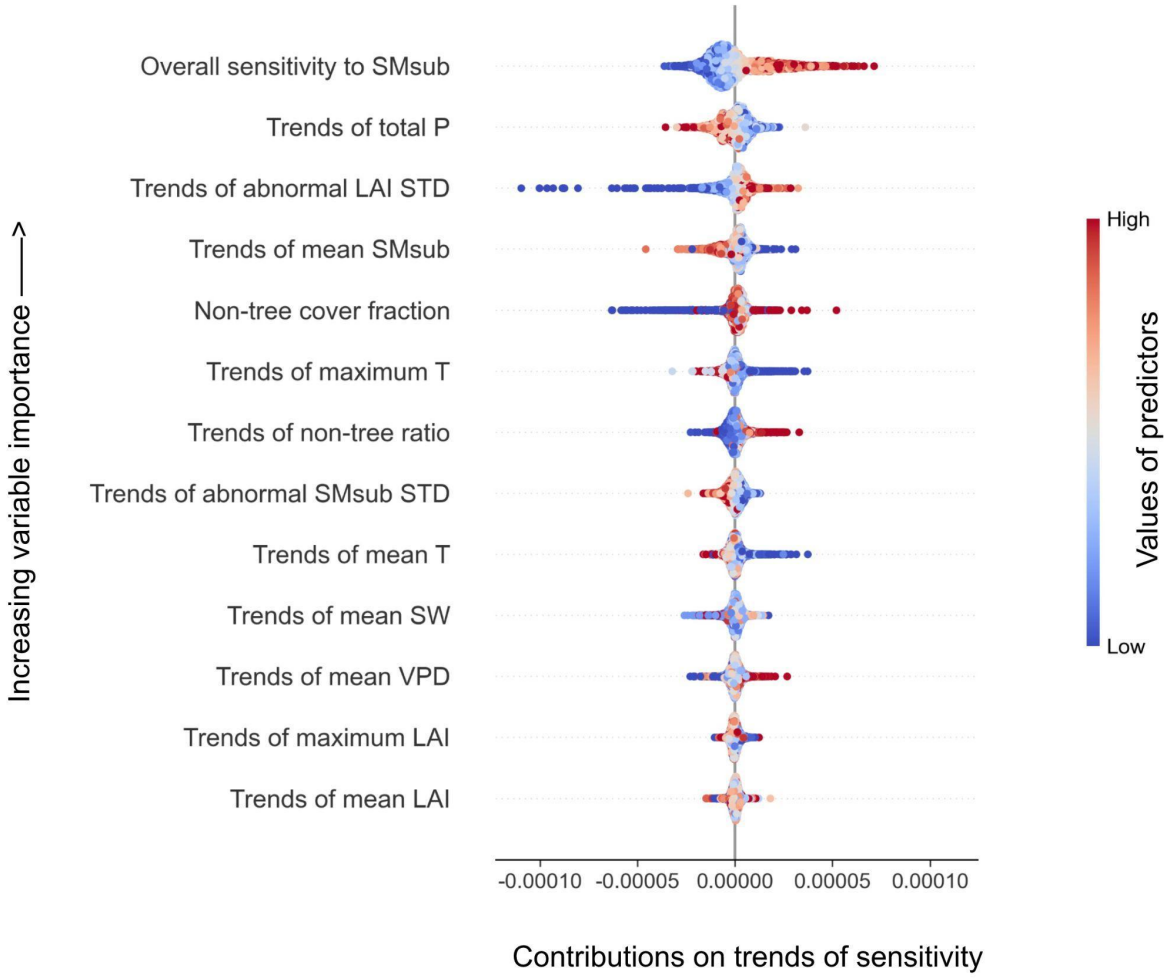

Figure 3.A9. Relative importance and marginal contributions (Shap values) of multiple factors to observed global trends in LAI sensitivity to sub-surface soil moisture (SMsub). STD denotes the standard deviation, T denotes temperature, P denotes precipitation, VPD denotes vapor pressure deficit, and SW denotes incoming short-wave solar radiation.

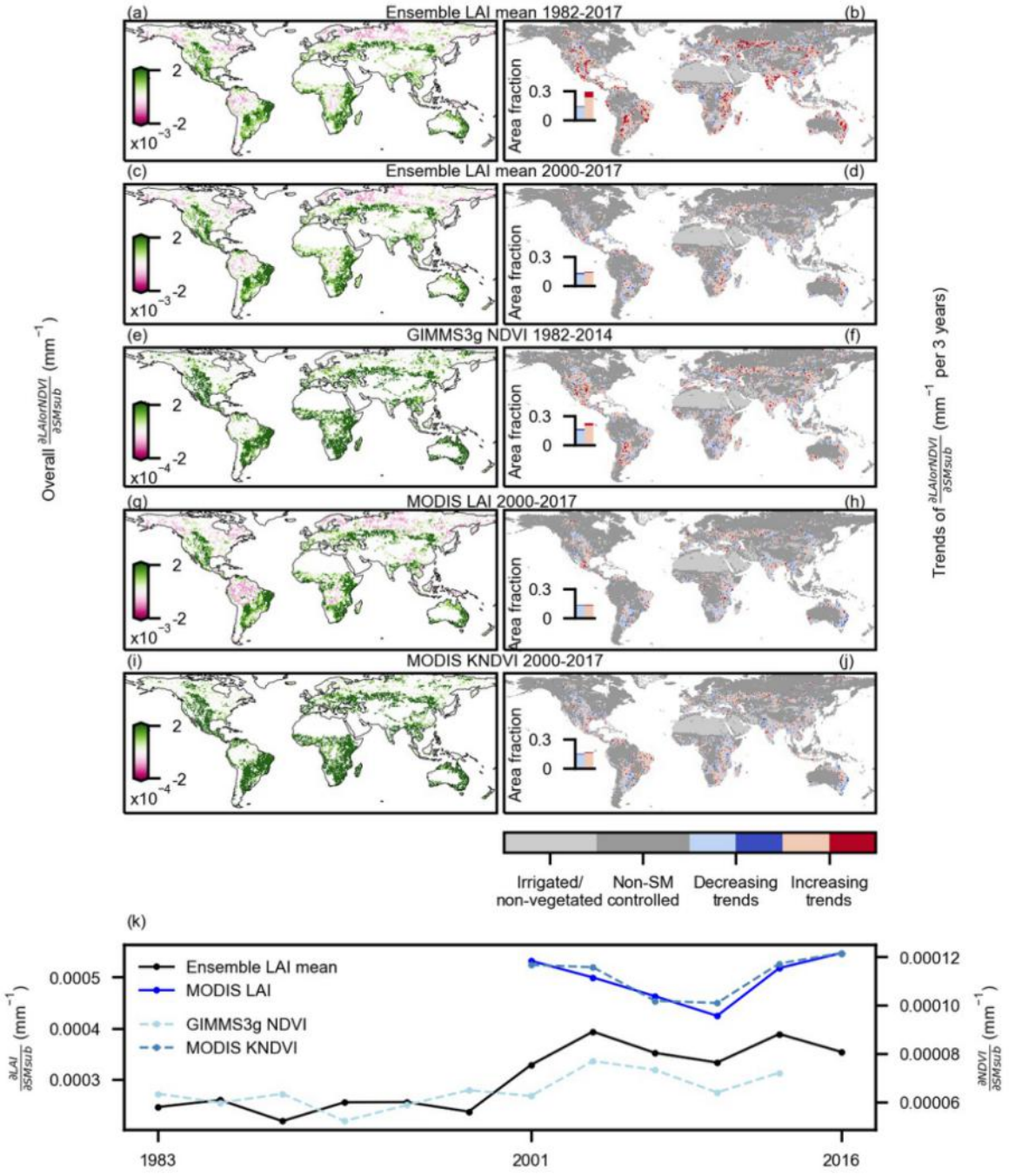

Figure 3.A10. Multiple-product comparisons of overall sensitivity, temporal variations of sensitivity and sensitivity trends of observed vegetation indices to sub-surface soil moisture. (a, c, e, h, i) Multiple-product comparisons of overall vegetation sensitivity to sub-surface soil moisture (Overall $\frac{\delta LAI}{\delta SMsub}$). (a, c, e, h, i) apply the two-sided significance test at the $p<0.01$ level as assessed with Theil-sen regressions for each grid cell, and grid cells which pass the significance test are colored by pink or green. (b, d, f, h, j) Multiple-product comparisons of global trends in vegetation sensitivity to sub-surface soil moisture (Trends of $\frac{\delta LAI}{\delta SMsub}$). Insets indicate the area fraction of decreasing and increasing trends in the study area. Light blue and red colors

denote insignificant changes (p>=0.1); dark blue and red colors denote significant changes (p<0.1). In (b, d, f, h, j), two-sided significance tests are done for each grid cell at the p<0.1 level as assessed with Mann-Kendall's test. (k) Multiple-product comparisons of temporal variations of LAI sensitivity to sub-surface soil moisture ($\frac{\delta LAI}{\delta SMsub}$). Multiple greenness products are as follows: averaged LAI from 5 long-term products (Ensemble LAI mean), MODIS LAI, GIMMS3g NDVI, MODIS kernel NDVI (MODIS kNDVI).

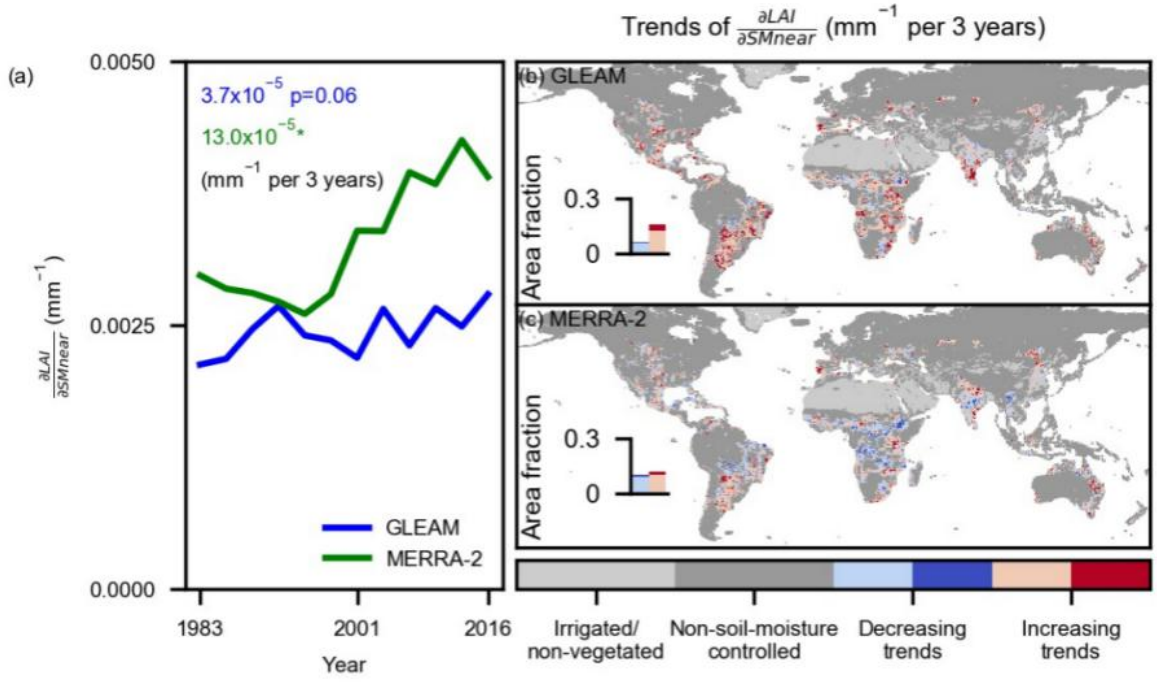

Figure 3.A11. Similar as in Figure 3.3 but for trends in observed LAI sensitivity to near-surface soil moisture from Gleam and MERRA-2. (a) Temporal variations of global mean LAI sensitivity to near-surface soil moisture ($\frac{\delta LAI}{\delta SMnear}$) are computed by 3-year blocks between 1982 and 2017. Text denotes slopes of trends; * denotes passing a two-sided significance test as assessed with Mann-Kendall at p<0.05 (Methods: Sensitivity trends). (b, c) Trends of LAI sensitivity to sub-surface soil moisture from Gleam and MERRA-2. Insets indicate the area fraction of decreasing and increasing trends within the study area. Light blue and red colors denote insignificant changes (p>=0.1); dark blue and red colors denote significant changes (p<0.1). In (b) and (c), two-sided significance tests are done for each grid cell at the p<0.1 level as assessed with Mann-Kendall's test.

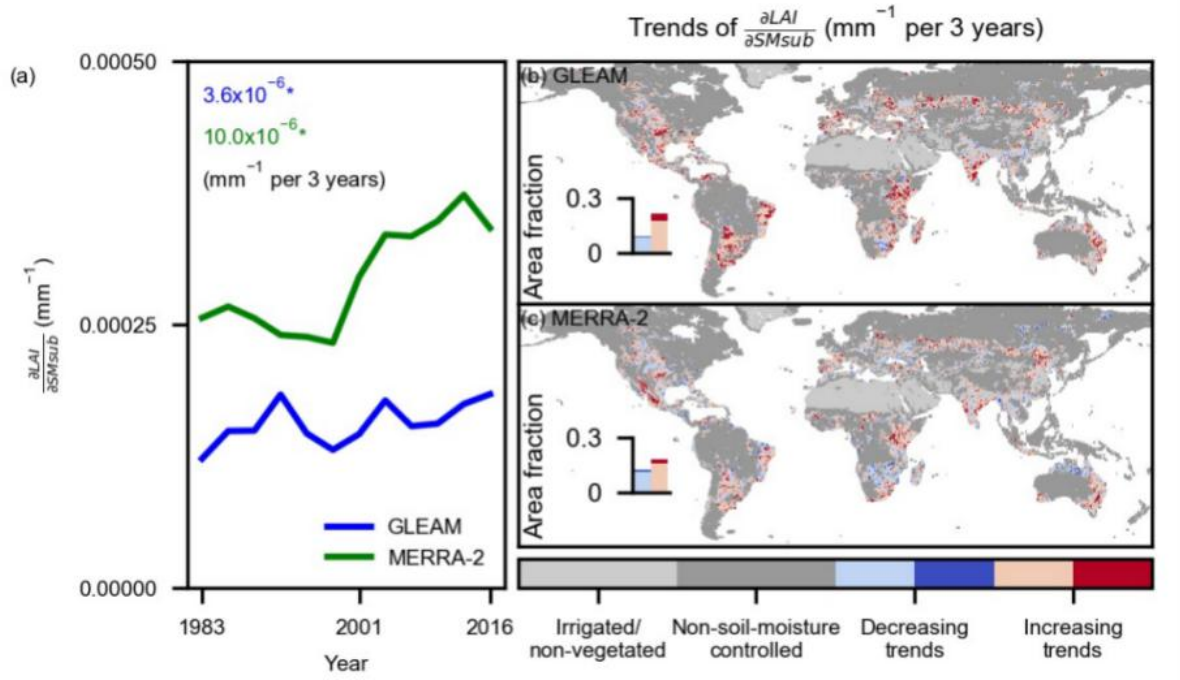

Figure 3.A12. Similar as in Figure 3.3 but for trends in observed LAI sensitivity to sub-surface soil moisture from Gleam and MERRA-2. (a) Temporal variations of global mean LAI sensitivity to sub-surface soil moisture ($\frac{\delta LAI}{\delta SMsub}$) are computed by 3-year blocks between 1982 and 2017. Text denotes slopes of trends; * denotes passing a two-sided significance test as assessed with Mann-Kendall at $p<0.05$ (Methods: Sensitivity trends). (b, c) Trends of LAI sensitivity to sub-surface soil moisture from Gleam and MERRA-2. Insets indicate the area fraction of decreasing and increasing trends within the study area. Light blue and red colors denote insignificant changes ($p>=0.1$); dark blue and red colors denote significant changes ($p<0.1$). In (b) and (c), two-sided significance tests are done for each grid cell at the $p<0.1$ level as assessed with Mann-Kendall's test.

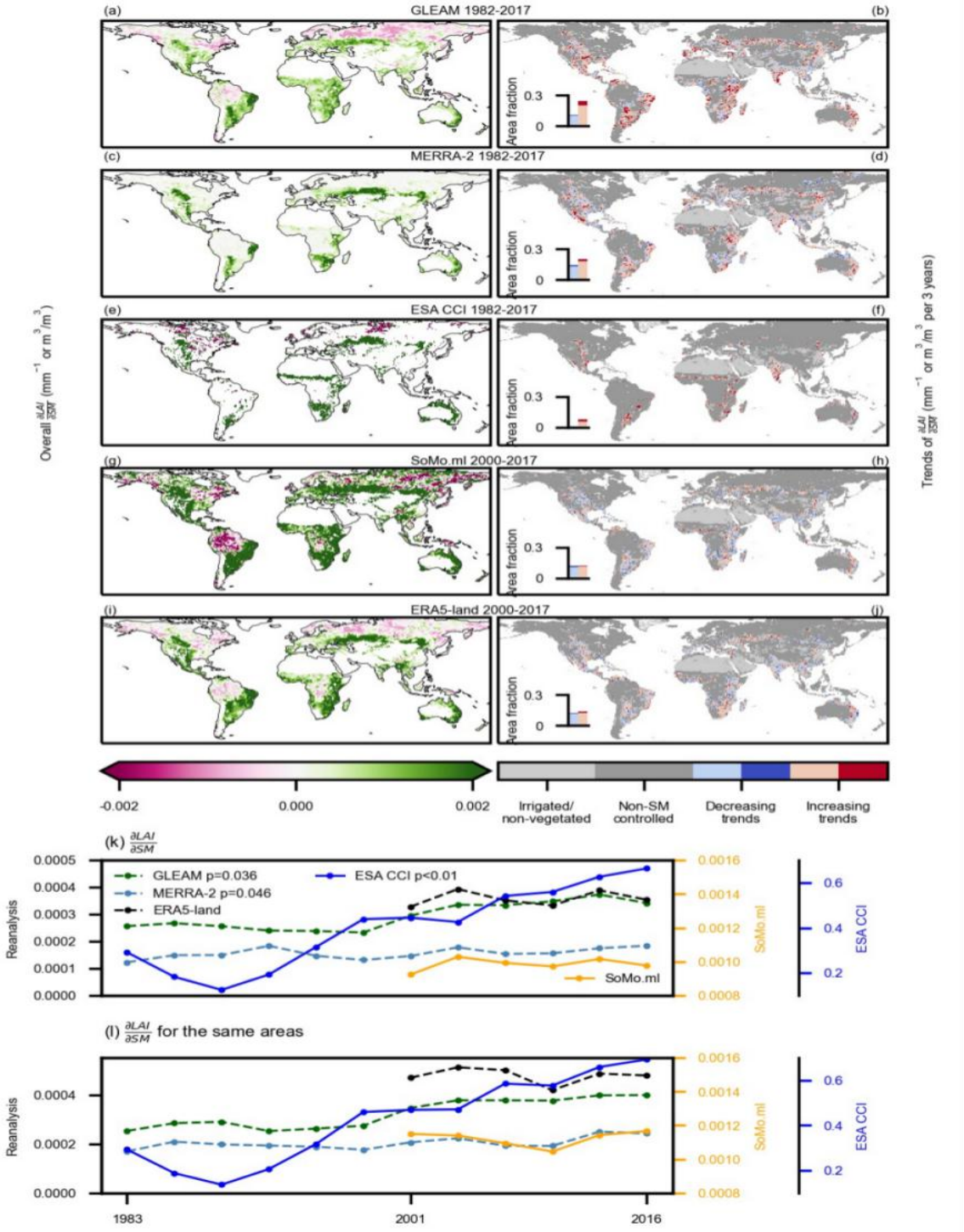

Figure 3.A13. Comparisons of overall sensitivity, temporal variations of sensitivity and sensitivity trends of LAI to multiple soil moisture (SM) products. Except for ESA CCI surface soil moisture, all the other products are sub-surface soil moisture. (a, c, e, h, i) Overall LAI sensitivity to soil moisture (Overall $\frac{\delta LAI}{\delta SM}$). (a, c, e, h, i) apply the two-sided significance test at the $p<0.01$ level as assessed with Theil-sen regressions for each grid cell, and grid cells which pass the significance test are colored by pink or green. (b, d, f, h, j) Global trends in LAI sensitivity to soil moisture (Trends of $\frac{\delta LAI}{\delta SM}$). Insets indicate the area fraction of decreasing and increasing

trends in the study area. Light blue and red colors denote insignificant changes (p>=0.1); dark blue and red colors denote significant changes (p<0.1). In (b, d, f, h, j), two-sided significance tests are done for each grid cell at the p<0.1 level as assessed with Mann-Kendall's test. (k) Temporal variations of LAI sensitivity to soil moisture ($\frac{\delta LAI}{\delta SM}$) averaged from global grid cells and (l) averaged from the same global areas which are available from all soil moisture analyses. P values from the two-sided significance test are indicated in (k) as assessed with Mann-Kendall's test. ESA CCI near-surface soil moisture is expressed in m3/m3, while all other sub-surface soil moisture products are in mm.

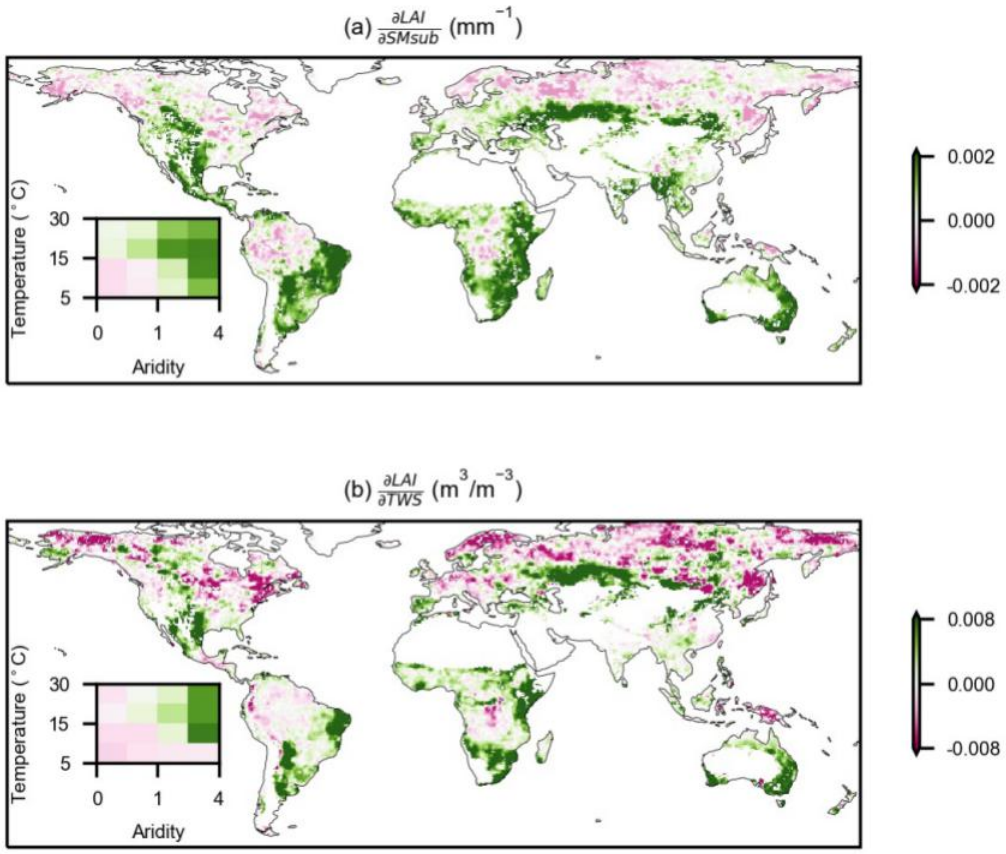

Figure 3.A14. Global sensitivity of LAI to (a) ERA5-Land sub-surface soil moisture ($\frac{\delta LAI}{\delta SMsub}$) and (b) GRACE total water storage ($\frac{\delta LAI}{\delta TWS}$) in the period 2003-2017. Inserts present median values of overall sensitivity across climate regimes. (a) and (b) apply the two-sided significance test at the p<0.01 level as assessed with Theil-sen regressions for each grid cell, and grid cells which pass the significance test are colored by pink or green.

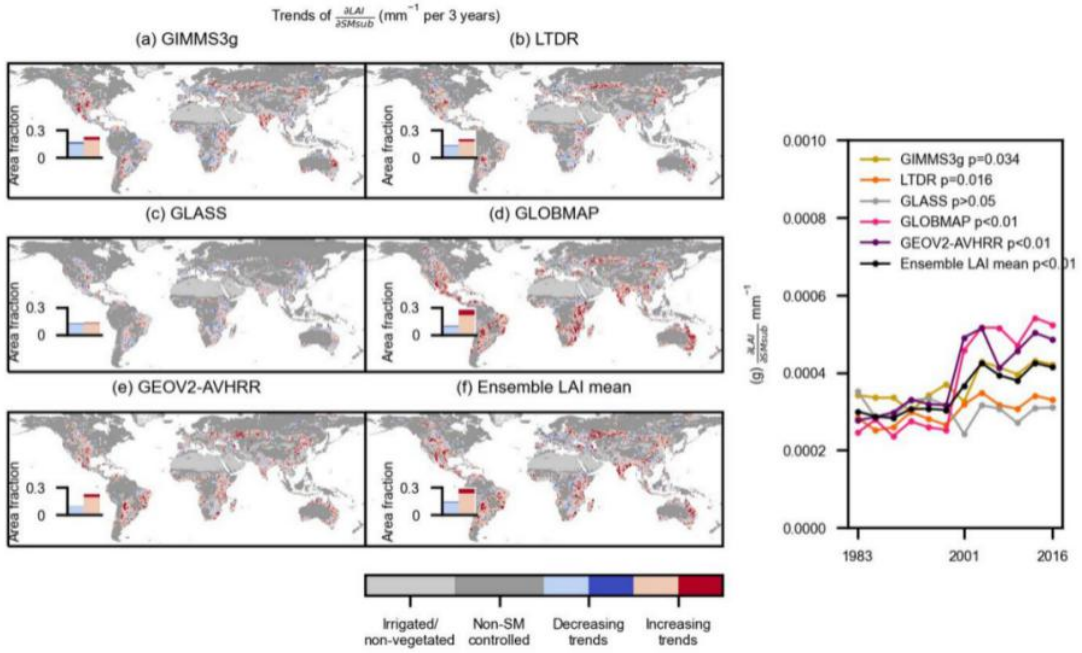

Figure 3.A15. Trends of LAI sensitivity and temporal variations of sensitivity to sub-surface soil moisture (SMsub) for individual LAI products. (a-f) Trends of LAI sensitivity to sub-surface soil moisture ($\frac{\delta LAI}{\delta SMsub}$). (g) Temporal variations of global LAI sensitivity to sub-surface soil moisture ($\frac{\delta LAI}{\delta SMsub}$). Trends of LAI sensitivity and temporal variations of LAI sensitivity to sub-surface soil moisture for individual LAI products. (a-f) Trends of LAI sensitivity to sub-surface soil moisture. (g) Temporal variations of global LAI sensitivity to sub -surface soil moisture. P values from the two-sided significance test are indicated in (g) as assessed with Mann -Kendall's test.

4 The drought effect on vegetation physiology inferred from space

Abstract

Drought has complex impacts on terrestrial vegetation and consequently affects the carbon and water cycles. Vegetation drought responses manifest through physiological modulations of its functioning such as reduced stomatal conductance or changes in vegetation structure such as the leaf area. However, physiological dynamics are poorly understood at large spatial scales due to a lack of direct observations. Here, we isolate the physiological drought response globally from satellite-derived data streams using machine learning techniques. We determine structural components of the satellite signals by separating the fractional variability explained by leaf area index changes, while the remaining variability constitutes the physiological response. We find that physiological changes in photosynthesis, evaporation, and plant hydraulics differ across regions with different aridity, with the strongest reductions in transitional and dry areas. Similar patterns as in these observation-based findings are found from simulations of the vegetation physiological response to drought, with a soil–plant–atmosphere continuum model coupled with a radiative transfer model. Overall, isolating and understanding the ecosystem physiology response to drought enables a better understanding of biogeochemical and biophysical feedbacks and the role of ecosystems for climate change.

This chapter includes:

Li, W., Pacheco-Labrador, J., Migliavacca, M., Miralles, D., Hoek van Dijke, A., Reichstein, M., Forkel, M., Zhang, W., Frankenberg, C., Panwar, A., Zhang, Q., Weber, U., Orth, R. (2023). Widespread and complex drought effects on vegetation physiology inferred from space. Nature Communications, accepted.

4.1 Introduction

Soil moisture droughts are increasing in terms of duration and intensity in many areas worldwide (IPCC 2021; Dai et al. 2018). Such droughts affect vegetation functioning and can increase the risk of carbon starvation and hydraulic failure, and consequently induce plant mortality (Anderegg et al. 2012). Since terrestrial vegetation directly regulates carbon and water fluxes, plant drought responses feed back to climate and can aggravate global warming (Bonan 2010; Anderegg et al. 2019). Vegetation functioning is affected by its structure (e.g., leaf demography and leaf area) (Biriukova et al. 2021) and its physiology (e.g., stomatal closure) (Novick et al. 2016). Likewise, a comprehensive characterization of the large-scale vegetation response to droughts requires disentangling the associated structural and physiological changes. Vegetation foliar cover emerges as one of the main properties of vegetation structure. Satellite-based vegetation greenness indices or leaf area index (LAI) products presenting green foliar cover have been widely studied to understand vegetation response to drought (Zhang et al. 2013; Wu et al. 2022; Morton et al. 2014).

On the other hand, vegetation physiology, such as maximum carboxylation rate and stomatal conductance, can be assessed at the site level (Fu et al. 2022), but they are only implicitly included in global observations (Chen et al. 2022). Vegetation physiology typically responds faster than structure to environmental stress, yet the drought response is commonly diagnosed by concurrent LAI changes (mostly structural signals) which could underestimate vegetation functional responses (Stocker et al. 2019; Morton et al. 2014; Hu et al. 2022; Yao Zhang et al. 2018). Drought-associated stress leads to reductions in stomatal conductance which in turn reduce transpiration and photosynthesis (Novick et al. 2016; Stocker et al. 2018). At the same time, increases in temperatures and radiation below optimal thresholds can promote photosynthesis by stimulating enzyme (Rubisco) activity and electron transport rate (He et al. 2022; Luo and Keenan 2020). This highlights the relevance of characterizing vegetation physiology changes to understand the vegetation drought response across the globe.

Recent advances in satellite remote sensing present multiple opportunities to monitor vegetation physiology and resulting functioning (see Figure 4.1) (Magney et al. 2019; Doughty et al. 2019; Smith et al. 2020; Jiao, Wang, and McCabe 2021; Zeng et al. 2022; Konings et al. 2021; Chen et al. 2022). Specifically, (i) solar-induced chlorophyll fluorescence (SIF) is an indicator for ecosystem photosynthesis, and the TROPOspheric Monitoring Instrument (TROPOMI) onboard the Sentinel-5p satellite provides global SIF imagery continuously since 2018 (Magney et al. 2019; Doughty et al. 2019; Köhler, et al. 2018), and overcomes problems with cloud-induced biases in previous SIF products and vegetation greenness indices (Morton et al. 2014). (ii) Ecosystem evapotranspiration (hereafter 'ET') instantly regulates land surface temperature (Mildrexler, Zhao, and Running 2011; Farella et al. 2022). Since ET cannot be directly observed at the global scale (Zhao et al. 2022), we approximate ET using land surface temperature from the Moderate Resolution Imaging Spectroradiometer (MODIS) and a simplified surface energy balance model (hereafter 'SSEB') (Panwar and Kleidon 2022; Panwar, Renner, and Kleidon 2020). (iii) Vegetation water content can be

observed using Vegetation Optical Depth (VOD) data from microwave remote sensing and can be used for measuring vegetation hydraulics. High-frequency VOD is sensitive to upper-canopy water content changes, such that it carries information about hydraulic regulation at the diurnal timescale, and also reflects canopy biomass changes at long time scales (Konings et al. 2021). For instance, VOD from the Advanced Microwave Scanning Radiometer 2 (AMSR2, X-band) has been used to monitor ecosystem hydraulics through the ratio of midday and midnight observations (hereafter referred as 'VOD ratio') (Konings and Gentine 2017; Anderegg et al. 2018; Zhang et al. 2019). Synthesizing these opportunities can facilitate the study of vegetation drought response from the perspective of plant physiology and enable a comprehensive diagnosis of drought effects on ecosystems globally.

In this study, we synergistically explore SIF, ET, and VOD ratio to study the global vegetation response to drought due to their inclusion of vegetation physiology. We use relative SIF (SIF divided by near-infrared reflected radiance; hereafter referred as 'SIFrel') (Yang and van der Tol 2018) to account for effects of incoming solar irradiation and satellite-observing angles on TROPOMI SIF imagery. Our study is based on data from March 2018–October 2021 at the 8-daily temporal and 0.25˚ spatial resolution (Methods Section: Observation-based data) where all data products are concurrently available. We define drought based on the soil moisture minimum during the growing season and only consider grid cells where the minimum of 40-year monthly soil moisture reanalysis records falls in our study period (Methods Section: Drought detection). Drought peaks for per grid cell are identified from 8-daily soil moisture data matching the temporal resolution of the satellite-based data streams, such that we can study the trajectories of ecosystem physiology before, during, and after drought peaks. We introduce a random forest-based approach to isolate the physiological components in SIFrel, ET, and VOD ratio (Appendix Figure 4.A1; Methods Section: Disentangling vegetation physiology). Thereby, we determine the structural response as the fraction of variability explained by concurrent changes in LAI in a random forest model, while the variability explained by hydro-meteorological variables in another random forest model indicates the physiological response. All vegetation and hydro-meteorological data are de-seasonalized and de-trended to minimize confounding effects (Methods Section: Data pre-processing). Note that seasonal cycles are computed based on only 4 years of data and therefore potentially affected by individual extreme years. However, we aggregate grid cell-based anomaly results in space across many grid cells of (e.g.) similar aridity, which improves the robustness of the results. Finally, we use the Soil Canopy Observation of Photochemistry and Energy flux (SCOPE) model to simulate the vegetation drought response and underlying physiological changes, and hence enable a mechanistic interpretation of our observational findings (Method Sections: SCOPE simulations) (van der Tol et al. 2014).

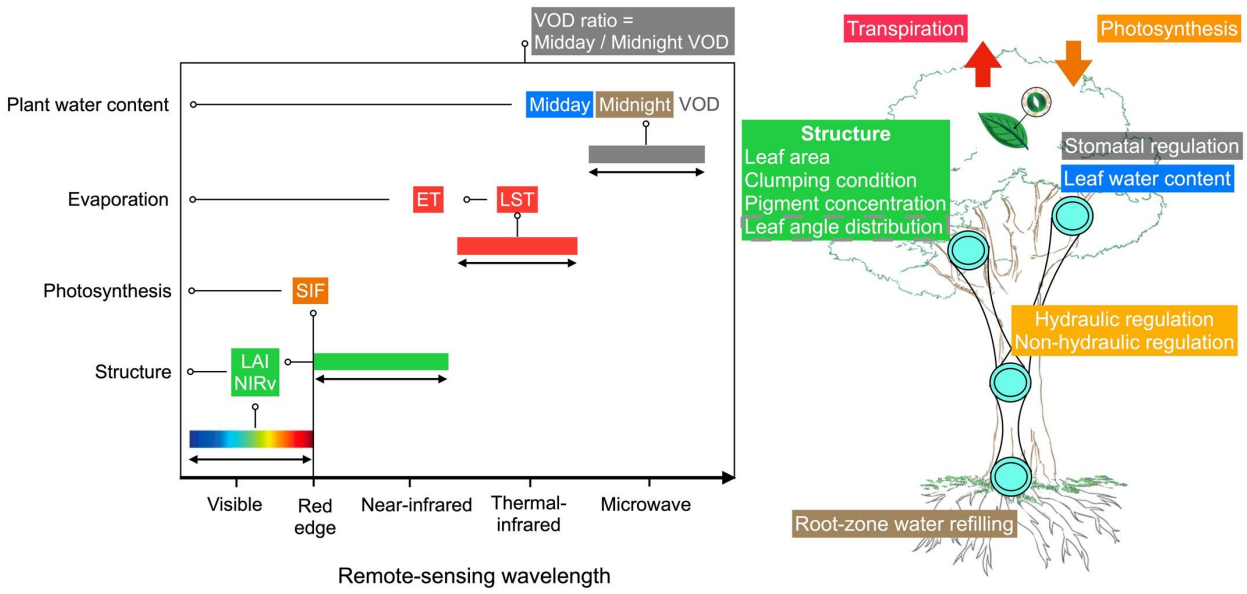

Figure 4.1. Overview of satellite-observed wavelength bands and their information related to vegetation functioning, structure, and physiology. Left: Considered wavelength bands and respective vegetation products employed in this study. Right: Functional, structural and physiological aspects of vegetation dynamics which can be inferred from the considered data. Colors of boxes suggest the mechanism link between data on the left and processes on the right. LAI: leaf area index; NIRv: the near-infrared reflectance of vegetation is an alternative product of vegetation canopy structure; SIF: sun-induced chlorophyll fluorescence; LST: land surface temperature; ET: evapotranspiration simulated by land surface temperature and a simplified surface energy balance model; VOD: vegetation optical depth. Leaf angle distribution is one of vegetation structural properties, but we note it by a dashed box because it is not globally available.

4.2 Data and methods

4.2.1 Observation-based data

We combine satellite remote-sensed Leaf Area Index (LAI), the near-infrared reflectance of vegetation (NIRv), solar-induced chlorophyll fluorescence (SIF), land surface temperature (LST) and Vegetation Optical Depth (VOD) data to investigate global vegetation drought responses (Figure 4.1). Among them, we use ungridded TROPOMI SIF (ftp://fluo.gps.caltech.edu/data/tropomi/) resampled to the 0.25˚ spatial resolution. This dataset can be used from March 2018 to October 2021. SIF is then normalized by near-infrared reflected radiance (relative SIF) to account for bidirectional reflectance effects and incoming solar irradiance (Yang and van der Tol 2018). Although previous studies indicate rare cloud cover influence on the SIF seasonality, cloud influence cannot be completely ruled out (Doughty et al 2019). Therefore, TROPOMI data are prefiltered to

remove soundings covered by heavy clouds (>0.5 of cloud fractions) to lessen potential cloud effects and maximize the number of observations during wet seasons.

MOD15A2H LAI (8-daily; https://lpdaac.usgs.gov/products/mod15a2hv006/), and MCD43C4 NIRv (daily; a product of NDVI multiply reflected near-infrared radiance; https://lpdaac.usgs.gov/products/mcd43c4v006/) are used to represent vegetation structure. Thermal reflectance from Moderate Resolution Imaging Spectroradiometer (MODIS) products is used to estimate ET including MYD11C1 Land surface temperature (daily LST; https://lpdaac.usgs.gov/products/myd11c1v006/). Good-quality data from MODIS products are selected based on quality flags. LST daily data are used in combination with a simplified surface energy balance model (SSEB) to estimate ET at the daily scale (Panwar and Kleidon 2022; Panwar, Renner, and Kleidon 2020). Due to no global available ET measurements, several global observation-based model-driven ET products have been developed (Jung et al. 2019; Mu, Zhao, and Running 2011). However, we do not consider these ET products because they commonly show less accuracy in extreme events where physiological changes are prevailing (Jung et al. 2019). For example, some of these products use greenness indices as inputs which are not independent of LAI that we need in our statistical methods. These model parameterisations rely on constraint data so that regions with scarce calibration data might be less representative of physiological changes. And the water stress in models depends on prescribed root-zone hydraulic strategies and stress functions. Therefore, we use daily MODIS LST data (with overpassing time at 13:30 pm) and ERA5-Land meteorological variables combined with a SSEB model to estimate ET. Additionally, hourly meteorological data (including air temperature, incoming shortwave and longwave radiation, surface pressure, atmospheric vapor pressure, soil moisture, wind speed) are required as inputs in the SSEB model and are available from ERA5-Land reanalysis (Muñoz-Sabater et al. 2021). To note that, we adapt SSEB from Panwar et al 2022 by the following two simplifications: (i) Daily minimum surface and air temperatures are assumed to be equal; (ii) Daily maximum LST is represented by MODIS LST at 13:30 pm. Therefore, daily ET is calculated by:

$$ET = \left(1 - \frac{C_p \cdot \rho \cdot (LST_{max} - Ta_{max}) \cdot (1.4 ga_{mean})}{1.4 Rs_{max}}\right) \cdot Rn_{mean} \quad (1)$$

where ET is with a unit of latent heat flux (Wm^{-2}), LST_{max} is MODIS land surface temperature at 13:00 pm (K), Ta_{max} is maximum hourly air temperature (K), Rs_{max} is maximum hourly net shortwave radiation (Wm^{-2}), and Rn_{mean} is daily mean net radiation (Wm^{-2}). C_p (1005 J kg^{-1} K^{-1}) is specific heat capacity and ρ (1.23 kg m^{-3}) is the simplified density of air. ga_{mean} (m s^{-1}) is mean diurnal variation of aerodynamic conductance. As summarized in Panwar and Kleidon (2022), ga_{mean} is different across vegetation types with higher values in forest ecosystems and lower values in grass ecosystems. We distinguish tree, short vegetation (grass and shrub) and soil, and depending on their respective fractional cover, ga_{mean} is set to 0.06, 0.0345, and 0.002 m s^{-1},

respectively. Among them, vegetation-related values are from Panwar and Kleidon (2022), and the soil-related value is from van der Tol et al. (2014).

We evaluate the ET at a 0.25˚ spatial resolution using 8-daily eddy-covariance-measured latent heat for 73 sites, which are from the ICOS-drought-2018 dataset (https://www.icos-cp.eu/data-products/YVR0-4898). The raw data was processed following the ONEFLUX pepline (Pastorello et al. 2021). Latent heat flux with a unit of Wm^{-2} is first gap filled using marginal distribution sampling (Reichstein et al. 2005), and then aggregated to the 8-daily scale by computing the mean value. We exclude the days when there are more than 20% value missing for each 8-day window to eliminate the potential resampling induced noise. Gridded ET data are matched to each site using the nearest method (Python version 3.9.7; xarray version 0.20.1), 47 sites remain with sufficient data. We show the distribution of correlation coefficient between raw data of EC-measured LE and ET across each site and find a median correlation of 0.88 for the whole growing season (Appendix Figure 4.A3) and 0.8 for drought-specific periods during 6 months (Appendix Figure 4.A4).

Microwave remote sensing provides great opportunities to monitor vegetation water content and has recently increased applications on drought-related ecological studies (Konings et al. 2021; Anderegg et al. 2018; Forkel et al. 2022). Multi-frequency VOD products are available and are irrespective of cloud cover, and high frequencies are more sensitive to the upper part of canopy changes. Since we aim at studying vegetation physiological dynamics, X-band VOD at 10.7GHz from LPDR v2 is used, as it is sensitive to upper-canopy water content which relates to the stomatal regulation (http://files.ntsg.umt.edu/data/LPDR_v2/) (Du et al. 2017). LPDR X-band VOD from AMSR2 sensors for the period of 2018-2021 has day-night observational capabilities, although its spatial resolution at 0.25˚ is relatively coarser than VOD data from sun-synchronous orbits and coarser than other vegetation observations such as TROPOMI SIF and MODIS bands (for which 0.05˚ is available to use). Both the daytime and nighttime VOD contain information about vegetation water content, which scales with above-ground biomass and relative moisture content (Konings et al. 2021). Vegetation water content can be used to represent leaf water potential and associated plant hydraulics (Zhang et al. 2019). Day-time VOD (overpassing time at 13:30pm) are normally regulated by plant hydraulics caused by the imbalance between transpiration and root-zone water supply. Night-time VOD (overpassing time at 1:30am) is driven by root-zone soil moisture refilling and is almost linearly linked to soil water potential (Zhang et al. 2019). Given pre-dawn equilibrium between leaf water potential and root-zone water potential, a combination of midday and midnight VOD can largely reduce structural variations and can be used to investigate the ecosystem isohydricity (Wu et al. 2021; Konings and Gentine 2017). Here we calculate the ratio between midday and midnight VOD (VOD ratio), and by investigating the responses of VOD ratio to soil moisture we can study ecosystem isohydricity changes under drought (Zhang et al. 2019). We note that a potential bias caused by the night-time VOD product is that some regions might have incomplete root-zone water refilling at 1:30am and the near-linear relationship between night-time VOD and soil water potential

cannot hold, so we test excluding regions which show greater growing-season averages of midday than midnight VOD in Appendix Figure 4.A9 (Konings & Gentine 2017).

Concomitant hydro-meteorological data from ERA5-Land reanalysis include air temperature, incoming shortwave radiation, vapor pressure deficit, 1-m soil moisture and precipitation (Muñoz-Sabater et al. 2021; https://cds.climate.copernicus.eu/cdsapp#!/dataset/10.24381/cds.e2161bac?tab=overview). 1-m soil moisture is calculated based on three layers of ERA5-Land soil moisture weighted by layer thickness of 7, 21, and 72 cm. Climate regimes are defined by the aridity index, which is calculated as the ratio of the 2018–2021 mean net radiation and unit-converted precipitation from ERA5-Land, with higher values meaning drier climate regimes.

4.2.2 Data pre-processing

Appendix Figure 4.A1 presents a flowchart of data pre-processing and further analysis. All vegetation and hydro-meteorological data from March 2018 to October 2021 are aggregated into the 0.25˚ spatial resolution and 8-daily temporal resolution where all data are available. To minimize noise in daily SIF, ET and VOD and to match 8-daily LAI and NIRv, 8-daily data are produced by moving 16-day averages (TROPOMI's revisiting cycle) with 8-day overlaps, and data gaps higher than 20% in 16 days are set as no data in aggregation results. TROPOMI has different overpassing time within 16 days, and mixing multiple overpassing time-related phase angles help to lessen biases of sun-sensor geometries (Doughty et al. 2019). Moving window averages are also applied for all the other vegetation and hydro-meteorological reanalysis data to keep the consistency. All data are used in the form of anomalies, as we are exclusively interested in abnormal behavior of vegetation drought responses than the seasonality. For this, mean seasonal cycles are calculated for each month (January to December) and trends are derived by using a locally-weighted smoothing function with moving 40% windows of March 2018 to October 2021 which are then removed to extract vegetation and hydro-meteorological data anomalies. Mean seasonal cycles for over 4 years are not able to derive due to some data availability, and also subtracting long-term mean seasonal cycles could introduce bias due to climate-driven phenology shifts.

This study focuses on the regions characterized mostly by significant vegetation cover and without dense human activities. For this, we remove regions having sparse vegetation cover (<5%) and a high irrigation fraction (>10%). The vegetation cover is calculated as the sum of trees, shrubs, grasses cover fractions from ESA CCI Landcover v2.1.1 dataset from the year 2020 (https://www.esa-landcover-cci.org/). The irrigation fraction was collected around the year 2005 (http://www.fao.org/aquastat/en/geospatial-information/global-maps-irrigated-areas/latest-version/; Siebert et al. 2015). Vegetation fractional cover data is also used to distinguish tree dominant, and shrub and grass dominant ecosystems by the ratio between tree/(shrub and grass) with a threshold of 0.5.

4.2.3 Drought detection

We study vegetation responses to drought during growing seasons, which are defined with temperatures higher than 5 ˚C and mean seasonal cycles of SIF higher than 0.2 mW m^{-2} sr^{-1} nm^{-1}. The reason to use mean seasonal cycles of SIF to account for growing seasons instead of dynamic SIF values is to largely keep vegetation post-drought anomalies, e.g., in savannas. For growing-season data, we evaluate soil moisture dryness across grid cells during 2018–2021 using 40-year ERA5-Land soil moisture reanalysis. For this purpose, we calculate yearly minima using monthly soil moisture records and rank these yearly minima, since long-term soil moisture with coarse temporal resolutions of monthly compared to 8-daily is more representative of drought severity. We focus on the grid cells where the lowest yearly minima occur in 2018–2021, so that severe drought events could exist in these regions during this recent time period. Drought peaks are detected based on the lowest 8-daily soil moisture during 2018–2021 across each grid cell. We then study the vegetation data anomalies during the course of drought from 3 months before until 3 months after drought peaks. Drought durations are used to attribute the spatial variation of vegetation anomalies, and are defined by the number of time steps of soil moisture anomalies back to zero or positive values before and after drought peaks, respectively.

4.2.4 Disentangling vegetation physiology

Since vegetation physiology responds significantly to drought stress, we adapt an existing approach to disentangle physiological influence from LAI-driven structural changes (Yu et al. 2022, 202; Beringer et al. 2007). We use the way of disentangling the physiological component of SIFrel as an example. Due to an existing nonlinear relationship between SIFrel and LAI, we fit a random forest regression model to account for nonlinearity (Breiman 2001) to predict SIFrel using LAI as the only predictor per grid cell. The predicted drought-period SIFrel is hence expected to present the SIFrel structural component. A leave-out strategy of model training is applied to avoid potential over-fitting due to the relatively straightforward power of random forest modelling but limited input information. In this way, the drought-period data are excluded from the training model when predicting drought-period SIFrel, while the model can still learn SIFrel–LAI relationships under dry conditions from the non-drought years and extrapolate such relationships to the drought-period prediction. However, to note that, the random forest model could still underestimate high values or overestimate low values, and result in the less significant variation of vegetation structural changes. The leave-out window in the main result is defined as 24-time steps (192 days), while results using 12- and 6-time steps are shown in Appendix Figure 4.A10 with similar patterns of significant negative physiological changes in dry regions.

To account for potential observational noise in predicted variables (e.g., SIFrel) which are supposed to have lower signal-to-noise ratios than greenness indices and reanalysis data, a second random forest model is established to fully consider inputs including LAI and hydro-meteorological anomalies using the whole

growing-season data. This model is used to predict SIF anomalies during drought periods, aiming at giving more reliable SIF variations while lessening data noise. The derived out-of-bag (OOB) scores from cross-validation are used to evaluate the model performance, with lower values indicating larger difficulties to predict SIF due to the bad data quality or human activities such as tree logging. Hence, regions with OOB scores lower than zero are disregarded in the result of disentangling vegetation physiology. Finally, SIF physiological components can be extracted per grid cell as the difference between the SIF anomalies predicted as a function of structure and hydro-meteorology, and as a function of structure only.

Same steps are applied to disentangle physiological components of ET and VOD ratio using LAI and random forests. NIRv is additionally used to replace LAI as an indicator of vegetation structure in the random forest model. Using NIRv confirms our main findings relating severe water stress with downregulation of vegetation physiology in dry regions, while NIRv explains larger variations of SIFrel and ET and results in less variations of their physiology due to the additional information in NIRv related to vegetation fractional changes but potentially confounded by soil moisture related soil reflectance (Zeng et al. 2019; Badgley, Field, and Berry 2017).

Apart from trusting the extrapolation ability of using random forest in our main method, we test two alternative methods using the variance decomposition. One is to use a Multiple linear regression model (MLR), and treat LAI and hydro-meteorological data as predictor variables and SIFrel as the target variable, regardless of drought or non-drought periods. The sum of variance explained by hydro-meteorological data only from the Multiple linear regression model for the drought period can be treated as the SIFrel physiological component under drought. Another one is to again use a random forest model which accounts for non-linear relationships instead of MLR and apply explainable machine learning (SHapley Additive exPlanations; hereafter 'SHAP'; Lundberg & Lee 2017) to disentangle hydro-meteorological contributions on SIFrel during drought as the SIFrel physiological component. These two methods are also applied for the case of ET and VOD ratio. Results from these two methods support findings using our main methodology (Appendix Figure 4.A9), while decomposition methods might underestimate structural components due to the collinearity between vegetation structure (i.e., LAI) and hydro-meteorological anomalies and larger numbers of predictor variables to account for physiological influence.

4.2.5 Attribution analysis

We conduct an attribution analysis to better understand potential drivers of vegetation physiology under drought spatially. We select multiple variables related to land-surface climate and vegetation characteristics, drought-specific hydro-meteorological variables, and drought durations in explaining vegetation physiology. We train a random forest model and use these considered variables as predictors to predict SIFrel, ET, and VOD ratio related physiology, respectively, across all study grid cells (Breiman 2001). Using cross-validation out-of-bag R^2, we evaluate the model sufficiency in explaining physiological variations. Then, we use the

SHAP values to quantify the marginal contributions of each predictor variable and identify the relative importance among different variables by ranking the averaged absolute SHAP values (Lundberg & Lee 2017).

4.2.6 SCOPE simulations

The state-of-the-art model the Soil Canopy Observation of Photochemistry and Energy flux (SCOPE) (v 1.73) couples radiative transfer, energy balance and photosynthesis submodels to predict vegetation carbon, water and energy exchanges with spectroradiometric variables directly linked to physiology (e.g., SIF, or thermal radiances), and can be used to interpret remote sensing observations (van der Tol et al. 2014) and test physiological assumptions (Biriukova et al. 2021). SCOPE predicts photosynthesis as a function of plant traits, irradiance, leaf temperature and other meteorological conditions using Farquhar and Collatz equations for C3 and C4 plants, separately (Farquhar, von Caemmerer, and Berry 1980; Collatz, Ribas-Carbo, and Berry 1992). The modular nature of SCOPE allows separately simulating dark-adapted fluorescence and steady-state (light-adapted) fluorescence (van der Tol et al. 2014). The difference between both radiances is that only the steady-state fluorescence is modulated by physiology in response to environmental conditions. This fact has been successfully exploited in former studies to assess methods separating structural and physiological information from SIF time series (Biriukova et al. 2021).

The aim of SCOPE simulations is not to accurately reproduce observations, but produce a comparable variability of vegetation responses to drought and remote sensing view-angle observations that assess the validity of the metrics and analyses applied to observations. In this context, simulations provide: (i) vegetation functioning i.e. photosynthesis; (ii) vegetation physiology i.e. stomatal conductance, LUE and WUE; (iii) physiology-driven relative SIF to resembling TROPOMI data computed as the difference between light-adapted (physiologically-regulated) and dark-adapted SIF (Biriukova et al. 2021), and then normalized by the reflected radiance at 740nm. As the observations, SCOPE outputs are then averaged every 8 days, deseasonalized, detrended, and used to study vegetation physiology responding to defined drought periods as in observation-based results.

For this purpose, we use originally 8-daily MODIS LAI and NDVI and linearly-interpolate into hourly (8-daily LAI and NDVI are from 16-day averages with 8-day overlaps to be consistent with observational results; See Methods Section: Data pre-processing), and hourly hydro-meteorological data from ERA5-Land reanalysis as SCOPE inputs from March 2018 to October 2021. Hydro-meteorological data include 2 m air temperature, incoming shortwave radiation, incoming longwave radiation, surface pressure, atmospheric vapor pressure, 10 m wind speed, and 1 m soil moisture. 1000 grid cells are initially randomly selected based on the regions with severe drought events (Methods Section: Drought detection) for SCOPE to run. After removing grid cells with bad prediction performance in terms of SIFrel, ET and VOD ratio in observation-based analysis, around 600 grid cells remain to make the observation-based results and SCOPE results comparable. Simulations are performed at 0.25-degree spatial resolution. For each grid cell, we account for

the spatial variability of plant functional types (PFT) by separately simulating each PFT. To do so, daily MODIS LAI input is scaled by a specific PFT fraction for each site to run the simulation, and then model outputs are averaged as a function of relative fraction covers for three main PFTs for each site. PFT data is from ESA CCI Landcover v2.1.1 dataset including broadleaf evergreen tree, broadleaf deciduous tree, needleleaf evergreen tree, needleleaf deciduous tree, broadleaf evergreen shrub, broadleaf deciduous shrub, needleleaf evergreen shrub, needleleaf deciduous shrub, natural grass, managed grass and bare soil.

Parameter setting processes are as follows. Plant pigments such as leaf chlorophyll content and carotenoid content are simulated with seasonal changes based on varying MODIS NDVI and PFT-characteristic fixed parameters (Croft et al. 2020). The seasonal variability of the deciduous PFTs is reduced by a factor of 0.2 and the difference is distributed within the deciduous PFTs of the pixel by following (Asner, Scurlock, and Hicke 2003). Chlorophyll content can be simulated by a saturating function of NDVI, so we select ten timestamps of the time series evenly covering the range of MODIS NDVI, and numerically optimize the parameters by minimizing the difference between MODIS NDVI and the predicted NDVI weighted average of the selected timestamps. Then at each iteration, the chlorophyll content of each PFT is assigned following the same scheme, and carotenoid content is set as 0.35 times chlorophyll content. To avoid anomalous pigment values and soil reflectance, the soil bright parameter of SCOPE at each site is also optimized. For this, whenever NDVI is negative, chlorophyll content is set to zero and an additional parameter determining the fraction of snow cover is allowed to be larger than 0. Soil reflectance is then linearly mixed with a snow spectra from the USGS Spectral Library. To better simulate energy partitioning in sparse vegetated areas, we constrain the relationship between soil moisture content and soil resistance to evaporation from the pore space with MODIS LST which strongly controls soil evaporation and affects vegetation transpiration. Similar as in constraining leaf chlorophyll content, we select ten points of our study time series evenly covering the LST range and optimize the resistance for dry soils (Pacheco-Labrador et al. 2019).

We run SCOPE at a random hour for each day and each site to save the computation time, and to allow the variability of view angles which is also existing in TROPOMI SIF, and then SCOPE outputs are averaged every 8 days to mix view angles for simulated reflectance and to mix the averaged physiological performance throughout the day. SCOPE v1.73 does not impose any photosynthesis limitation as a function of soil moisture; however, we used a default function of SCOPE to determine soil resistance for ET from the pore space, limiting soil latent heat flux in dry soils. We also test applying a soil moisture constraint on Vcmax using the empirical relationship (Bayat et al. 2019), but this approach has only been tested in dry ecosystems and overestimates photosynthetic stress in ecosystems with access to deep soil water layers.

4.3 Results and discussion

4.3.1 Diagnosing the global vegetation drought response from space

Figure 4.2 (a,b) shows wet and dry regions distinguished by aridity with severe soil moisture droughts during 2018–2021 occurring in South America, central Africa, Eurasia, and Northern and Eastern Australia. These drought events with additional timing information shown in Fig. S2 have also been featured in recent literature, for instance, the 2018 European drought (Buras, Rammig, and Zang 2020) and the 2017–2019 southeastern Australian drought (Dunne and Kuleshov 2022). Figure 4.2 (c-j) presents anomalies of all vegetation data streams in wet and dry regions, respectively, averaged across selected grid cells where there are more than 20 data points available during drought.

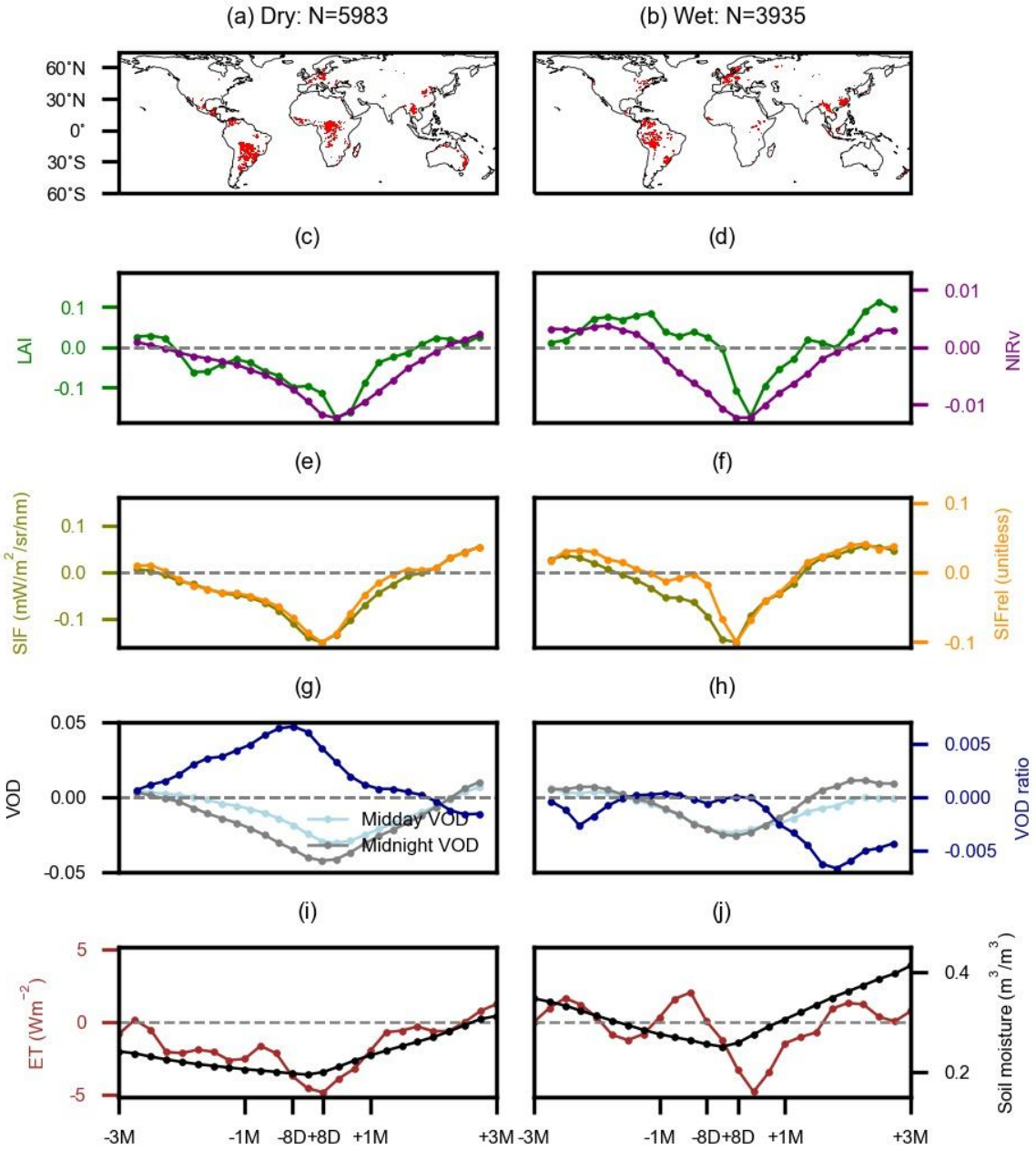

Figure 4.2. Evolution of drought-related anomalies of multiple remote-sensing vegetation variables. Drought-associated regions are shown by distinguishing (a) dry regions (aridity > 1) and (b) wet regions

(aridity <= 1). Results for dry regions are in (c, e, g, i), and for wet regions in (d, f, h, j). In (a, b), grid cells with fewer than 20 available data points out of the displayed 24 time steps in total are disregarded for this figure, the remaining grid cells that we use to present averaged values across vegetation variables are colored in red. (c, d) LAI and NIRv, (e, f) SIF and relative SIF (SIFrel), (g, h) VOD at midday, midnight and the ratio between midday and midnight (VOD ratio), (i, j) ET and soil moisture. All vegetation variables are anomalies. Soil moisture in (i, j) is in absolute values for presenting the actual water amount.

We present the vegetation drought response between 3 months before and 3 months after drought peaks, and find overall contrasting patterns between dry and wet regions. Wet regions more often show LAI increases from drought development until drought peaks, as the drought-associated sunny conditions stimulate vegetation green-up (Figure 4.2 c,d) (Janssen et al. 2021). We further consider the near-infrared reflectance of the vegetation (NIRv) which is a greenness index integrating soil background effects, and can also be used to represent canopy structure and derive a comparable SIF physiology by accounting for the SIF escape ratio (Figure 4.2 c,d) (Badgley et al. 2017; Zeng et al. 2019). NIRv increases in early drought development periods in wet regions compared to dry regions, even though NIRv increases are less pronounced compared to LAI anomalies as NIRv is more sensitive to decreases in soil moisture (Li et al. 2021; Walther et al. 2019).

Vegetation photosynthesis approximated by SIF shows continuous decreases preceding the drought peak with more consistent negative anomalies in dry regions (Figure 4.2 e,f). SIF increases a month after drought peaks, and wet ecosystems recover more quickly than dry ecosystems, as the new leaf flushing promotes photosynthesis (Lee et al. 2013; Lopes et al. 2016). SIFrel shows similar dynamics to SIF, but SIFrel anomalies are much weaker during drought development in wet regions. Similar results are revealed in previous studies that after correcting the influence of incoming solar irradiance and viewing angles, SIFrel can more accurately observe increases in vegetation photosynthesis during drought in Amazon forests (Yang et al. 2018; Doughty et al. 2019; Green et al. 2020).

Midday and midnight VOD anomalies both decrease during drought development and reach their lowest values shortly after soil moisture minima, and then recover at similar timing as SIFrel (Figure 4.2 g,h). There are clear differences between dry and wet regions, with midday VOD decreasing much less compared to midnight VOD in dry regions than in wet regions. As a result, dry regions present a gradual rising anomaly in VOD ratio during drought development compared to the climatology of VOD ratio, which indicates plant stomata closure to maintain canopy water content when VPD is high or soil dryness is severe (Grossiord et al. 2020). Previous studies have also illustrated similar water saving strategies based on VOD data but mostly for seasonal or long-term shifts (Wu et al. 2021; Konings and Gentine 2017).

ET anomalies before drought peak present more increases in wet regions than in dry regions, which is in line with previous findings using independent datasets (Figure 4.2i,j) (Zhao et al. 2022; Schumacher et al. 2022). The temporal fluctuation of ET anomalies is larger than for other variables, reflecting potential instantaneous

atmospheric effects on ET are strong. Note that it may also be related to estimation noises, so we validate the estimated ET inferred from LST by comparing it with observations from 47 eddy covariance towers. ET estimates and observations show good agreement across towers in different climate regimes and with different land cover types (Appendix Figure 4.A3). We also evaluate drought-specific ET estimates, and the relationship between ET estimates and observations are more linear compared to ET estimates for all growing seasons (Appendix Figure 4.A4). Besides, ET estimates during drought show slightly higher accuracy in drier than in wetter regions. The better ET estimates in dry regions or in dry periods are related to aerodynamic controls on surface temperatures, which are generally stronger in densely vegetated regions or during dry seasons, but aerodynamic controls can only be parameterized at the large scale (Panwar and Kleidon 2022; Panwar, Renner, and Kleidon 2020).

Contrasting vegetation responses across wet and dry regions might be related to different degrees of plant water stress. The absolute moisture content in the top meter of soil is much higher in wet regions than that in dry regions (Figure 4.2d,h), and deeper soil moisture and groundwater are expected to be more abundant to provide ecosystems in wet regions with sufficient water supply even during droughts (Stocker et al. 2021; Fan et al. 2017). The strongest reductions in vegetation-related variables are commonly found one time step after the actual soil moisture minimum, indicating a delay in the vegetation response to the first precipitation which stops the drying of the soil beyond peak drought (Wu et al. 2015). Figure 4.2 shows mean drought evolutions across many grid cells; However, due to the mixture of geographic heterogeneity and instantaneous hydro-meteorological changes, we note that the variability of vegetation drought responses across grid cells is considerable, as shown in Appendix Figures 4.A5 and 4.A6 with 25th and 75th percentiles of values across grid cells, respectively.

4.3.2 Vegetation physiological response to drought

Moving beyond multiple vegetation drought trajectories in Figure 4.2, we compare anomalies of SIFrel, ET, and VOD ratio and respective disentangled physiology across aridity classes in Figure 4.3. We only consider regions where SIFrel, ET, and VOD ratio can be estimated by the full random forest model which uses LAI and hydro-meteorological variables as predictors, to filter out areas with low data quality or intense human influence (Appendix Figure 4.A7). Afterwards, physiology is derived by removing the anomalies related to structural changes as indicated by the random forest model based on LAI only (Appendix Figure 4.A1; Methods Section: Disentangling vegetation physiology). We find that overall patterns of vegetation functional anomalies across drought phases and aridity are largely resembled by their physiological changes. Moderate-to-dry regions show the strongest physiological regulation during and shortly after drought peaks, and clear physiological anomalies in these regions occur since a month before the drought peaks which is earlier than wet regions. Specifically, severe decreases are found on the physiological controls on SIFrel and ET whereas clear increases are found for VOD ratio in moderate to dry regions. Results suggest that, in these regions, drought stress strongly downregulates light use efficiency and stomatal conductance. Magnitudes of

physiological changes are smaller compared to anomalies of SIFrel and ET, which indicates the additional structural influence on photosynthesis and ET. VOD ratio and its physiology are similar in terms of magnitudes and directional changes, indicating that VOD ratio largely captures physiological changes (Zhang et al. 2019).

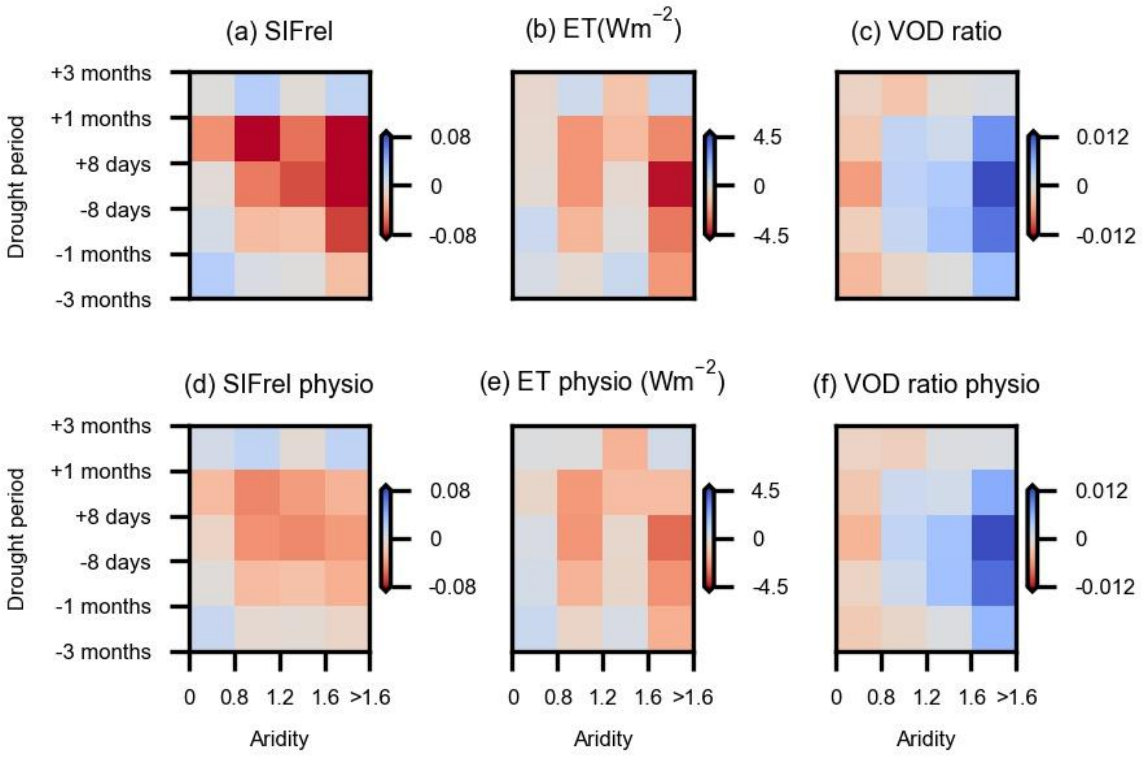

Figure 4.3. Vegetation functional and physiological response to drought. Ecosystem functioning: (a) SIFrel, (b) ET, and (c) VOD ratio anomalies. Ecosystem physiology: response after removing the LAI-related variations in estimating (d) SIFrel, (e) ET, and (f) VOD ratio anomalies. Each aridity-drought period box shows the median value across grid cells and time windows. Aridity classes are chosen to yield a similar number of grid cells in each group on the x-axis.

The derived SIFrel physiological changes suggest strong decreases of light use efficiency in transitional and dry regions under drought (Figure 4.3c), likely related to changes of metabolic limitations such as reduction in Rubisco activity, and hydraulic limitations such as stomatal regulation (He et al. 2022; Stocker et al. 2018). For this we compare SIFrel and SIF results and find no systematic difference in physiological controls (Appendix Figure 4.A8). Furthermore, ET estimated from the surface energy balance model largely reflects plant transpiration, and physiological changes in ET are associated with changes in stomatal conductance (Figure 4.3d). In extremely dry regions, severe stomatal controls occur when plants experience water stress, due to low soil moisture or high VPD (Novick et al. 2016; Carminati and Javaux 2020). Note that both negative changes in ET and positive changes in VOD ratio similarly indicate stronger stomatal control. Still, differences between the ET and VOD ratio results are found in some moderate dry regions (aridity between 1.2-1.6) because other hydraulic processes can also affect ET, such as root conductance. By comparing midday and midnight VOD, we assume that plants are able to extract water from the soil during the night to compensate for daytime losses, such that the nighttime plant water content would be higher and in equilibrium with the available soil moisture (Konings & Gentine 2017; Zhang et al. 2019). However, we find some grid

cells in semi-arid and boreal regions where absolute midnight VOD is lower than midday VOD, such that our hypothesis does not hold everywhere; excluding these regions does not affect our results (Appendix Figure 4.A9).

Our disentangled physiological signals from SIFrel could be confounded by the fluorescence escape probability which depends on the canopy architecture such as LAI and leaf angle distributions, and removing LAI-related signals might not fully account for changes in the escape probability (Frankenberg and Berry 2018). Also, only using LAI to represent canopy structure might include uncertainties, such as in the LAI retrieval process. For this, we apply NIRv as an alternative indicator of canopy structure that accounts for escape probability (YL Zeng et al. 2019) and find similarly strong physiological controls in dry regions (Appendix Figure 4.A10). However, after correcting for fluorescence escape probability, the strongest decreases of SIFrel respective physiology slightly shift to drier regions. The magnitude of the physiological control upon SIFrel, ET, and VOD ratio are clearly reduced when using NIRv to remove structural components. In fact, NIRv reflects not only canopy greenness but also soil moisture and resulting soil reflectance, which might confound the detection of the physiological components since soil moisture is one of the main drivers of vegetation physiology (Li et al. 2021; Walther et al. 2019)

Aridity cannot solely explain physiological changes under drought. Therefore, we aim to quantify the relevance of drought duration, aridity, vegetation characteristics, and drought-specific hydro-meteorological variables in regulating spatial variations of physiological responses to drought. For this purpose, we average physiological changes of SIFrel, ET, and VOD ratio across 3-month drought development and drought recovery periods, respectively. We then perform an explainable machine learning attribution analysis (SHapley Additive exPlanations, hereafter 'SHAP') to quantify the relative importance of relevant variables on each of these physiological variables and drought periods (Methods Section: Attribution analysis). Considered variables in the attribution analysis can explain >0.35 (cross-validation R^2) of the spatial variability of physiological changes from each data stream. Results show that, in general, aridity and tree cover fraction are the most relevant controls of spatial variations of vegetation physiological changes during drought development (Figure 4.4a-c), even though tree cover fraction is less important in the case of SIFrel. This is confirmed when displaying the pre-drought peak physiological anomalies of SIFrel, ET and VOD ratio in aridity-tree cover fraction panels with stronger physiological controls occurring in dry and high grass and shrub-covered regions during drought peaks (Appendix Figure 4.A11; Konings et al. 2017). In addition, meteorological anomalies also influence vegetation physiology during drought development such as shortwave incoming radiation for SIFrel, precipitation for ET, and VPD for VOD ratio, which are supported by previous research (Bao et al. 2022; Zhao et al. 2022; Konings, Williams, and Gentine 2017). The duration of the period during which soil moisture is below seasonal average before drought peak is one of the dominant physiological controls of SIFrel while not for ET and VOD ratio, implying long-duration drought affects more severely on biogeochemical processes related to plant carbon uptake. During drought recovery, we compare

concurrent meteorological anomalies and drought-development meteorological anomalies, and find that coinciding soil moisture or VPD anomalies dominantly control the spatial patterns of physiological recovery (Yu et al. 2022). We also find that hydro-meteorological variables are relatively more important in regulating ecosystem physiology during drought recovery than overall land-surface climate and vegetation characteristics, except for VOD ratio, which is consistently controlled by aridity (Figure 4.4d-f).

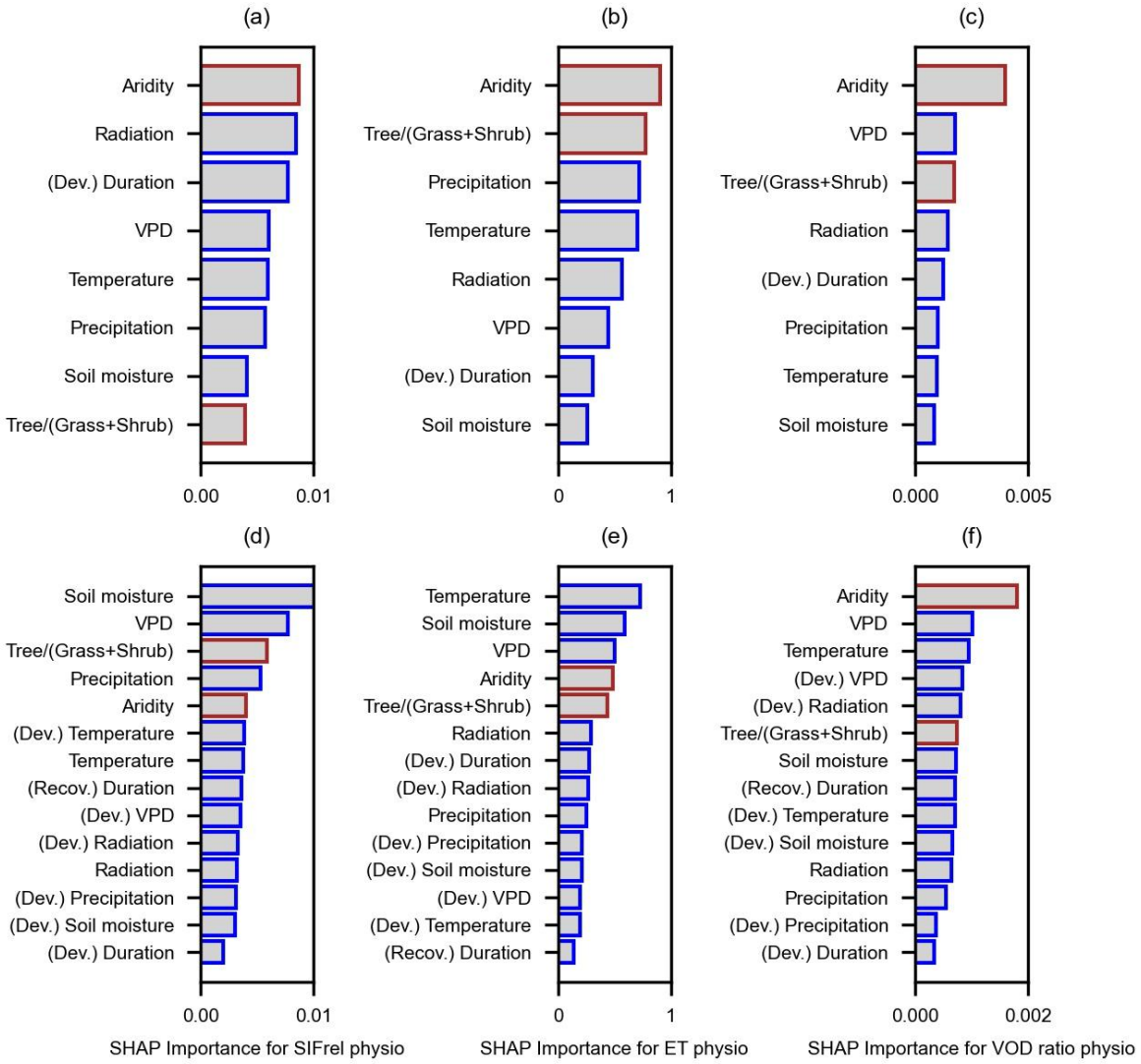

Figure 4.4. Exploring drivers of spatial patterns of global vegetation physiological anomalies under drought. Considered drivers include mean climate and vegetation characteristics (in brown), drought-specific hydro-meteorological anomalies and drought durations (in blue). Results show their relevance in explaining the spatial variability of anomalies in (a) SIFrel physiology, (b) ET physiology and (c) VOD ratio during drought development. (d-f) Similar as in (a-c) but for drought recovery periods where we consider drought-development (Dev.) and recovery (Recov.) related durations and hydro-meteorological anomalies. The unit of relative importance is the same for each physiological variable. Radiation refers to shortwave incoming radiation.

We test the robustness of our approach to isolate the physiological changes from SIFrel, ET and VOD ratio anomalies by (i) changing our model training strategy and (ii) applying two alternative approaches (see also Method Section: Disentangling vegetation physiology). To lessen potential overfitting, we use leave-out strategy to train random forest models and to obtain prediction results. We leave 24 time steps out to train one model and predict results for these 24 time steps for presenting the main results, but models might be subject to our selected time window. Thus, we test different time windows at 12 and 6 time steps and find no significant differences in the diagnosed vegetation physiological responses to drought (Appendix Figure 4.A12). For two alternative approaches, we apply the SHAP method to the full random forest model which predicts SIFrel, ET and VOD ratio, respectively, with LAI and hydro-meteorological information. We regard hydro-meteorological explained variance from SHAP values as the physiological component. In the second alternative method, we fit a multivariate regression model instead of random forests, and isolate explained variations related to the hydro-meteorological information as physiology. Both approaches yield similar results, as shown in Figure 4.3, and support our findings of strong physiological regulations in moderate to dry regions (Appendix Figure 4.A13). Furthermore, to test if multiple drought events occurring in some regions during our study period could affect the selected most severe drought event, we repeat our global analysis without regions where the second-strongest drought occurs in our study time period. The results in Fig. S14 are similar to the patterns in Fig. 3, indicating that multiple drought events have no major impact on our analysis. Finally, we also test to detect drought peaks by minimum soil moisture anomalies, and find results also supporting our key findings of physiological drought responses (Appendix Figure 4.A15 c-e). Note that absolute soil moisture minima and its anomalies minima can have different timing; Years of severe drought are largely similar, but soil moisture minima occur more frequently in very dry seasons whereas soil moisture anomaly minima often occur in less dry seasons when soil moisture variability is high (Appendix Figure 4.A15 a,b).

4.3.3 Mechanisms underlying the physiological response to drought

In addition to the observation-based analysis, we employ SCOPE, a soil–plant–atmosphere continuum model coupled with a radiative transfer model, to perform simulations of the vegetation response to the considered soil droughts. This allows us to validate and mechanistically understand the diagnosed physiological signals. We choose the SCOPE model as it considers vegetation physiology and produces radiance spectra for the remote sensing application (Method Section: SCOPE simulations, Van der Tol et al. 2014). Similar to our analysis method on observations, SCOPE uses LAI and hydro-meteorological data as inputs. Note that given the considerable computational effort, we randomly selected 600 grid cells to model. We provide another version of Figure 4.3 (d-f) where these 600 grid cells are considered which shows similar resulting patterns (Appendix Figure 4.A16). The computed physiological SIF response to drought (Figure 4.5a) is largely consistent with our observation-based estimates. SIF physiology from SCOPE is calculated by the difference of the SIF yield between dark-adapted plants and steady-state plants. Dark-adapted SIF represents an

unstressed reference independent of the environmental conditions, while the steady-state SIF can additionally be regulated by environmental stresses such as light saturation and high VPD (van der Tol et al. 2014; Biriukova et al. 2021). Simulated SIFrel physiology and light use efficiency (LUE) anomalies are similar to observed SIFrel physiology during drought development, including drought peaks with strong decreases in transitional regions (aridity between 0.8-1.2). However, physiological changes recover more quickly in the model than observational estimates after drought. This can be understood as SCOPE does not account for legacy effects such as those arising from water deficits or energy surpluses (van der Tol et al. 2014). The simulated stomatal conductance shows decreases in dry regions, which agrees with observed VOD ratio anomalies that indicate strong stomatal regulation. The strong stomatal regulation in dry regions is consistent with comparatively less decreases in water use efficiency (WUE), and contrasting WUE patterns between wet and dry regions are in line with previous research (Yang et al. 2016). However, we do not find dominant dry-ecosystem increases in WUE as suggested by Yang et al. (2016), related to simulated increases in ET. Note that SCOPE does not account for soil moisture and respective drought stress such that the drought simulations are mechanistically only affected by atmospheric dryness. However, high VPD is typically strongly related to soil moisture drought stress (Baldocchi et al. 2022), and in observation-based analysis VPD plays a more essential role in regulating drought-development physiology compared to soil moisture (Figure 4.4 a-c).

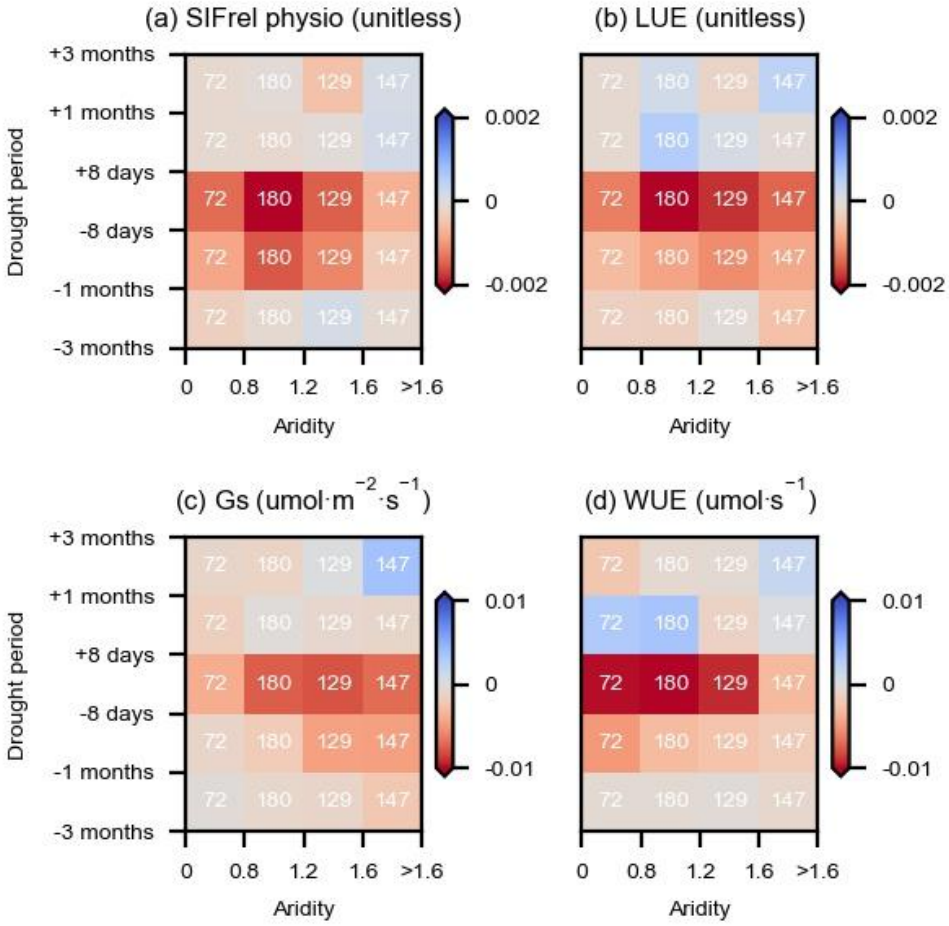

Figure 4.5. Mechanisms underlying the physiological response to drought. (a) Relative SIF physiology (SIFrel physio) is the difference of SIF yield between dark-adapted and steady-state plants; (b) Light use efficiency (LUE) is calculated by the ratio between GPP and absorbed photosynthetically active radiation; (c) Stomatal conductance (Gs); (d) Water use efficiency (WUE) is calculated by the ratio between GPP and ET. Note that instead of the entire study domain this is based on 600 randomly chosen grid cells considered in the observation-based analyses. Observation-based results for the same grid cells are presented in Appendix Figure 4.A16.

While SCOPE presents clear evidence of vegetation physiological response to drought which supports our observation-based findings, the observation-driven physiology is intrinsically limited by data sufficiency. Canopy structure is commonly quantified by the combination of the leaf area, the leaf angle distribution and the clumping degree (Gonsamo, Walter, and Pellikka 2011). The clumping correction is employed in MODIS LAI (Yan et al. 2016), while the leaf angle distribution is not available globally with dynamic records (marked in Figure 4.1 with a dashed box). The physiological changes that we diagnose should be seen as unique physiological variability, or a conservative estimate, but the synchronous physiological dynamics compared to LAI is not considered in the result.

4.4 Conclusions

In this study, we take advantage of recent advances in satellite remote sensing and machine learning applications to advance the understanding of the large-scale vegetation drought response. In particular, we isolate the physiology-driven effects of drought on vegetation functioning at a large spatial scale. We find that the observed drought responses of photosynthesis and evapotranspiration are largely resembled by concurrent changes in vegetation physiology. Further, as physiological changes such as stomatal regulation and light use efficiency differ between regions with different aridity and land cover types, the observed large-scale photosynthesis and evapotranspiration drought responses inherit this physiology-driven pattern to show stronger reductions in dry areas. The physics-based model SCOPE confirms the diagnosed effects of physiological changes during drought. Specifically, the model allows us to understand the underlying processes and reveals stomatal regulation and decreased light use efficiency. Thus, we have been able to qualitatively disentangle physiological effects of drought from remote sensing and detect widespread physiological effects of drought. This opens the potential to accurately infer the biogeochemical and biophysical feedbacks of ecosystems to climate change and to benchmark respective Earth system models, particularly as uncertainties in vegetation feedback limit the accuracy of drought projections.

4.A Appendix

This appendix includes the supplementary materials of the presented manuscript.

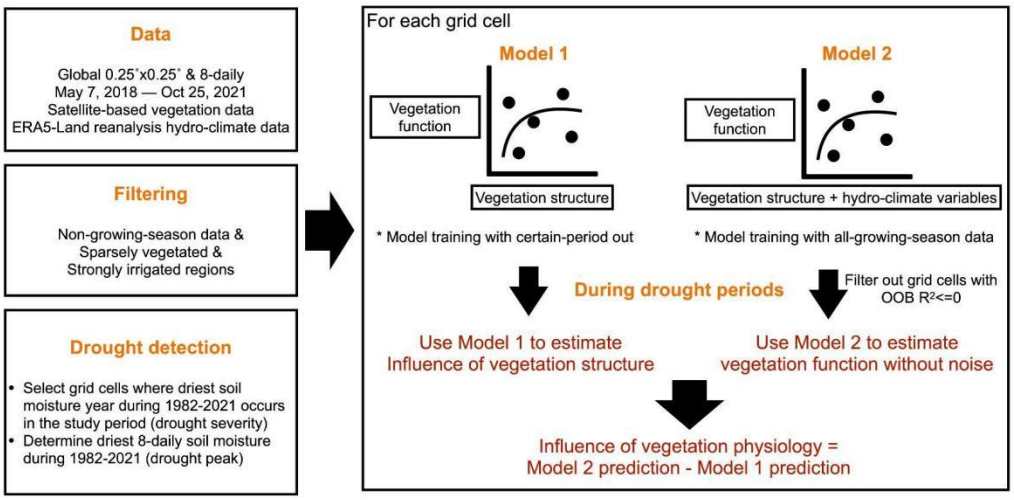

Figure 4.A1. The flow chart of data-processing and disentangling physiological components from functional vegetation data. Details about data-processing can be found in the Method section. Vegetation functional related indices include SIFrel and ET. When disentangling vegetation physiological components, two types of models are implemented: Model 1 with LAI as the only predictor is trained using the leave-out strategy which can help to overcome an over-fitting- related overestimation of structural influence on predictions. The leave-out strategy is applied for removing 6, 12, 24 time-step data (each time step is 8 days) to test the method robustness. Model 1 can then be used to infer the influence of vegetation structure; Model 2 includes LAI and hydro-climate variables (temperature, solar radiation, precipitation, soil moisture, and vapor pressure deficit) as predictors to predict 'true' vegetation functions (e.g. relative SIF) while removing potential data noise. The difference between the 'true' vegetation function and structural component is hence the vegetation physiological component. We apply the disentangling method for each grid cell and for each vegetation functional related indices.

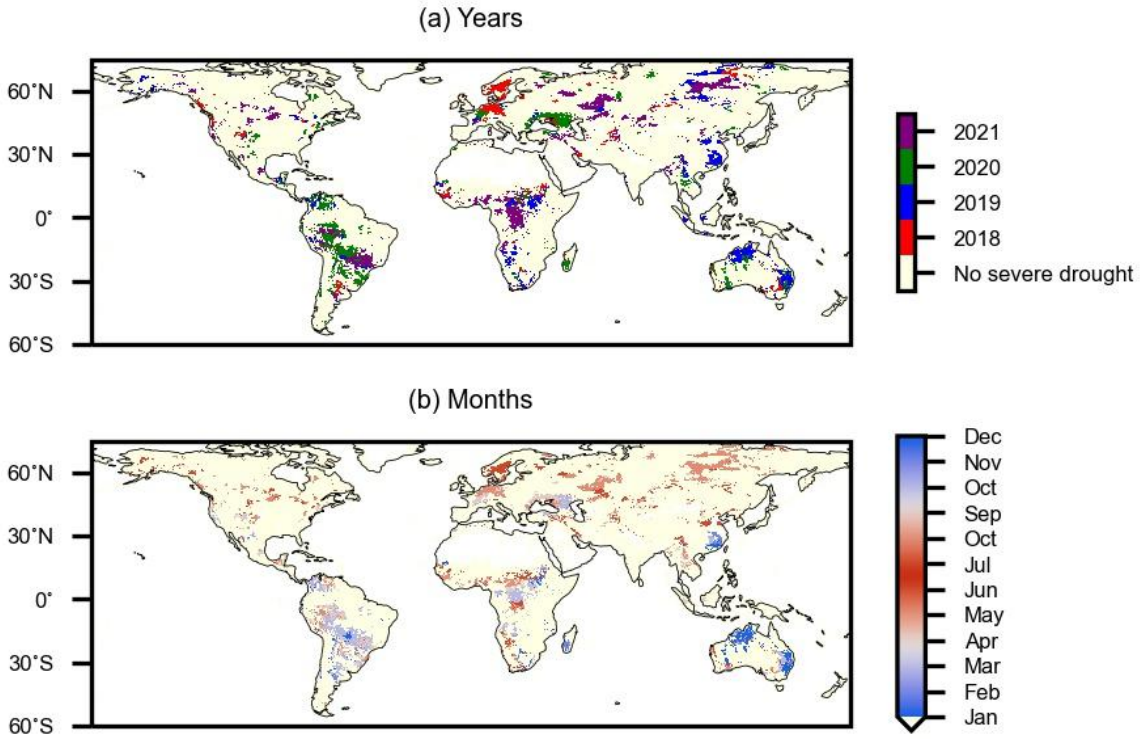

Figure 4.A2. Timing of drought peaks as detected by soil moisture minima during local growing seasons in the study period March 2018–October 2021. Grid cells without severe drought events in this period are disregarded.

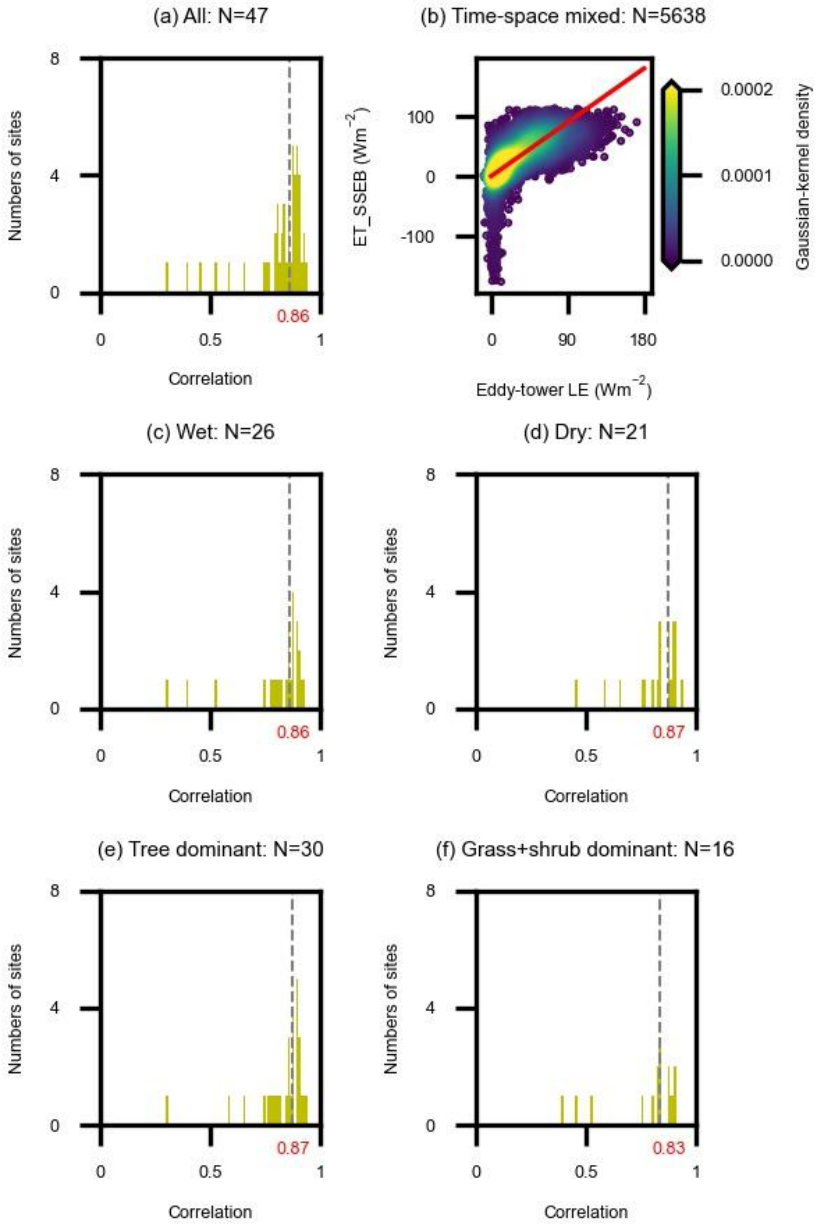

Figure 4.A3. Comparisons between SSEB-based ET and eddy covariance-measured LE (LE obs) for the whole growing season. (a, c-f) The distribution of correlation between SSEB-based ET and LE obs for all sites and sub-sites distinguished by aridity and tree/(grass+shrub) ratios. Grey dashed lines and red texts denote the median values of correlations across sites. (b) The distribution of SSEB-based ET and LE obs values corresponding to each site and time step.

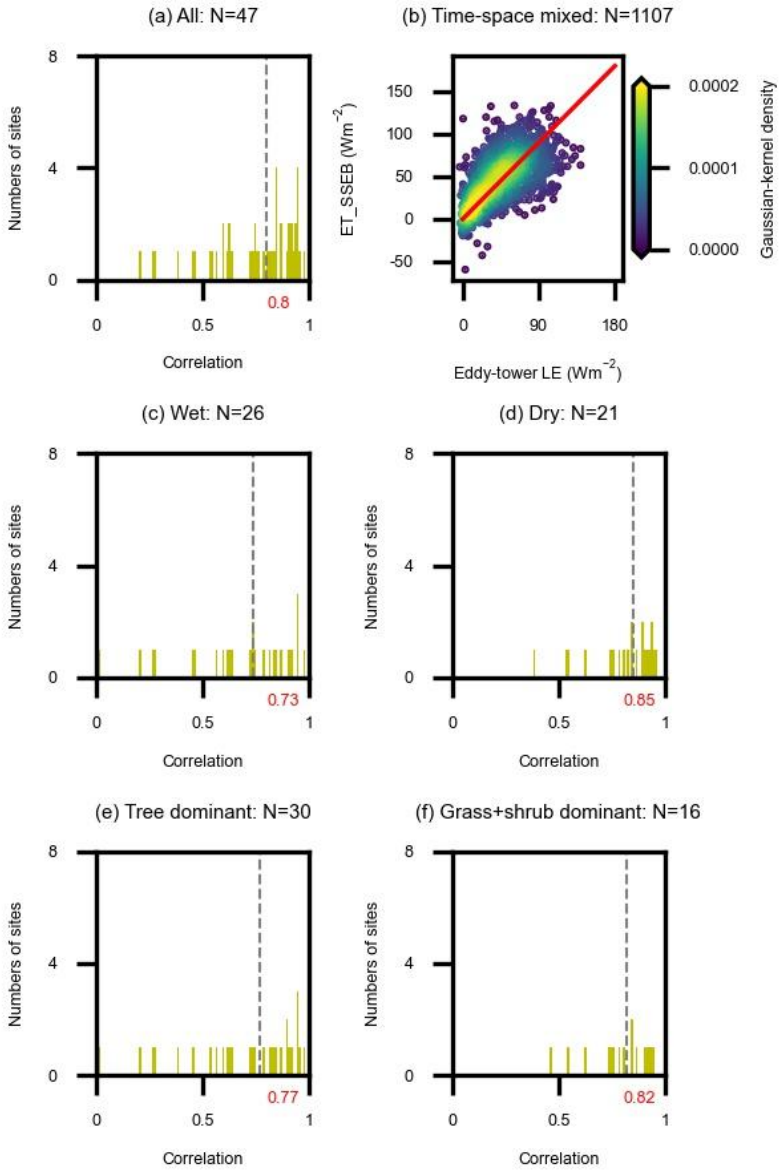

Figure 4.A4. Similar as in Figure 4.A3 but for 6-month drought periods defined by gridded soil moisture data. Grey dashed lines and red texts denote the median values of correlations across sites.

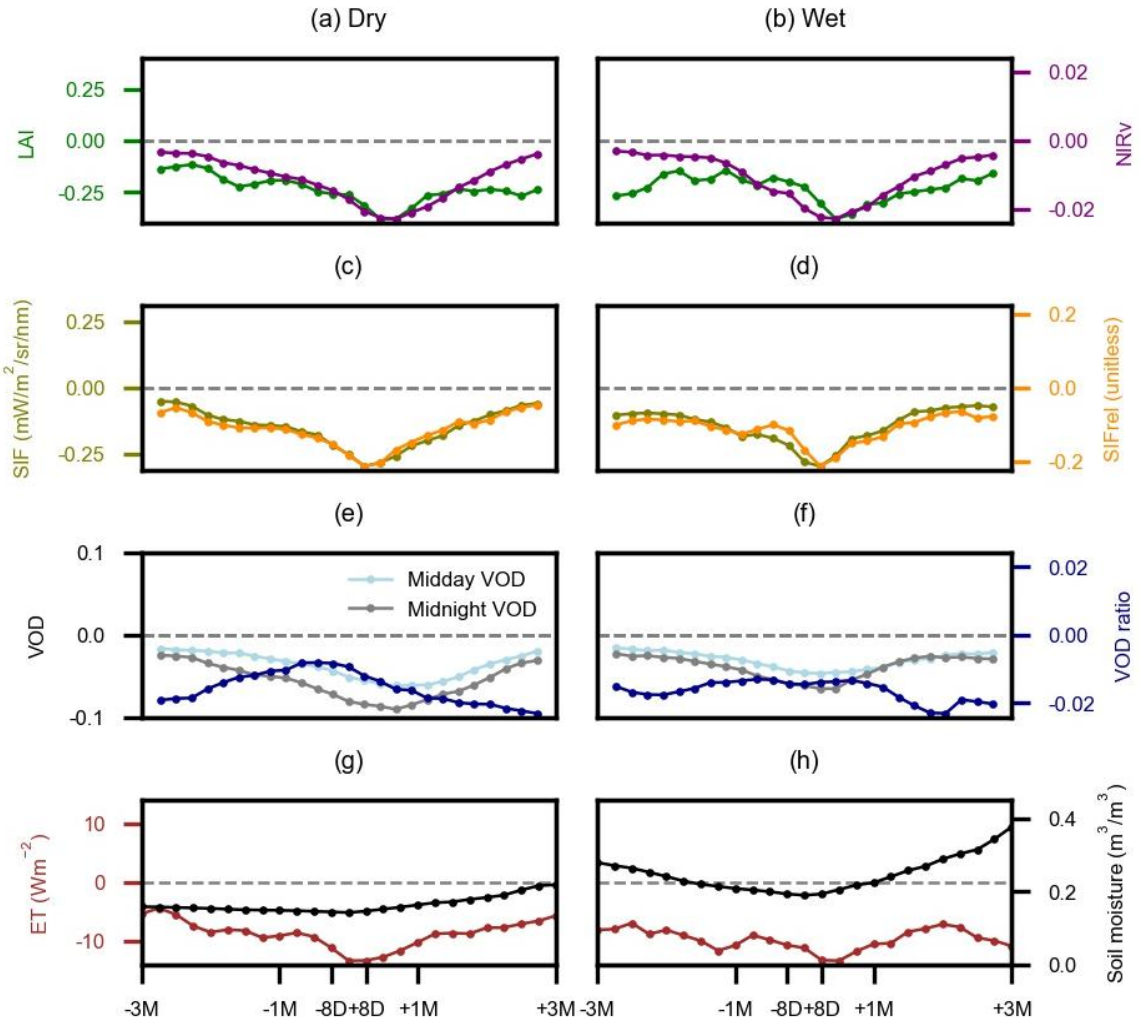

Figure 4.A5. Similar as in Figure 4.2 but values are expressed as the 25th percentile of total value ranges across time steps and aridity.

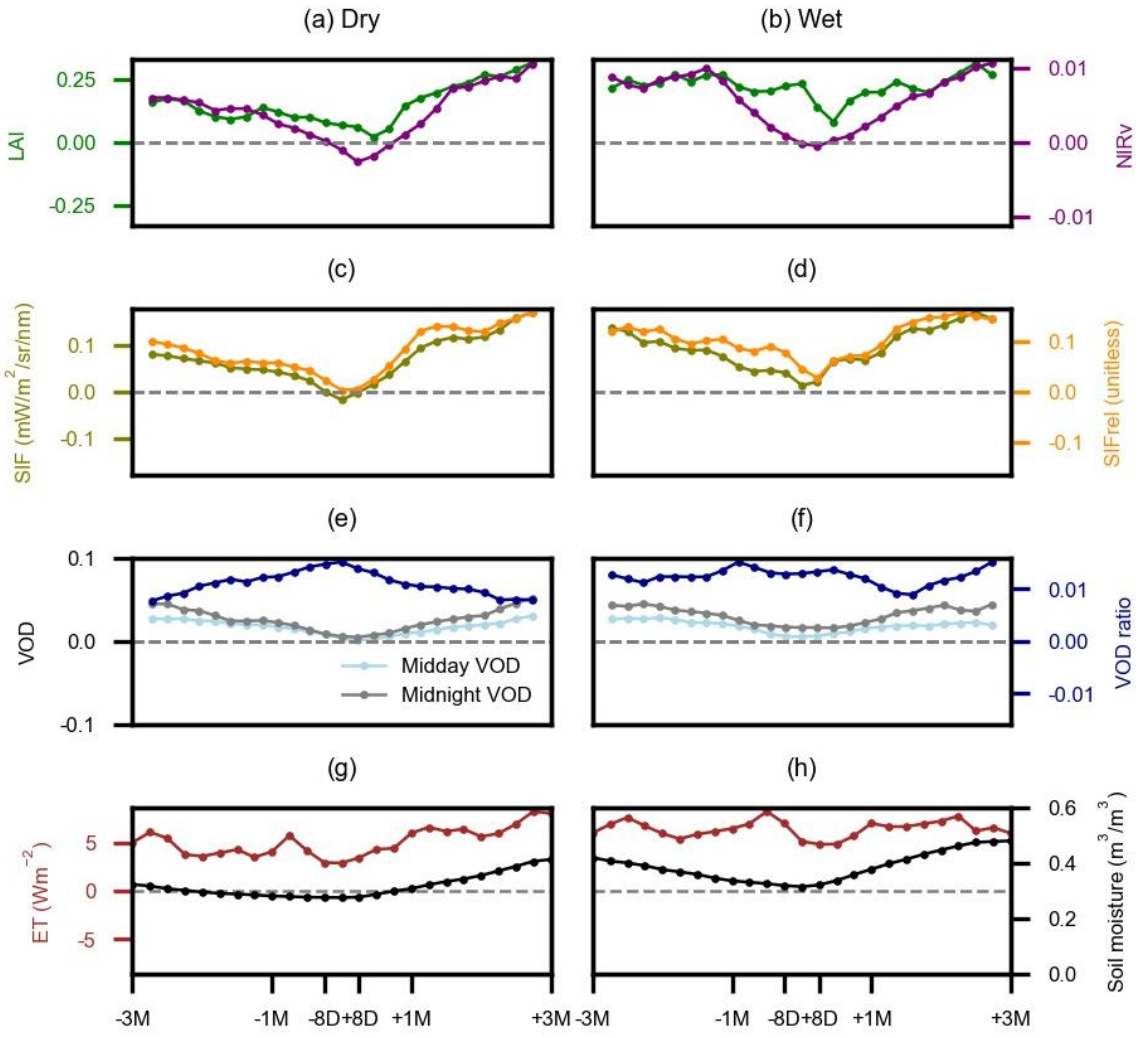

Figure 4.A6. Similar as in Figure 4.2 but values are expressed as the 75th percentile of total value ranges across time steps and aridity.

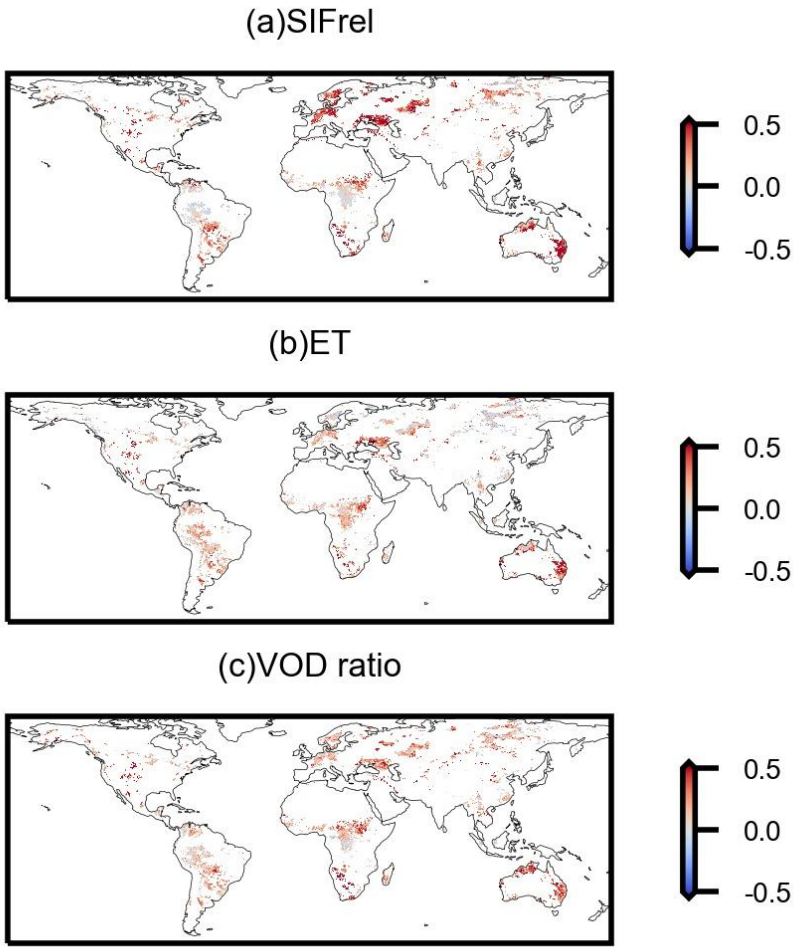

Figure 4.A7. The out-of-bag score from the cross-validation of random forests including LAI and hydro-meteorological data as inputs to predict SIFrel, ET, and VOD ratio.

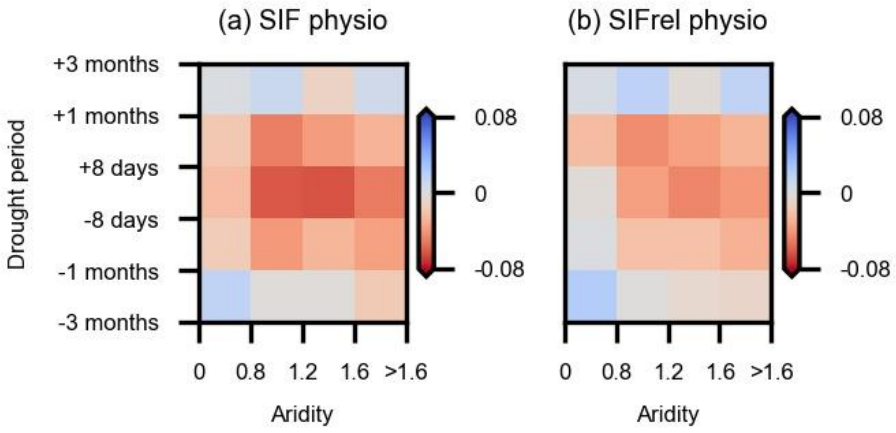

Figure 4.A8. Same as in Figure 4.4d but using (a) SIF instead of (b) SIFrel to present physiological changes of vegetation photosynthesis.

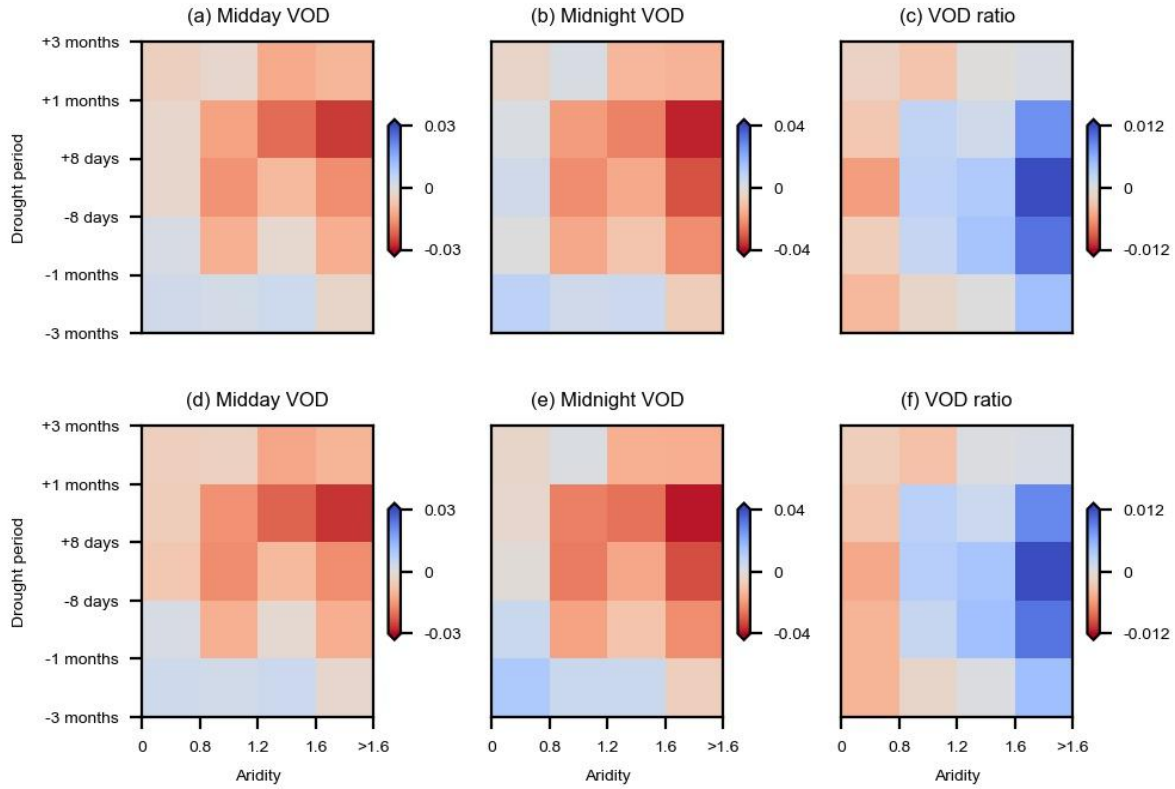

Figure 4.A9. Anomalies of midday, midnight VOD, and VOD ratio during droughts across aridity (a, b, c) before and (d, e, f) after removing regions with incomplete growing-season root-zone water refilling at 1:30am.

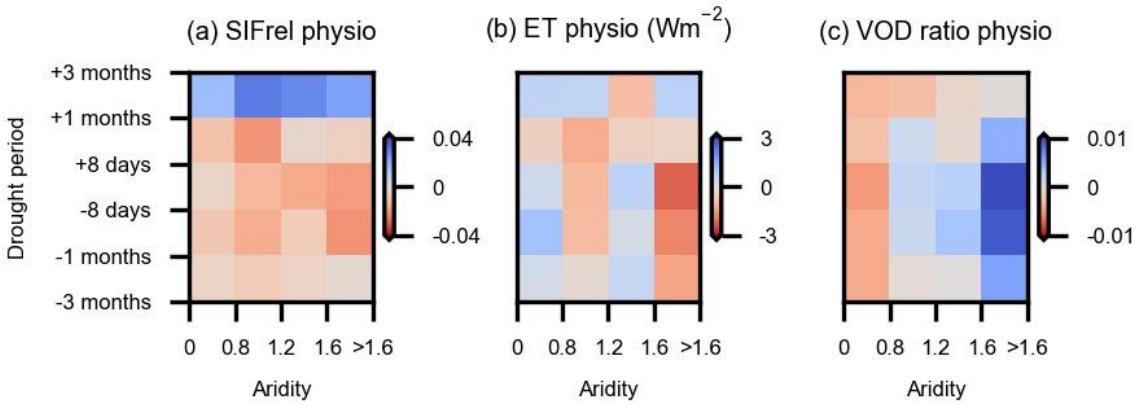

Figure 4.A10. Vegetation physiological controls on (a) SIFrel, (b) ET, and (c) VOD ratio using NIRv to reflect vegetation structure.

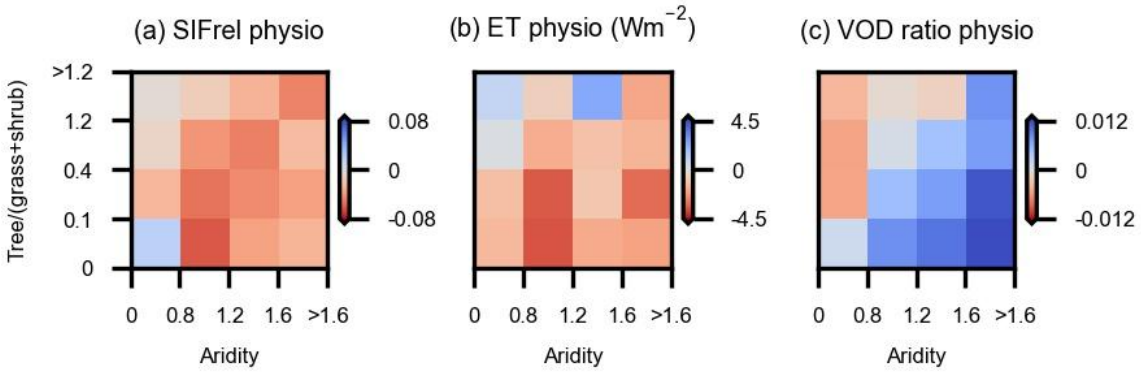

Figure 4.A11. Vegetation physiological responses to drought across aridity and vegetation types during 8-day before drought until drought peaks. Vegetation types are represented by the ratio between the tree cover fraction and the cover fraction of grass and shrub.

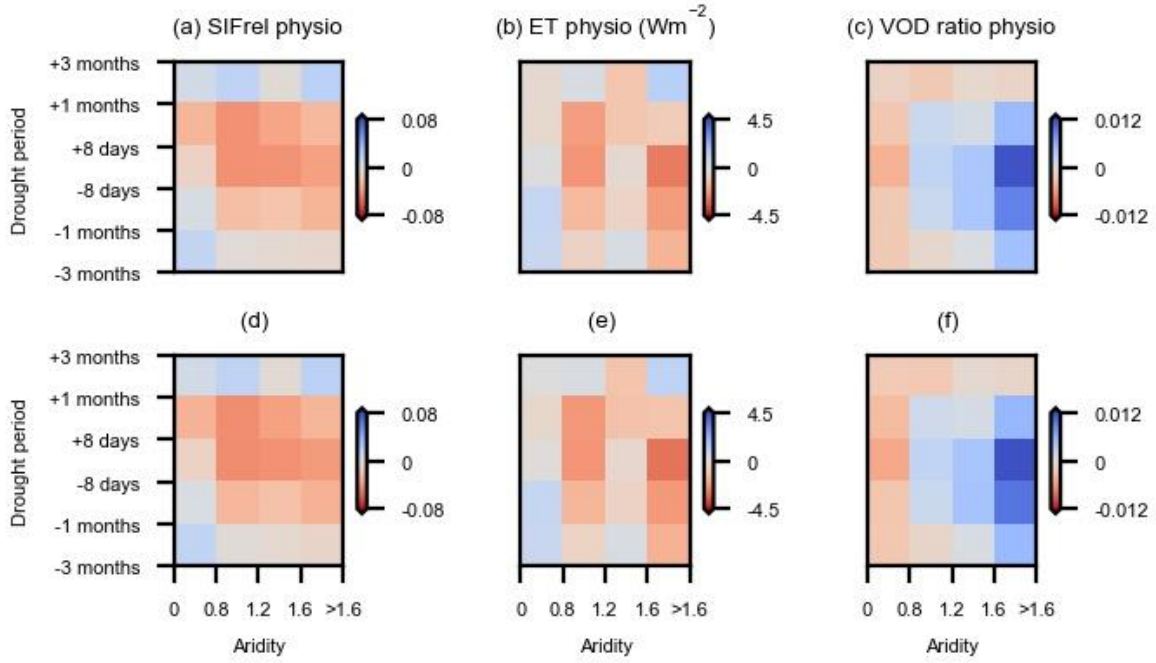

Figure 4.A12. Same as in Figure 4.3 (d-f) but leaving out (a, b, c) 12 time steps or (d, e, f) 6 time steps to train random forest models by LAI.

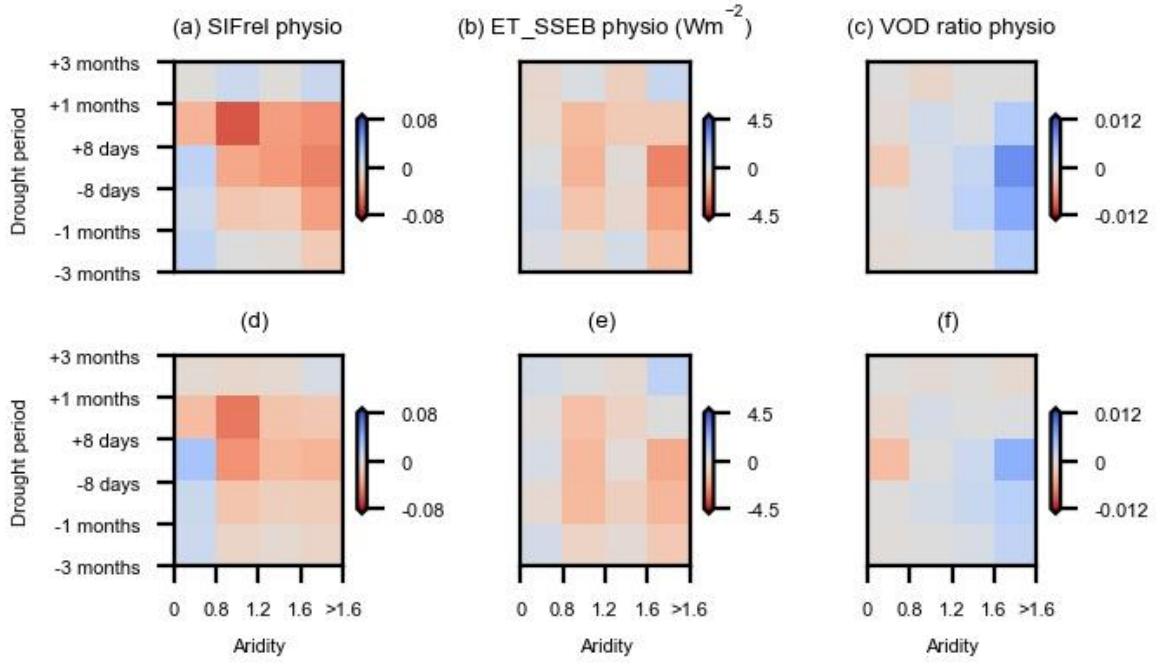

Figure 4.A13. Similar as in Figure 4.3 (d-f) but disentangling physiological variations using alternative methods of (a-c) SHAP values on random forests and (d-f) multiple linear regression.

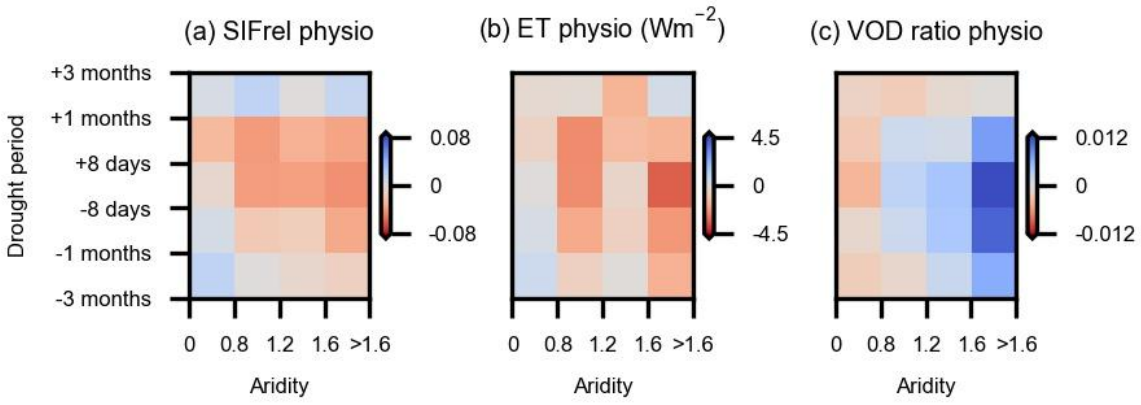

Figure 4.A14. Same as in Figure 4.3 (d-f) but for regions where the second-strongest drought during the last 40 years is not in 2018–2021.

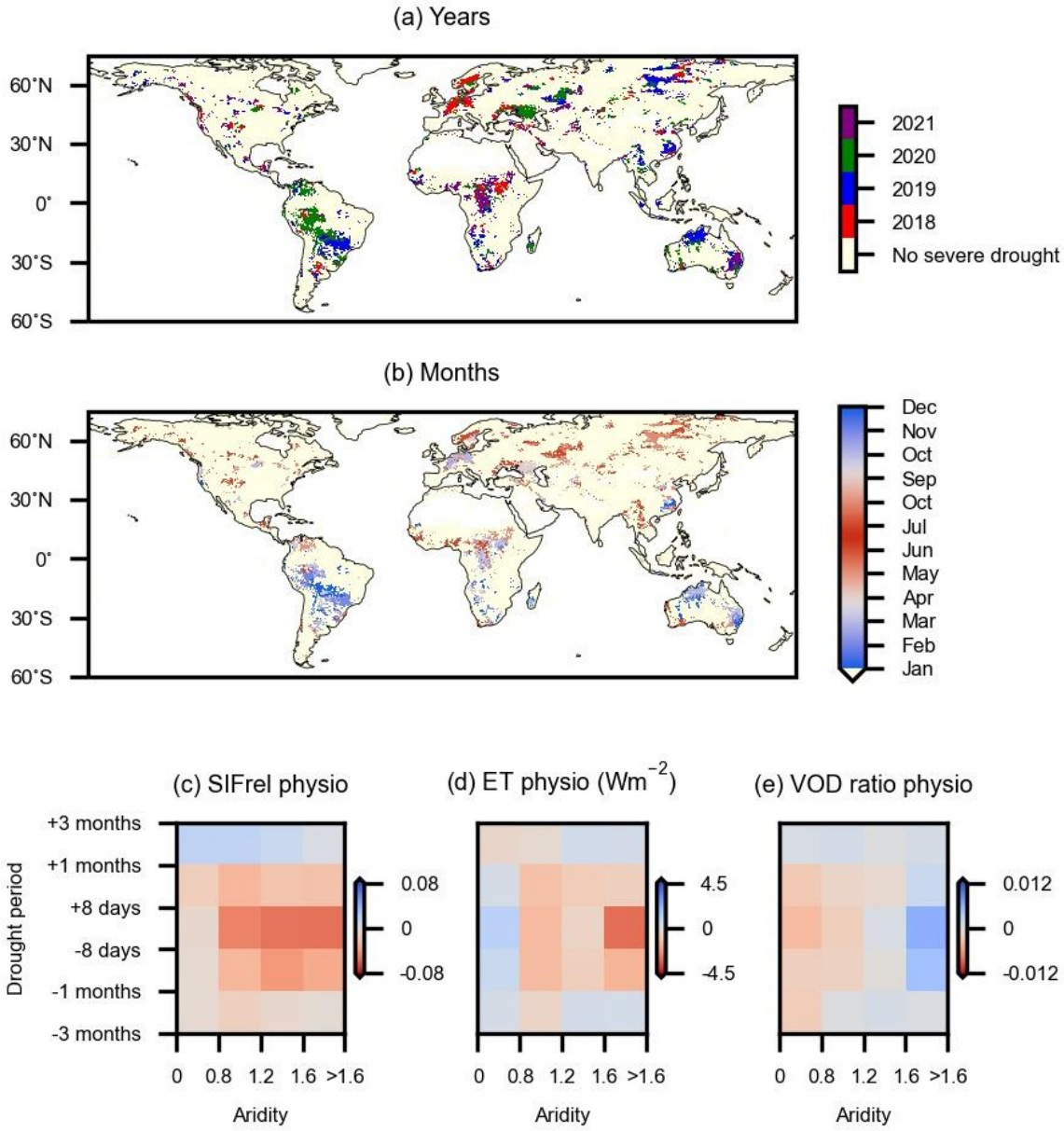

Figure 4.A15. (a, b) Timing of drought peaks similar as in Figure 4.A2, and (c, d, e) vegetation physiological response to drought similar as in Figure 4.3 (d-f), but drought peaks are detected by minimum soil moisture anomalies in the growing season.

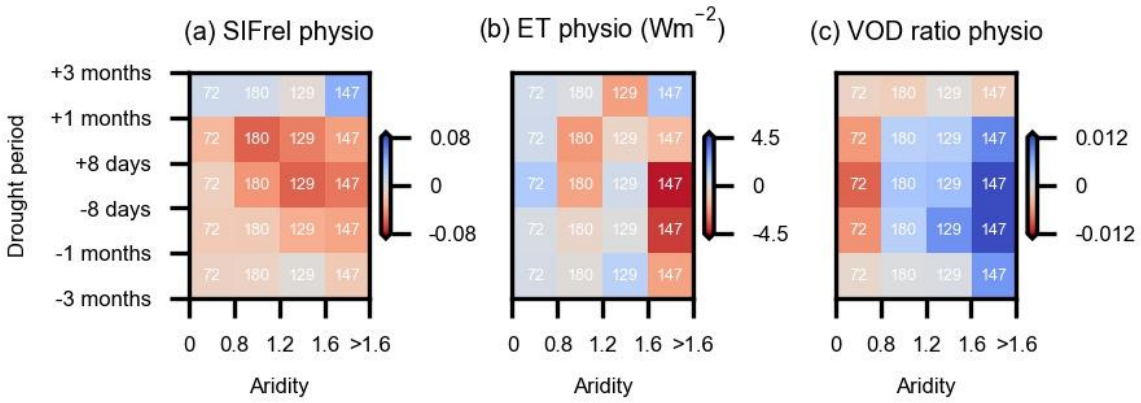

Figure 4.A16. Same as in Figure 4.3 (d-f) for observations but focusing on the grid cells selected for SCOPE outputs.

5 Drought propagation into the terrestrial water cycle

Abstract

Drought' s intensity and duration have increased in many regions over the last decades. However, the propagation of drought-induced water deficits through the terrestrial water cycle is not fully understood at a global scale. Here we study responses of monthly evaporation and runoff to soil moisture droughts occurring between 2001 and 2015 using independent gridded datasets based on machine learning-assisted upscaling of satellite and in-situ observations. We find that runoff and evaporation show generally contrasting drought responses across climate regimes. In wet regions, runoff is strongly reduced while evaporation is decoupled from soil moisture decreases and enhanced by sunny and warm weather typically accompanying soil moisture droughts. In drier regions, evaporation is reduced during droughts due to vegetation water stress, while runoff is largely unchanged as precipitation deficits are typically low in these regions and ET decreases are buffering runoff reductions. While these water flux drought responses are controlled by the large-scale climate regimes, they are additionally modulated by local vegetation characteristics. Evaporation increases more strongly (or reduces less strongly) in highly tree-covered regions, which in turn induces stronger runoff deficits. Land surface models capture the observed water cycle responses to drought in the case of runoff, but not for evaporation where the evaporation deficit (surplus) is overestimated (underestimated), related to a misrepresentation of the general soil moisture-evaporation interplay. In summary, our study illustrates how the joint analysis of machine learning-enhanced Earth observations can advance the understanding of global eco-hydrological processes, as well as the validation of land surface models.

This chapter has been submitted as:

Li, W., Reichstein, M., O, S., May, C., Destouni, G., Migliavacca, M., Kraft, B., Weber, U., Orth, R. (2023). Contrasting drought propagation into the terrestrial water cycle between dry and wet regions. Earth’s Future, accepted.

5.1 Introduction

Rising anthropogenic greenhouse gas concentrations and the consequent global warming and have increased the intensity and duration of drought in many regions (Canadell et al. 2021; Dai, Zhao, and Chen 2018). Drought affects a variety of environmental and socio-economical sectors, and has been identified as one of the most impactful natural hazards (Blauhut, Gudmundsson, and Stahl 2015; Rene Orth et al. 2022). Some well-known large drought episodes have occurred in recent years, such as the European droughts in 2003 and 2018 (Büntgen et al. 2021; Fink et al. 2004), the 2010 Russian drought (Barriopedro et al. 2011), the 2001–2009 millennium drought in Australia (van Dijk et al. 2013) and the 2012–2014 drought in California (AghaKouchak et al. 2015). Drought conditions are typically introduced by an anomalous atmospheric circulation inducing rainfall deficits and can then propagate further into the biosphere and hydrosphere. Drought involves potential consequences for ecosystem services and food security, and its propagation into the water cycle affects water resources (Wang et al. 2016). Drought propagation has been investigated since many years, but mostly focusing on hydrological variables (Eltahir and Yeh 1999; Peters et al. 2006; Van Loon 2015; Van Loon 2013), while drought can also propagate into the land ecosystems to affect e.g. evaporative cooling and evaporation recycling. Recent studies focused on soil moisture drought propagation across geospheres with effects on blue-water (runoff) and green-water (evaporation, 'ET' hereafter) fluxes; they used, for example, catchment-measured and modeled data in Europe (Orth and Destouni 2018) or model-based indices such as the Standardised Precipitation-Evapotranspiration Index and the Standardised Runoff Index to assess global biospheric and hydrologic responses (Fuentes, Padarian, and Vervoort 2022). However, these studies are not consistently based on observation-based data and hence subject to modeling assumptions about e.g., water stress impacts on land surface energy and water balances.

Soil moisture drought incorporates both the deficit of precipitation water input and high atmospheric water demand, and has been widely employed in previous drought analyses (Chatterjee et al. 2022; Seneviratne et al. 2012; Teuling et al. 2013; O et al. 2022). Soil moisture drought can reduce streamflow and groundwater levels, and lead to the decrease of overall runoff. Runoff is indispensable for aquatic ecosystems, and for the food and energy production through irrigation (Destouni, Jaramillo, and Prieto 2013), and it can be strongly and quickly reduced under drought, challenging the freshwater management (Orth and Destouni 2018; Fuentes, Padarian, and Vervoort 2022). In addition, soil moisture drought can trigger ET anomalies which may further affect the land water balance in general and runoff in particular. Even though evaporation from soils and other surfaces is also relevant, ET consists mainly of plant transpiration. Therefore, ET anomalies are primarily associated with vegetation functioning, including that of agricultural crops and natural vegetation. In wet regions, drier than usual soil moisture conditions are typically accompanied by abnormal high temperatures and radiation which induce ET surpluses (Orth and Destouni 2018); By contrast, in dry regions soils become too dry under drought and cannot satisfy vegetation water demand and likely induce reductions in vegetation productivity and growth (Mishra and Singh 2010). ET anomalies induce anomalies in the regional

atmospheric water content and this can be transported into downwind regions to cause remote water balance effects (Schumacher et al. 2022; Hoek van Dijke et al. 2022). Understanding the propagation of soil moisture drought into the terrestrial water cycle can help to identify areas of particularly high vulnerability for water deficit propagation. Moreover, it can inform potential drought mitigation measures, e.g., irrigation or dam regulations, to maintain the ecosystem's environmental and socio-economic services.

Land surface models (LSMs) simulate ET and runoff as these fluxes are essential components of the land energy and water balances, and of land-atmosphere exchanges of energy and water (Pitman 2003). LSMs typically represent a suite of physical processes through parameterizations, and therefore, the models are inherently uncertain given (i) potentially ignored mechanisms and processes and (ii) inaccurate or simplified representations of processes; as the land surface is heterogeneous with respect to soil, vegetation and water flow characteristics, and this information is difficult to observe and accurately represent in models (Ukkola et al. 2016; Warren et al. 2015; Clark et al. 2015). In this context, previous studies have found that the seasonal dynamics of ET are well captured in LSMs, while ET variability at the inter-annual scale and during water-stressed conditions is not properly reproduced (Berg and Sheffield 2018; Ukkola et al. 2016; Best et al. 2015). This is related to the inaccurate representation of soil moisture controls on vegetation and of sub-surface hydrological processes such as infiltration and preferential flow. Besides, although LSMs can estimate total runoff, i.e. the sum of surface runoff and drainage runoff, reasonably well in terms of annual means, the accuracy relies on the quality of the precipitation forcing data (Zhou et al. 2012; Fallah, O, and Orth 2020). LSMs do capture realistic monthly runoff variability, but poorly reproduce observed covariations between runoff and soil moisture or precipitation (Ghajarnia, Kalantari, and Destouni 2021). Crow et al. (2018) and Tian et al. (2018) have found that LSMs differ in their estimations of peak-flow runoff, which is related to uncertainties in the representation of infiltration.

Benefiting from the growing suite of satellite-based Earth observations and in-situ measurements, as well as from developing machine learning techniques, global observation-based soil moisture, evapotranspiration and runoff datasets have recently become available and can be used to understand land surface drought responses (e.g., O and Orth 2021; Jung et al. 2019; Ghiggi et al. 2021; O et al. 2022). Machine learning algorithms can learn complex relationships between ground measurements and meteorological conditions to extrapolate the ground measurements to unobserved regions using globally available meteorology data (Papale and Valentini 2003; Tramontana et al. 2016). As such, machine learning-based datasets are directly derived from observations, and independent of physically-based models, presenting a new opportunity to assess the model uncertainty.

In this study, we detect droughts based on minimum warm-season soil moisture during the period 2001 and 2015 in each grid cell using the SoMo.ml dataset (O and Orth 2021) across global vegetated areas. And we analyze the related response of ET from FLUXCOM (Jung et al. 2019) and of runoff from the G-RUN ensemble (Ghiggi et al. 2021). Thereby we benefit from the opportunity that since recently all major land

water state and flux variables are available from state-of-the-art observation-based machine learning-extrapolated global datasets. We determine ET and runoff anomalies under drought development and recovery periods, and then investigate their relationship with climate regimes, vegetation types, soil characteristics, topography and human activities (AghaKouchak et al. 2014). Further, we compare the drought propagation into ET and runoff between observation-based data and an ensemble of state-of-the-art LSMs from TRENDY models. In this context, we additionally employ a hybrid hydrological model which aims to combine the flexibility of machine learning with physical constraints and is hence in between data-driven and process-based modeling approaches (Reichstein et al. 2019; Kraft et al. 2022).

5.2 Data and methods

5.2.1 Observation-based data

An overview of all employed datasets is presented in Table 1. The three main focused variables of this study, ET, runoff and soil moisture, represent water fluxes and storage, and are obtained from global gridded datasets which upscale in-situ measurements using machine learning techniques, and are independent from each other in terms of input data. We use SoMo.ml soil moisture to detect drought periods (O and Orth 2021) (https://doi.org/10.17871/bgi_somo.ml_v1_2020). SoMo.ml comes with 0.25˚ spatial resolution and covers the period from 2000 to 2019. It distinguishes three soil layers (0-10cm, 10-30cm, 30-50cm), while we use a depth-weighted average of the three layers in this study. The underlying Long Short-Term Memory machine learning model has been demonstrated to learn relationships between in-situ soil moisture measurements and meteorological data, and to extrapolate soil moisture dynamics to unobserved regions (O and Orth 2021; O et al. 2022).

We use ET from FLUXCOM to analyze its anomalies during drought conditions (Jung et al. 2019). FLUXCOM ET is based on ensembles of machine learning approaches for upscaling in-situ measurements from FLUXNET eddy covariance towers. We use the FLUXCOM ET product which is based exclusively on remote-sensing data to model ET, and therefore independent of meteorological and soil moisture data (Jung et al. 2019). FLUXCOM ET from the remote sensing setup provides 8-daily data at 0.0833˚ spatial resolution from 2001 to 2015.

We use runoff from the G-RUN ensemble runoff dataset to analyze respective anomalies during drought (Ghiggi et al. 2021, https://figshare.com/articles/dataset/G-RUN_ENSEMBLE/12794075). The G-RUN ensemble product comes at 0.5˚ spatial resolution and covers the time period 1902 to 2019. It is the second version of G-RUN (Ghiggi et al. 2019) and uses random forests and global meteorological data to upscale a comprehensive dataset of international in-situ streamflow observations. G-RUN Ensemble runoff has been shown to compare well with independent observations from large river basins, and compared with other runoff products over the period 1982-2010 (Ghiggi et al. 2021).

We validate our main analysis in two ways: (i) To complement our drought analysis based on soil moisture deficits in the top 50cm of the soil, we additionally use terrestrial water storage from GRACE which also includes deep soil moisture and groundwater dynamics to detect drought (Landerer and Swenson 2012; Swenson and Wahr 2006) (https://podaac.jpl.nasa.gov/dataset/TELLUS_GRAC-GRFO_MASCON_CRI_GRID_RL06_V2); (ii) To validate the ET drought responses detected with FLUXCOM's global gridded data, we use flux tower ET measurements based on the eddy covariance method and obtained from the FLUXNET2015 dataset. We calculate monthly ET anomalies by removing long-term trends and mean seasonal cycles after the quality control and gap filling (Pastorello et al. 2021). We focus on 39 sites with more than 8 years of continuous data since 2001.

5.2.2 Land surface modelled data

We compare our observation-based results with drought responses simulated by state-of-the-art land surface models from the TRENDY v7 ensemble. All three variables, ET, runoff and soil moisture, are derived in monthly resolution from each TRENDY model: CABLE-POP, CLM5.0, ISAM, JSBACH, JULES, LPJ-GUESS, LPX, ORCHIDEE-CNP, and VISIT. In particular, we use simulations from Scenario 3 which fully account for changes in CO2, climate and land use (Le Quéré et al. 2018; Sitch et al. 2015). To be consistent with observation-based data, we convert the units of soil moisture, ET and runoff from LSMs from originally kg/m^{-2}, $kg/m^{-2}s^{-1}$ and $kg/m^{-2}s^{-1}$ to mm, mm/d and mm/d, respectively. The TRENDY models provide data at different spatial resolutions ranging from 0.5˚ to 2˚, such that we downscale the outputs to 0.5˚ spatial resolution to match the observational datasets. The downscaling is done by using the same values from surrounding lower-resolution grid cells.

In addition, we use ET, runoff and soil cumulative water deficit simulated from the hybrid hydrological model, H2M, which combines physical process representations with machine learning algorithms (Kraft et al. 2022) (https://doi.org/10.17617/3.65). The model consists of a simple hydrological scheme, which represents the water storage of snow, soil cumulative water deficit, and groundwater, and ensures the conservation of water across compartments. It uses a recurrent neural network to generate spatio-temporally varying parameters which are derived by calibration against FLUXCOM ET, GRUN runoff, GRACE terrestrial water storage, and GLOBSNOW snow water equivalent. Thus, the model is data-driven yet physically constrained by the water balance equations which improves the performance beyond physical model-based LSMs.

5.2.3 Auxiliary data

To study the meteorological conditions associated with drought, we use 0.5˚-resolution ERA5-Land meteorological data including 2-m air temperature, short-wave incoming solar radiation (hereafter 'solar radiation'), precipitation, and vapor pressure deficit (VPD) (Muñoz-Sabater et al. 2021). The ET and runoff responses to drought are analyzed across different climate regimes which we characterize by the aridity index.

The index is calculated using ERA5-Land precipitation and net radiation as the ratio of the long-term mean net radiation and unit-converted precipitation, with higher values denoting drier climate conditions. The aridity index used in the flux tower ET analysis is calculated using flux tower net radiation and precipitation.

To understand the multifaceted controls of the spatial patterns of ET and runoff anomalies at drought peaks, we consider a range of land surface characteristics listed in Table 1, including variables related to climate (aridity index), vegetation (tree cover fraction, anisohydricity index, and leaf area index, 'LAI' hereafter), topography obtained at 250 m resolution (medians and standard deviations of elevation, slope, roughness and aspect for each 0.5˚ grid cell), soil type (fractions of silt, clay and sand) and human activities (population and irrigation density).

Table 5.1. Overview of employed datasets.

	Variables	Resource	Descriptions	Reference(s)
Observation-based soil moisture and water fluxes	Soil moisture	SoMo.ml	Root-zone soil moisture from 0 to 50 cm	(O. and Orth 2021)
	Evaporation	FLUXCOM	Eddy covariance and remote sensing-based evaporation	(Jung et al. 2019)
	Runoff	G-RUN Ensemble	Catchment data-based runoff	(G. Ghiggi et al. 2021)
Modelled soil moisture and water fluxes	Soil moisture; Evaporation; Runoff	TRENDY v7	Output from physically-based land surface models	(Le Quéré et al. 2018; Sitch et al. 2015)
Soil moisture and water fluxes from the hybrid modeling	Soil moisture; Evaporation; Runoff	H2M	Output from the hybrid hydrological model	(B Kraft et al. 2022)
Water fluxes and ancillary data from the eddy covariance measurements	Evaporation Runoff Temperature Net radiation Precipitation	FLUXNET 2015	Water fluxes and ancillary in-situ data derived using the eddy covariance method	(Pastorello et al. 2021)
Dynamic ancillary data	Terrestrial water storage	GRACE	Global water storage anomalies relative to a mean storage	(Landerer and Swenson 2012; Swenson and Wahr 2006)

	Temperature Precipitation Solar radiation VPD	ERA5-Land	Reanalysis data	(Muñoz-Sabater et al. 2021)
Static ancillary data	Aridity index	ERA5-Land	The ratio between net radiation and precipitation	(Muñoz-Sabater et al. 2021)
	Tree cover fraction	Vegetation Continuous Fields Version 1 data product (VCF5KYR)	Satellite-detected cover of tall vegetation as a fraction of total vegetation cover in a grid cell	https://lpdaac.usgs.gov/products/vcf5kyrv001/
	Anisohydricity index	Advanced Microwave Scanning Radiometer on EOS Aqua (AMSR-E) X-band VOD	Indication of vegetation water regulation with lower values showing higher regulation	(Li et al. 2017)
	Leaf area index	MOD15A2H	The amount of leaf material in an ecosystem	https://lpdaac.usgs.gov/products/mod15a2hv006/
	Medians and standard deviations of the elevation, slope, roughness and aspect	Generated from originally global 250 m GMTED2010	Terrain characteristics	(Amatulli et al. 2018)
	Population	GPW v4	Inhabitants between 2005 and 2014	https://sedac.ciesin.columbia.edu/data/collection/gpw-v4

Irrigation density	Global Map of Irrigation Areas	The amount of irrigated area in 2005 in percentage of the total area	(Siebert et al. 2015)
Soil type	GLDAS	Fractions of clay, sand and silt	(Reynolds, Jackson, and Rawls 2000)

5.2.4 Data processing

Our analysis focuses on gridded global datasets with 0.5˚ spatial resolution and monthly time steps. Data from daily products are aggregated to the monthly time scale by calculating averages across all days of each month. The study time period is 2001-2015 as constrained by the concurrent availability of all relevant datasets. Our analyses focus on grid cells where the fraction of total vegetation cover from 2001 to 2015 is higher than 5% to exclude non- or low-vegetated areas such as deserts and lakes. When studying ET, runoff and other hydro-climate conditions under drought, we focus exclusively on anomalies, which are obtained by removing the mean seasonal cycles and long-term trends. Mean seasonal cycles are calculated using 15-year data for specific months, and long-term trends are derived by using a locally-weighted smoothing filter with a smoothing window size of 40% of the time series length.

5.2.5 Drought detection

We study ET and runoff responses to drought within vegetation growing seasons, so that we remove monthly time periods where the temperature from ERA5-Land is lower than 5˚C. We then select the most extreme drought event for each grid cell based on the lowest soil moisture value in our study period from 2001 to 2015 using observation-based and land surface modeling data, respectively. We analyze ET and runoff anomalies at these drought peak months, and additionally focus on the development and recovery periods by considering the 3 months before and after (Orth and Destouni 2018). We also study the drought duration which is defined as (i) the drought development period starting when soil moisture is decreasing below the seasonal mean (= start of dry anomaly) until drought peak, and (ii) the drought recovery period which extends from drought peak until the soil moisture is for the first time above the seasonal mean again (=end of dry anomaly).

In the analysis of flux tower ET located in the northern hemisphere, since soil moisture is not always measured at each site, we use a cumulative water deficit index (CWD) to detect drought peaks. First, we

remove monthly time periods where the eddy tower temperature is lower than 5˚C. CWD is calculated by accumulating site-measured precipitation (P) and ET for each year (Yu et al. 2022):

$$CWD_t = \min\ (0,\ CWD_{t-1} + P_t - ET_t) \qquad (5.1)$$

where t indicates the monthly time step. The initial value of CWD is set to zero. Potential data gaps are filled with ET from the GLEAM product and precipitation from i) 0.25˚-resolution gridded ERA5 data and ii) machine-learning downscaled precipitation product (Besnard et al. 2019). CWD is reset to zero at the end of each year to close the annual water balance.

5.2.6 Attribution analysis

Attribution analysis is conducted to understand spatial patterns of ET and runoff anomalies associated with the drought peaks. For this purpose, we train random forests to model ET and runoff anomalies at drought peaks, respectively, across all global grid cells with several ancillary land surface data (see Table 5.1). Using cross-validation we ensure a useful model performance with cross-validation out-of-bag R2 higher than 0.5 (Breiman 2001). Then we evaluate the relevance of individual variables using the Shapley Additive Explanations (SHAP) attribution method which is a robust explainable machine learning method (Lundberg and Lee 2017). SHAP is a game theoretic approach to explain the output of the random forest model by accounting for contributions of individual variables to the overall prediction. This way, to understand the most important controls of ET responses to drought we calculate SHAP values to quantify the marginal contributions of each predictor on the target variable ET, and rank the variable importance by the sum of contributions across all grid cells. To understand the most important controls of runoff responses to drought, we then use runoff anomalies to replace ET anomalies to repeat the attribution analysis. When studying spatial patterns of ET anomalies under drought we also use runoff drought anomalies as predictors, and vice versa.

5.3 Results and discussion

5.3.1 Detecting soil moisture drought

The months and years when the driest soil moisture values are detected across the globe are shown in Figure 5.1. Regions over Africa, the Middle East and Greenland are excluded due to the sparse vegetation. The month-of-year of drought peak occurrence varies across latitudes: In the northern hemisphere, drought occurs from June to October as a consequence of the interplay of limited water input and higher ET in summer and autumn months; Near the equator, drought rather occurs from January to May, corresponding to the meteorological dry seasons in northern South America, Central Africa, India and Southeast Asia; In the Southern Hemisphere drought occurs mostly also in meteorological dry months e.g. from July to December in Amazon, except for the southern parts of South America, South Africa and Australia. Drought peak months across Australia are variable and are modulated by the local climate regimes (Peel, Finlayson, and McMahon

2007). Spatial patterns of drought years show more heterogeneity than the month-of-year results, while larger clusters correspond well with drought events reported in previous studies, such as the 2003 European drought (Fink et al. 2004), the 2010 western Russian drought (Barriopedro et al. 2011), 2012–2014 drought in California (AghaKouchak et al. 2015) and the 2010 Amazon drought (Lewis et al. 2011).

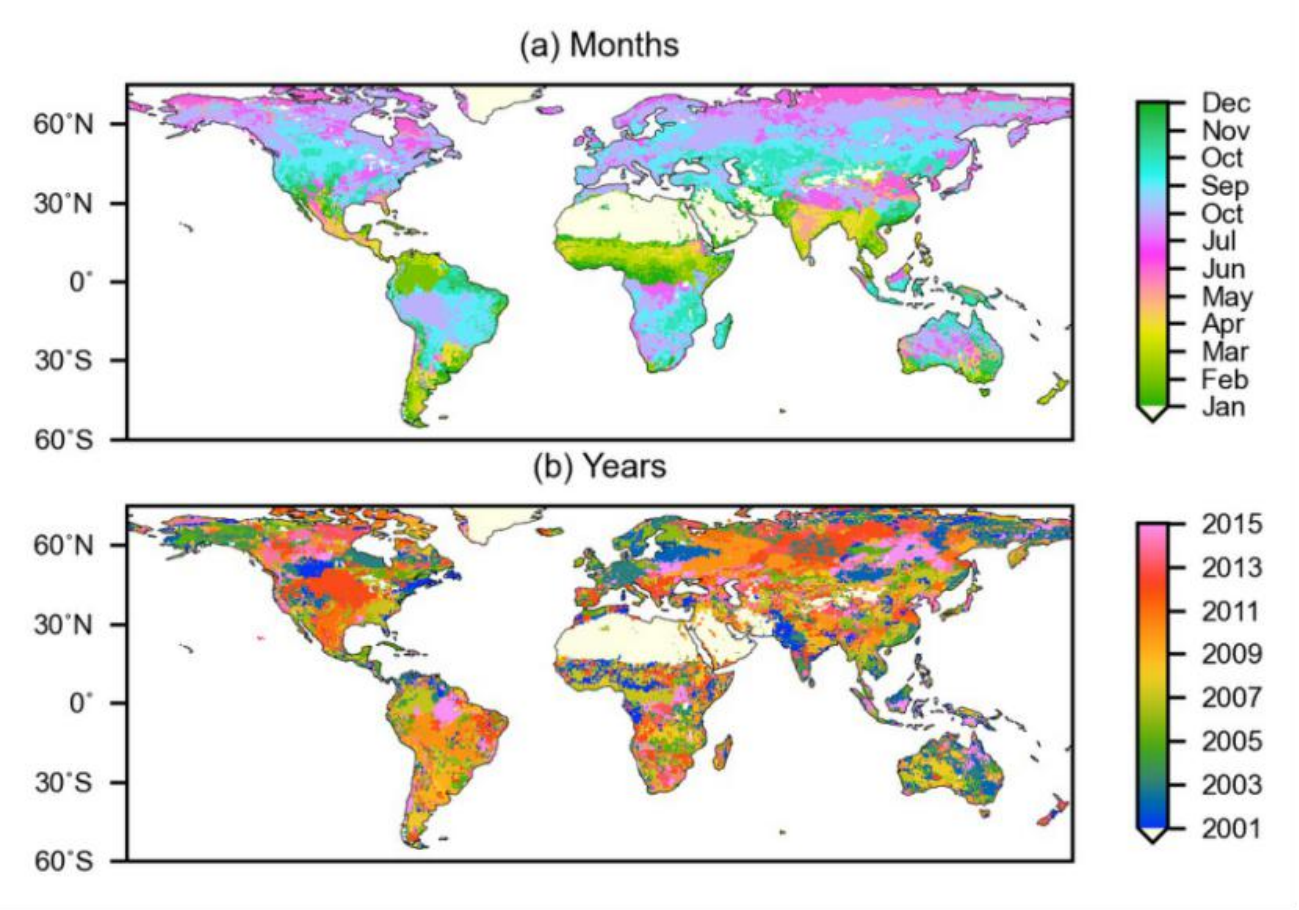

Figure 5.1. Timing of drought peaks as detected by monthly soil moisture minima from the observation-based dataset during the study period 2001-2015.

5.3.2 Water cycle response to drought in observation-based data

The global distributions of ET and runoff anomalies at soil moisture drought peaks are shown in Figure 5.2. Compared to long-term average conditions, ET shows both increases and decreases under drought (Figure 5.2a). Significantly positive ET anomalies are found in the high latitudes and the tropics, while significantly negative ET anomalies occur mostly in the subtropics and mid-latitudes. Negative ET anomalies are larger in an absolute sense and more widespread than positive ET anomalies. By contrast, runoff anomalies are reduced during drought peaks across most of the globe with the strongest negative values located in the Amazon and Asian tropics (Figure 5.2b). Exclusively focusing on ET and runoff reductions which can affect regional ecosystems and also socio-economic systems, we find that ET reductions are slightly stronger than runoff

reductions across the globe (Figure 5.2c), and the preferential propagation of soil moisture deficits into runoff in northern Europe confirms results from a previous study (Orth and Destouni 2018).

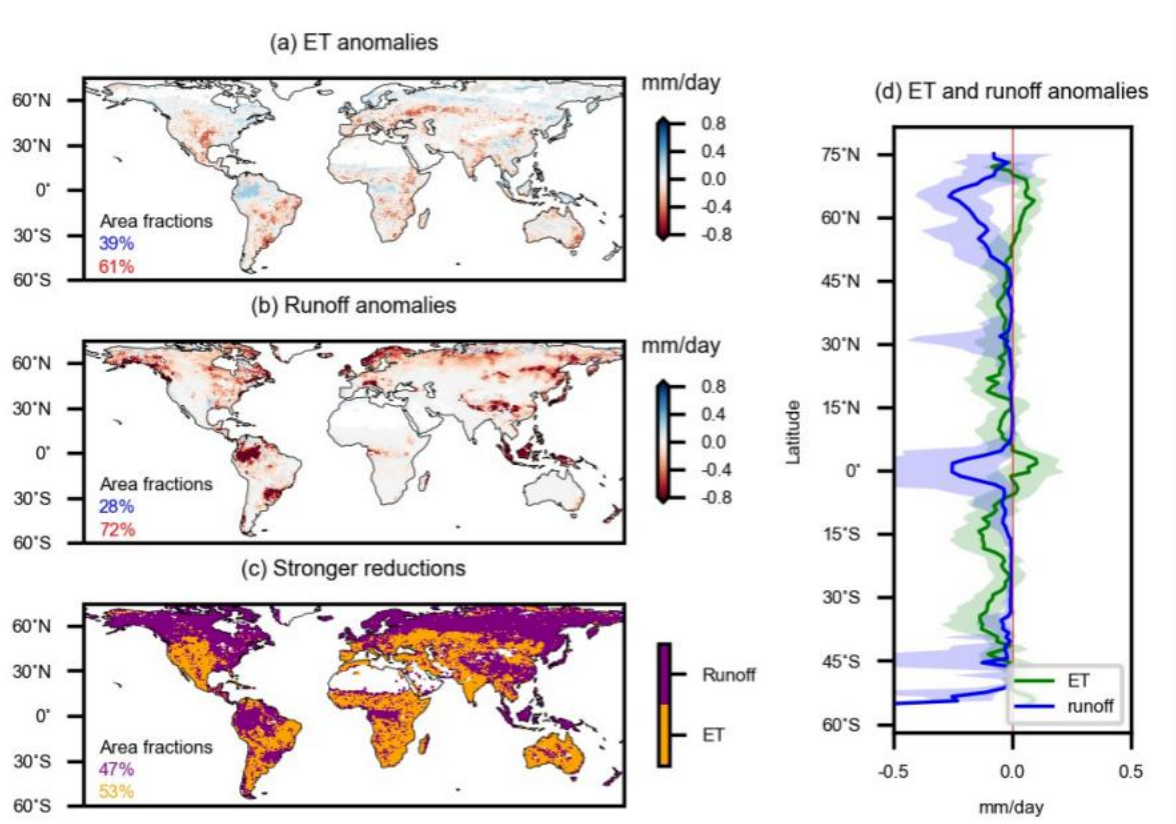

Figure 5.2. Mapping (a) ET and (b) runoff anomalies at drought peaks. (c) Variable with stronger reductions. (d) Latitudinal patterns of ET and runoff anomalies. The solid line and shaded areas show the median and interquartile ranges, respectively. In (a, b), area fractions are given for positive and negative changes, respectively, and in (c) area fractions are given where ET or runoff are more reduced during peak drought.

Latitudinal patterns of ET and runoff anomalies in Figure 5.2d present two peaks of ET surpluses in boreal regions around 65˚N and around the equator. These regions are typically wet (Appendix Figure 5.A1a) and energy-limited (Denissen et al. 2021; Li et al. 2021) such that even during periods with soil moisture deficits, the soil moisture content is sufficient to sustain plant photosynthesis and associated transpiration (O et al. 2022). Further, soil moisture drought in high latitudes is typically accompanied by sunny and warm weather benefiting boreal ecosystem productivity, which is often limited by low temperatures and waterlogging (Ohta et al. 2014). Similarly, tropical regions are also wet and often have limited radiation supplies (Li et al. 2021). Interestingly, runoff anomalies show opposite patterns to ET anomalies in boreal and tropical regions as a consequence of severe decreases in soil moisture anomalies (Appendix Figure 5.A1b) and ET surpluses (Condon, Atchley, and Maxwell 2020). In low latitudes around 0˚-40˚N and 15˚S-35˚S, ET reductions typically exceed runoff reductions which indicates a considerable green-water vulnerability to drought in these areas (Figure 5.2d). Although subtropical regions show mostly low runoff reductions, some sub-regions such

as southern China and eastern South America exhibit much stronger runoff decreases where their unique topography could influence rainfall-infiltration processes.

5.3.3 Understanding the observed water cycle response to drought

Next, we perform an attribution analysis to understand the controlling factors of the spatial patterns of ET and runoff drought responses shown in Figure 5.2 a,b. We find that tree cover fraction, VPD anomalies, runoff anomalies and aridity are the four most important predictors for the ET responses to soil moisture drought (Appendix Figure 5.A2 a). Higher VPD is associated with the higher ET deficits at drought peaks, because plants close stomata to prevent water loss when VPD is high (Fu et al. 2022; Novick et al. 2016). Similarly, aridity and tree cover fraction are also found as main controls to explain the spatial patterns of runoff responses to soil moisture drought (Appendix Figure 5.A2b). In addition, precipitation and soil moisture anomalies are very relevant explanatory variables; ET anomalies also strongly regulate the spatial variability of runoff anomalies at drought peaks where negative relationships between ET and runoff anomalies are expected, as available precipitation is partitioned into both fluxes and ET reductions could buffer runoff deficits. We note that such an attribution analysis can only reveal plausible land surface characteristics controlling the water cycle drought response, but it cannot detect actual causal relationships. Further, many of the variables identified as controls of the spatial patterns of the ET and runoff drought responses are not employed in the derivation of the ET and runoff products. This means that our attribution results are not an artifact of the derivation of the data products.

After identifying aridity and tree cover fraction as major modulators of the ET and runoff drought responses, we investigate these two drivers further in Figure 5.3 by grouping the global ET and runoff drought responses (Figure 5.2 a,b) according to classes of aridity and tree cover fraction. Figure 5.3 confirms systematic gradients of ET and runoff drought anomalies across aridity and tree cover classes. ET increases in low aridity (wet) regions where vegetation is not limited by water availability and is enhanced by drought-associated increases in atmospheric water demand (Green et al. 2020). ET decreases during soil moisture droughts in dry regions where aridity is higher than 1 (Figure 5.3a). In these regions, water availability often limits vegetation functioning even under normal conditions (O et al. 2022). Higher ET surpluses (or lower deficits) are found in regions with abundant tall vegetation. This can be explained as (i) tall trees likely have deeper-reaching roots to access deeper soil moisture and groundwater (Stocker et al. 2021), and (ii) they have better water saving strategies during pre-drought periods (Konings and Gentine 2017), such that they can benefit more from the drought-related radiation and temperature increases to enhance transpiration.

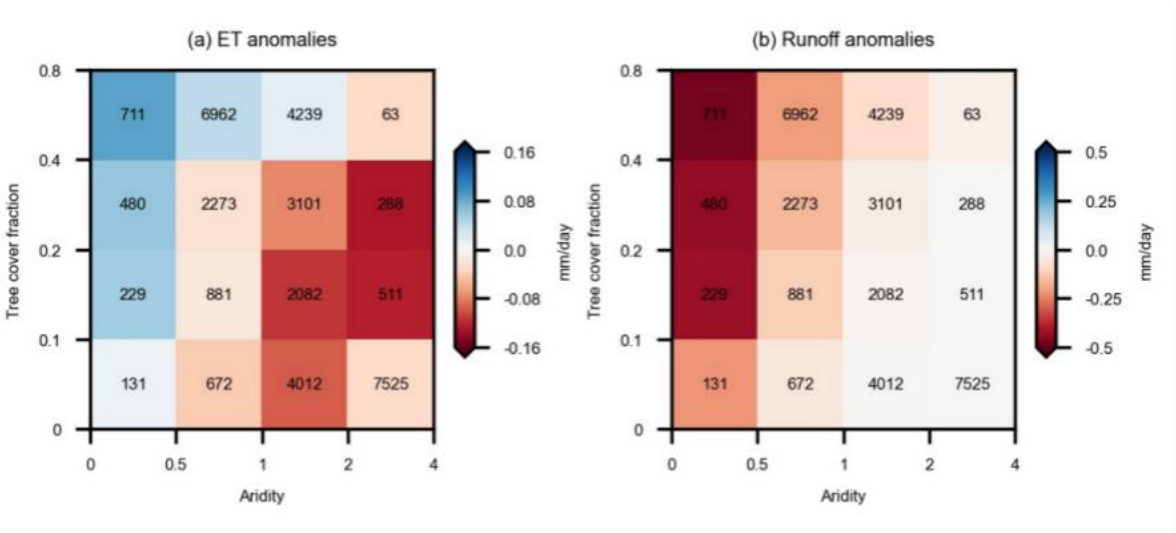

Figure 5.3. (a) Evaporation and (b) runoff anomalies at drought peaks expressed as medians across grid cells in each aridity and tree cover regime. The number in each box indicates the amount of grid cells in each regime. Aridity is computed as the ratio between long-term net radiation and precipitation with higher values indicating drier conditions. A few grid cells with fractions of tree cover exceeding 0.8 are included in the 0.4-0.8 group for simplicity.

Different from ET, runoff responses to drought show the most significant deficits in very wet regions with high tree covers. This is related to severe soil moisture deficits amplified by the concurrent ET surpluses, which leave a smaller fraction of available water for runoff (Appendix Figure 5.A1). Additionally, the precipitation deficits in wet regions are typically larger than in dry regions (Appendix Figure 5.A3c). Also, in areas with dense tree cover, more precipitation water is likely intercepted, enhancing evaporation and decreasing the water amount available for runoff (Owens, Lyons, and Alejandro 2006). Figure 5.3 displays median ET and runoff anomalies, but we note, that the variability of ET and runoff anomalies within each aridity-tree cover class is substantial (Appendix Figures 5.A4, 5.A5). This is related to land surface heterogeneity and the influences of other controls of the water cycle drought response (Appendix Figure 5.2).

Furthermore, we study the role of drought duration for the observed ET and runoff responses. For this purpose, we repeat the analysis of Figure 5.3 for different subsets of droughts with different development and recovery period lengths, and find overall similar ET and runoff drought responses across aridity-tree cover classes (Appendix Figure 5.A6). ET and runoff anomalies are more negative in cases of longer duration for both drought development and recovery, reflecting more pronounced soil moisture stress (Appendix Figure 5.A6 a and b). Interestingly, the intensity of the ET drought response is stronger related to the drought development duration and less affected by the drought recovery period, while the opposite is observed for the runoff drought response (Appendix Figure 5.A6 c-f). The lower influence of drought recovery duration on ET implies that ET recovery utilizes incoming precipitation water after drought peak which in turn can delay soil moisture and runoff recovery. Moreover, we reproduce Figure 5.3 with the second strongest drought in each

grid cell and find no systematic differences except for slight lower magnitudes of ET and runoff anomalies, suggesting that the studied spatial variations of drought influence are generally representative of other drought events occurring in the same grid cells (Appendix Figure 5.A7).

Moving beyond the focus on peak drought anomalies, we also study changes of water fluxes over the whole course of droughts. Apparent ET surplus can be found from one month before until drought peaks in wet regions which corresponds to the appearance of increased temperature and radiation (Figure 5.4a; Appendix Figure 5.A3 d and e). In very dry regions, negative ET anomalies can be found already three months before drought peaks corresponding to concurrently low soil water availability (Figure 5.4a; Appendix Figure 5.A3a). Runoff reductions start to be one or two months before drought peaks in line with precipitation anomalies (Figure 5.4b; Appendix Figure 5.A3c).

When focusing on the recovery period, we do not find substantial ET anomalies after drought peaks despite the fact that the soil moisture deficit is still significant (Appendix Figure 5.A3b). The quick recovery of ET can be attributed to precipitation events which initiates drought recovery, and through ET recovery this incoming water directly compensates for high VPD (Appendix Figure 5.A3f). Correspondingly, runoff deficits continue for one-two months (Figure 5.4b) following low soil moisture (and hence baseflow) and preferential partitioning of precipitation water input to ET. Furthermore, we also map the contrasting ET and runoff anomalies during drought development and recovery periods in Appendix Figure 5.A8. ET surpluses are found predominantly in the drought development period and in high latitude and tropical regions, while runoff reductions are most substantial in these regions in both drought phases.

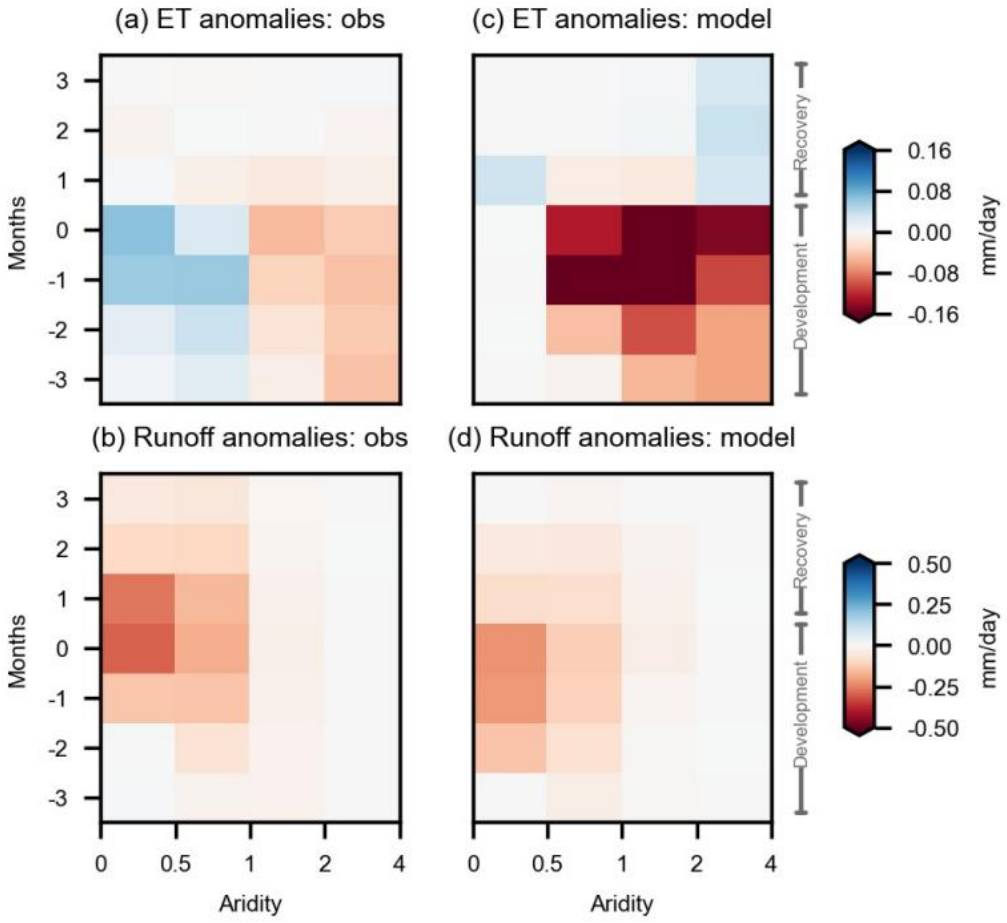

Figure 5.4. (a,c) ET and (b,d) runoff anomalies before, during and after drought peaks expressed as medians across grid cells in different aridity regimes. Results are shown for (a,b) observations (obs) and (c,d) median values of ensembles of land surface models (model). Month 0 denotes the drought peak; negative months (-3, -2, -1) denote drought development periods and positive months (1, 2, 3) denote the drought recovery periods.

In this observation-based analysis, droughts are identified from soil moisture deficits in the top 50 cm, such that deep soil moisture or groundwater are not directly considered. For this reason, we repeat the drought detection using terrestrial water storage measured from the GRACE satellite mission, and similarly we determine the ET and runoff anomalies for times with very low terrestrial water storage. We find very similar results of observation-based ET and runoff anomalies during drought periods (Appendix Figure 5.A9). Interestingly, in wet regions, GRACE-detected droughts involve an earlier onset of ET surpluses and less pronounced ET surpluses at drought peaks. In these regions, vegetation can benefit from its deep-reaching roots during the early drought stages of soil moisture droughts, while it is not the case for total water storage droughts. In addition, an earlier onset of runoff reductions in wet regions is found for droughts detected through terrestrial water storage. This is probably related to reductions in sub-surface runoff, which are not fully captured in the case of topsoil droughts. Overall, our results highlight that topsoil droughts do not affect the water cycle fundamentally different from droughts of total water storage and confirm the robustness of our

findings. This also demonstrates the validity of our approach for further comparing the observation-based drought responses simulated by land surface models from which we employ total soil moisture to detect droughts.

5.3.4 Water cycle response to drought in land surface models

Next, we analyze the output from state-of-the-art land surface models from the TRENDY ensemble. As shown in Figure 5.4c, the models overestimate drought-related ET reductions in dry regions. By contrast, drought-related runoff reductions simulated by LSMs show similar patterns and magnitudes as in the observation-based results, with the largest decreases in wettest regions during two months before and after drought peaks. Runoff recovers slightly more quickly than the observation-based result, which can be related to oversimplifications of sub-surface hydrological processes (Ukkola et al. 2016) and less or no simulated ET surpluses leaving more water for runoff. Compared with these multi-model averages, the results from individual models show similar response patterns for wet vs. dry regions but different magnitudes of simulated ET and runoff anomalies (Appendix Figure 5.A10). Global and latitudinal ET and runoff anomalies under drought simulated by LSMs show that the strong runoff reductions in boreal and tropical regions are properly captured, whereas ET reductions in these regions are overestimated and ET surpluses are not reproduced (Appendix Figure 5.A11). Also, the global spatial patterns of runoff anomalies are better captured by LSMs than those of the ET anomalies, even though the overall agreement of the patterns with observation-based results is limited in both cases (Appendix Figures 5.A12, 5.A13). Given that global distributions of drought peak months and years from LSMs are largely similar to observation-based results (Appendix Figures 5.A14 and 5.A15), LSMs biased representation of drought propagation into the ET deficits is not strongly associated with the soil moisture drought timing. Moreover, ensemble-mean ET and runoff anomalies from the LSMs during drought development and recovery periods are shown in Appendix Figure 5.A16. Runoff reduction patterns are overall well captured in LSMs, while ET deficit during drought development and ET surpluses during drought recovery are overestimated in many regions compared with observation-based results.

To complement the physical-based LSM simulations, we consider simulations from the hybrid hydrological model H2M in Appendix Figure 5.A17, which combines machine-learning data-driven approaches and physical-based modeling. We find stronger ET decreases in medium-dry to dry regions in H2M and also in LSMs. H2M ET is driven by data and has a closed water balance in contrast to FLUXCOM ET, so that the potential underestimation of extreme magnitudes of ET can be partly offset by forcing water balance closure. However, similarly as in the case of the TRENDY LSMs, H2M does not accurately reproduce the observed contrast of positive and negative ET responses to drought peaks across humid and arid regions. H2M slightly misrepresenting the positive changes in wet regions found in ground observations (Appendix Figure 5.A18) is possibly related to biases in implicit physical assumptions such as causal pathways of the water cycle, and related to biases due to trade-offs between the physical constraints (Kraft et al. 2022). Note, however, that

better agreement with FLUXCOM is somewhat expected, as the H2M model is calibrated against FLUXCOM ET and other observational products and hence not as independent as the TRENDY models.

We find similar biases in ET and runoff drought anomalies from H2M compared with the TRENDY simulations, even though the positive ET response in humid regions is captured better while the recovery of ET anomalies is slower than that in the reference data. Note, however, that better agreement with the reference data results is somewhat expected as the H2M model is calibrated against these datasets and hence not as independent as the TRENDY models.

Since the independent observation-based datasets employed here involve uncertainties and might not always complement each other to fully close the water balance, we seek to confirm the results of FLUXCOM ET drought responses which show considerable differences with modeled results. Therefore, we additionally analyze in-situ measurements of ET from flux-towers with the eddy covariance technique. To detect drought peaks at the towers, we determine minima in the cumulative water deficit, as soil moisture measurements are not consistently available. We find substantial variability of drought peak ET anomalies across sites highlighting the role of local climate (Appendix Figure 5.A18). Overall, there is a tendency for positive than negative ET anomalies at wet sites, while negative anomalies are dominant at dry sites. Therefore, eddy-tower-measured ET results confirm the ET drought responses found from the global gridded dataset despite the impact of subgrid-scale land surface heterogeneity, and with different gap-filled methods when detecting drought peaks using cumulative water deficit we find similar results.

5.3.5 A spotlight on the ET drought response across observations and models

We then study the general representation of the ET-soil moisture coupling in LSMs inferred from the correlation between them across all growing season months of the entire study period, as this can help to understand the biases in the simulation of respective drought anomalies. Figure 5.5a shows that ET responds positively to soil moisture changes in water-limited regions, including central North America, central Eurasia, Australia, eastern and South Africa. In contrast, a negative ET-soil moisture relationship is found in energy-limited regions in boreal Eurasia, tropical regions, eastern North America, north and central Europe and central eastern Asia. This negative relationship results from soil moisture anomalies typically behaving opposite to temperature and radiation anomalies which are actually controlling ET anomalies in these regions. Although LSMs capture the positive relationships between ET and soil moisture in dry regions, they cannot represent the negative coupling in humid regions (Figure 5.5b), which is also the case for most individual models (Appendix Figure 5.A19). When we relate the peak-drought ET biases from LSMs to the biases of their ET-soil moisture coupling (Figure 5.5c), we find that higher ET-soil moisture correlation biases coincide with exaggerated negative ET anomalies at drought peaks. This result illustrates that deficiencies in capturing overall land-atmosphere interactions also affect the estimation of water flux anomalies during droughts.

These deficiencies could be a joint result of several individual uncertainties in the LSMs related to e.g. the representation of vegetation water stress, soil hydraulics and structure, atmospheric boundary layer parameterizations, or to parameterizations related to plant functional types, as illustrated in previous studies (Ukkola et al. 2016; Powell et al. 2013; Zhao et al. 2022; De Kauwe et al. 2015). The modelled drought response can be affected by an incomplete representation of water stress considering e.g. solely soil moisture or solely VPD (Humphrey et al. 2021). In our results, the bias of ET-soil moisture coupling in models is found in all individual models (Appendix Figure 5.A20), implying that the diverse vegetation water stress functions in different models do not dominate biases in ET-soil moisture interactions. The misrepresentation of the ET-soil moisture coupling in wet regions could be related to the missing consideration of biophysical processes such as waterlogging which inhibits vegetation growth and transpiration, especially in energy-limited tropical and boreal regions (Ohta et al. 2014). Thereby, water stress applies not only in the case of dry soils but also for very wet soils. Further, the misrepresentation of soil hydraulic conductivity in models contributes largely to the underestimation of dry-regions soil evaporation during drought (Zhao et al. 2022), which helps to explain the overall stronger ET deficits in dry regions (Figure 5.4c). Since ET depends strongly on vegetation phenology (as represented by e.g. leaf area), the misrepresentation of LAI sensitivity to soil moisture can also partly explain the ET-soil moisture deficiencies (Li et al. 2022).

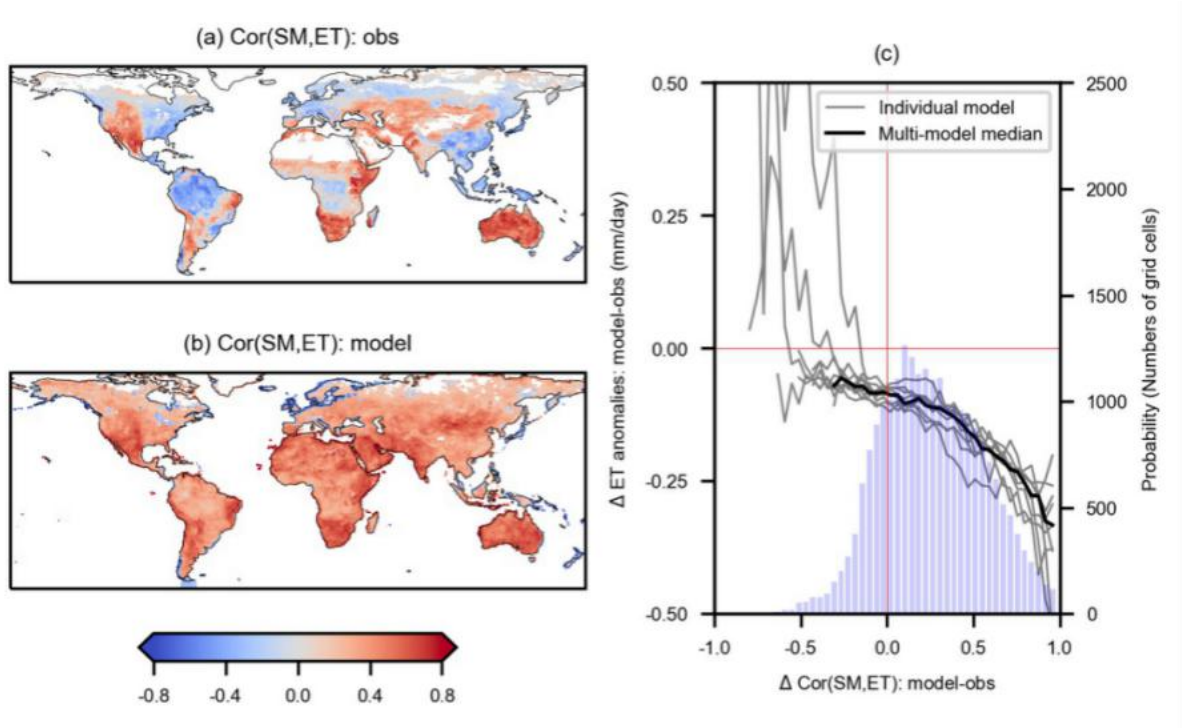

Figure 5.5. Comparing global patterns of the land-atmosphere coupling in (a) observations (obs) and (b) ensemble median values of land surface models (model). (c) Relationships between biases of simulated ET anomalies at drought peak (y-axis) and the respective differences between modeled and observed ET-soil moisture coupling (x-axis) as shown in (a) and (b). The solid black line denotes multi-model median results and grey lines show results from individual models. Blue bars at the bottom indicate the distribution of

modeled and observed correlation differences. Two-sided significance tests are done in (a, b) for displaying results from each grid cell at the $p<0.05$ level as assessed with Spearman correlation.

5.4 Conclusions

In conclusion, ET and runoff, the two main terrestrial water fluxes, show contrasting responses to soil moisture droughts (Figure 5.6). Drought propagation into runoff is stronger and longer-lasting than into ET with the largest reduction in wet regions at drought peaks, driven primarily by precipitation anomalies and ET surpluses. The propagation of soil moisture deficits into reduced ET is only found in dry regions, while in wet regions, vegetation functioning is not limited by water availability and benefits from sunny and warm weather conditions typically accompanying soil moisture droughts in these regions. These emerging large-scale signals are mainly related to regional climate, i.e., aridity, and are modulated by heterogeneous land surface characteristics (e.g., fraction of tree cover and topography). The interplay of these drivers relevant at different spatial scales determines the observed drought propagation into the water cycle, and explains its spatial heterogeneity.

Further, these results are obtained with machine learning-based datasets. While these datasets also have particular shortcomings such as inaccurate or incomplete underlying predictor variables, our findings are in line with previous research covering some aspects of our analysis. More importantly, these datasets provide global gridded estimates of key land surface variables independent from physically-based models. Therefore, they present a great opportunity to validate global drought response patterns which so far could only be obtained with models.

Land surface models can overall represent the timing and magnitude of drought-related runoff anomalies. However, they largely fail to capture the ET surplus observed during drought in wet regions and overestimate drought propagation into ET reductions in dry regions. These problems are due to biases in the model's land-atmosphere coupling which might further be related to potential missing biogeochemical and biophysical processes and aggravated by problems in simulating vegetation phenology during droughts. Overall, our results characterize regions with drought-vulnerable water fluxes which should be taken into account when developing strategies of freshwater management to overcome water shortages under drought.

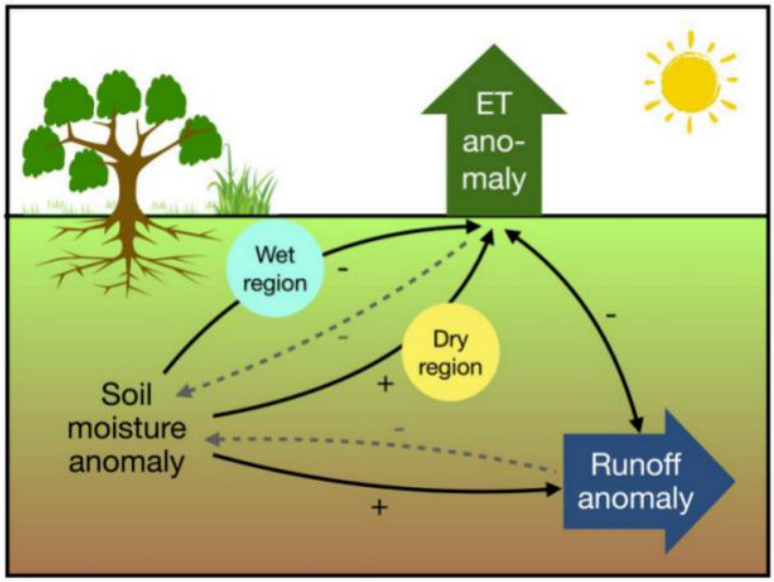

Figure 5.6. Schematic illustration of the interplay between soil moisture and surface water flux anomalies. Soil moisture drought, resulting from anomalous meteorological conditions, induces ET deficits in dry regions via vegetation water stress and reduced transpiration. In wet regions, ET is decoupled from soil moisture and enhanced by associated temperature and radiation increases. In both cases, ET anomalies feed back to soil moisture through enhancing or mitigating the initial deficit. Runoff is reduced during drought as a result of reduced soil moisture and its reduction is aggravated by ET surpluses through increases of soil moisture deficits specifically in wet regions. Dashed lines are shown for completeness as these feedback processes also exist, while our study mainly focuses on the process indicated with solid lines.

5.A Appendix

This appendix includes the supplementary materials of the presented manuscript.

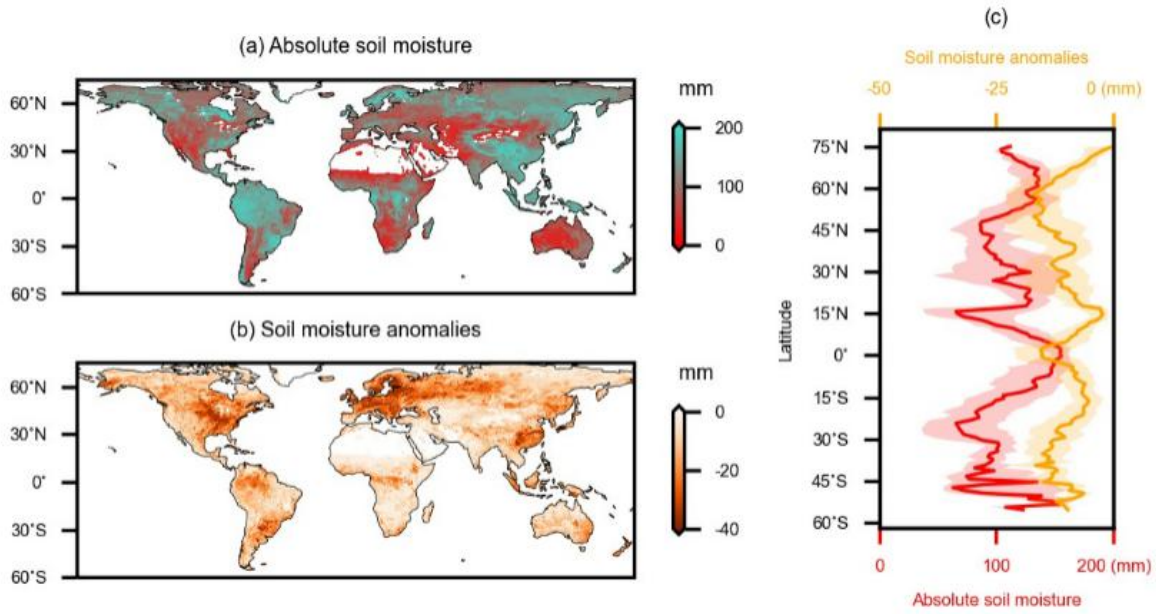

Figure 5.A1. Mapping (a) absolute soil moisture and (b) soil moisture anomalies at drought peaks. (c) Latitudinal patterns of displayed absolute soil moisture and soil moisture anomalies. In (c), the solid line and shaded areas show the median and interquartile ranges of absolute soil moisture and soil moisture anomalies across latitudes, respectively.

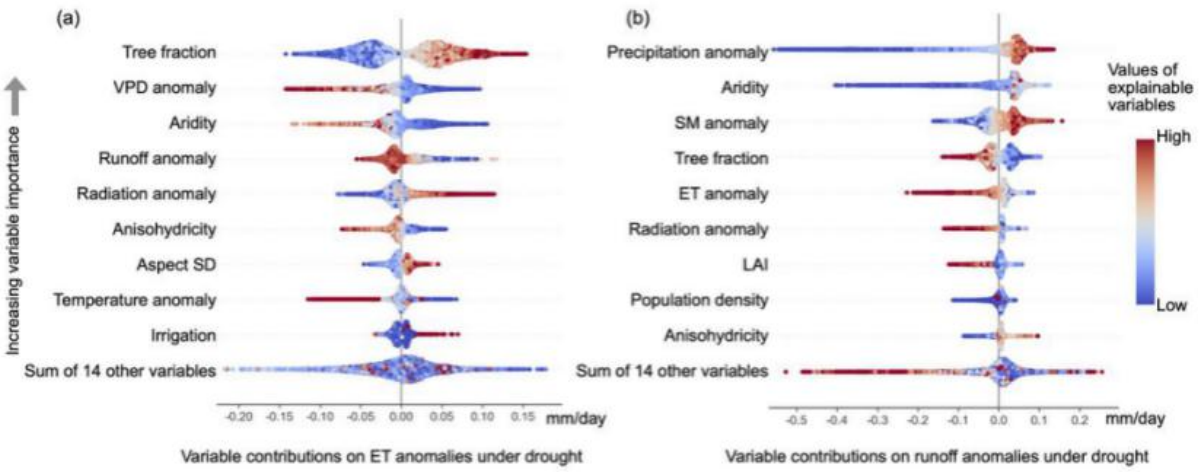

Figure 5.A2. Variables regulating (a) ET and (b) runoff drought responses. Relative importance is shown by the order of explanatory variables in the y-axis. Positive (negative) contributions of these variables on ET or runoff anomalies at drought peaks are shown in the x-axis in each row. Red (blue) colors indicate larger (smaller) values of explanatory variables. Colors combined with signs of the x-axis values indicate positive or negative relationships between explanatory variables and water fluxes drought responses, e.g., high tree fraction contributes positively to ET anomalies (red data points contribute to ET in the value range mostly between 0-0.15 mm/day) in the first row. SD denotes the standard deviation. MD denotes the median values. All plotting variables plus 14 not shown variables in each subplot are summarized in Table 5.1.

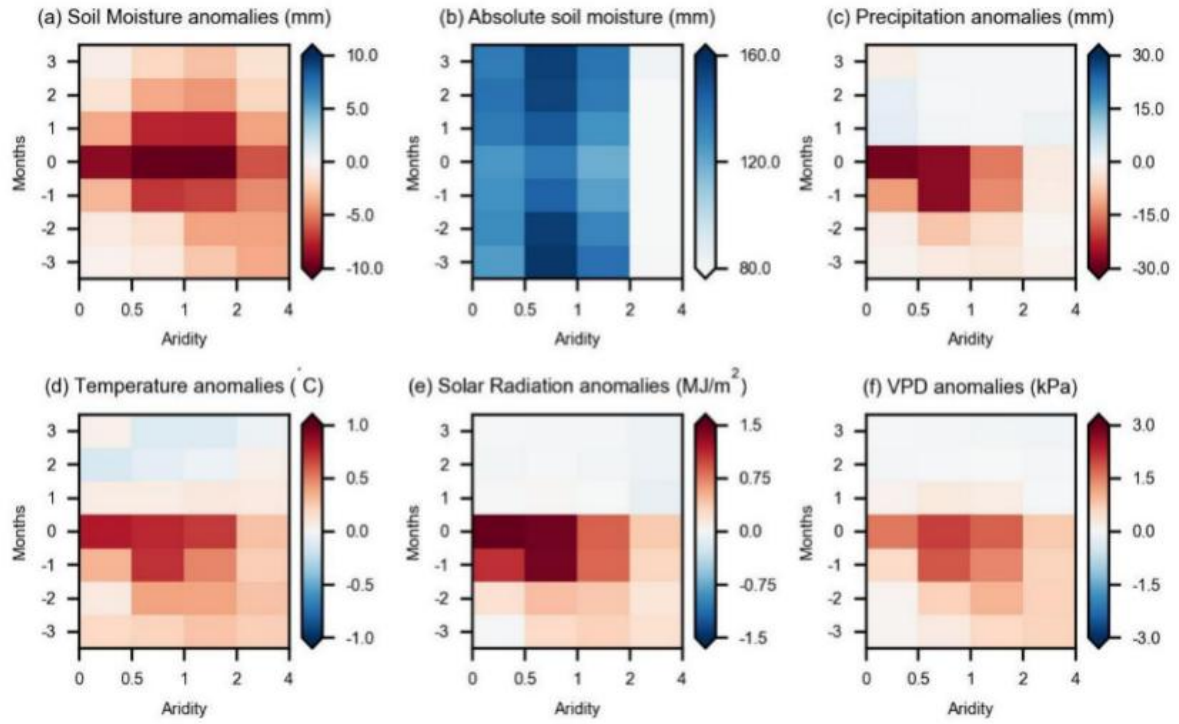

Figure 5.A3. Hydro-climate-condition changes during the course of drought from ERA5-land reanalysis grouped by aridity expressed as medians across grid cells. Month 0 denotes the drought peak months; negative months (-3, -2, -1) denote drought development periods and positive months (1, 2, 3) denote the drought recovery periods.

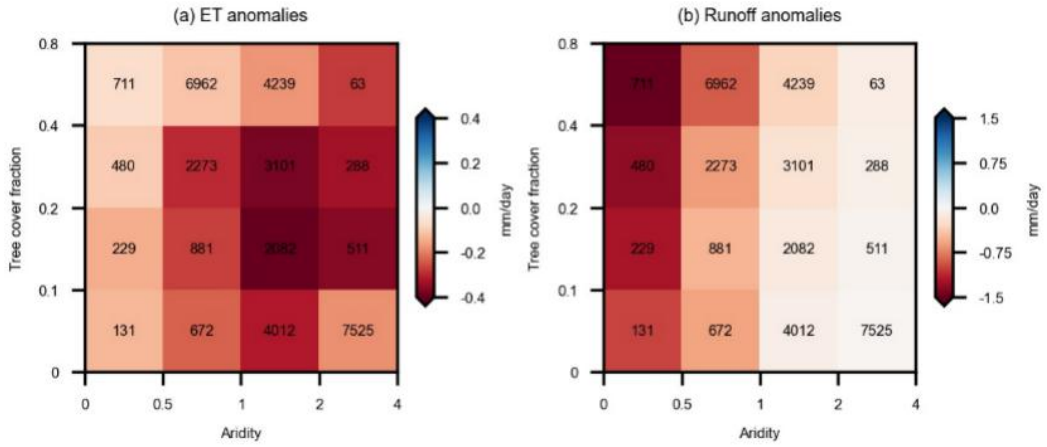

Figure 5.A4. (a) ET and (b) runoff anomalies at drought peaks expressed as the 25th percentile of value ranges across aridity and tree cover regimes. The number in each box indicates the amount of global grid cells in each regime. Aridity is computed as the ratio between long-term net radiation and precipitation, higher values indicate drier conditions. A few grid cells showing tree cover fraction over 0.8 are moved to the 0.4-0.8 group for simplicity.

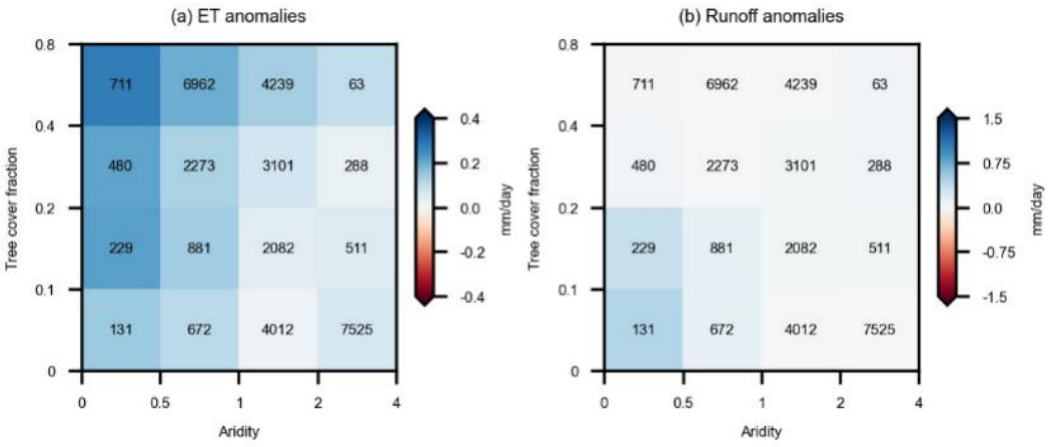

Figure 5.A5. Same as Figure 5.A1 but for ET and runoff anomalies at drought peaks expressed as the 75th percentile of value ranges across aridity and tree cover regimes.

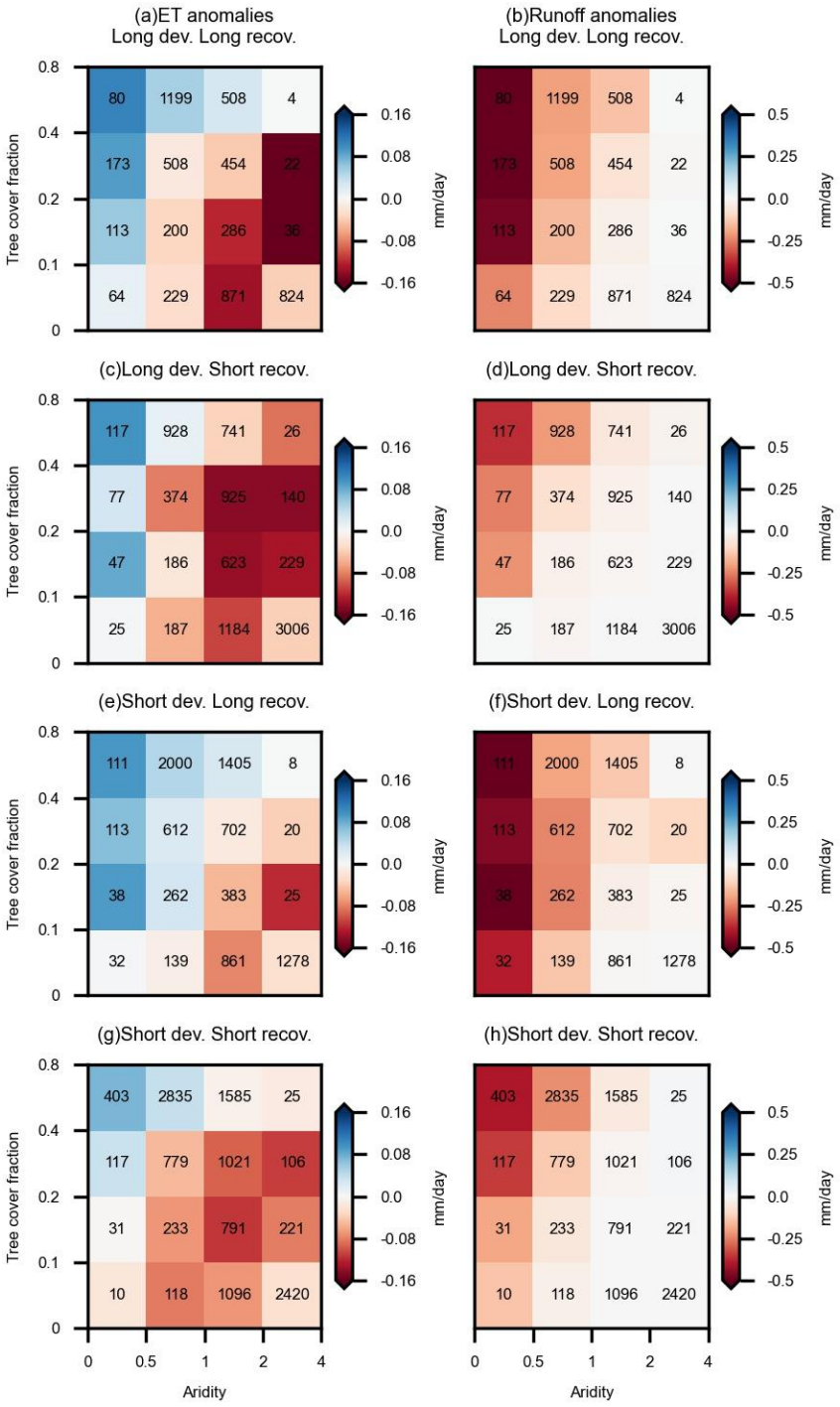

Figure 5.A6. Similar as in Figure 5.3 but grouping grid cells with different drought duration. (a, b) The duration of drought development and recovery is above the 50th percentile of all existing duration values; (c, d) The duration of drought development is above the 50th percentile of all existing duration values, while the duration of drought recovery is below the 50th percentile; (e, f) The duration of drought recovery is above the 50th percentile of all existing duration values, while the duration of drought development is below the 50th percentile; (g, h) The duration of drought development and recovery is below the 50th percentile of all existing duration values.

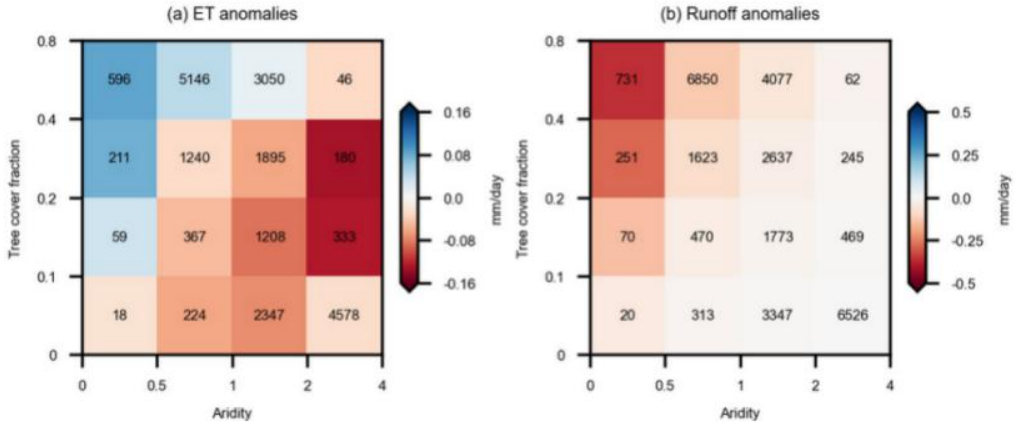

Figure 5.A7. Similar as in Figure 5.3 but for the second drought selected by the second minimum soil moisture for each grid cell where it is at least 6-month before or after the first drought.

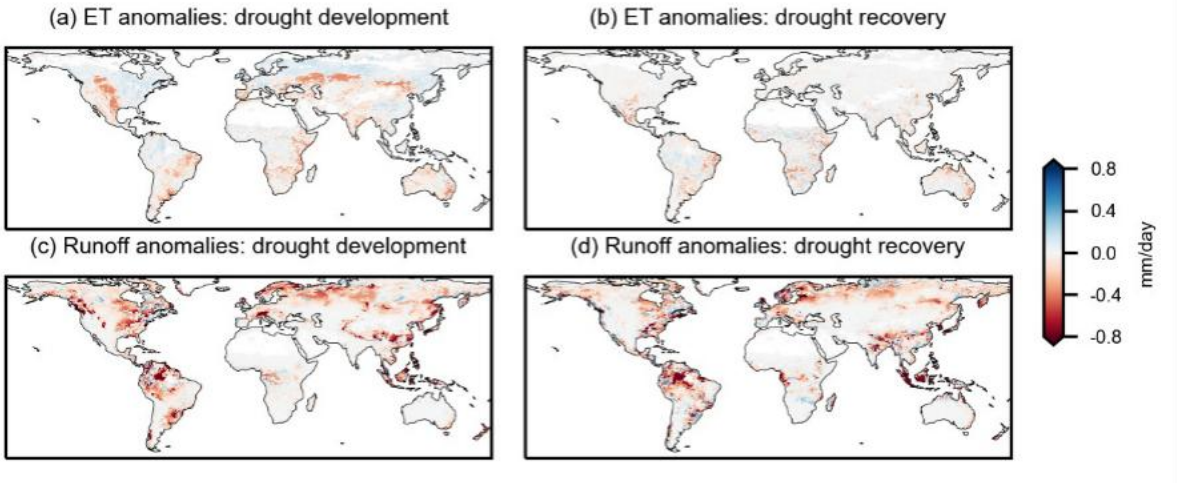

Figure 5.A8. Observed global patterns of (a) ET anomalies during drought development, (b) ET anomalies during drought recovery, (c) runoff anomalies during drought development, and (d) runoff anomalies during drought recovery.

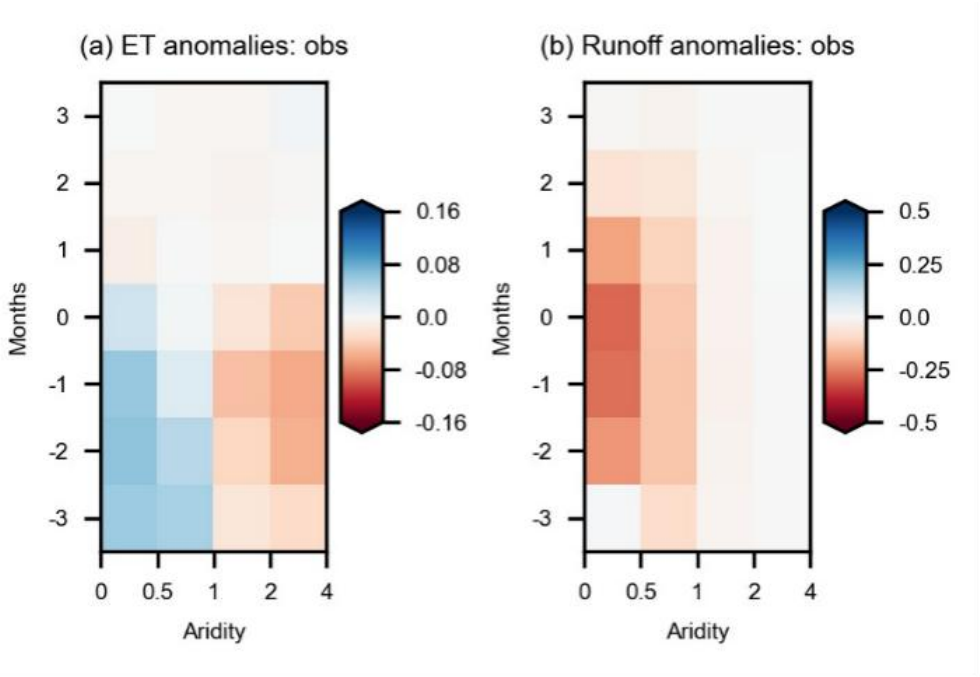

Figure 5.A9. (a) ET and (b) runoff changes (mm/day) during the course of drought detected by GRACE total water storage grouped by aridity.

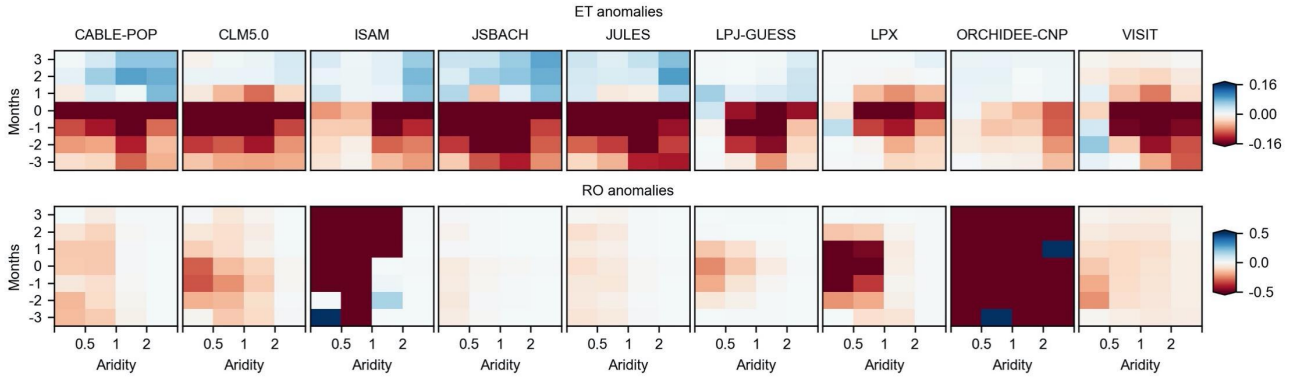

Figure 5.A10. ET and runoff changes (mm/day) during the course of drought from individual LSMs grouped by aridity expressed as medians across grid cells. Month 0 denotes the drought peak months; negative months (-3, -2, -1) denote drought development periods and positive months (1, 2, 3) denote the drought recovery periods.

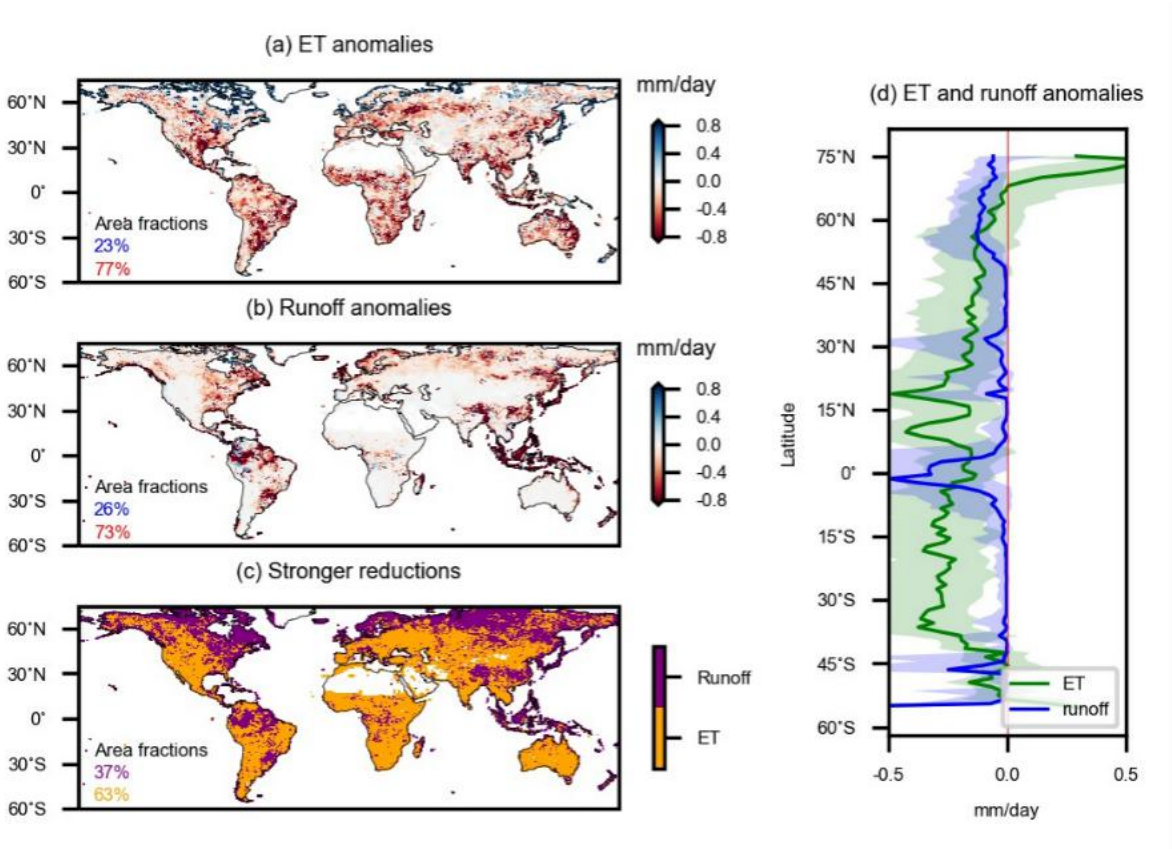

Figure 5.A11. Similar as Figure 5.2 but for multi-model median values from LSMs. (a) ET and (b) runoff anomalies during the drought peak months. (c) Variable with stronger reductions. (d) Latitudinal patterns of displayed ET and runoff anomalies. The solid line and shaded areas show the median and interquartile ranges of ET and runoff anomalies across latitudes, respectively. In (a, b), area fractions are given for positive and negative changes, respectively, and in (c) area fractions are given where ET or runoff are more reduced during peak drought.

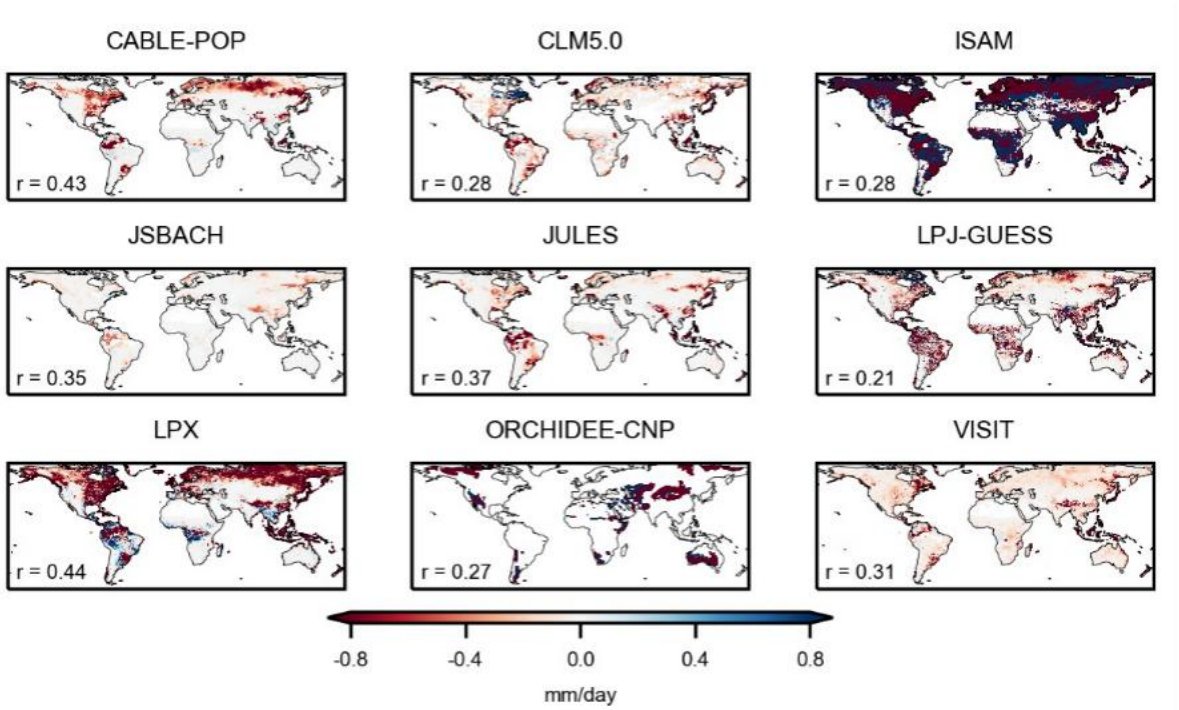

Figure 5.A12. Spatial patterns of runoff anomalies during the drought peak month from individual LSMs. The r values denote spatial correlations with observation-based results in Figure 5.2b.

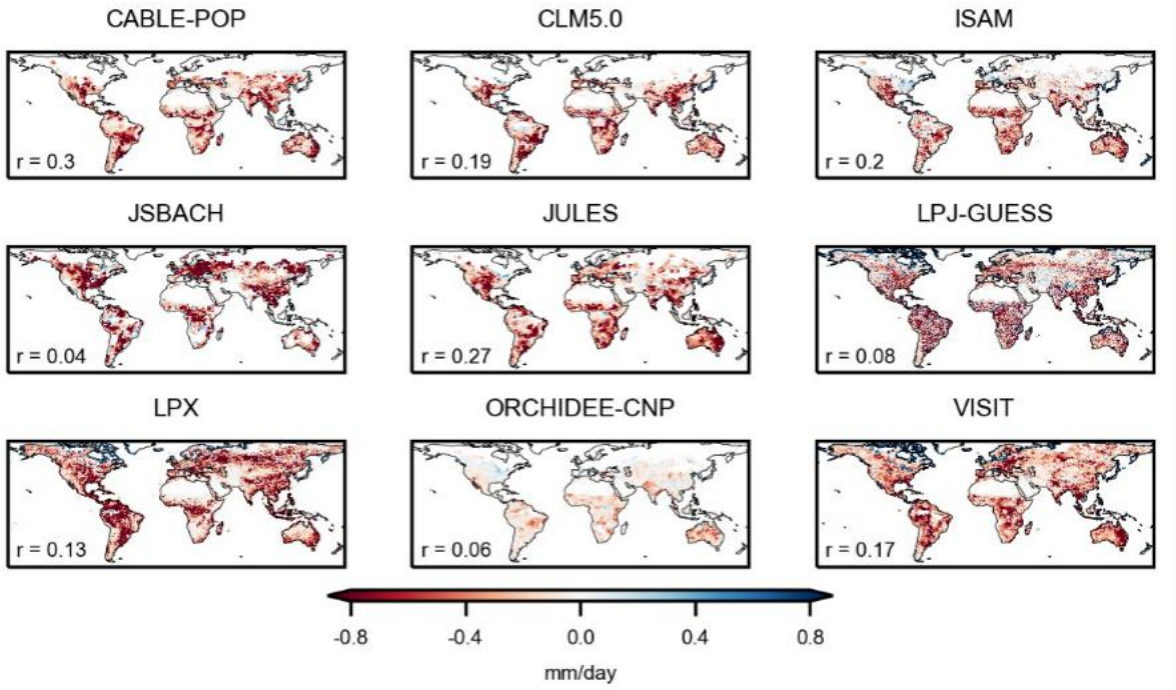

Figure 5.A13. Spatial differences in ET anomalies during the drought peak months from individual LSMs. The r values denote spatial correlations with observation-based results in Figure 5.2a.

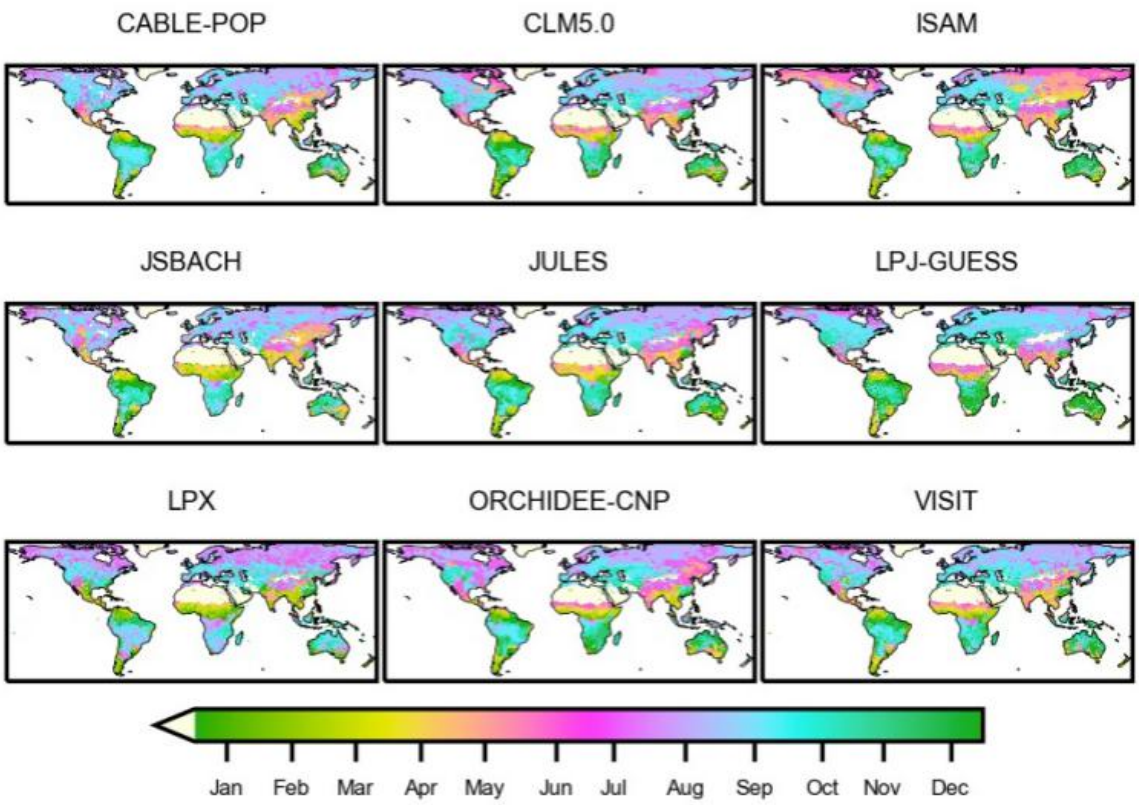

Figure 5.A14. Months-of-year of drought peaks between 2001 to 2015 as detected from monthly total-column soil moisture simulated by LSMs.

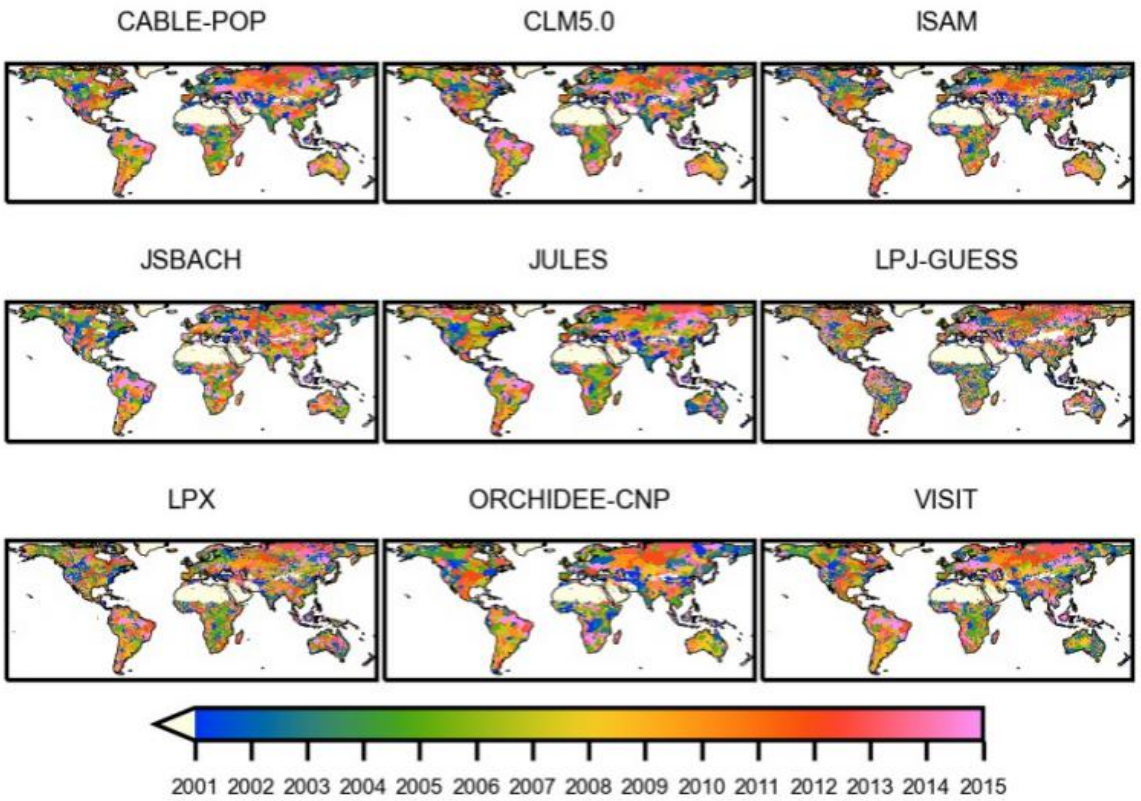

Figure 5.A15. Years of drought peaks between 2001 to 2015 as detected from monthly total-column soil moisture simulated by LSMs.

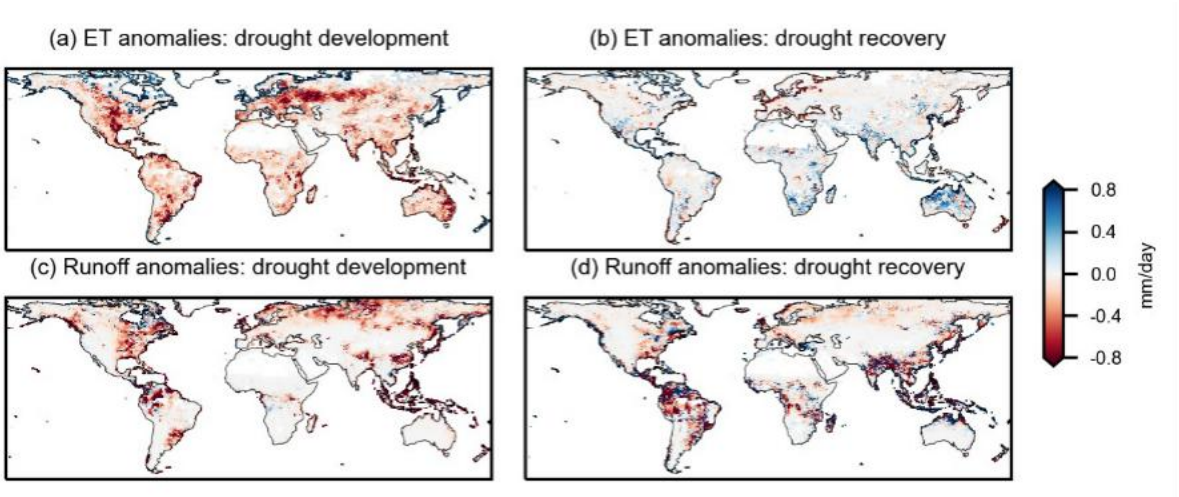

Figure 5.A16. Global patterns of (a) ET anomalies during the drought development, (b) ET anomalies during the drought recovery, (c) runoff anomalies during the drought development, and (d) runoff anomalies during the drought recovery from median values of ensembles of land surface models.

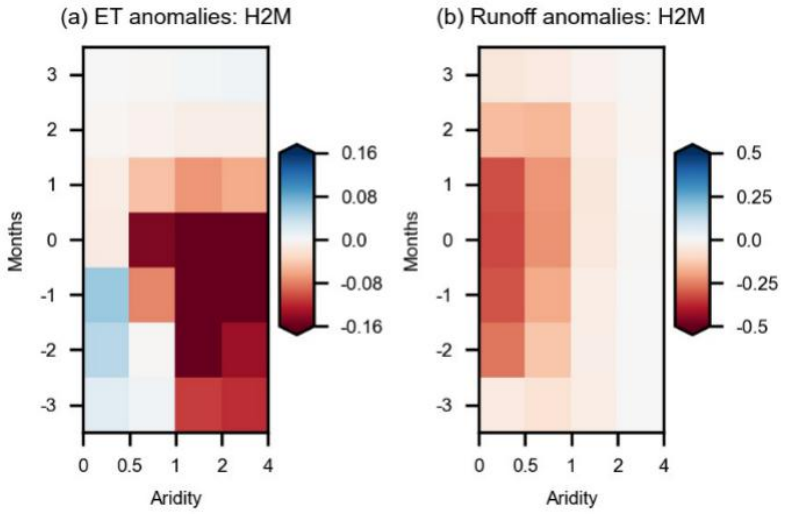

Figure 5.A17. (a) ET and (b) runoff changes (mm/day) during the course of drought from H2M hybrid modeling outputs grouped by aridity.

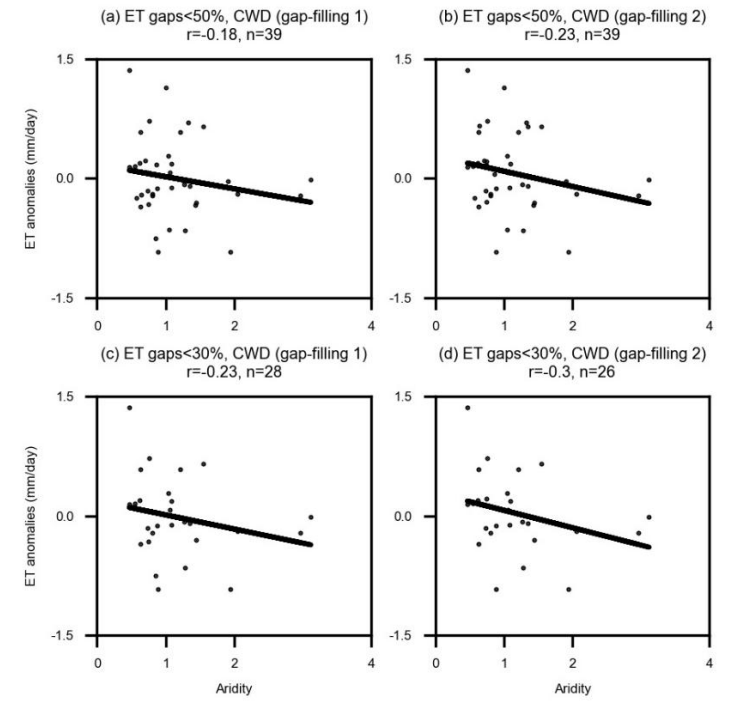

Figure 5.A18. ET anomalies measured at flux towers during drought peak months are evaluated against aridity of each measurement site. The number of sites used for each panel is indicated with n. Hourly measurements are aggregated to monthly data; results are shown from sites with less than (a, b) 50% missing ET data and less than (c, d) 30% missing ET data, which are gap-filled using ET from GLEAM only for step of calculating cumulative water deficit (CWD). Drought peaks are detected through the monthly CWD where

either gridded ERA5 precipitation is used to fill gaps (gap-filling 1) or downscaled ERAinterim precipitation is used to fill gaps using machine learning algorithms (gap-filling 2; Besnard et al. 2019).

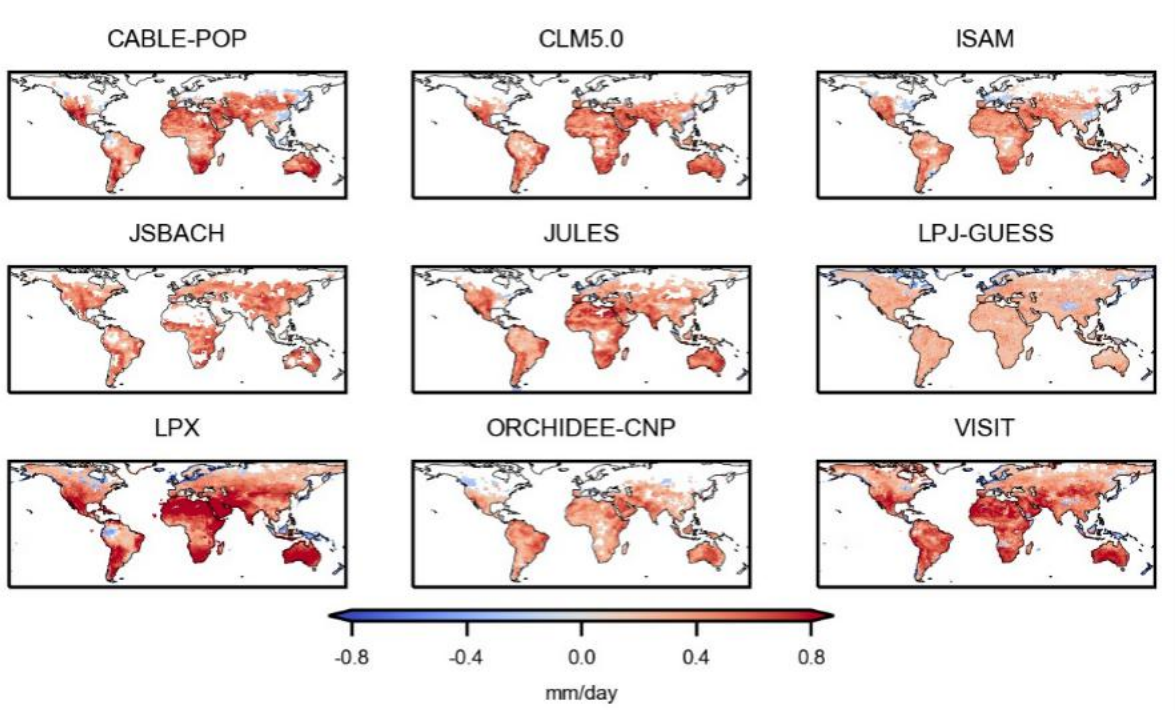

Figure 5.A19. Monthly correlations between ET and soil moisture from individual models during 2001-2015. Two-sided significance tests are done for each colored grid cell at the $p<0.05$ level as assessed with Spearman correlation.

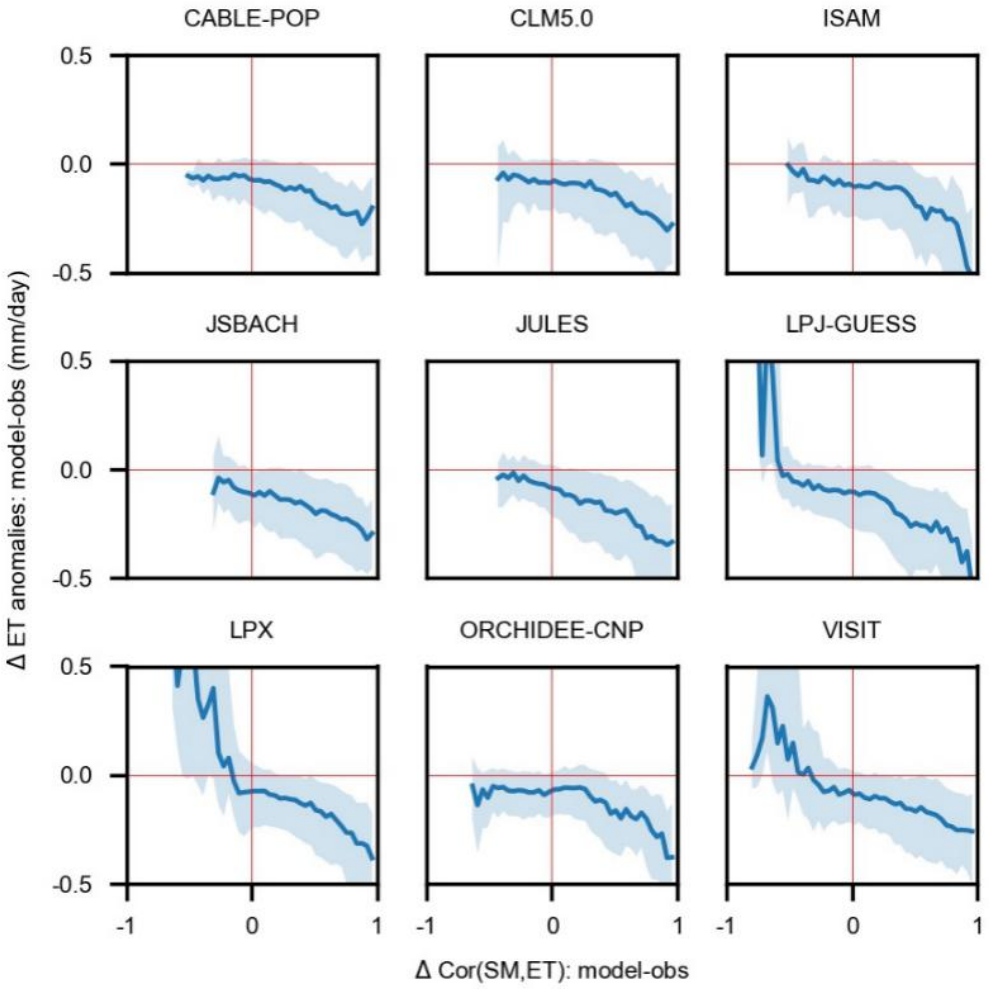

Figure 5.A20. Relationships between biases of simulated ET anomalies at drought peaks (y-axis) and the respective differences between modeled and observed ET-soil moisture monthly relationships from 2001 to 2015 (x-axis). The solid lines denote median results and shaded areas denote interquartile ranges across spatial grid cells. Cor(SM, ET) denotes soil moisture-ET correlations. Two-sided significance tests are done for included grid cells at the $p<0.05$ level as assessed with Spearman correlation.

6 Drivers of high river flows in European near-natural catchments

Abstract

High streamflow in rivers can lead to flooding, which may have severe impacts on economy, society and ecosystems. Therefore, it is imperative to understand their underlying physical mechanisms. Previous research has illustrated the relevance of several hydrological drivers, such as precipitation, snowmelt and soil moisture. However, the relative importance of these drivers compared with each other is unclear. Moreover, the role of vegetation-related drivers is not well studied. In this study, we focus on high river flows and consider a comprehensive set of potential drivers and analyze their relative importance. This is done with streamflow observations from over 250 near-natural catchments located across Europe during 1984-2007, which are matched with driver data from various observation-based sources. Not surprisingly, we find that precipitation is the most relevant driver of high river flows in most catchments. In addition, and more interestingly, we show that next to precipitation a diversity of other drivers is relevant for high flows, including shallow soil moisture, deep soil moisture, snowmelt, evapotranspiration and leaf area index. These non-precipitation drivers tend to be even more relevant for more extreme high flows. The relative importance of most considered drivers is similar across daily, weekly and monthly time scales. The spatial patterns of the relevance of precipitation, snowmelt and soil moisture for supporting high river flows are controlled by vegetation types and terrain characteristics, while climate and basin area are less important. By analyzing a comprehensive selection of drivers of high river flow in a powerful framework which accounts for co-linearities between drivers, this study advances the understanding of flood generation processes and informs respective model development.

This chapter has been submitted as:

Lam'barki, M.*, Li, W.*, O, S., Zhan, C., and Orth, R. Beyond precipitation: diversity of drivers of high river flows in European near-natural catchments, to be submitted. (* The authors contributed equally to this work.)

6.1 Introduction

Hydrological extremes have significant impacts on society and ecosystems (Kundzewicz and Kaczmarek 2000; Alfieri et al. 2020; Orth et al. 2022; Merz et al. 2021; Bradford and Heinonen 2008). For example, droughts and floods have been more devastating than other natural hazards in terms of their socio-economic damage (Barredo 2007; Naumann et al. 2015; Gao et al. 2019). Knowledge about flood generation mechanisms is key to optimize flood management and protection strategies to mitigate impacts (Merz et al. 2021).

Most major floods are characterized by a synergistic combination of atmospheric circulation patterns delivering large amounts of precipitation, and antecedent basin properties that condition the climate-runoff relationship (Hirschboeck 1991; Liu et al. 2019). Therefore, river flooding remains complex to understand as it is not exclusively linked with heavy precipitation but also depends on other factors such as antecedent soil conditions or snowmelt (Berghuijs et al. 2016; Bertola et al. 2020). For example, soil moisture excess has been shown to be the most relevant hydroclimatic variable to explain flood seasonality in Western Europe (Berghuijs et al. 2019). It has also been shown that wet antecedent soil moisture amplified the floods in the upper Danube in June 2013 (Blöschl et al. 2013).

An analysis of literature in the Web of Science (www.webofscience.com) reveals the focus of recent flood research; flood-related articles often refer to precipitation (19'556 articles during 2002-2021, see Table S1 for detailed search commands), sometimes to vegetation (7'066 articles), and relatively rarely to snow (2'813 articles) and soil moisture (2'804 articles). There are only 11 articles referring to all these drivers simultaneously. And in these 11 articles the focus is mainly on regional and/or modelling studies, and they use some drivers for explanation of the results rather than including them in the actual analysis. This leaves a knowledge gap in the joint understanding of a variety of observation-based controls of high river flows across continental-scale areas. Also, this highlights that it is important to extend the focus towards jointly investigating a multitude of potential drivers of extremes (Brunner, Slater, et al. 2021), especially in the context of climate change where increasing precipitation may not necessarily translate to increasing streamflow (Sharma, Wasko, and Lettenmaier 2018; Brunner, Swain, et al. 2021). Moreover, the consideration of several drivers across many catchments allows to analyze the spatial variability in the relevance of individual drivers of high river flows. This way, it is possible to determine which climate, terrain or vegetation characteristics influence these spatial patterns.

Moreover, flood generation processes not only vary across catchments but also vary across different time scales. Previous studies have recognized this by separating different kinds of floods such as flash floods, short rain floods, long rain floods, excess rainfall floods, rain/snowmelt floods, and snowmelt floods (Merz and Blöschl 2003; Sikorska, Viviroli, and Seibert 2015; Stein, Pianosi, and Woods 2020; Tarasova et al. 2019). This way, different levels of streamflow may result from similar amounts of precipitation or snowmelt depending on the time scale during which they hit a catchment. This is further modulated by the soil moisture

and vegetation conditions during the respective time frame. Many flood-related studies have employed a weekly time scale to infer potential flood drivers e.g. (Berghuijs et al. 2016; Blöschl et al. 2017; Stein, Pianosi, and Woods 2020; Tramblay et al. 2021; Wasko, Nathan, and Peel 2020), while the relative relevance of flood drivers at different time scales (daily, monthly) remains more unclear. This illustrates the importance of jointly considering different time scales in the analysis of high river flows, in particular because floods as rare extreme events are likely induced by a similarly rare combination of processes or drivers acting across time scales.

The objective of this study is to determine relevant drivers of high river flows in Europe across different time scales in a data-driven way. This is done by jointly analyzing the relationship of high river flows with a multitude of drivers in a comprehensive statistical framework which can account for co-linearities between drivers and for mismatches between the river flow and driver dynamics. Our selection of drivers is based on physical linkages with the land water balance and river flows, and includes vegetation-related variables such as evapotranspiration and leaf area index reflecting interception capacity. As shallow and deep soil moisture might differently affect baseflow and overland flow, we also consider soil moisture separately from different layers. Note that this analysis focuses on high river flows rather than actual floods. While there might be a strong correspondence between them, streamflow data are more accurate and abundant and hence employed in this study to characterize high flow events. Finally, we attribute the determined spatial patterns of the relevance of the main drivers of high flows to vegetation, terrain, catchment and climate characteristics in order to advance the understanding of flood generation processes and to inform hydrological model development.

6.2 Data and methods

6.2.1 Streamflow data

We use daily streamflow observations during 1984-2007 obtained from 436 river gauging stations from Stahl et al. 2010 who consolidate data from UNESCO's European Water Archive, regional and national agencies and the EU WATCH (WATer and global CHange) project. These data have been employed and validated in various previous studies, e.g. to build a European flood database (Hall et al. 2015) to empirically evaluate streamflow trends in Europe (Stahl et al. 2010), to analyze water storage sensitivity to streamflow (Berghuijs et al. 2016), and to estimate continental-scale runoff (Gudmundsson and Seneviratne 2015). Our study focuses on high flows as determined from high quantiles of daily streamflow. These extreme river flows can potentially coincide with flooding events where water overtops the river channel.

6.2.2 Hydro-meteorological and dynamic vegetation data

We use hydro-meteorological and vegetation-related variables from various sources as potential drivers of high river flows (see Table 6.1). We focus on drivers with a physical link to streamflow. As these datasets are

gridded we are matching the grid cells with the locations of the catchments from which we have streamflow measurements using the method of the nearest neighbor. Then, time series are obtained from the respective grid cell and jointly analyzed with the corresponding streamflow observations. The set of considered drivers includes for example vertically resolved soil moisture, evapotranspiration and leaf area index. The latter is included as a proxy for interception, and its daily estimates are calculated by linear interpolation of monthly values to avoid gaps related to missing daily satellite information due to cloud cover. Further, we take into account precipitation variability by calculating the ratio between the peak daily precipitation and the cumulative precipitation during the considered time scale/window (hereafter referred to as distribution of rainfall).

Table 6.1. Overview of considered drivers of high flow.

Variable	Dataset	Type	Unit	Temporal resolution	Spatial resolution	References
Precipitation and precipitation variability (see text)	E-OBS gridded data (v.20)	Interpolated from station observations	mm	daily	0.25°× 0.25°	Cornes et al. (2018)
Evapotranspiration	Global Land Evaporation Amsterdam Model (v3.5a)	Model-based	mm			Martens et al. (2016)
Snowmelt	Simple Water Balance Model	Model-based	mm			Orth and Seneviratne (2015)
Soil moisture from multiple depths (layer 1 : 0 - 7cm , layer 2: 7 - 28 cm , layer 3: 28 - 100 cm)	ERA5	Reanalysis	$m^3\ m^{-3}$			Hersbach et al. (2020)
Leaf Area Index	GEOV2-AVHRR	Derived from satellite observations	-	monthly interpolated into	0.5° x 0.5°	Verger (CNES-Theia ,

	daily	2014)

Daily snowmelt is obtained using the Simple Water Balance Model (Orth and Seneviratne 2015), using observation-based forcing data Therein, snowmelt is estimated as water equivalent using a degree-day approach; whenever precipitation occurs in combination with a temperature below threshold, snow is formed and stored until temperatures rise above the threshold where the snow is assumed to melt proportionally to the temperature difference to the threshold (Orth and Seneviratne 2013; Orth and Seneviratne 2015). The model is forced with net radiation from the ERA-5 dataset (Hersbach et al. 2020) and precipitation and air temperature from the E-OBS dataset. This is done for the grid cells corresponding to the considered 436 catchments during the study time period. Calibration parameter values are used from (Fallah, O, and Orth 2020) who calibrated the model against streamflow observations.

The data of potential drivers of high flows are mostly considered from grid cells of 0.25˚ spatial resolution such that they represent an area of approximately 625 km^2 which is roughly similar to the mean size of the considered catchments.

6.2.3 Static datasets

To attribute the identified spatial patterns of the relevance of the considered drivers, we consider a range of static data. This includes a characterization of the climate through (i) the long-term mean temperature as inferred from E-OBS data, and (ii) the aridity index as computed from the ratio of average net solar radiation (in MJ m^{-2} day^{-1}) and unit-adjusted precipitation (in mm day^{-1}) from the ERA-5 dataset. We further use the tree cover fraction which is obtained from the VCF5KYR data product and corresponds to the proportion of the ground covered by the vertical projection of tree crowns (Song et al. 2018). We also include catchment attributes such as basin area and to characterize the terrain we consider mean elevation and slope, which are obtained from a digital elevation model with an original spatial resolution of 250 m (Amatulli et al. 2018) which we aggregated to 0.25˚ spatial resolution.

6.2.4 Catchment selection

This study aims to focus on near-natural catchments with no or minor disturbance on river flow due to human intervention. We assess this through the reproducibility of streamflow dynamics by a conceptual model. Using the Simple Water Balance Model (Orth and Seneviratne 2013; Orth and Seneviratne 2015) and calibration parameters obtained from (Fallah, O, and Orth 2020), we obtain modeled runoff for each individual catchment. Then we calculate the level of agreement between modeled and observed streamflow for each catchment and disregard catchments where the agreement is weaker than a threshold score for the Nash-Sutcliffe efficiency of 0.36, which is adopted from O et al, 2020. We assume that in these catchments the streamflow dynamics are affected by non-natural processes such as irrigation or other forms of human management. Further,

catchments with more than 10% of missing runoff data are excluded.

As a result, 251 near-natural catchments from 12 countries are selected (Figure 6.1). Basin sizes range from 7 to 3780 km^2, however, with only a small number of catchments (23) with a basin size greater than 1000 km^2. These catchments are located across the European continent with fewer samples in the East and the South but nevertheless spanning a considerable climate gradient.

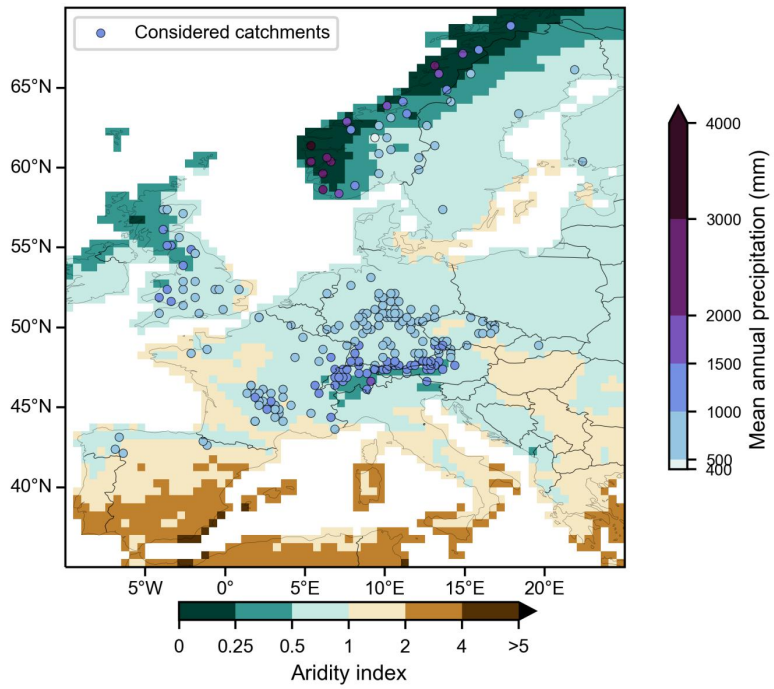

Figure 6.1. Locations and climate conditions of the considered near-natural catchments.

6.2.5 Identification of high flow events

To study potential drivers in generating high flows with different magnitudes, we select high flow events from daily streamflow records of each catchment which exceed different thresholds. In particular, we consider the 90th, 95th, 98th, 99th, and 99.5th percentiles of the entire daily streamflow time series of each catchment. For each threshold, we ensure to select high flows which are independent from one another by considering only the daily streamflow peaks which are at least one month apart from each other. The number of selected events for each catchment and percentile threshold and their corresponding magnitudes are shown in Appendix Figure 6.A1.

6.2.6 Deriving high flow drivers across time scales

After selecting high flow events, the main drivers of these events are computed for each catchment considering the variables listed in Table 6.1. First, we remove the mean seasonal cycles from both the streamflow and driver data in order to focus on anomalies. We assume that society and ecosystems in each

catchment are adapted to the usual streamflow evolution (i.e., mean seasonal cycle) and most affected by strong deviations from this. The mean seasonal cycles are determined for each variable by averaging values from the same day-of-year across all available years (e.g., the mean seasonal temperature on the 1st of January corresponds to the average of temperature the 1st of January in each individual year between 1984 and 2007). To remove random variations in the computed mean season cycle, a smoothing function of the calculated seasonal cycle is performed using a centered moving average including 5 previous and subsequent values to calculate the average at each time step.

A novel aspect of our study is the consideration of different time scales in the determination of relevant high flow drivers. For this purpose, we average the driver data anomalies across weekly (7 days) and monthly (30 days) time windows which are positioned before each high flow event. Results for the daily time scale are derived using the concurrent driver data at the day of the high flow.

6.2.7 Quantifying the importance of potential drivers of high flows

An overview of our workflow is shown in Figure 6.2. For each catchment and each high flow magnitude we consider all detected daily high flow values together with the corresponding driver anomaly values. This is done separately for each of the considered time scales. We evaluate the relevance of each considered driver using the dredge function from the MuMIn package in the R programming environment (Barton 2009), which generates numerous multivariate linear regression models considering all possible combinations of considered drivers to predict the considered high flows. These models are then ranked according to their prediction performance using Akaike's information criterion (AIC) which takes into account the goodness of fit together with the complexity (i.e., number of involved drivers) of each model. Then, we select all models of which the difference between the AIC and the AIC of the best model is less than 4 (Denissen et al. 2022). This step ensures that the influence of co-linearities between drivers on our results is minimized which could otherwise lead to inaccurate estimations of their relevance; Models with correlated drivers tend to have less beneficial AIC scores as the overlapping information content of co-varying drivers reduces the model performance normalized by the considered number of drivers.

Since drivers are selected such as they would be physically linked to runoff, we disregard regression models where the slope between runoff and evapotranspiration or leaf area index is positive, as this indicates confounding effects where e.g., precipitation increases evapotranspiration (and also leaf area index) and runoff at the same time such that evapotranspiration (and leaf area index) is not an actual driver. If all selected multivariate regression models exhibit estimated positive slopes between runoff and evapotranspiration or leaf area index, we re-compute the multivariate regression analysis for the given catchment without consideration of evapotranspiration or leaf area index as potential drivers of high flows.
As a next step, from the remaining regression models in each catchment we select models with sufficient predictive power (adjusted $R^2 > 0.3$) to ensure that the contained drivers can actually explain the high flow

variability. This also serves as a test of the agreement between the independent streamflow and driver datasets. From the remaining multivariate regression models in each catchment, we determine the most relevant driver. This is done by computing the average of the high flow variance explained by each driver across regression models, weighted by the model's AICs. Then, by comparing the fractions of high flow variance explained by each driver, we determine the most and second-most relevant drivers in each catchment.

We further apply an alternative methodology where we compute Spearman correlations between the selected high flow anomalies and the respective driver anomaly values in each catchment. Also, this analysis is done separately for each considered time scale. The most relevant driver is then determined by the highest correlation coefficient. Similar to the other methodology, positive correlations between evapotranspiration and runoff, and between leaf area index and runoff are not considered.

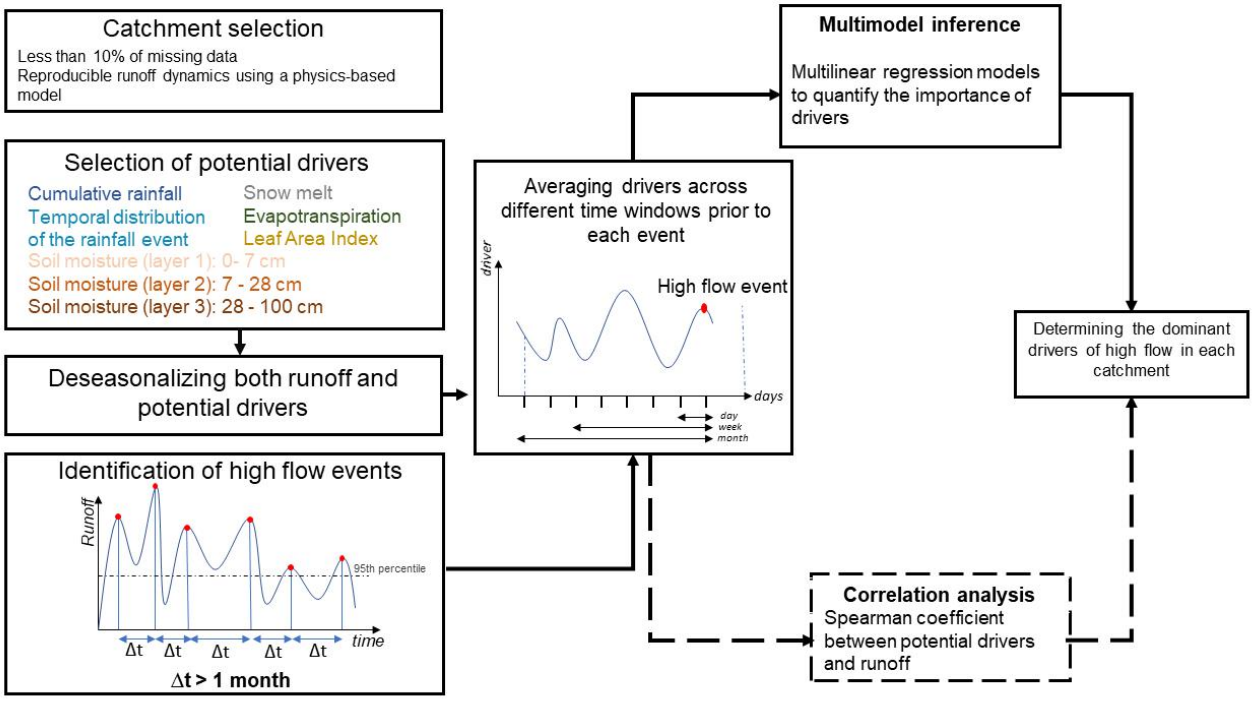

Figure 6.2. Illustration of our workflow. We use runoff data from selected catchments in conjunction with time series of potential drivers physically related to runoff. Independent high flow events are identified from the runoff time series in each catchment, and time series of considered drivers' anomalies are averaged across different time windows before each event. Finally, we investigate relationships between the averaged driver values and the high flow magnitudes using two independent methodologies.

6.2.8 Attribution analysis

We study the controls of the spatial patterns of the importance of main high flow drivers, namely precipitation, snow melt and soil moisture. This is done by correlating the driver importance from all catchments with the considered attribution controls including climate, vegetation and terrain parameters. Thereby, we use partial

correlations to mitigate the effect of co-linearities between attribution controls and to isolate the individual effect of each control. For the driver importance we apply a normalization to make them comparable across catchments by using a ratio of explained variance of the driver and the average R^2 (which is the total explained variance) of all finally considered regression models for each catchment. In the case of soil moisture, we add the explained fractions of high flow variance from all three layers.

6.3 Results and discussion

6.3.1 Determining dominant drivers of high flows across time scales and flow magnitudes

The most relevant drivers of high flows as determined with the multi-model inference approach are shown for each catchment in Figure 6.3. Antecedent precipitation is the most relevant driver in the majority of the considered European catchments. This is observed for all considered time scales, and most pronounced at the weekly time scale. This is also demonstrated by the mean explained variance of high flows given in the legend, which varies between 0.29 and 0.34. Snowmelt is overall the second most relevant driver of high flows, both in terms of the number of catchments where it is the most relevant predictor of high flows, and the relatively large explained fraction of variance of high flows. Snow melt is most relevant in the Alps, the Massif Central in France, and across (other) uplands of Central Europe, and its importance peaks at the weekly time scale. Catchments where no main driver could be determined as no regression model was left after all filtering steps (in particular after the $R^2 > 0.3$ filtering) are shown in gray.

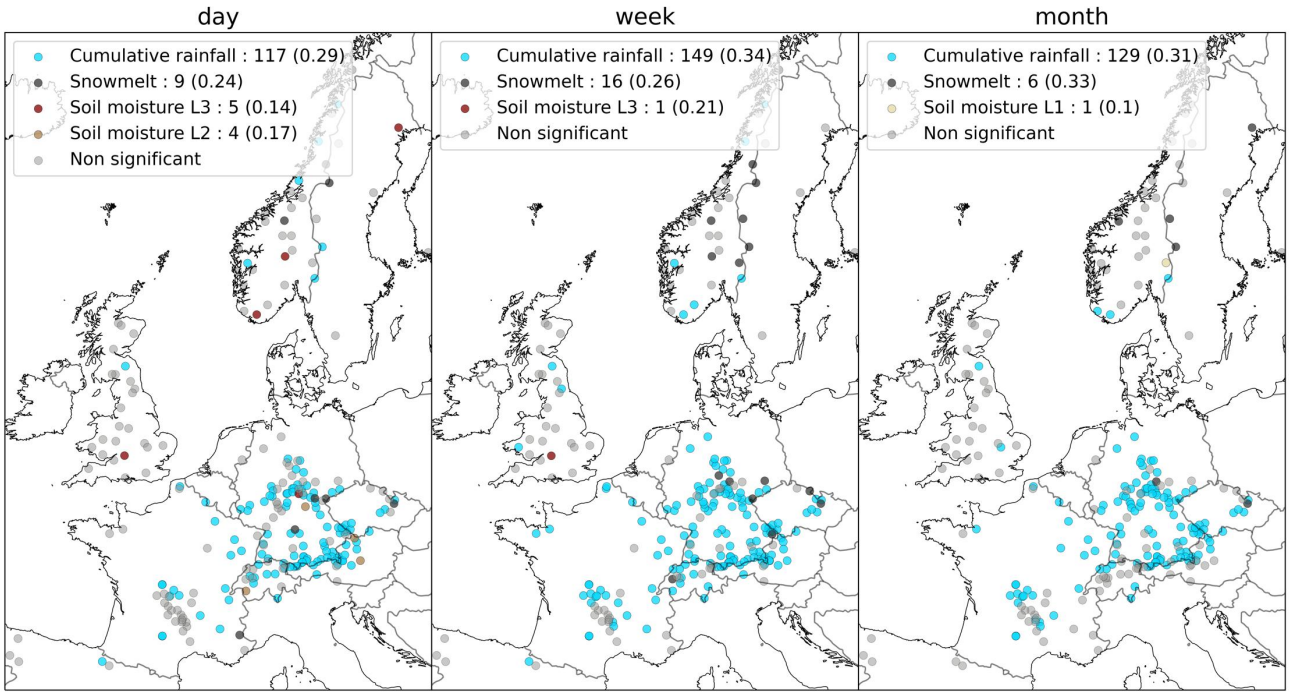

Figure 6.3. Illustration of the most influential driver of high flows in each catchment as shown through color-coding. In each catchment all independent high flow events exceeding the 90th percentile are considered, in the three time scales (daily, weekly, monthly) that precede the events. Statistics in the legend indicate the number of catchments where each driver is most influential, and the respective mean fraction of explained high flow variance across these catchments. Non-significant results correspond to the catchments where the average R^2 of the models is below 0.3 or if runoff in all the models has a positive relationship with evapotranspiration or leaf area index.

In addition, we also investigate extreme high flows exceeding the 95th, 98th and 99th percentile (Appendix Figure 6.A2). The results are similar to the findings in Figure 6.3 with antecedent precipitation is the most relevant driver of high flows. However, there are more catchments with most relevant drivers of high flow other than precipitation such that the diversity of most relevant drivers is overall enhanced towards more extreme high flows. For example, soil moisture and the distribution of the precipitation across the considered time scale emerge as most relevant drivers in some catchments.

Another interesting result is that the explained variance of high flows of the dominant drivers is similar across time scales. This indicates that studying drivers at different time scales is relevant to understand high flow dynamics, whereas daily, weekly and monthly time scales are similarly important. Multilayer soil moisture has a higher explained variance for events of the 99th percentile, suggesting the soil water storage is more relevant for the more extreme high flow generation.

The spatial patterns of most important drivers in Figure 6.3 are confirmed with a methodology based on correlations between high flows and drivers (see Section 6.2.7) as shown in Appendix Figure 6.A4. While the

obtained correlations are highly significant for the results of the 90th percentile high flow threshold, this is less the case for the higher thresholds as the number of considered high flow events decreases (Appendix Figure 6.A4).

Although the most important high flow driver, antecedent precipitation, is consistent across many catchments, high flow magnitudes, and time windows, the second-most important drivers are generally more diverse, as illustrated in Figure 6.4. This diversity is even increasing towards more extreme events (Appendix Figure 6.A5). This indicates the difficulty to understand extreme high flow generation, and highlights the essentials of considering multifaceted controls of high flow generation. Interestingly, Figure 6.4 also shows that evapotranspiration and surface soil moisture become more relevant towards longer time scales while deep soil moisture gets less relevant. In the case of evapotranspiration this is probably related to the fact that this becomes larger when aggregated across longer time periods. The shift in the relevance of shallow versus deeper soil moisture with increasing time scales could be explained with stronger precipitation events at short time scales which might saturate the surface soil such that the soil moisture in deeper layers becomes more relevant to buffer or enhance the resulting streamflow. By contrast, at longer time scales the precipitation is typically distributed to several events which might not be sufficient to saturate the surface soil such that this layer then determines more which fraction of the precipitation contributes to streamflow.

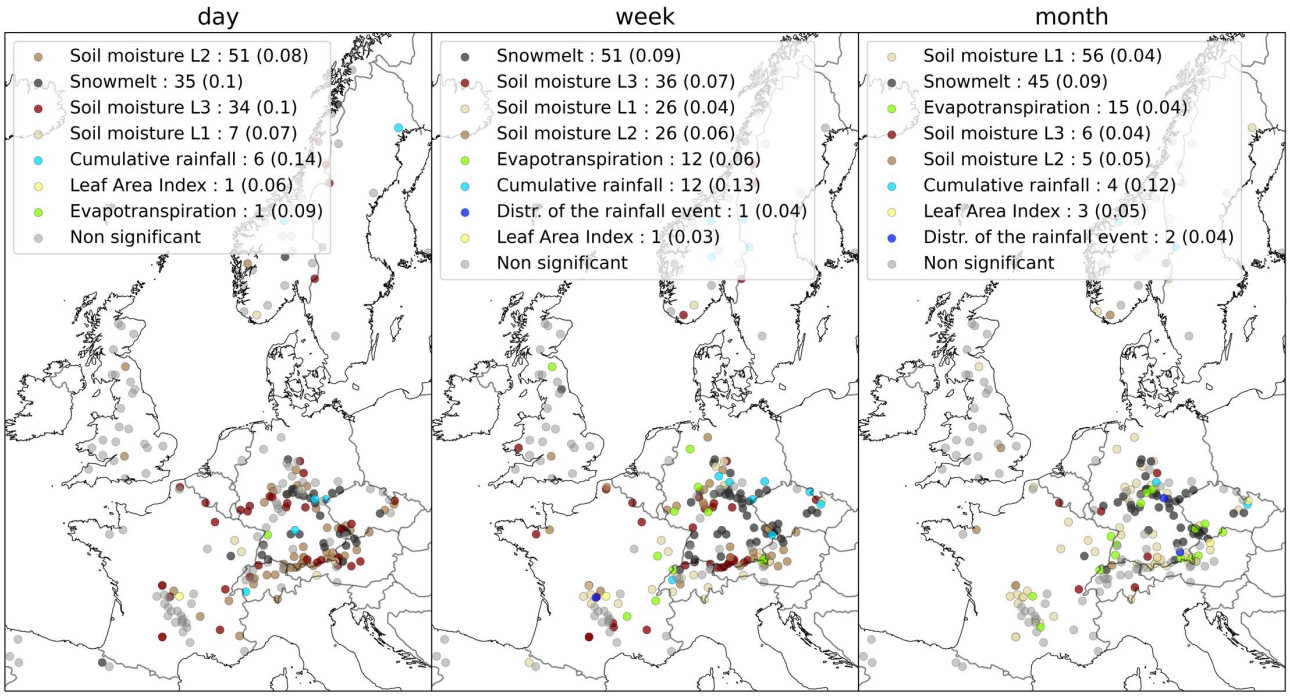

Figure 6.4. Illustration of the second most influential drivers of extreme high flows exceeding the 90th percentile. Similar format as in Figure 6.3.

Next, we summarize the results of the most and second-most relevant drivers of high flows across time scales and high flow magnitudes in Figure 6.5. Results are shown for both considered methodologies of determining

the most relevant high flow drivers. Both methods demonstrate that antecedent precipitation is the dominant driver of high flows across all considered time scales and flow magnitudes. Snowmelt is overall the second most important driver. Note that as soil moisture layers are considered separately the overall relevance of soil moisture might be underestimated in Figure 6.5. However, the results in Figure 6.3 and Appendix Figure 6.A3 in terms of the number of catchments where snow melt or any soil moisture layer is the most relevant high flow driver do not indicate a strong bias in the results of Figure 6.5.

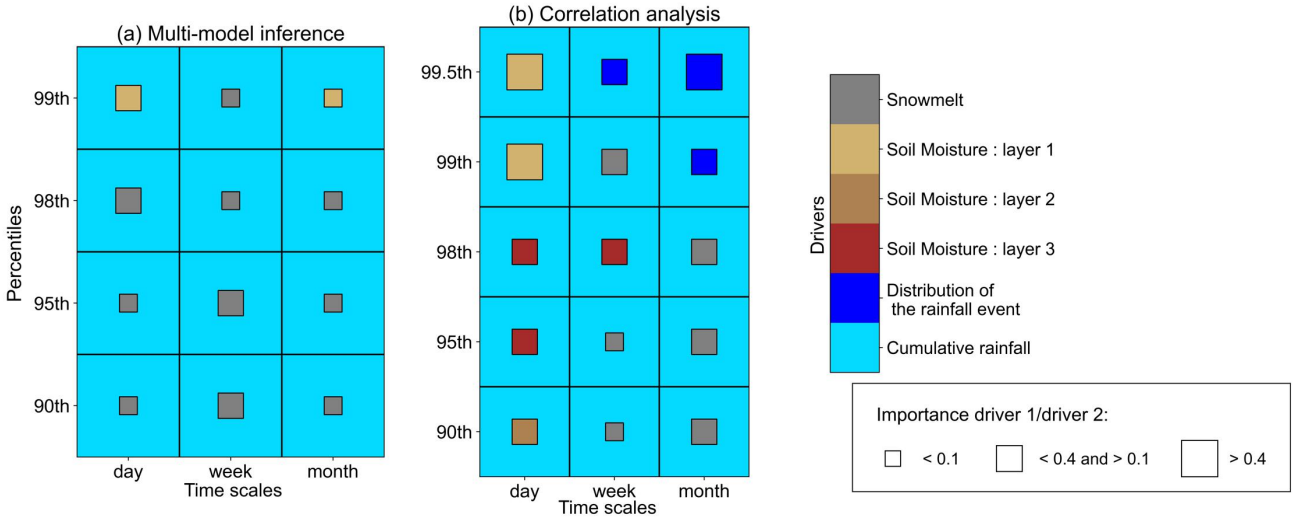

Figure 6.5. Summary of our results. Box colors indicate the most influential drivers across time scales and high flow magnitudes, as determined from the number of catchments where a particular driver is found to be most influential. Second most relevant drivers are shown within each box through color-coding. Results shown for (a) multi-model regression inference methodology and (b) an independent correlation analysis. Note that results for the 99.5th percentile could not be computed for the multi-model inference approach due to the low number of such extreme high flows.

The correlation analysis generally supports the multi-model inference results, even though soil moisture is found as a second-most important driver for many high flow magnitudes at the daily time scale instead of snowmelt. The correlation analysis allows to compute results for very extreme high flows exceeding the 99.5th percentile while the multimodel inference method does not detect any suitable regression models which can be fitted for such few remaining high flow events in most catchments. For such extreme high flows, the distribution of rainfall and soil moisture become more relevant in a greater number of catchments, even though still less catchments where precipitation is found to be most relevant. These results are, however, not statistically significant due to the low number of considered extreme high flows. Our results therefore confirm previous studies which have demonstrated that river floods are usually generated by the interactions between event precipitation, antecedent soil wetness, and snowmelt 16/01/2023 15:14:00 . The current study additionally shows that a multitude of drivers other than precipitation become increasingly relevant towards more extreme high flows.

6.3.2 Attribution analysis

We furthermore study the controls of the spatial variations of the relevance of main high flow drivers. Figure S6 shows the relevance of precipitation in each catchment, soil moisture and snowmelt. As described in Section 6.2.8 we consider climate, basin and terrain attributes as potential controls in this context. Figure 6.6 provides the results and shows that tree over fraction is overall most important in explaining spatial patterns of the relevance of precipitation, snowmelt and soil moisture for high flows. It remains also an important control when considering only the tree cover fraction, the elevation and the slope (Appendix Figure 6.A7).

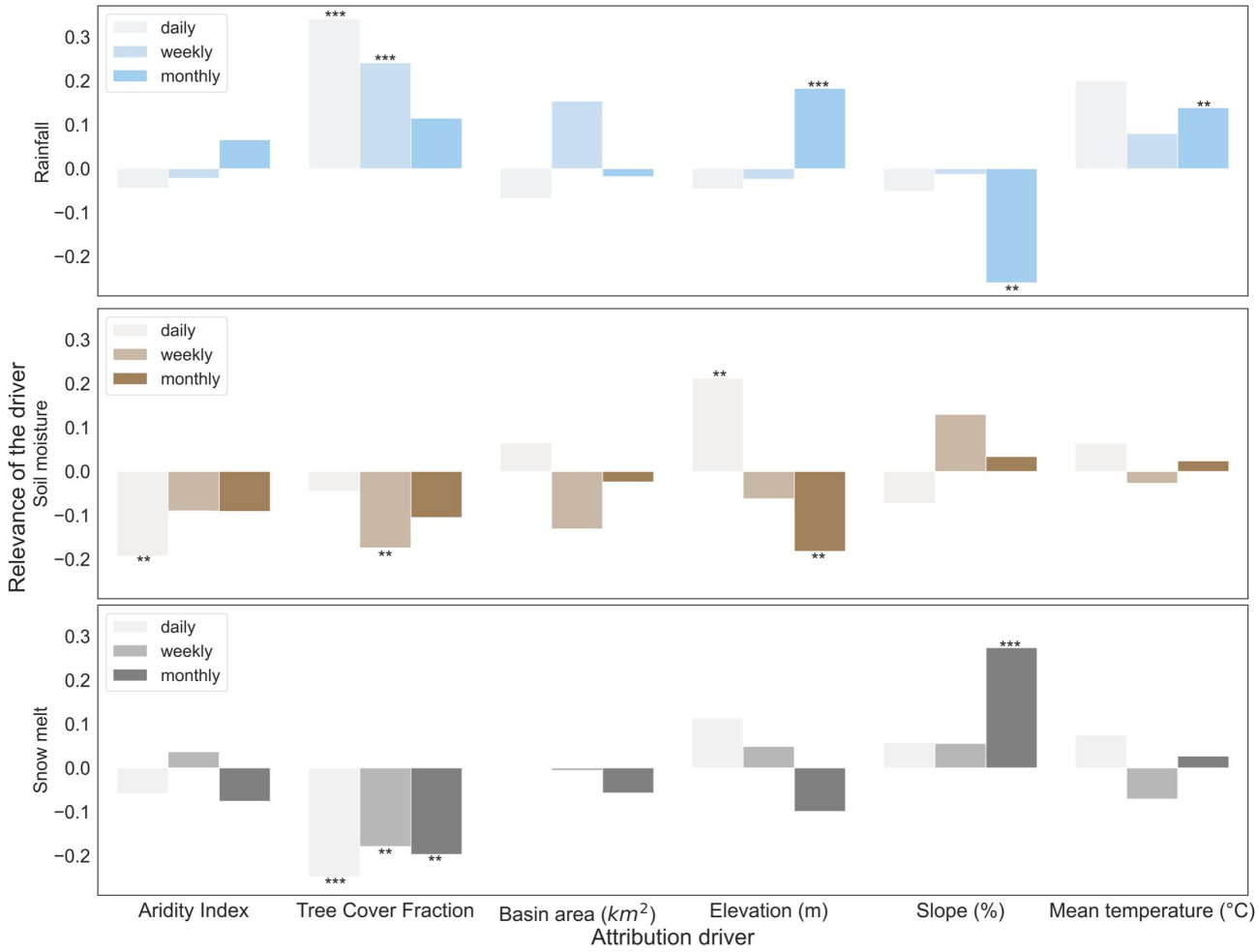

Figure 6.6. Attributing the spatial patterns of the relevance of considered drivers of high flows to climate, vegetation and terrain characteristics for high flow events exceeding the 90th percentile. Vertical axis corresponds to the partial correlation between driver relevance and each attribution variable. Results are shown for the considered different time scales. Stars on top of the bars indicate statistically significant partial correlations (** : p-value <0.05 , *** : p-value < 0.005).

In more tree-covered regions the relevance of precipitation for causing high flows tends to increase while that of snowmelt and soil moisture tends to decrease. This might be related to litterfall which impedes the infiltration of water into soils and hence increases the fraction of precipitation contributing directly to

streamflow, while the contributions of soil moisture and snowmelt are decreased. We find an increased relevance of precipitation in warmer catchments which is probably related to the higher rain-to-snow ratio. By contrast the results for slope and elevation are hard to interpret and further research, potentially with more diverse catchments offering more variability in terms of slope and elevation allowing to derive more informative and significant results. In general, the results for precipitation are opposite to those of snowmelt and soil moisture, indicating that whenever a considered control favors precipitation this comes at the expense of the relevance of snowmelt and soil moisture, and vice versa.

6.3.3 Limitations

While we test the robustness of our results with two independent methods, the main findings have to be seen in the light of some limitations related to our data and methodology. First, there is a spatial mismatch between the catchment area and the grid cells from which the driver data is derived. While there is an overlap between the different regions, the time series do not exactly represent the same areas. However, in most catchments the employed driver data corresponds sufficiently well with the observed high flow dynamics as tested with the R^2 threshold in the multimodel inference approach such that there seems to be a sufficient level of agreement between the considered data streams. This could in principle be different for smaller versus larger catchments but the attribution analysis indicated that the results do not vary according to catchment size.

Second, it is possible that trends in the considered data streams could influence our results and induce shifts in the relevance of high flow drivers over time. However, the visual inspection of the streamflow time series in many catchments does not indicate trends in our target variable such that this should not affect our results.
Third, even though we are considering a comprehensive set of potential drivers of high river flows there might be more influential drivers representing alternative processes which are not captured by our analysis. This applies for example to groundwater which we could not include here due to a lack of sufficient data.
Finally, the attribution analysis is somewhat limited by the fact that only European catchments are considered here such that the spatial variability of climate, vegetation and terrain characteristics is rather low. Future research focusing on larger sets of catchments with more diversity in these aspects could provide more significant insights into the spatial variations of the relevance of main flood drivers.

6.4 Conclusion

This study provides a quantitative mapping of the importance of drivers of high river flow in near-natural European catchments. We consider a comprehensive set of drivers, and use a powerful statistical approach based on multiple multivariate regressions to determine their relative importance across time scales and high flow magnitudes. In agreement with previous knowledge and literature, we find that antecedent precipitation anomalies are the most important driver of high flows in most catchments. In some other catchments snowmelt and soil moisture are found to be the most relevant drivers. Moving beyond the state of the art we

find a remarkable diversity of second-most important drivers across Europe. This includes vegetation-related drivers such as evapotranspiration. Overall, observed daily high flow dynamics can be explained similarly well using drivers from the daily, weekly and monthly time scales. This indicates that mechanisms acting at different time scales contribute similarly and jointly to high flow events. While the most important drivers are similar across time scales, we find interesting variations for the second-most relevant drivers where evapotranspiration and surface soil moisture become more relevant towards longer time scales while deep soil moisture gets less relevant. Furthermore, for more extreme high flows we find a greater diversity of most important drivers across the considered catchments. Therefore, while moderate high flows are strongly associated with antecedent precipitation, the most extreme events can only be fully understood when considering a comprehensive selection of drivers. The spatial variations in the relevance of considered high flow drivers can be attributed to vegetation and terrain characteristics of the catchments. Our findings thereby illustrate that it is beneficial for flood monitoring and prediction to jointly consider several time scales and a comprehensive set of drivers physically related to streamflow dynamics. This way, identifying the relative importance of high flow generating mechanisms can reveal regional patterns of causes of floods in Europe and inform future model development. More recent model developments have focused on incorporating more processes into models. Our results based on multiple independent datasets provide an improved benchmark for evaluating all relevant hydrological processes in the model in a comprehensive manner. Further, given the relatively weak link between future precipitation and runoff changes, increasing attention has been paid to non-precipitation flood drivers (Brunner, Slater, et al. 2021). In this context, the framework introduced in this study provides a starting point to a data-driven investigation of possible future changes in high flow generation drivers and mechanisms globally to efficiently advance flood adaptation and resilience.

6.A Appendix

This appendix includes the supplementary materials of the presented manuscript.

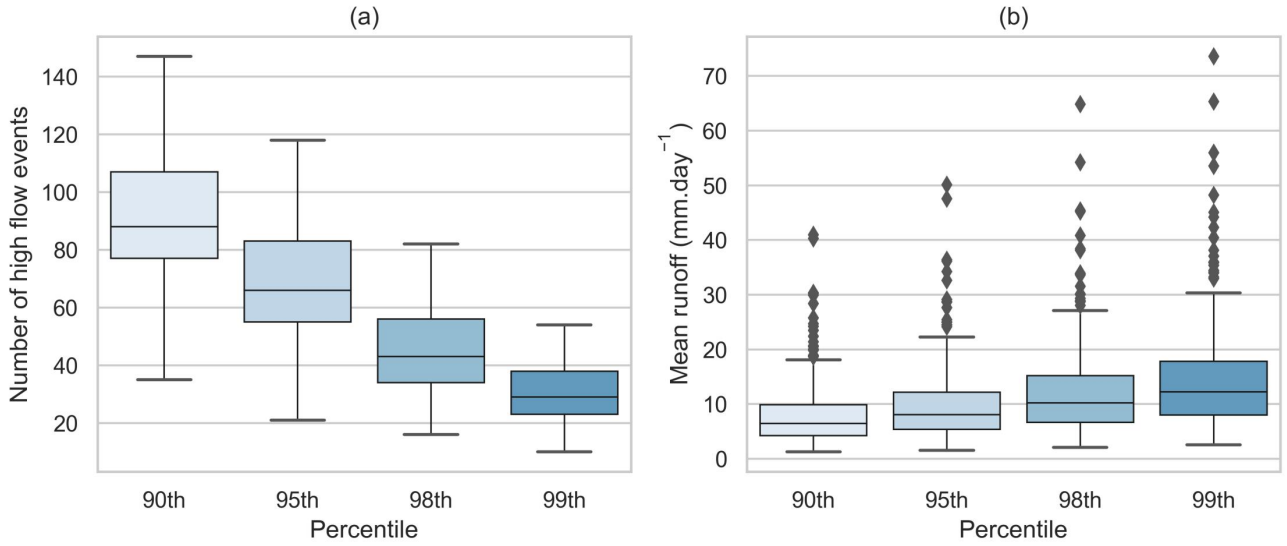

Figure 6.A1. Boxplots of the number of high flow events for (a) each catchment and percentile and (b) their corresponding runoff magnitude.

(a) Dominant driver for different time scales preceding the high flow event (Q > 95th percentile)

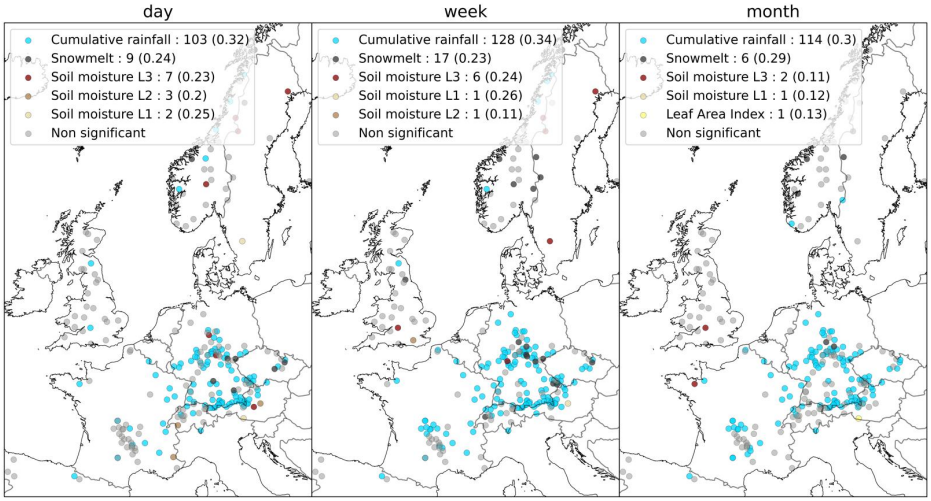

(b) Dominant driver for different time scales preceding the high flow event (Q > 98th percentile)

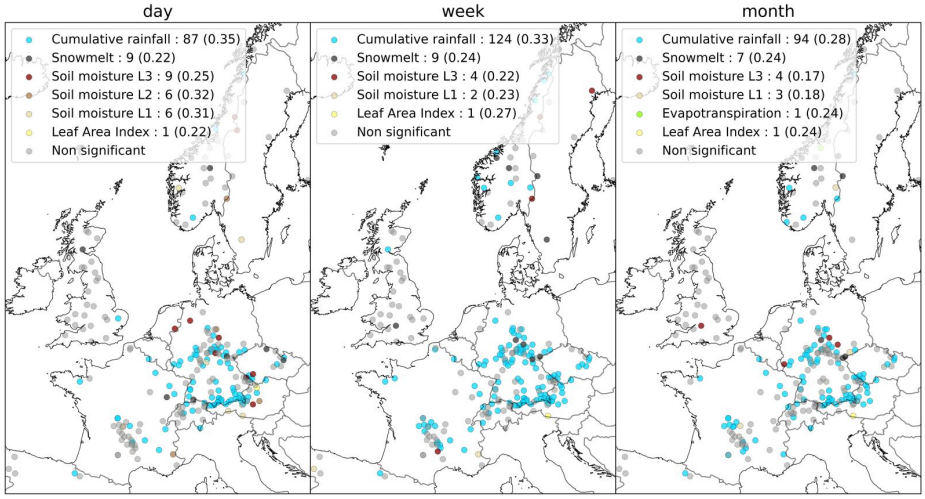

(c) Dominant driver for different time scales preceding the high flow event (Q > 99th percentile)

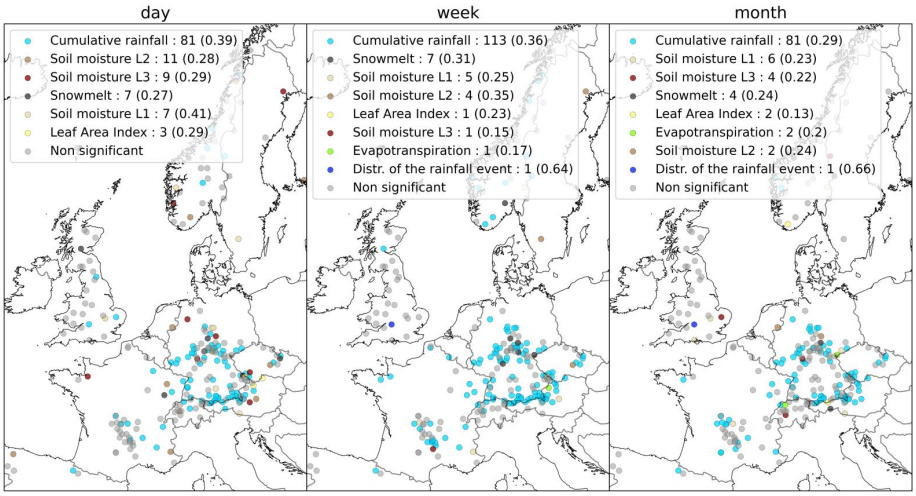

Figure 6.A2. Illustration of most influential drivers of extreme high flows exceeding the (a) 95th, (b) 98th and (c) 99th percentile using the multi-inference method.

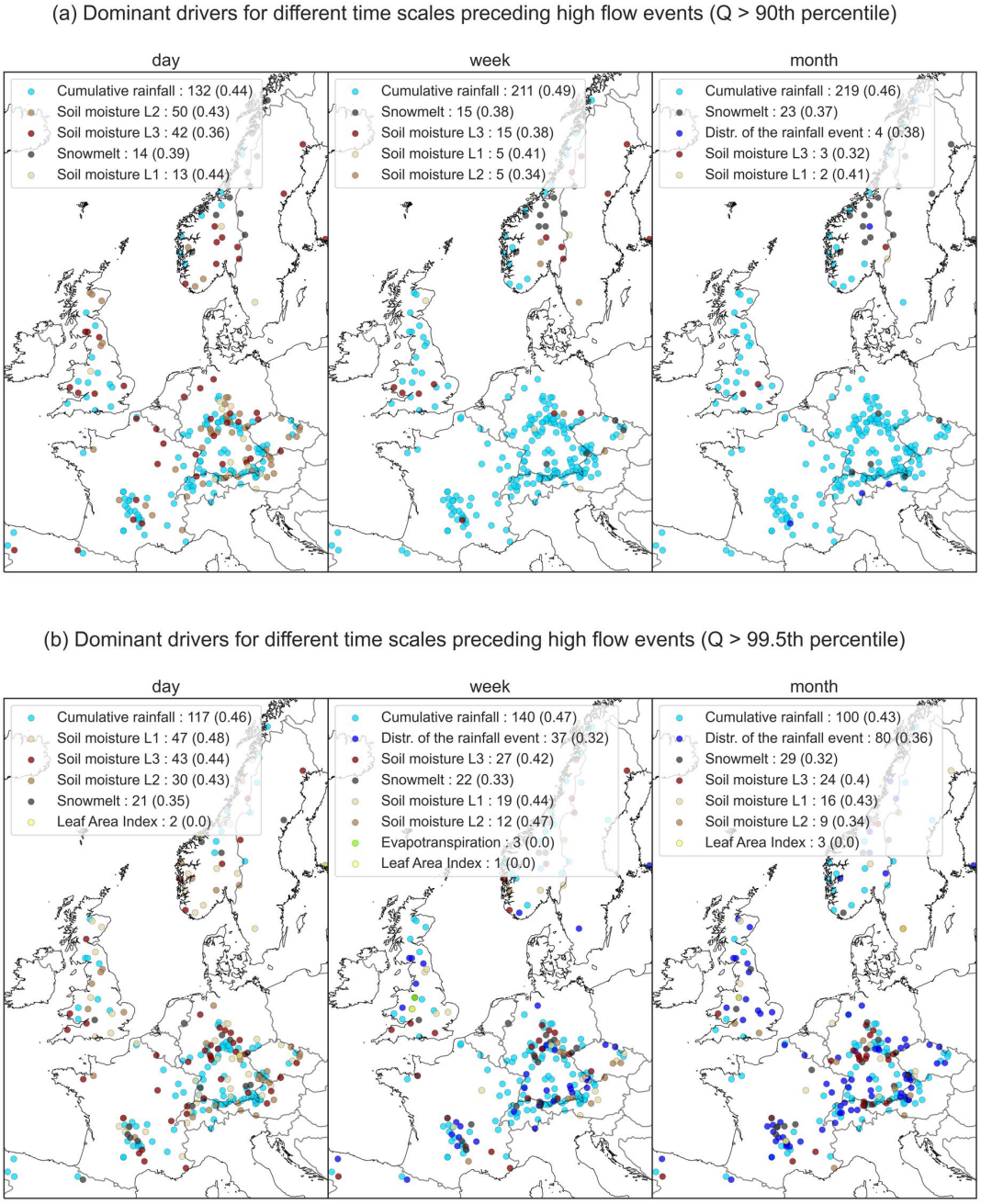

Figure 6.A3. Illustration of most influential drivers of extreme high flows exceeding the (a) 90th and (b) 99.5th percentile using the correlation analysis method.

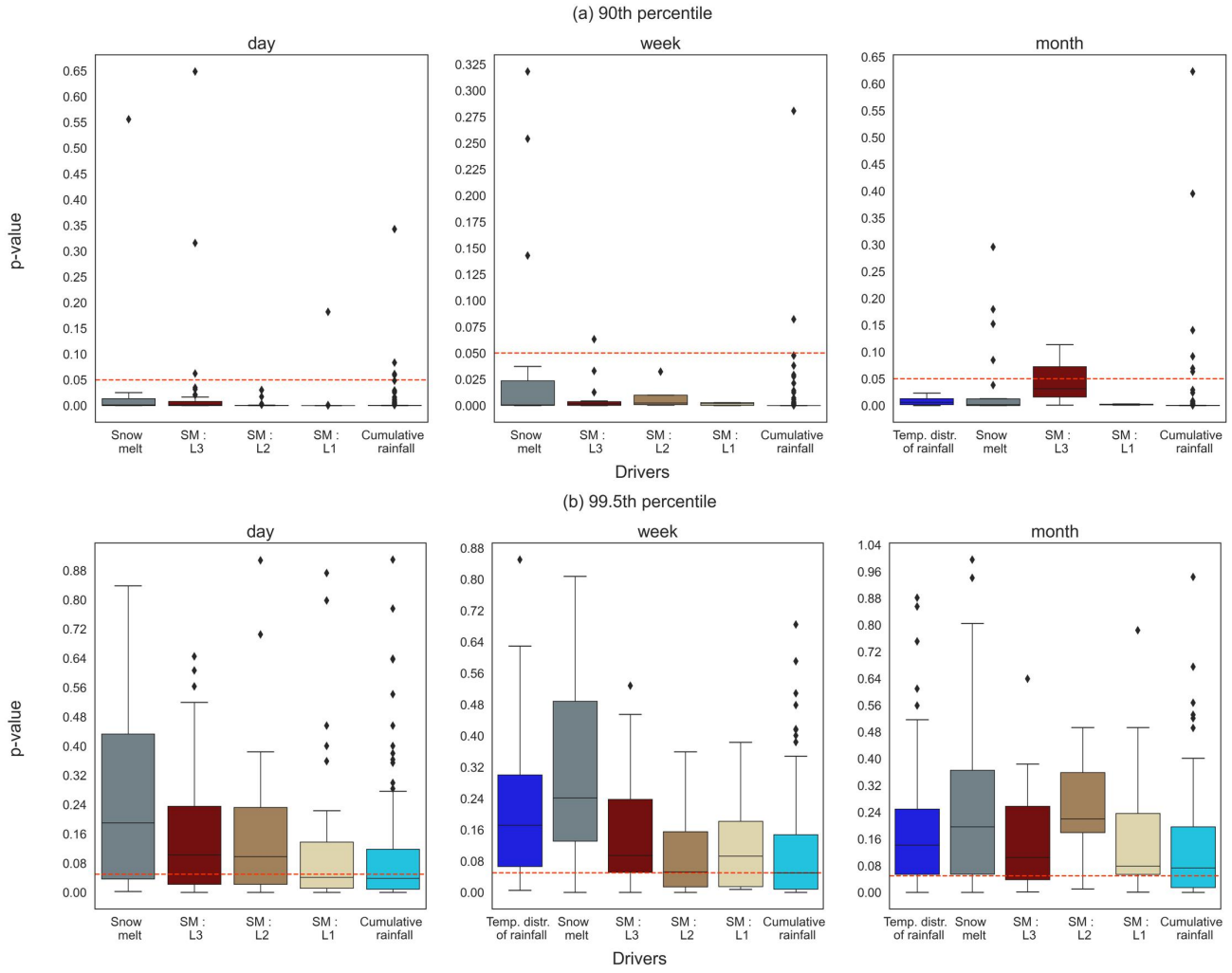

Figure 6.A4. Significance of the correlation analysis across different percentiles and drivers.

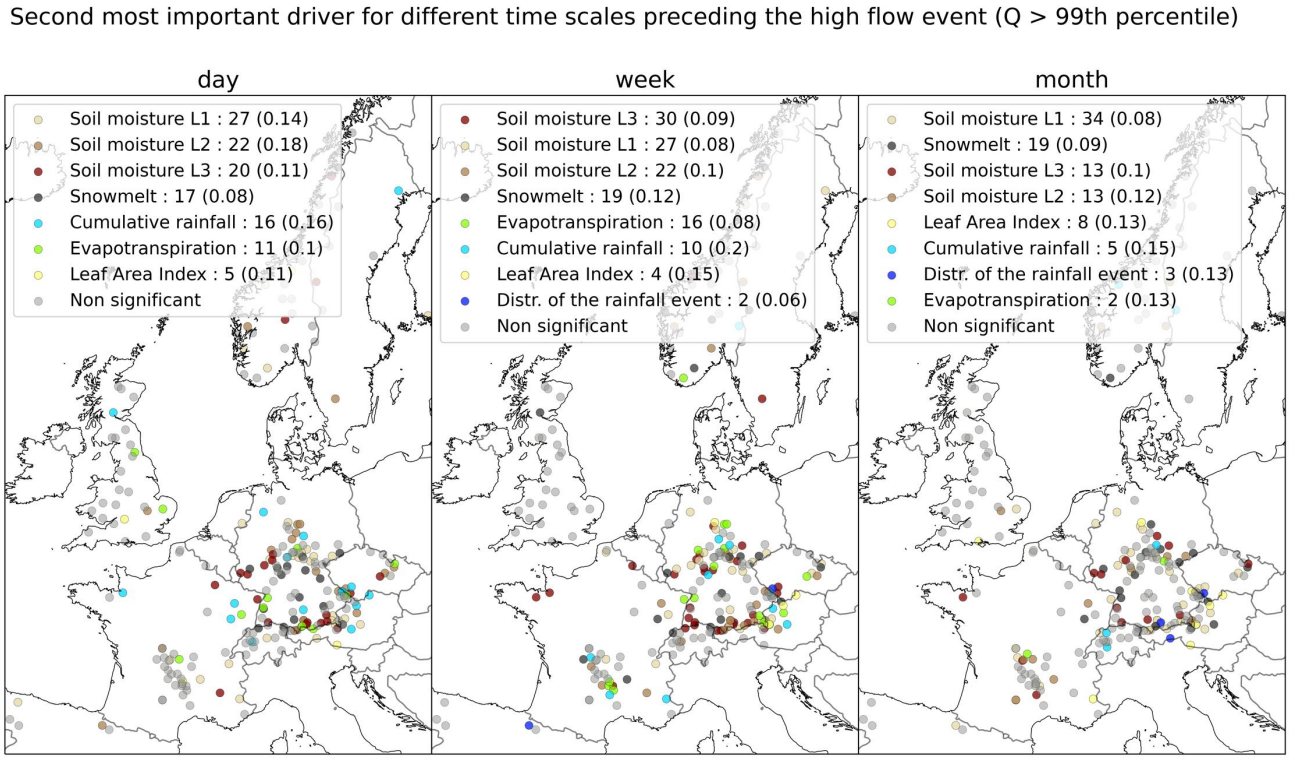

Figure 6.A5. Illustration of the second most influential drivers of extreme high flows exceeding the 99th percentile using the multi-inference method.

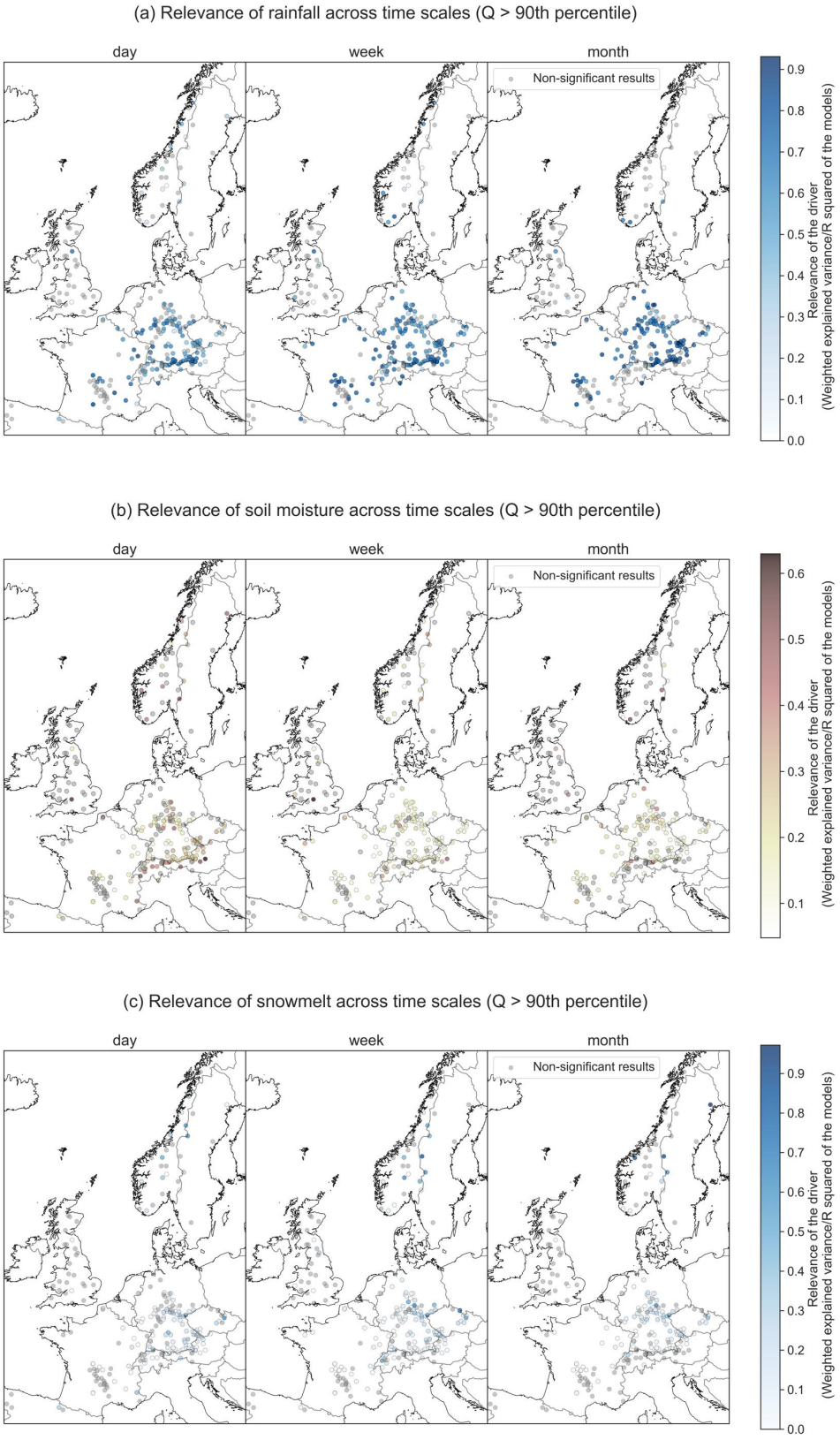

Figure 6.A6. Illustration of the relevance of (a) rainfall, (b) soil moisture and (c) snow melt in the selected catchments of extreme high flows exceeding the 90th percentile using the multi-inference method.

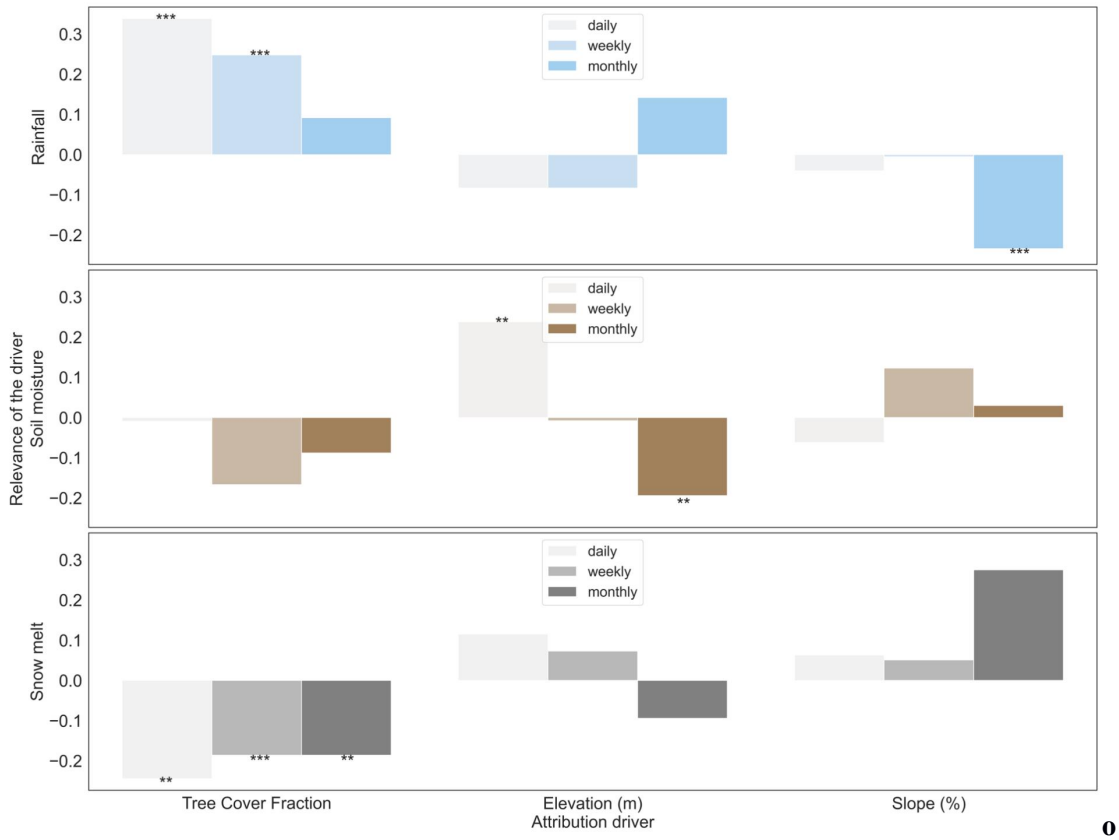

Figure 6.A7. Attributing the spatial patterns of the relevance of considered drivers of high flows to vegetation and terrain characteristics for high flow events exceeding the 90th percentile. Vertical axis corresponds to the partial correlation between driver relevance and each attribution variable. Results are shown for the considered different time scales. Stars on top of the bars indicate statistically significant partial correlations (** : p-value <0.05 , *** : p-value < 0.005).

Table 6.A1. Searches for flood-related articles (TS: topic, PY: Year Published).

Searches	Web of Science Query
1	TS = ((flood* near/50 (rain*)) OR (flood* near/50 (precipitation*))) AND PY= 2002-2021
2	TS=((flood* near/50 evapo*) OR (flood* near/50 vegetation*)) AND PY=2002-2021
3	TS=((flood* near/50 (snow*)) OR (flood* near/50 (melt*))) AND PY=2002-2021
4	TS=((flood* near/50 (soil* near/1 moisture*)) OR (flood* near/50 (soil* near/1 water*))) AND PY=2002-2021
5	#1 AND #2 AND #3 AND #4

7 Synthesis

This thesis synthesizes five studies to address three main questions in the context of vegetation-water interactions. These studies analyze data from multiple data sources including satellite observations, hydro-meteorological reanalysis, eddy-covariance and catchment-level measurements, land surface modelled data, and physical-based SCOPE modelled data to solve questions related to the soil moisture controlling regime on vegetation and the vegetation modulating regime on hydrological extremes. Data-driven approaches are widely used in this thesis to quantify soil moisture impacts on vegetation changes and drivers of hydrological extremes which can shed light on constraining land surface modelling.

7.1 What is the relationship between vegetation productivity and water supply?

Overall, the root-zone soil moisture is the predominant driver of vegetation productivity and greenness in more than half of the global study area, and vegetation sensitivity to root-zone soil moisture is increasing widely in semi-arid and arid regions related to ecological characteristics and long-term trends of precipitation. From a long-term to short-term perspective, soil moisture drought influence on vegetation largely depends on physiological responses which strongly downregulate in dry regions compared to wet regions. **Chapters 2-4** analyze spatiotemporal relationships between vegetation and soil moisture, and soil moisture drought influence on vegetation. These studies reveal the dry-region vulnerability to water availability. I answer the first question by highlighting three main aspects:

7.1.1 The relative importance of soil moisture for vegetation productivity compared to other meteorological drivers when accounting for the vertical soil moisture discretization

Chapter 2 presents the dominant hydro-meteorological controls of global vegetation productivity anomalies represented by SIF during 2007-2018 as inferred by Permutation importance in random forests. By comparing controlling patterns accounting for multi-layer soil moisture or only a total soil moisture column, the study reveals substantial differences: significantly extended water-controlling regimes appear when considering water reservoirs from different soil layers. Hence, more accurate global water- and energy-controlling regimes are identified at the half-monthly scale. After improving water-controlling-regime identification, I map dominant hydro-meteorological controls on SIF which vary with latitudes and associated climatic regimes: temperature in higher latitudes with cold and wet climate, solar radiation in lower latitudes with warm and humid climate, and root-zone soil moisture in between with dry climate conditions.

Revisiting global vegetation controls complements previous studies that have evaluated global vegetation controls (Denissen et al. 2020; Seneviratne et al. 2010; Walther et al. 2019; Seddon et al. 2016; Nemani et al. 2003; Madani et al. 2017; Li and Xiao 2020). In terms of second-order drivers, VPD jointly regulates vegetation productivity in humid regions, whereas precipitation and near-surface soil moisture complement the root-zone soil moisture in controlling vegetation productivity is found in semi-arid regions where temperature is normally high. The higher relevance of root-zone soil moisture compared to near-surface is found on controlling photosynthesis in widespread semi-arid and arid regions from three soil moisture reanalysis datasets and an observation-based gridded soil moisture product, highlighting the sub-surface importance in the global vegetation system. This observation-based inference of sub-surface impacts on vegetation moves beyond previous findings that are based on physical models or site-level experiments (A et al. 2019; Schlaepfer et al. 2017). The soil moisture controlling regimes of vegetation productivity are not only shaped by background climate conditions but also by vegetation characteristics. Grass- and shrub-dominant ecosystems also show consistently predominant controls from shallow to deep root-zone soil moisture on their productivity. The importance of deep root-zone soil moisture on vegetation is found to be tightly associated

with vegetation rooting depths, because plants are trained to face seasonal dryness and can adapt to surface water-scarce conditions by their deep-reaching rooting system and plasticity (Fan et al. 2017; Schenk and Jackson 2009). Moreover, the importance of soil moisture controls on vegetation productivity is shifting across seasons in transitional ecosystems which experience stronger soil moisture controls in the late growing season compared to the early growing season. A follow-up study finds similar shifts in terms of varying soil moisture importance between vegetation productivity minimum and maximum extremes (Kroll et al. 2022). These findings highlight the importance of soil moisture on regulating vegetation growth in dry seasons and in dry regions.

Chapter 3 addresses the relationship between vegetation and soil moisture across space by analyzing the long-term changes in the sensitivity of monthly anomalies of vegetation productivity (i.e., LAI) to soil moisture anomalies during 1982-2017. First, the long-term overall sensitivity across space and across near-surface and sub-surface soil moisture layers is derived from an explainable machine learning algorithm to fully account for interactions among LAI and all considered hydro-meteorological drivers. Overall sensitivity of LAI to sub-surface soil moisture shows significantly positive values across prevailing global semi-arid and arid areas during 36 years, highlighting again a long-term relevance of this moisture reservoir on regulating vegetation dynamics. By building upon the response curve of overall LAI sensitivity and mean soil moisture across ecosystems, a spatially non-linear vegetation water response can be found with drier regions showing higher sensitivity, supporting previous findings from in-situ measurements (Stocker et al. 2018). So far, soil moisture impacts on vegetation across space have been explored, while changes in vegetation responses to soil moisture across decades are still understudied.

7.1.2 Changes in the relationship between vegetation productivity and soil moisture across decades

In **Chapter 3**, next to the overall sensitivity, trends of LAI sensitivity to soil moisture are calculated by quantifying temporal variations of LAI sensitivity from 3- or 5-year non-overlapped moving windows during 1982-2016. Sensitivity trends are quantified in only water-controlled regions where the relationship between LAI and soil moisture is significantly positive. Increasing trends are found for around twice of areas than that of decreasing trends, and these trends are robust across ensembles of observation-based LAI and soil moisture products. Increases in LAI sensitivity during the last three decades indicate that small changes in water supply are able to trigger dramatic changes in LAI and associated carbon, water and energy cycles. Increasing vegetation sensitivity to water also gives possible evidence to explain increased negative GPP extremes in the last several decades (Gampe et al. 2021). Key findings in **Chapter 3** also complements work from Jiao et al. (2021) which observes expanded areas and seasons where vegetation productivity is dominantly controlled by water availability from observations and (Denissen et al. 2022) which simulates an enhanced water limitation on ecosystem evaporation from ensembles of Earth system models.

Further, to understand the controls of LAI sensitivity trends, multiple hydro-climate and ecological variables are considered in terms of their importance in explaining the spatial variation of sensitivity trends. Trends of annual precipitation and overall sensitivity of LAI to soil moisture are key drivers of LAI sensitivity trends to soil moisture. The strongest increasing trends occur in regions with the highest overall sensitivity combined with declining trends in precipitation, suggesting an aggravated vulnerability of extreme water-sensitive ecosystems. Instead, ecosystems with medium to low overall sensitivity are experiencing a less significantly increasing or even decreasing sensitivity, as these ecosystems adapt to abnormal water supplies by species diversity, composition shifts or long-term physiological changes (Anderegg et al. 2018; Guerrieri et al. 2019; Kannenberg et al. 2021). A recent study detects a similar increasing sensitivity of vegetation to precipitation in dry regions supporting our results in **Chapter 3**, and their finding about elevated atmospheric CO_2 complements our attribution and interpretation of drivers of sensitivity changes (Zhang et al. 2022). Long-term changes in the vegetation response to soil moisture changes are discussed so far, while the short-term response of vegetation to soil moisture drought is discussed in the next section.

7.1.3 Ecosystem functional and physiological responses to soil moisture drought

Chapter 4 focuses on the influence of soil moisture drought on ecosystem functions and physiology globally at the 8-daily time scale during 2018-2021 using TROPOMI SIF, MODIS Land surface temperature (LST), X-band VOD, MODIS LAI and hydro-meteorological reanalysis data. Drought peak is defined by the soil moisture minimum per grid cell in the respective growing seasons of the study time period, and is evaluated in terms of its severity using a reanalysis-based 40-year soil moisture record. The duration of drought development and recovery periods is defined by the time steps between the drought peak time and the time steps that soil moisture anomalies back to or greater than zero, and is used to understand drought influence across space. Two ecosystem functional properties are studied: (i) Photosynthesis which is presented by SIF, and (ii) evaporation which is estimated by LST and meteorological inputs using a simplified energy balance model and is evaluated against eddy-covariance measured evaporation across multiple sites. Vegetation water content is presented by VOD, and the ratio between midday and midnight VOD (VOD ratio) is an indicator of vegetation hydraulic regulation. First, this study presents photosynthesis, evaporation, and VOD ratio anomalies during the drought development and recovery periods. Results show contrasting patterns of ecosystem drought responses across aridity classes with drier regions experiencing stronger decreases in vegetation indices, implying that dry ecosystems are generally more vulnerable to extremes such as drought and heatwaves compared to wet regions (Flach et al. 2018). Among these vegetation observations, LAI shows clear increases in wet regions whereas SIF generally shows weak changes under drought, complementing previous findings about strong decoupling between LAI and GPP in wet regions (Hu et al. 2022; Yang et al. 2018).

Vegetation functions are composed by structural and physiological changes. To disentangle vegetation physiological response to drought, two experiments (by accounting for hydro-meteorological or not) of

random forest models use LAI as a predictor variable to predict SIF, evaporation, and VOD ratio, separately (see Section 4.2 for details). The respective physiological components contributing to the total changes of SIF, evaporation, and VOD ratio are disentangled using the difference between these two experiments of random forest predictions. Results show that ecosystem functional responses to drought are largely resembled by physiological changes, and reveal strong decreases of vegetation physiological changes in transition to dry regions. In wet regions, LAI clearly increases while physiological changes are weak or negative, supporting previous studies which emphasize stronger drought stress on GPP rather than that on greenness indices (Stocker et al. 2019; Morton et al. 2014; Hu et al. 2022). To further interpret the remote-sensing-derived physiological response to drought, we additionally employ a radiative transfer model SCOPE which accounts for plant physiology. Thus, physiological signals from evaporation and VOD ratio are largely explained by stomatal regulation as supported by SCOPE, and physiological signals from SIF are mainly associated with photosynthetic light use efficiency as a result of stomatal regulation and other non-hydraulic processes such as the maximum carboxylation rate. Changes of remote-sensing-derived signals provide global evidence of physiological regulations, expanding the previous understanding based on site measurements and models (Fu et al. 2022; Stocker et al. 2019, 2018; Novick et al. 2016). By further analyzing spatial variations of physiological changes during the 3-month drought development period, ecosystem physiology can largely be explained by climate and vegetation characteristics. Physiological changes show more decreases in dry and low tree covered regions, likely related to the lack of deeper water availability or the missing accessibility of deeper water sources. In addition, physiological components of SIF, evaporation, and VOD ratio are mediated by meteorological controls and drought duration, while the soil moisture importance seems less relevant in developing drought. Physiological changes during the 3-month drought recovery are mostly primarily controlled by concurrent soil moisture and VPD variations. Soil moisture is important in regulating vegetation physiological response to drought recovery which is related to root-zone recharge in rising hydraulic conductance.

7.2 Can vegetation regulate hydrological extremes?

Yes, vegetation plays an essential role in modulating hydrological extremes. **Chapters 5 and 6** reveal that vegetation regulates drought and floods through two main pathways: instantaneous changes of ecosystem functions such as evaporation, and ecosystem long-term characteristics such as tree cover fractions.

Chapter 5 focuses on the drought propagation from soil moisture across geospheres into runoff and evaporation using monthly gridded datasets derived through machine learning-assisted upscaling of site-level measurements from 2001 to 2015. Soil moisture drought in this study is defined and detected as minimum monthly soil moisture across entire growing seasons. Overall, runoff anomalies under drought are reduced across most of the global study area. Latitudinal patterns present two dominant areas for runoff reductions in boreal and tropical regions as a consequence of substantial decreases in precipitation as well as dramatic evaporation increases. The latitudinal patterns highlight the role of evaporation in regulating runoff and

associated sub-surface components of the hydrological cycle, which is also presented by previous studies (Teuling et al. 2013; Orth and Destouni 2018).

Evaporation consists mainly of plant transpiration during drought, even though evaporation from soil and other surfaces is not negligible (Miralles et al. 2016). Therefore, vegetation is very relevant for evaporation responses to drought. In wet boreal and tropical regions, drier than usual soil moisture is typically accompanied by higher than usual temperature and illumination conditions which promote vegetation to transfer water to the atmosphere through transpiration (Van Loon 2015). Hence, more water is lost in the soil and subsurface, aggravating the drought and its propagation into the hydrological water cycle. The globally mapped drought-propagation pattern of runoff and evaporation complements previous results obtained from European catchments and modelling (Orth and Destouni 2018). In addition, **Chapter 5** assesses that the long-term averaged fractional cover of trees is as important as climate regimes in regulating evaporation-runoff drought responses, after quantifying multiple land surface characteristics covering vegetation, climate, topography, and human activities. Tree-dominated ecosystems are found to be associated with stronger evaporation increases even in the case of comparable aridity class, because these ecosystems can benefit from drought-associated sunny weather and have sufficient deeper water sources (Stocker et al. 2021). The detected evaporation increases in forests during drought or heatwaves in this study confirms previous findings (Teuling et al. 2010; Zhao et al. 2022; O et al. 2022). In turn, runoff responses to drought show the most significant deficits in tree covered wet regions.

Chapter 6 studies the generating mechanisms of high river flows in Europe using streamflow observations from over 250 near-natural catchments. Hydrological and ecological variables from different data sources are considered as potential drivers of high river flows. High river flows are selected based on different thresholds reaching from 90th to 99.5th percentiles of daily streamflow data during 1984-2007. Multi-model inference is used to infer the relative importance of high flow drivers by partly accounting for potential collinearity among drivers (see details in Section 6.2). Results show that precipitation is the predominant driver of high flows, followed by other hydrological drivers, i.e., snow melt and soil moisture, largely confirming previous studies (Berghuijs et al. 2019; Blöschl et al. 2013). However, vegetation-related drivers such as LAI and evaporation have only been used to estimate soil moisture or snow melt, but the direct ecological impacts on high flows are understudied (Berghuijs et al. 2019; Duan et al. 2021; Merz and Blöschl 2003).

Our study also investigates that in 90th percentile of high flow events, dynamic vegetation variations only appear as secondary drivers in most catchments, while by focusing on more extreme high flows there are more catchments showing a dominant control by vegetation, with overall hydrological variables are still prevailingly relevant across many catchments. The second main point that illustrates the role of vegetation in regulating high flows is through background catchment characteristics such as vegetation types. Among multiple potential drivers including climate, terrain, and vegetation characteristics and the basin area, we find that the fraction of tree cover significantly regulates the importance of hydrological drivers in generating high

flow events. Higher tree cover is associated with higher importance of precipitation while lower importance of soil moisture and snow melt, providing additional evidence to support previous studies that the interception of water on the leaves and litterfall potentially impedes the soil infiltration and promote streamflow directly (Page et al. 2020; Medina Camarena, Wübbelmann, and Förster 2022).

7.3 Can land surface models capture the observed vegetation-water interplay?

Land surface models (LSMs) capture the interaction between vegetation and soil moisture specifically in distinguishing water and energy-limited regimes. However, the sensitivity of vegetation to soil moisture is generally overestimated and is largely misrepresented in the case of near-surface soil moisture. Increasing trends of vegetation sensitivity to soil moisture are not properly captured by LSMs, mislead by the overall sensitivity in models which is related to the potential misrepresentation of plant water stress and hydraulic processes in models.

Chapters 3 and 5 evaluate the performance of ensembles of TRENDY land surface models in representing vegetation-soil moisture interplay from different perspectives. Both studies find the performance of models in terms of the vegetation-soil moisture interplay differs across regions. **Chapter 5** performs an analysis to understand the bias of the evaporation drought response by calculating the correlation between monthly evaporation and soil moisture during fifteen years. The result shows that although the significantly positive correlation in dry ecosystems is well captured compared to the observed result, the vegetation-soil moisture interplay is largely misrepresented in wet regions. The misrepresented positive correlation between evaporation and soil moisture largely explains the overestimation of the evaporation deficit under drought when soil moisture decreases. Such overestimation of the evaporation reductions under drought has also been detected in a previous study (Ukkola et al. 2016). Since the correlation between soil moisture and evaporation is only one-dimensional evaluation, it is not explicitly clear if other dominant controls add additional biases in the vegetation-water interplay rather than the sole bias in the soil moisture constraint.

For this, **Chapter 3** quantifies the sensitivity of LAI to soil moisture after isolating marginal contributions of other meteorological forcing variables on LAI. Results show that the overall sensitivity better distinguishes water- and energy-limited regimes on LAI than that on ET in **Chapter 5** with the most positive sensitivity in semi-arid and arid regions and weak negative values appearing in very humid regions. However, there are still discrepancies when comparing observation-based and LSMs-based results. These discrepancies not only exist in specific regions but also differ across soil layers. The sensitivity of LAI to near-surface soil moisture in dry regions such as Southern Africa tends to be underestimated by models, whereas in warm and wet regions such as the Amazon tropics the sensitivity tends to be overestimated. A similar overestimation in the Amazon tropics in terms of GPP sensitivity to precipitation is found in Green et al. (2020) potentially due to poor empirically constraints of vegetation water stress implemented in models; In dry regions, a small fraction of bare-soil evaporation cools temperatures and mitigates the atmospheric water demand which can still be

beneficial for plant growth, while in the models the bare-soil evaporation is less constrained related to an omission of soil structure (Zhao et al. 2022). In the case of sub-surface soil moisture, LSMs generally overestimate the positive sensitivity of LAI with the strongest overestimation in extra-tropical and boreal regions, partly confirming the finding from **Chapter 5**. An overestimation of vegetation-soil moisture interplay in less water-sensitive regions is likely related to the missing consideration of biophysical processes such as waterlogging which inhibits vegetation growth and transpiration (Ohta et al. 2014; Pan et al. 2021). In addition to evaluating long-term overall LAI sensitivity to soil moisture, **Chapter 3** also explores whether LSMs can reproduce the observed trends of LAI sensitivity. However, no clear trends are found in LSMs which is mainly due to the already partly misrepresented overall LAI sensitivity and the related vegetation water response function, while decreases in precipitation trends do play a role in inducing an increasing LAI sensitivity in models. Last but not least, the performance of LSMs might show different soil moisture controls on vegetation productivity or on ecosystem evaporation, because vegetation productivity or evaporation are incorporated in and simulated by different biophysical and biogeochemical processes (Harper et al. 2021; Forzieri et al. 2020; Zhao et al. 2022; Rogers et al. 2017).

7.4 Limitations

This thesis applies data-driven approaches to understand drivers of vegetation and hydrological extremes. Limitations in data and methods which could introduce uncertainties into some analyses are discussed below.

7.4.1 Difficulties in predicting SIF in tropical regions

In **Chapter 2**, GOME-2 SIF is employed but can be influenced by the South Atlantic Anomaly where energetic particles increase and orbiting satellites are exposes to higher-than-usual levels of ionizing radiation, so that the SIF retrievals are noisy in South America (Köhler, Guanter, and Joiner 2015; Joiner et al. 2013). Thus, it is difficult to predict SIF with noise by random forests using multiple hydro-meteorological variables, and this study has to disregard large South American regions that are evaluated with bad random forests performance. GOME-2 SIF has generally relatively low signal-to-noise ratio compared to MODIS spectral vegetation indices, and it has a coarse spatial resolution (0.5˚) across global grid cells and can be affected by the cloud cover, degrading the quality of the satellite retrievals. Hence, this study provides a relatively lower accuracy of random forest modelling especially in humid regions where cloud cover easily happens compared to drier regions. In practice, a study from a diagnostic perspective seeks to better understand underlying processes within considered variables which is not influenced a lot by the generally low values of random forests cross-validation; This is different from a prognostic model that always requires a better prediction performance.

Chapter 4 studies drought-induced vegetation responses at the 8-daily temporal scale and 0.25˚ spatial scale, and TROPOMI SIF is employed and can be predicted using a similar combination of hydro-meteorological

data in random forests which show much better prediction performance. However, the prediction of SIF in core tropical regions is still not significantly improved with the advance of SIF data quality. Three reasons can likely explain the difficulties in predicting SIF in tropical regions: (i) Missing variables and processes in regulating SIF such as lagged effects of phenology or meteorology, which are not considered in the random forests. I performed some initial tests including lagged LAI and meteorological variables but could not find a significant improvement in prediction. (ii) The quality of gridded hydro-meteorological data. In tropical regions there are scarce in-situ measurements for the derivation of gridded data products, and satellite soil moisture observations are of poorer quality in densely vegetated regions (Ma et al. 2023). (iii) Human management such as deforestation and reforestation. Future research should test these aspects for a better prediction of vegetation productivity in tropical regions. For **Chapter 4** I disregard bad-performance regions and focus on regions where SIF can be well predicted to disentangle the related vegetation physiological response to drought.

7.4.2 Observing terrestrial photosynthesis and evaporation

There are some potential uncertainties when using SIF to present vegetation photosynthesis. First, the fluorescence escaping probability is associated with canopy structure and has a potential to confound the relationship between SIF and GPP. In **Chapter 2**, SIF is not corrected by the fluorescence escaping probability, because the relatively strong correlation between SIF and GPP at the bi-weekly time scale has been widely illustrated in previous studies (Green et al. 2020; Zeng et al. 2019; Guanter et al. 2012). Further, sun-sensor geometry could also confound scatter reflectance of SIF signals such as illustrated in Amazon studies (He et al. 2017; Samanta et al. 2010), while the correlation between SIF and GPP is not influenced that much referring to a global analysis (Chen et al. 2021). Nevertheless, better considering these effects might improve the presentation of GPP dynamics and associated global controlling regimes especially for studies focusing on finer spatial or temporal resolutions. Therefore, in **Chapter 4**, a correction of sun-sensor geometry on TROPOMI SIF is applied to better capture vegetation functional responses to drought at short time scales (8-daily). NIRv is also employed to replace LAI as a proxy of vegetation structure when disentangling SIF physiology, partly because NIRv is a good indicator of the fluorescence escape probability (Zeng et al. 2019).

A remaining issue is related to the decoupling between SIF and GPP under heatwaves, but the state-of-the-art studies reveal the not negligible decoupling effect at the leaf-to-canopy scale but not at the ecosystem scale (Helm et al. 2020; Wohlfahrt et al. 2018; Martini et al. 2022). Further analyses are needed to quantify if there is any influence at the ecosystem scale, as this scale mixes horizontal and vertical canopy structure and other surfaces such as soil more than smaller scales.

Evaporation also cannot be directly observed globally. There are multiple ways of estimating it as mentioned in Section 1.4.1. In **Chapter 5**, I use FLUXCOM evaporation which is an upscaled product based on eddy

covariance measurements and machine learning (Jung et al. 2019). In **Chapter 4**, to be independent of satellite greenness indices which are commonly used in the models of FLUXCOM or other global evaporation products, I estimate evaporation with a simplified surface energy balance model using MODIS LST observations and meteorological reanalysis data at 0.25˚ spatial resolution. Evaporation in both studies contains uncertainties as explained in Section 1.4.1, so I use eddy covariance measured evaporation to confirm the robustness of results derived from the large-scale data. However, to better match the footprint of eddy covariance measurements, future studies need to estimate evaporation using MODIS data from a finer spatial resolution.

7.4.3 Methods related to variable importance quantification

Variable importance quantification is widely performed throughout **Chapters 2-6**. In **Chapter 6**, one potential uncertainty of identifying variable importance is related to different data quality and resolutions across predictor variables. For example, the multi-weekly LAI data has to be interpolated into daily data to match daily streamflow, and gridded data need to be matched to the nearest location of each catchment with different spatial heterogeneity. In **Chapter 6**, the catchment size is tested and does not significantly impact the generating mechanism of high river flows, implying that matching gridded data of different resolutions to the catchment level does not introduce large biases. Mixtures of in-situ measurements and satellite-derived data need to be used with special caution in the future work.

Further, a variable importance identification or a statistical inference of relationships between target variable and explanatory variables do not suggest any causality. One needs to use causal statistical methods, or controlling experiments with site measurements or physical modelling to address a causality inference of specific biosphere-atmosphere interaction processes (Krich et al. 2019; Claessen et al. 2019; Humphrey et al. 2021; Zhou et al. 2021).

Last but not least, the consideration of potential drivers is empirical-based and largely determined by the data availability. Therefore, missing considered vegetation and hydrological drivers could result in an incomplete understanding of inferred relationships between drivers and target variables using random forests. For example, nutrient variability is mostly ignored in understanding global vegetation dynamics but has been illustrated as one of the key drivers (Wang et al. 2020). Also, random forests are not designed to naturally incorporate time-series memory effects of predictor variables, while there are other advanced machine learning methods to naturally account for such effects such as the long short-term memory recurrent neural network architectures (Kraft et al. 2019).

7.5 Outlook

This thesis uses data-driven approaches to understand soil moisture and meteorological impacts on vegetation productivity and greenness from spatial and temporal perspectives, including the vegetation functional

response to drought, vegetation regulation on hydrological extremes, and evaluations of land surface models. The obtained results encourage follow-up studies to further investigate (i) vegetation sensitivity to soil moisture, (ii) vegetation functioning and respective structure and physiology and (iii) extreme events that actually impact on ecological and societal properties.

7.5.1 Vegetation sensitivity to soil moisture and its implications

Chapter 3 detected widespread increases in LAI sensitivity to soil moisture, which indicates an amplified response of vegetation density i.e., LAI to water availability. LAI partly co-varies with photosynthesis, transpiration, and vegetation water content, but physiological regulations and ecosystem adaptations might result in differences in their individual sensitivity to soil moisture. Importantly, LAI, photosynthesis, transpiration, and vegetation water content affect different ecosystem services. A fundamental question is that if vegetation photosynthesis, transpiration, and vegetation water content are also amplified in terms of their sensitivity to soil moisture during the last decades similarly as LAI, or they are experiencing different changes. Research groups around the world are working on more robust long-term products of photosynthesis, transpiration, and vegetation water content, taking advantage of SIF, VOD, and other related observations (Wang et al. 2022; Moesinger et al. 2020). Hence, more opportunities for research might emerge in the future to further investigate trends in vegetation-water interactions.

Regarding consequences of changes in global vegetation-water sensitivity, an increasing sensitivity likely induces decreases in ecosystem resilience. Ecosystem resilience indicates if the ecosystem can easily adapt to environmental changes or is highly dependent on preceding ecosystem status (Holling 1996). Increased sensitivity or decreased resilience has a potential to raise ecosystem disturbance such as wildfire, forest mortality, and climate extremes such as heatwaves. Follow-up studies can, for instance, quantify the impact of increasing vegetation sensitivity to soil moisture on the observed decline of forest resilience such as detected from Forzieri et al. (2022).

7.5.2 Vegetation functioning and related structure and physiology

Different processes related to vegetation structure and physiology, and the motivation of disentangling variations in vegetation structure and physiology are discussed in Section 1.2.3. **Chapter 4** makes efforts in better understanding their individual responses to drought. Follow-up studies should further improve the understanding of structure and physiology by a comprehensive comparison of available methods and data, which can then advance considerable applications. Methods do not need to be limited by an extrapolation method or a variance decomposition in random forests used in **Chapter 4**. Instead, some other common statistical methods such as principal component analysis and time-frequency decomposition methods can be also used. I perform initial tests on the time-frequency decomposition, but data noise from different satellite products belong to different temporal frequencies and can challenge the partitioning of observed signals into

structure and physiology if using a fixed frequency threshold. A previous study, however, successfully partitioned structure and physiology using the time-frequency decomposition based on SCOPE modelling data without observational noise (Biriukova et al. 2021). Therefore, a comprehensive evaluation of different partitioning methods and their applications in satellite data is needed to better quantify vegetation physiological properties.

Other key properties that are essential for canopy structure such as leaf angle distributions are still not available in terms of global dynamic observations, hence the current understanding of vegetation structure is largely based on LAI data (Vicari, Pisek, and Disney 2019; Yang et al. 2022). Further developments of the above-mentioned structural products can better capture the representation of vegetation structural dynamics. Using our established paradigm of analyzing vegetation structure and physiology, follow-up studies can derive a better understanding of vegetation feedback on climate from observations and models, and address the current uncertainties in climate projections.

7.5.3 Extreme events: floods and drought

Chapters 4-6 study drought and high river flows to advance the related process understanding. However, the definition of extreme events in these studies is only based on the intensity of very low or very high values of water variability, i.e., lowest soil moisture for drought detection whereas highest streamflow for high flow detection. Another aspect of drought definition, the drought duration, is not explicitly considered in the applied drought definition, although it is commonly associated with drought intensity. I did consider drought duration by using it to explain the spatial variation of drought-induced changes in **Chapters 4 and 5**. Nevertheless, the periods of drought development and recovery are fixed to 3 months before and after drought peaks for both studies. On the one hand, given months simplify the method and can still evaluate how fast drought influences vegetation and the water cycle; On the other hand, the evaluation of magnitudes of drought influence is influenced by the fixed study period. Further studies should account for more flexible drought-associated time periods e.g., using a given threshold of low soil moisture to better determine and consider drought influential periods. Further, when studying vegetation responses to drought, ecological drought with an influence-oriented definition (e.g., using GPP anomalies) can study more aspects of vegetation physiology such as hydraulic failure or carbon starvation. **Chapters 4 and 5** analyze hydrological drought influence on vegetation which can largely be regulated by the deeper water availability, while follow-up studies need to understand vegetation physiological regulation under ecological drought which is crucially related to forest mortality to complement studies from smaller scales (McDowell et al. 2008; Sadiqi et al. 2022).

In **Chapter 6**, high river flows are defined by different thresholds of high streamflow values, but additionally future research could also quantify the affected areas as inferred by inundation areas. By applying satellite observations to classify inundation areas, further studies can combine the volume and areas of high river flows

to focus on the flood generation which is essential for planning flood management to prevent agriculture and infrastructure damage (Zimba et al. 2018).

References

A, Y., Wang, G., Liu, T., Xue, B., Kuczera, G., 2019. Spatial variation of correlations between vertical soil water and evapotranspiration and their controlling factors in a semi-arid region. J. Hydrol. 574, 53–63. https://doi.org/10.1016/j.jhydrol.2019.04.023

AghaKouchak, A., Cheng, L., Mazdiyasni, O., Farahmand, A., 2014. Global warming and changes in risk of concurrent climate extremes: Insights from the 2014 California drought: Global Warming and Concurrent Extremes. Geophys. Res. Lett. 41, 8847–8852. https://doi.org/10.1002/2014GL062308

AghaKouchak, A., Feldman, D., Hoerling, M., Huxman, T., Lund, J., 2015. Water and climate: Recognize anthropogenic drought. Nature 524, 409–411. https://doi.org/10.1038/524409a

Albergel, C., de Rosnay, P., Balsamo, G., Isaksen, L., Munoz-Sabater, J., 2012. Soil Moisture Analyses at ECMWF: Evaluation Using Global Ground-Based In Situ Observations. J. Hydrometeorol. 13, 1442–1460. https://doi.org/10.1175/jhm-d-11-0107.1

Albergel, C., Dorigo, W., Reichle, R., Balsamo, G., De Rosnay, P., Muñoz-Sabater, J., Isaksen, L., De Jeu, R., Wagner, W., 2013. Skill and global trend analysis of soil moisture from reanalyses and microwave remote sensing. J. Hydrometeorol. 14, 1259–1277.

Albergel, C., Dutra, E., Munier, S., Calvet, J.C., Munoz-Sabater, J., de Rosnay, P., Balsamo, G., 2018. ERA-5 and ERA-Interim driven ISBA land surface model simulations: which one performs better? Hydrol. Earth Syst. Sci. 22, 3515–3532. https://doi.org/10.5194/hess-22-3515-2018

Alfieri, L., Dottori, F., Salamon, P., Wu, H., Feyen, L., 2020. Global Modeling of Seasonal Mortality Rates From River Floods. Earths Future 8. https://doi.org/10.1029/2020EF001541

Amatulli, G., Domisch, S., Tuanmu, M.-N., Parmentier, B., Ranipeta, A., Malczyk, J., Jetz, W., 2018. A suite of global, cross-scale topographic variables for environmental and biodiversity modeling. Sci. Data 5, 180040. https://doi.org/10.1038/sdata.2018.40

Anderegg, W.R.L., Berry, J.A., Smith, D.D., Sperry, J.S., Anderegg, L.D.L., Field, C.B., 2012. The roles of hydraulic and carbon stress in a widespread climate-induced forest die-off. Proc. Natl. Acad. Sci. 109, 233–237. https://doi.org/10.1073/pnas.1107891109

Anderegg, W.R.L., Konings, A.G., Trugman, A.T., Yu, K., Bowling, D.R., Gabbitas, R., Karp, D.S., Pacala, S., Sperry, J.S., Sulman, B.N., Zenes, N., 2018. Hydraulic diversity of forests regulates ecosystem resilience during drought. Nature 561, 538–541. https://doi.org/10.1038/s41586-018-0539-7

Anderegg, W.R.L., Trugman, A.T., Bowling, D.R., Salvucci, G., Tuttle, S.E., 2019. Plant functional traits and climate influence drought intensification and land–atmosphere feedbacks. Proc. Natl. Acad. Sci. 116, 14071–14076. https://doi.org/10.1073/pnas.1904747116

Arora, V.K., Boer, G.J., 2005. A parameterization of leaf phenology for the terrestrial ecosystem component of climate models. Glob. Change Biol. 11, 39–59. https://doi.org/10.1111/j.1365-2486.2004.00890.x

Asner, G.P., Scurlock, J.M.O., A. Hicke, J., 2003. Global synthesis of leaf area index observations: implications for ecological and remote sensing studies: Global leaf area index. Glob. Ecol. Biogeogr. 12, 191–205. https://doi.org/10.1046/j.1466-822X.2003.00026.x

Badgley, G., Anderegg, L.D.L., Berry, J.A., Field, C.B., 2019. Terrestrial gross primary production: Using NIRV to scale from site to globe. Glob Chang Biol 25, 3731–3740. https://doi.org/10.1111/gcb.14729

Badgley, G., Field, C.B., Berry, J.A., 2017. Canopy near-infrared reflectance and terrestrial photosynthesis. Sci. Adv. 3, e1602244. https://doi.org/10.1126/sciadv.1602244

Baldocchi, D.D., Keeney, N., Rey-Sanchez, C., Fisher, J.B., 2022. Atmospheric humidity deficits tell us how soil moisture deficits down-regulate ecosystem evaporation. Adv. Water Resour. 159, 104100. https://doi.org/10.1016/j.advwatres.2021.104100

Ball, J. T., Woodrow, I. E., & Berry, J. A. (1987). A model predicting stomatal conductance and its contribution to the control of photosynthesis under different environmental conditions. In Progress in photosynthesis research (pp. 221-224). Springer, Dordrecht. https://doi.org/ 10.1007/978-94-017-0519-6_48

Balsamo, G., Agusti-Parareda, A., Albergel, C., Arduini, G., Beljaars, A., Bidlot, J., Bousserez, N., Boussetta, S., Brown, A., Buizza, R., Buontempo, C., Chevallier, F., Choulga, M., Cloke, H., Cronin, M., Dahoui, M., De Rosnay, P., Dirmeyer, P., Drusch, M., Dutra, E., Ek, M., Gentine, P., Hewitt, H., Keeley, S., Kerr, Y., Kumar, S., Lupu, C., Mahfouf, J., McNorton, J., Mecklenburg, S., Mogensen, K., Munoz-Sabater, J., Orth, R., Rabier, F., Reichle, R., Ruston, B., Pappenberger, F., Sandu, I., Seneviratne, S., Tietsche, S., Trigo, I., Uijlenhoet, R., Wedi, N., Woolway, R., Zeng, X., 2018. Satellite and In Situ Observations for Advancing Global Earth Surface Modelling: A Review. REMOTE Sens. 10. https://doi.org/10.3390/rs10122038

Balsamo, G., Albergel, C., Beljaars, A., Boussetta, S., Brun, E., Cloke, H., Dee, D., Dutra, E., Munoz-Sabater, J., Pappenberger, F., de Rosnay, P., Stockdale, T., Vitart, F., 2015. ERA-Interim/Land: a global land surface reanalysis data set. Hydrol. Earth Syst. Sci. 19, 389–407. https://doi.org/10.5194/hess-19-389-2015

Balsamo, G., Beljaars, A., Scipal, K., Viterbo, P., van den Hurk, B., Hirschi, M., Betts, A.K., 2009. A Revised Hydrology for the ECMWF Model: Verification from Field Site to Terrestrial Water Storage and Impact in the Integrated Forecast System. J. Hydrometeorol. 10, 623–643. https://doi.org/10.1175/2008JHM1068.1

Bao, S., Wutzler, T., Koirala, S., Cuntz, M., Ibrom, A., Besnard, S., Walther, S., Šigut, L., Moreno, A., Weber, U., Wohlfahrt, G., Cleverly, J., Migliavacca, M., Woodgate, W., Merbold, L., Veenendaal, E., Carvalhais, N.,

2022. Environment-sensitivity functions for gross primary productivity in light use efficiency models. Agric. For. Meteorol. 312, 108708. https://doi.org/10.1016/j.agrformet.2021.108708

Barredo, J.I., 2007. Major flood disasters in Europe: 1950–2005. Nat. Hazards 42, 125–148. https://doi.org/10.1007/s11069-006-9065-2

Barriopedro, D., Fischer, E.M., Luterbacher, J., Trigo, R.M., García-Herrera, R., 2011. The Hot Summer of 2010: Redrawing the Temperature Record Map of Europe. Science 332, 220–224. https://doi.org/10.1126/science.1201224

Barton, K., 2009. Mu-MIn: Multi-model inference. R Package Version 0.12.2/r18.

Bayat, B., van der Tol, C., Yang, P., Verhoef, W., 2019. Extending the SCOPE model to combine optical reflectance and soil moisture observations for remote sensing of ecosystem functioning under water stress conditions. Remote Sens. Environ. 221, 286–301. https://doi.org/10.1016/j.rse.2018.11.021

Beer, C., Reichstein, M., Tomelleri, E., Ciais, P., Jung, M., Carvalhais, N., Rödenbeck, C., Arain, M.A., Baldocchi, D., Bonan, G.B., Bondeau, A., Cescatti, A., Lasslop, G., Lindroth, A., Lomas, M., Luyssaert, S., Margolis, H., Oleson, K.W., Roupsard, O., Veenendaal, E., Viovy, N., Williams, C., Woodward, F.I., Papale, D., 2010. Terrestrial Gross Carbon Dioxide Uptake: Global Distribution and Covariation with Climate. Science 329, 834–838. https://doi.org/10.1126/science.1184984

Berdugo, M., Delgado-Baquerizo, M., Soliveres, S., Hernandez-Clemente, R., Zhao, Y., Gaitan, J., Gross, N., Saiz, H., Maire, V., Lehman, A., Rillig, M., Sole, R., Maestre, F., 2020. Global ecosystem thresholds driven by aridity. SCIENCE 367, 787-+. https://doi.org/10.1126/science.aay5958

Berg, A., Sheffield, J., 2018. Soil Moisture–Evapotranspiration Coupling in CMIP5 Models: Relationship with Simulated Climate and Projections. J. Clim. 31, 4865–4878. https://doi.org/10.1175/JCLI-D-17-0757.1

Berg, A., Sheffield, J., Milly, P.C.D., 2017. Divergent surface and total soil moisture projections under global warming. Geophys. Res. Lett. 44, 236–244. https://doi.org/10.1002/2016GL071921

Berghuijs, W.R., Harrigan, S., Molnar, P., Slater, L.J., Kirchner, J.W., 2019. The Relative Importance of Different Flood‐Generating Mechanisms Across Europe. Water Resour. Res. 55, 4582–4593. https://doi.org/10.1029/2019WR024841

Berghuijs, W.R., Woods, R.A., Hutton, C.J., Sivapalan, M., 2016. Dominant flood generating mechanisms across the United States: Flood Mechanisms Across the U.S. Geophys. Res. Lett. 43, 4382–4390. https://doi.org/10.1002/2016GL068070

Beringer, J., Hutley, L.B., Tapper, N.J., Cernusak, L.A., 2007. Savanna fires and their impact on net ecosystem productivity in North Australia. Glob. Change Biol. 13, 990–1004. https://doi.org/10.1111/j.1365-2486.2007.01334.x

Bertola, M., Viglione, A., Lun, D., Hall, J., Blöschl, G., 2020. Flood trends in Europe: are changes in small and big floods different? Hydrol. Earth Syst. Sci. 24, 1805–1822. https://doi.org/10.5194/hess-24-1805-2020

Besnard, S., Carvalhais, N., Arain, M.A., Black, A., Brede, B., Buchmann, N., Chen, J., Clevers, J.G.P.W., Dutrieux, L.P., Gans, F., Herold, M., Jung, M., Kosugi, Y., Knohl, A., Law, B.E., Paul-Limoges, E., Lohila, A., Merbold, L., Roupsard, O., Valentini, R., Wolf, S., Zhang, X., Reichstein, M., 2019. Memory effects of climate and vegetation affecting net ecosystem CO2 fluxes in global forests. PLOS ONE 14, e0211510. https://doi.org/10.1371/journal.pone.0211510

Besnard, S., Santoro, M., Cartus, O., Fan, N., Linscheid, N., Nair, R., Weber, U., Koirala, S., Carvalhais, N., 2021. Global sensitivities of forest carbon changes to environmental conditions. Glob. Change Biol. 27, 6467–6483. https://doi.org/10.1111/gcb.15877

Best, M.J., Abramowitz, G., Johnson, H.R., Pitman, A.J., Balsamo, G., Boone, A., Cuntz, M., Decharme, B., Dirmeyer, P.A., Dong, J., Ek, M., Guo, Z., Haverd, V., van den Hurk, B.J.J., Nearing, G.S., Pak, B., Peters-Lidard, C., Santanello, J.A., Stevens, L., Vuichard, N., 2015. The Plumbing of Land Surface Models: Benchmarking Model Performance. J. Hydrometeorol. 16, 1425–1442. https://doi.org/10.1175/JHM-D-14-0158.1

Biriukova, K., Pacheco‐Labrador, J., Migliavacca, M., Mahecha, M.D., Gonzalez‐Cascon, R., Martín, M.P., Rossini, M., 2021. Performance of Singular Spectrum Analysis in Separating Seasonal and Fast Physiological Dynamics of Solar‐Induced Chlorophyll Fluorescence and PRI Optical Signals. J. Geophys. Res. Biogeosciences 126. https://doi.org/10.1029/2020JG006158

Blauhut, V., Gudmundsson, L., Stahl, K., 2015. Towards pan-European drought risk maps: quantifying the link between drought indices and reported drought impacts. Environ. Res. Lett. 10, 014008. https://doi.org/10.1088/1748-9326/10/1/014008

Blöschl, G., Hall, J., Parajka, J., Perdigão, R.A.P., Merz, B., Arheimer, B., Aronica, G.T., Bilibashi, A., Bonacci, O., Borga, M., Čanjevac, I., Castellarin, A., Chirico, G.B., Claps, P., Fiala, K., Frolova, N., Gorbachova, L., Gül, A., Hannaford, J., Harrigan, S., Kireeva, M., Kiss, A., Kjeldsen, T.R., Kohnová, S., Koskela, J.J., Ledvinka, O., Macdonald, N., Mavrova-Guirguinova, M., Mediero, L., Merz, R., Molnar, P., Montanari, A., Murphy, C., Osuch, M., Ovcharuk, V., Radevski, I., Rogger, M., Salinas, J.L., Sauquet, E., Šraj, M., Szolgay, J., Viglione, A., Volpi, E., Wilson, D., Zaimi, K., Živković, N., 2017. Changing climate shifts timing of European floods. Science 357, 588–590. https://doi.org/10.1126/science.aan2506

Blöschl, G., Nester, T., Komma, J., Parajka, J., Perdigão, R.A.P., 2013. The June 2013 flood in the Upper Danube Basin, and comparisons with the 2002, 1954 and 1899 floods. Hydrol. Earth Syst. Sci. 17, 5197–5212. https://doi.org/10.5194/hess-17-5197-2013

Bonan, G.B., 2010. Ecological climatology: concepts and applications, 2. ed., reprint. ed. Cambridge University Press, Cambridge.

Bradford, M.J., Heinonen, J.S., 2008. Low Flows, Instream Flow Needs and Fish Ecology in Small Streams. Can. Water Resour. J. 33, 165–180. https://doi.org/10.4296/cwrj3302165

Breiman, L., 2001. Random forests. Mach. Learn. 45, 5–32. https://doi.org/10.1023/A:1010933404324

Breiman, L., 1996. Out-of-bag estimation.

Brunner, M.I., Slater, L., Tallaksen, L.M., Clark, M., 2021a. Challenges in modeling and predicting floods and droughts: A review. WIREs Water 8. https://doi.org/10.1002/wat2.1520

Brunner, M.I., Swain, D.L., Wood, R.R., Willkofer, F., Done, J.M., Gilleland, E., Ludwig, R., 2021b. An extremeness threshold determines the regional response of floods to changes in rainfall extremes. Commun. Earth Environ. 2, 173. https://doi.org/10.1038/s43247-021-00248-x

Budyko, M.I., 1974. Climate and life. Academic Press, New York.

Buermann, W., Forkel, M., O'Sullivan, M., Sitch, S., Friedlingstein, P., Haverd, V., Jain, A.K., Kato, E., Kautz, M., Lienert, S., Lombardozzi, D., Nabel, J., Tian, H., Wiltshire, A.J., Zhu, D., Smith, W.K., Richardson, A.D., 2018. Widespread seasonal compensation effects of spring warming on northern plant productivity. Nature 562, 110–114. https://doi.org/10.1038/s41586-018-0555-7

Büntgen, U., Urban, O., Krusic, P.J., Rybníček, M., Kolář, T., Kyncl, T., Ač, A., Koňasová, E., Čáslavský, J., Esper, J., Wagner, S., Saurer, M., Tegel, W., Dobrovolný, P., Cherubini, P., Reinig, F., Trnka, M., 2021. Recent European drought extremes beyond Common Era background variability. Nat. Geosci. 14, 190–196. https://doi.org/10.1038/s41561-021-00698-0

Buras, A., Rammig, A., Zang, C.S., 2020. Quantifying impacts of the 2018 drought on European ecosystems in comparison to 2003. Biogeosciences 17, 1655–1672. https://doi.org/10.5194/bg-17-1655-2020

Camps-Valls, G., Campos-Taberner, M., Moreno-Martinez, A., Walther, S., Duveiller, G., Cescatti, A., Mahecha, M., Munoz-Mari, J., Garcia-Haro, F., Guanter, L., Jung, M., Gamon, J., Reichstein, M., Running, S., 2021. A unified vegetation index for quantifying the terrestrial biosphere. Sci. Adv. 7. https://doi.org/10.1126/sciadv.abc7447

Canadell, J.G., Monteiro, P.M., Costa, M.H., Da Cunha, L.C., 2021. [Global Carbon and other Biogeochemical Cycles and Feedbacks"] in Climate Change 2021: The Physical Science Basis. Contribution of Working Group I to the Sixth Assessment Report of the Intergovernmental Panel on Climate Change. Cambridge University Press.

Carminati, A., Javaux, M., 2020. Soil Rather Than Xylem Vulnerability Controls Stomatal Response to Drougnt. TRENDS PLANT Sci. 25, 868–880. https://doi.org/10.1016/j.tplants.2020.04.003

Chatterjee, S., Desai, A.R., Zhu, J., Townsend, P.A., Huang, J., 2022. Soil moisture as an essential component for delineating and forecasting agricultural rather than meteorological drought. Remote Sens. Environ. 269, 112833. https://doi.org/10.1016/j.rse.2021.112833

Chen, A., Mao, J., Ricciuto, D., Xiao, J., Frankenberg, C., Li, X., Thornton, P.E., Gu, L., Knapp, A.K., 2021. Moisture availability mediates the relationship between terrestrial gross primary production and solar‐induced chlorophyll fluorescence: Insights from global‐scale variations. Glob. Change Biol. 27, 1144–1156. https://doi.org/10.1111/gcb.15373

Chen, J.M., Wang, R., Liu, Y., He, L., Croft, H., Luo, X., Wang, H., Smith, N.G., Keenan, T.F., Prentice, I.C., Zhang, Y., Ju, W., Dong, N., 2022. Global datasets of leaf photosynthetic capacity for ecological and earth system research. Earth Syst. Sci. Data 14, 4077–4093. https://doi.org/10.5194/essd-14-4077-2022

Claessen, J., Molini, A., Martens, B., Detto, M., Demuzere, M., Miralles, D.G., 2019. Global biosphere–climate interaction: a causal appraisal of observations and models over multiple temporal scales. Biogeosciences 16, 4851–4874. https://doi.org/10.5194/bg-16-4851-2019

Clark, M.P., Fan, Y., Lawrence, D.M., Adam, J.C., Bolster, D., Gochis, D.J., Hooper, R.P., Kumar, M., Leung, L.R., Mackay, D.S., Maxwell, R.M., Shen, C., Swenson, S.C., Zeng, X., 2015. Improving the representation of hydrologic processes in Earth System Models: REPRESENTING HYDROLOGIC PROCESSES IN EARTH SYSTEM MODELS. Water Resour. Res. 51, 5929–5956. https://doi.org/10.1002/2015WR017096

Cleveland, W.S., 1979. Robust locally weighted regression and smoothing scatterplots. J. Am. Stat. Assoc. 74, 829–836.

Collatz, G., Ribas-Carbo, M., Berry, J., 1992. Coupled Photosynthesis-Stomatal Conductance Model for Leaves of C4 Plants. Funct. Plant Biol. 19, 519. https://doi.org/10.1071/PP9920519

Condon, L.E., Atchley, A.L., Maxwell, R.M., 2020. Evapotranspiration depletes groundwater under warming over the contiguous United States. Nat. Commun. 11, 873. https://doi.org/10.1038/s41467-020-14688-0

Cox, P.M., Pearson, D., Booth, B.B., Friedlingstein, P., Huntingford, C., Jones, C.D., Luke, C.M., 2013. Sensitivity of tropical carbon to climate change constrained by carbon dioxide variability. Nature 494, 341–344.

Croft, H., Chen, J.M., Wang, R., Mo, G., Luo, S., Luo, X., He, L., Gonsamo, A., Arabian, J., Zhang, Y., Simic-Milas, A., Noland, T.L., He, Y., Homolová, L., Malenovský, Z., Yi, Q., Beringer, J., Amiri, R., Hutley, L., Arellano, P., Stahl, C., Bonal, D., 2020. The global distribution of leaf chlorophyll content. Remote Sens. Environ. 236, 111479. https://doi.org/10.1016/j.rse.2019.111479

Crow, W.T., Chen, F., Reichle, R.H., Xia, Y., Liu, Q., 2018. Exploiting Soil Moisture, Precipitation, and Streamflow Observations to Evaluate Soil Moisture/Runoff Coupling in Land Surface Models. Geophys. Res. Lett. 45, 4869–4878. https://doi.org/10.1029/2018GL077193

Cutler, A., Cutler, D.R., Stevens, J.R., 2012. Random forests, in: Ensemble Machine Learning. Springer, pp. 157–175.

Dai, A., Zhao, T., Chen, J., 2018. Climate Change and Drought: a Precipitation and Evaporation Perspective. Curr. Clim. Change Rep. 4, 301–312. https://doi.org/10.1007/s40641-018-0101-6

De Kauwe, M.G., Medlyn, B.E., Tissue, D.T., 2021. To what extent can rising [CO 2] ameliorate plant drought stress? New Phytol. 231, 2118–2124. https://doi.org/10.1111/nph.17540

De Kauwe, M.G., Zhou, S.-X., Medlyn, B.E., Pitman, A.J., Wang, Y.-P., Duursma, R.A., Prentice, I.C., 2015. Do land surface models need to include differential plant species responses to drought? Examining model predictions across a mesic-xeric gradient in Europe. Biogeosciences 12, 7503–7518. https://doi.org/10.5194/bg-12-7503-2015

De Keersmaecker, W., Lhermitte, S., Tits, L., Honnay, O., Somers, B., Coppin, P., 2015. A model quantifying global vegetation resistance and resilience to short-term climate anomalies and their relationship with vegetation cover. Glob. Ecol. Biogeogr. 24, 539–548. https://doi.org/10.1111/geb.12279

Dechant, B., Ryu, Y., Badgley, G., Zeng, Y.L., Berry, J.A., Zhang, Y.G., Goulas, Y., Li, Z.H., Zhang, Q., Kang, M., Li, J., Moya, I., 2020. Canopy structure explains the relationship between photosynthesis and sun-induced chlorophyll fluorescence in crops. Remote Sens. Environ. 241, 17. https://doi.org/10.1016/j.rse.2020.111733

Denissen, J.M.C., Orth, R., Wouters, H., Miralles, D.G., van Heerwaarden, C.C., de Arellano, J.V.-G., Teuling, A.J., 2021. Soil moisture signature in global weather balloon soundings. Npj Clim. Atmospheric Sci. 4, 13. https://doi.org/10.1038/s41612-021-00167-w

Denissen, J.M.C., Teuling, A.J., Pitman, A.J., Koirala, S., Migliavacca, M., Li, W., Reichstein, M., Winkler, A.J., Zhan, C., Orth, R., 2022. Widespread shift from ecosystem energy to water limitation with climate change. Nat. Clim. Change 12, 677–684. https://doi.org/10.1038/s41558-022-01403-8

Denissen, J.M.C., Teuling, A.J., Reichstein, M., Orth, R., 2020. Critical Soil Moisture Derived From Satellite Observations Over Europe. J. Geophys. Res. Atmospheres 125. https://doi.org/10.1029/2019JD031672

Destouni, G., Jaramillo, F., Prieto, C., 2013. Hydroclimatic shifts driven by human water use for food and energy production. Nat. Clim. Change 3, 213–217. https://doi.org/10.1038/nclimate1719

Dorigo, W., Wagner, W., Albergel, C., Albrecht, F., Balsamo, G., Brocca, L., Chung, D., Ertl, M., Forkel, M., Gruber, A., Haas, E., Hamer, P.D., Hirschi, M., Ikonen, J., de Jeu, R., Kidd, R., Lahoz, W., Liu, Y.Y., Miralles, D., Mistelbauer, T., Nicolai-Shaw, N., Parinussa, R., Pratola, C., Reimer, C., van der Schalie, R., Seneviratne, S.I., Smolander, T., Lecomte, P., 2017. ESA CCI Soil Moisture for improved Earth system understanding: State-of-the art and future directions. Remote Sens. Environ. 203, 185–215. https://doi.org/10.1016/j.rse.2017.07.001

Dormann, C.F., Elith, J., Bacher, S., Buchmann, C., Carl, G., Carré, G., Marquéz, J.R.G., Gruber, B., Lafourcade, B., Leitao, P.J., 2013. Collinearity: a review of methods to deal with it and a simulation study evaluating their performance. Ecography 36, 27–46.

Doughty, R., Kohler, P., Frankenberg, C., Magney, T.S., Xiao, X.M., Qin, Y.W., Wu, X.C., Moore, B., 2019. TROPOMI reveals dry-season increase of solar-induced chlorophyll fluorescence in the Amazon forest. Proc. Natl. Acad. Sci. U. S. A. 116, 22393–22398. https://doi.org/10.1073/pnas.1908157116

Drusch, M., Scipal, K., de Rosnay, P., Balsamo, G., Andersson, E., Bougeault, P., Viterbo, P., 2009. Towards a Kalman Filter based soil moisture analysis system for the operational ECMWF Integrated Forecast System. Geophys. Res. Lett. 36, L10401. https://doi.org/10.1029/2009GL037716

Du, J., Kimball, J.S., Jones, L.A., Kim, Y., Glassy, J., Watts, J.D., 2017. A global satellite environmental data record derived from AMSR-E and AMSR2 microwave Earth observations. Earth Syst. Sci. Data 9, 791–808. https://doi.org/10.5194/essd-9-791-2017

Duan, Y., Luo, M., Guo, X., Cai, P., Li, F., 2021. Study on the Relationship between Snowmelt Runoff for Different Latitudes and Vegetation Growth Based on an Improved SWAT Model in Xinjiang, China. Sustainability 13, 1189. https://doi.org/10.3390/su13031189

Dunne, A., Kuleshov, Y., 2022. Drought risk assessment and mapping for the Murray–Darling Basin, Australia. Nat. Hazards. https://doi.org/10.1007/s11069-022-05576-5

Duveiller, G., Hooker, J., Cescatti, A., 2018. The mark of vegetation change on Earth's surface energy balance. Nat. Commun. 9, 679. https://doi.org/10.1038/s41467-017-02810-8

Eltahir, E.A.B., Yeh, P.J.-F., 1999. On the asymmetric response of aquifer water level to floods and droughts in Illinois. Water Resour. Res. 35, 1199–1217. https://doi.org/10.1029/1998WR900071

Fallah, A., O, S., Orth, R., 2020. Climate-dependent propagation of precipitation uncertainty into the water cycle. Hydrol. Earth Syst. Sci. 24, 3725–3735. https://doi.org/10.5194/hess-24-3725-2020

Fan, Y., Miguez-Macho, G., Jobbágy, E.G., Jackson, R.B., Otero-Casal, C., 2017. Hydrologic regulation of plant rooting depth. Proc. Natl. Acad. Sci. 114, 10572–10577. https://doi.org/10.1073/pnas.1712381114

Fang, H., Baret, F., Plummer, S., and Schaepman‐Strub, G., 2019. An Overview of Global Leaf Area Index (LAI): Methods, Products, Validation, and Applications, Reviews of Geophysics, 57, 739–799, https://doi.org/10.1029/2018RG000608.

Farella, M.M., Fisher, J.B., Jiao, W., Key, K.B., Barnes, M.L., 2022. Thermal remote sensing for plant ecology from leaf to globe. J. Ecol. 110, 1996–2014. https://doi.org/10.1111/1365-2745.13957

Farquhar, G.D., von Caemmerer, S., Berry, J.A., 1980. A biochemical model of photosynthetic CO2 assimilation in leaves of C3 species. Planta 149, 78–90. https://doi.org/10.1007/BF00386231

Fatichi, S., Ivanov, V.Y., 2014. Interannual variability of evapotranspiration and vegetation productivity. Water Resour. Res. 50, 3275–3294. https://doi.org/10.1002/2013WR015044

Feng, S., Hu, Q., Huang, W., Ho, C.-H., Li, R., Tang, Z., 2014. Projected climate regime shift under future global warming from multi-model, multi-scenario CMIP5 simulations. Glob. Planet. Change 112, 41–52.

Fink, A.H., Brücher, T., Krüger, A., Leckebusch, G.C., Pinto, J.G., Ulbrich, U., 2004. The 2003 European summer heatwaves and drought -synoptic diagnosis and impacts: European heatwave - impacts. Weather 59, 209–216. https://doi.org/10.1256/wea.73.04

Flach, M., Sippel, S., Gans, F., Bastos, A., Brenning, A., Reichstein, M., Mahecha, M.D., 2018. Contrasting biosphere responses to hydrometeorological extremes: revisiting the 2010 western Russian heatwave. Biogeosciences 15, 6067–6085. https://doi.org/10.5194/bg-15-6067-2018

Forkel, M., Andela, N., Harrison, S.P., Lasslop, G., van Marle, M., Chuvieco, E., Dorigo, W., Forrest, M., Hantson, S., Heil, A., Li, F., Melton, J., Sitch, S., Yue, C., Arneth, A., 2019. Emergent relationships with respect to burned area in global satellite observations and fire-enabled vegetation models. Biogeosciences 16, 57–76. https://doi.org/10.5194/bg-16-57-2019

Forkel, M., Migliavacca, M., Thonicke, K., Reichstein, M., Schaphoff, S., Weber, U., Carvalhais, N., 2015. Codominant water control on global interannual variability and trends in land surface phenology and greenness. Glob Chang Biol 21, 3414–35. https://doi.org/10.1111/gcb.12950

Forkel, M., Schmidt, L., Zotta, R.-M., Dorigo, W., and Yebra, M., 2023. Estimating leaf moisture content at global scale from passive microwave satellite observations of vegetation optical depth, Hydrol. Earth Syst. Sci., 27, 39–68, https://doi.org/10.5194/hess-27-39-2023

Fort, F., Volaire, F., Guilioni, L., Barkaoui, K., Navas, M., Roumet, C., 2017. Root traits are related to plant water-use among rangeland Mediterranean species. Funct. Ecol. 31, 1700–1709. https://doi.org/10.1111/1365-2435.12888

Forzieri, G., Alkama, R., Miralles, D.G., Cescatti, A., 2017. Satellites reveal contrasting responses of regional climate to the widespread greening of Earth. Science 356, 1180–1184. https://doi.org/10.1126/science.aal1727

Forzieri, G., Dakos, V., McDowell, N.G., Ramdane, A., Cescatti, A., 2022. Emerging signals of declining forest resilience under climate change. Nature 608, 534–539. https://doi.org/10.1038/s41586-022-04959-9

Forzieri, G., Miralles, D.G., Ciais, P., Alkama, R., Ryu, Y., Duveiller, G., Zhang, K., Robertson, E., Kautz, M., Martens, B., Jiang, C., Arneth, A., Georgievski, G., Li, W., Ceccherini, G., Anthoni, P., Lawrence, P., Wiltshire, A., Pongratz, J., Piao, S., Sitch, S., Goll, D.S., Arora, V.K., Lienert, S., Lombardozzi, D., Kato, E., Nabel, J.E.M.S., Tian, H., Friedlingstein, P., Cescatti, A., 2020. Increased control of vegetation on global terrestrial energy fluxes. Nat. Clim. Change 10, 356–362. https://doi.org/10.1038/s41558-020-0717-0

Fournier, A., Daumard, F., Champagne, S., Ounis, A., Goulas, Y., Moya, I., 2012. Effect of canopy structure on sun-induced chlorophyll fluorescence. Isprs J. Photogramm. Remote Sens. 68, 112–120. https://doi.org/10.1016/j.isprsjprs.2012.01.003

Frankenberg, C., Berry, J., 2018. Solar Induced Chlorophyll Fluorescence: Origins, Relation to Photosynthesis and Retrieval, in: Comprehensive Remote Sensing. Elsevier, pp. 143–162. https://doi.org/10.1016/B978-0-12-409548-9.10632-3

Frankenberg, C., Fisher, J.B., Worden, J., Badgley, G., Saatchi, S.S., Lee, J.-E., Toon, G.C., Butz, A., Jung, M., Kuze, A., Yokota, T., 2011. New global observations of the terrestrial carbon cycle from GOSAT: Patterns of plant fluorescence with gross primary productivity: CHLOROPHYLL FLUORESCENCE FROM SPACE. Geophys. Res. Lett. 38, n/a-n/a. https://doi.org/10.1029/2011GL048738

Frankenberg, C., Yin, Y., Byrne, B., He, L., Gentine, P., 2021. Comment on "Recent global decline of CO2 fertilization effects on vegetation photosynthesis" COMMENT. SCIENCE 373. https://doi.org/10.1126/science.abg2947

Fu, Z., Ciais, P., Prentice, I.C., Gentine, P., Makowski, D., Bastos, A., Luo, X., Green, J.K., Stoy, P.C., Yang, H., Hajima, T., 2022. Atmospheric dryness reduces photosynthesis along a large range of soil water deficits. Nat. Commun. 13, 989. https://doi.org/10.1038/s41467-022-28652-7

Fuentes, I., Padarian, J., Vervoort, R.W., 2022. Spatial and Temporal Global Patterns of Drought Propagation. Front. Environ. Sci. 10, 788248. https://doi.org/10.3389/fenvs.2022.788248

Gampe, D., Zscheischler, J., Reichstein, M., O'Sullivan, M., Smith, W.K., Sitch, S., Buermann, W., 2021. Increasing impact of warm droughts on northern ecosystem productivity over recent decades. Nat. Clim. Change 11, 772–779. https://doi.org/10.1038/s41558-021-01112-8

Gao, L., Tao, B., Miao, Y., Zhang, L., Song, X., Ren, W., He, L., Xu, X., 2019. A Global Data Set for Economic Losses of Extreme Hydrological Events During 1960 - 2014. Water Resour. Res. 55, 5165–5175. https://doi.org/10.1029/2019WR025135

Garonna, I., de Jong, R., Stöckli, R., Schmid, B., Schenkel, D., Schimel, D., Schaepman, M.E., 2018. Shifting relative importance of climatic constraints on land surface phenology. Environ. Res. Lett. 13. https://doi.org/10.1088/1748-9326/aaa17b

Gelaro, R., McCarty, W., Suárez, M.J., Todling, R., Molod, A., Takacs, L., Randles, C.A., Darmenov, A., Bosilovich, M.G., Reichle, R., Wargan, K., Coy, L., Cullather, R., Draper, C., Akella, S., Buchard, V., Conaty, A., da Silva, A.M., Gu, W., Kim, G.-K., Koster, R., Lucchesi, R., Merkova, D., Nielsen, J.E., Partyka, G., Pawson, S., Putman, W., Rienecker, M., Schubert, S.D., Sienkiewicz, M., Zhao, B., 2017. The Modern-Era Retrospective Analysis for Research and Applications, Version 2 (MERRA-2). J. Clim. 30, 5419–5454. https://doi.org/10.1175/JCLI-D-16-0758.1

Ghajarnia, N., Kalantari, Z., Destouni, G., 2021. Data‐Driven Worldwide Quantification of Large‐Scale Hydroclimatic Covariation Patterns and Comparison With Reanalysis and Earth System Modeling. Water Resour. Res. 57. https://doi.org/10.1029/2020WR029377

Ghiggi, G., Humphrey, V., Seneviratne, S.I., Gudmundsson, L., 2021. G‐RUN ENSEMBLE: A Multi‐Forcing Observation‐Based Global Runoff Reanalysis. Water Resour. Res. 57. https://doi.org/10.1029/2020WR028787

Ghiggi, G., Humphrey, V., Seneviratne, S.I., Gudmundsson, L., 2019. GRUN: an observation-based global gridded runoff dataset from 1902 to 2014. Earth Syst. Sci. Data 11, 1655–1674. https://doi.org/10.5194/essd-11-1655-2019

Gómez-Ramírez, J., Ávila-Villanueva, M., Fernández-Blázquez, M.Á., 2019. Selecting the most important self-assessed features for predicting conversion to Mild Cognitive Impairment with Random Forest and Permutation-based methods. bioRxiv 785519.

Gonsamo, A., Walter, J.-M.N., Pellikka, P., 2011. CIMES: A package of programs for determining canopy geometry and solar radiation regimes through hemispherical photographs. Comput. Electron. Agric. 79, 207–215. https://doi.org/10.1016/j.compag.2011.10.001

Green, J.K., Berry, J., Ciais, P., Zhang, Y., Gentine, P., 2020. Amazon rainforest photosynthesis increases in response to atmospheric dryness. Sci. Adv. 6, eabb7232. https://doi.org/10.1126/sciadv.abb7232

Green, J.K., Seneviratne, S.I., Berg, A.M., Findell, K.L., Hagemann, S., Lawrence, D.M., Gentine, P., 2019. Large influence of soil moisture on long-term terrestrial carbon uptake. Nature 565, 476–479. https://doi.org/10.1038/s41586-018-0848-x

Greve, P., Orlowsky, B., Mueller, B., Sheffield, J., Reichstein, M., Seneviratne, S.I., 2014. Global assessment of trends in wetting and drying over land. Nat. Geosci. 7, 716–721. https://doi.org/10.1038/ngeo2247

Grossiord, C., Buckley, T.N., Cernusak, L.A., Novick, K.A., Poulter, B., Siegwolf, R.T.W., Sperry, J.S., McDowell, N.G., 2020. Plant responses to rising vapor pressure deficit. New Phytol. https://doi.org/10.1111/nph.16485

Gu, Y., Hunt, E., Wardlow, B., Basara, J. B., Brown, J. F., & Verdin, J. P. (2008). Evaluation of MODIS NDVI and NDWI for vegetation drought monitoring using Oklahoma Mesonet soil moisture data. Geophysical Research Letters, 35(22).

Guanter, L., Frankenberg, C., Dudhia, A., Lewis, P.E., Gómez-Dans, J., Kuze, A., Suto, H., Grainger, R.G., 2012. Retrieval and global assessment of terrestrial chlorophyll fluorescence from GOSAT space measurements. Remote Sens. Environ. 121, 236–251. https://doi.org/10.1016/j.rse.2012.02.006

Gudmundsson, L., Seneviratne, S.I., 2015. Towards observation-based gridded runoff estimates for Europe. Hydrol. Earth Syst. Sci. 19, 2859–2879. https://doi.org/10.5194/hess-19-2859-2015

Guerrieri, R., Belmecheri, S., Ollinger, S.V., Asbjornsen, H., Jennings, K., Xiao, J., Stocker, B.D., Martin, M., Hollinger, D.Y., Bracho-Garrillo, R., Clark, K., Dore, S., Kolb, T., Munger, J.W., Novick, K., Richardson, A.D., 2019. Disentangling the role of photosynthesis and stomatal conductance on rising forest water-use efficiency. Proc. Natl. Acad. Sci. 116, 16909–16914. https://doi.org/10.1073/pnas.1905912116

Guimberteau, M., Zhu, D., Maignan, F., Huang, Y., Yue, C., Dantec-Nedelec, S., Ottle, C., Jornet-Puig, A., Bastos, A., Laurent, P., Goll, D., Bowring, S., Chang, J., Guenet, B., Tifafi, M., Peng, S., Krinner, G., Ducharne, A., Wang, F., Wang, T., Wang, X., Wang, Y., Yin, Z., Lauerwald, R., Joetzjer, E., Qiu, C., Kim, H., Ciais, P., 2018. ORCHIDEE-MICT (v8.4.1), a land surface model for the high latitudes: model description and validation. Geosci. MODEL Dev. 11, 121–163. https://doi.org/10.5194/gmd-11-121-2018

Hall, J., Arheimer, B., Aronica, G.T., Bilibashi, A., Boháč, M., Bonacci, O., Borga, M., Burlando, P., Castellarin, A., Chirico, G.B., Claps, P., Fiala, K., Gaál, L., Gorbachova, L., Gül, A., Hannaford, J., Kiss, A., Kjeldsen, T., Kohnová, S., Koskela, J.J., Macdonald, N., Mavrova-Guirguinova, M., Ledvinka, O., Mediero, L., Merz, B., Medlyn, B. E., Dreyer, E., Ellsworth, D., Forstreuter, M., Harley, P. C., Kirschbaum, M. U. F., ... & Loustau, D. (2002). Temperature response of parameters of a biochemically based model of photosynthesis. II. A review of experimental data. Plant, Cell & Environment, 25(9), 1167-1179.

Merz, R., Molnar, P., Montanari, A., Osuch, M., Parajka, J., Perdigão, R.A.P., Radevski, I., Renard, B., Rogger, M., Salinas, J.L., Sauquet, E., Šraj, M., Szolgay, J., Viglione, A., Volpi, E., Wilson, D., Zaimi, K., Blöschl, G., 2015. A European Flood Database: facilitating comprehensive flood research beyond administrative boundaries. Proc. Int. Assoc. Hydrol. Sci. 370, 89–95. https://doi.org/10.5194/piahs-370-89-2015

Miralles, D. G., Jiménez, C., Jung, M., Michel, D., Ershadi, A., McCabe, M. F., Hirschi, M., Martens, B., Dolman, A. J., Fisher, J. B., Mu, Q., Seneviratne, S. I., Wood, E. F., and Fernández-Prieto, D., 2016. The WACMOS-ET project – Part 2: Evaluation of global terrestrial evaporation data sets, Hydrol. Earth Syst. Sci., 20, 823–842, https://doi.org/10.5194/hess-20-823-2016.

Harper, A.B., Williams, K.E., McGuire, P.C., Duran Rojas, M.C., Hemming, D., Verhoef, A., Huntingford, C., Rowland, L., Marthews, T., Breder Eller, C., Mathison, C., Nobrega, R.L.B., Gedney, N., Vidale, P.L., Otu-Larbi, F., Pandey, D., Garrigues, S., Wright, A., Slevin, D., De Kauwe, M.G., Blyth, E., Ardö, J., Black, A., Bonal, D., Buchmann, N., Burban, B., Fuchs, K., de Grandcourt, A., Mammarella, I., Merbold, L., Montagnani, L., Nouvellon, Y., Restrepo-Coupe, N., Wohlfahrt, G., 2021. Improvement of modeling plant responses to low soil moisture in JULESvn4.9 and evaluation against flux tower measurements. Geosci. Model Dev. 14, 3269–3294. https://doi.org/10.5194/gmd-14-3269-2021

Harris, I., Jones, P.D., Osborn, T.J., Lister, D.H., 2014. Updated high-resolution grids of monthly climatic observations - the CRU TS3.10 Dataset: UPDATED HIGH-RESOLUTION GRIDS OF MONTHLY CLIMATIC OBSERVATIONS. Int. J. Climatol. 34, 623–642. https://doi.org/10.1002/joc.3711

He, L., Chen, J.M., Liu, J., Mo, G., Joiner, J., 2017. Angular normalization of GOME-2 Sun-induced chlorophyll fluorescence observation as a better proxy of vegetation productivity: Angular Correction of SIF Observation. Geophys. Res. Lett. 44, 5691–5699. https://doi.org/10.1002/2017GL073708

He, M., Chen, S., Lian, X., Wang, X., Peñuelas, J., Piao, S., 2022. Global Spectrum of Vegetation Light‐Use Efficiency. Geophys. Res. Lett. 49. https://doi.org/10.1029/2022GL099550

Helm, L.T., Shi, H., Lerdau, M.T., Yang, X., 2020. Solar‐induced chlorophyll fluorescence and short‐term photosynthetic response to drought. Ecol. Appl. 30. https://doi.org/10.1002/eap.2101

Hersbach, H., Bell, B., Berrisford, P., Hirahara, S., Horanyi, A., Munoz-Sabater, J., Nicolas, J., Peubey, C., Radu, R., Schepers, D., Simmons, A., Soci, C., Abdalla, S., Abellan, X., Balsamo, G., Bechtold, P., Biavati, G., Bidlot, J., Bonavita, M., De Chiara, G., Dahlgren, P., Dee, D., Diamantakis, M., Dragani, R., Flemming, J., Forbes, R., Fuentes, M., Geer, A., Haimberger, L., Healy, S., Hogan, R.J., Holm, E., Janiskova, M., Keeley, S., Laloyaux, P., Lopez, P., Lupu, C., Radnoti, G., de Rosnay, P., Rozum, I., Vamborg, F., Villaume, S., Thepaut, J.N., 2020. The ERA5 global reanalysis. Q. J. R. Meteorol. Soc. 146, 1999–2049. https://doi.org/10.1002/qj.3803

Hirsch, R.M., Slack, J.R., Smith, R.A., 1982. Techniques of trend analysis for monthly water quality data. Water Resour. Res. 18, 107–121. https://doi.org/10.1029/WR018i001p00107

Hirschboeck, K.K., 1991. Climate and floods. US Geological Survey Water-Supply Paper.

Hoek van Dijke, A.J., Herold, M., Mallick, K., Benedict, I., Machwitz, M., Schlerf, M., Pranindita, A., Theeuwen, J.J.E., Bastin, J.-F., Teuling, A.J., 2022. Shifts in regional water availability due to global tree restoration. Nat. Geosci. 15, 363–368. https://doi.org/10.1038/s41561-022-00935-0

Hoekstra, N.J., Finn, J.A., Hofer, D., Lüscher, A., 2014. The effect of drought and interspecific interactions on depth of water uptake in deep-and shallow-rooting grassland species as determined by δ18 O natural abundance. Biogeosciences 11, 4493–4506.

Holling, C.S., 1996. Engineering resilience versus ecological resilience, in: Engineering within Ecological Constraints. National Academies Press, Washington, D.C., p. 4919. https://doi.org/10.17226/4919

Hu, Z., Piao, S., Knapp, A.K., Wang, X., Peng, S., Yuan, W., Running, S., Mao, J., Shi, X., Ciais, P., Huntzinger, D.N., Yang, J., Yu, G., 2022. Decoupling of greenness and gross primary productivity as aridity decreases. Remote Sens. Environ. 279, 113120. https://doi.org/10.1016/j.rse.2022.113120

Huang, K., Xia, J., 2019. High ecosystem stability of evergreen broadleaf forests under severe droughts. Glob. Change Biol. 25, 3494–3503. https://doi.org/10.1111/gcb.14748

Huang, M., Piao, S., Ciais, P., Peñuelas, J., Wang, X., Keenan, T.F., Peng, S., Berry, J.A., Wang, K., Mao, J., Alkama, R., Cescatti, A., Cuntz, M., De Deurwaerder, H., Gao, M., He, Y., Liu, Y., Luo, Y., Myneni, R.B., Niu, S., Shi, X., Yuan, W., Verbeeck, H., Wang, T., Wu, J., Janssens, I.A., 2019. Air temperature optima of

vegetation productivity across global biomes. Nat. Ecol. Evol. 3, 772–779. https://doi.org/10.1038/s41559-019-0838-x

Huete, A., 1997. A comparison of vegetation indices over a global set of TM images for EOS-MODIS. Remote Sens. Environ. 59, 440–451. https://doi.org/10.1016/S0034-4257(96)00112-5

Huete, A., Didan, K., Miura, T., Rodriguez, E.P., Gao, X., Ferreira, L.G., 2002. Overview of the radiometric and biophysical performance of the MODIS vegetation indices. Remote Sens. Environ. 83, 195–213.

Humphrey, V., Berg, A., Ciais, P., Gentine, P., Jung, M., Reichstein, M., Seneviratne, S.I., Frankenberg, C., 2021. Soil moisture–atmosphere feedback dominates land carbon uptake variability. Nature 592, 65–69. https://doi.org/10.1038/s41586-021-03325-5

Humphrey, V., Zscheischler, J., Ciais, P., Gudmundsson, L., Sitch, S., Seneviratne, S.I., 2018. Sensitivity of atmospheric CO2 growth rate to observed changes in terrestrial water storage. Nature 560, 628–631. https://doi.org/10.1038/s41586-018-0424-4

Hunter, J.D., 2007. Matplotlib: A 2D graphics environment. Comput. Sci. Eng. 9, 90–95.

Hutyra, L.R., Munger, J.W., Saleska, S.R., Gottlieb, E., Daube, B.C., Dunn, A.L., Amaral, D.F., De Camargo, P.B., Wofsy, S.C., 2007. Seasonal controls on the exchange of carbon and water in an Amazonian rain forest. J. Geophys. Res. Biogeosciences 112.

Ito, A., Oikawa, T., 2002. A simulation model of the carbon cycle in land ecosystems (Sim-CYCLE): a description based on dry-matter production theory and plot-scale validation. Ecol. Model. 151, 143–176. https://doi.org/10.1016/S0304-3800(01)00473-2

Jackson, T. J., Chen, D., Cosh, M., Li, F., Anderson, M., Walthall, C., ... & Hunt, E. R. (2004). Vegetation water content mapping using Landsat data derived normalized difference water index for corn and soybeans. Remote Sensing of Environment, 92(4), 475-482.

Janssen, T., van der Velde, Y., Hofhansl, F., Luyssaert, S., Naudts, K., Driessen, B., Fleischer, K., Dolman, H., 2021. Drought effects on leaf fall, leaf flushing and stem growth in the Amazon forest: reconciling remote sensing data and field observations. Biogeosciences 18, 4445–4472. https://doi.org/10.5194/bg-18-4445-2021

Jeong, S.-J., Schimel, D., Frankenberg, C., Drewry, D.T., Fisher, J.B., Verma, M., Berry, J.A., Lee, J.-E., Joiner, J., 2017. Application of satellite solar-induced chlorophyll fluorescence to understanding large-scale variations in vegetation phenology and function over northern high latitude forests. Remote Sens. Environ. 190, 178–187.

Jiang, C., Ryu, Y., Fang, H., Myneni, R., Claverie, M., Zhu, Z., 2017. Inconsistencies of interannual variability and trends in long-term satellite leaf area index products. Glob. CHANGE Biol. 23, 4133–4146. https://doi.org/10.1111/gcb.13787

Jiao, W., Chang, Q., Wang, L., 2019. The Sensitivity of Satellite Solar‐Induced Chlorophyll Fluorescence to Meteorological Drought. Earths Future. https://doi.org/10.1029/2018ef001087

Jiao, W., Wang, L., McCabe, M.F., 2021a. Multi-sensor remote sensing for drought characterization: current status, opportunities and a roadmap for the future. Remote Sens. Environ. 256, 112313. https://doi.org/10.1016/j.rse.2021.112313

Jiao, W., Wang, L., Smith, W.K., Chang, Q., Wang, H., D'Odorico, P., 2021b. Observed increasing water constraint on vegetation growth over the last three decades. Nat. Commun. 12, 3777. https://doi.org/10.1038/s41467-021-24016-9

Jing, W., Song, J., Zhao, X., 2018. Validation of ECMWF multi-layer reanalysis soil moisture based on the OzNet hydrology network. Water 10, 1123.

Joiner, J., Guanter, L., Lindstrot, R., Voigt, M., Vasilkov, A.P., Middleton, E.M., Huemmrich, K.F., Yoshida, Y., Frankenberg, C., 2013. Global monitoring of terrestrial chlorophyll fluorescence from moderate-spectral-resolution near-infrared satellite measurements: methodology, simulations, and application to GOME-2. Atmospheric Meas. Tech. 6, 2803–2823. https://doi.org/10.5194/amt-6-2803-2013

Jonard, F., Feldman, A.F., Short Gianotti, D.J., Entekhabi, D., 2022. Observed Water- and Light-Limitation Across Global Ecosystems (preprint). Biodiversity and Ecosystem Function: Terrestrial. https://doi.org/10.5194/bg-2022-25

Jung, M., Koirala, S., Weber, U., Ichii, K., Gans, F., Camps-Valls, G., Papale, D., Schwalm, C., Tramontana, G., Reichstein, M., 2019. The FLUXCOM ensemble of global land-atmosphere energy fluxes. Sci. Data 6, 74. https://doi.org/10.1038/s41597-019-0076-8

Kannenberg, S.A., Driscoll, A.W., Szejner, P., Anderegg, W.R.L., Ehleringer, J.R., 2021. Rapid increases in shrubland and forest intrinsic water-use efficiency during an ongoing megadrought. Proc. Natl. Acad. Sci. 118, e2118052118. https://doi.org/10.1073/pnas.2118052118

Kobayashi, S., Ota, Y., Harada, Y., Ebita, A., Moriya, M., Onoda, H., Onogi, K., Kamahori, H., Kobayashi, C., Endo, H., Miyaoka, K., Takahashi, K., 2015. The JRA-55 Reanalysis: General Specifications and Basic Characteristics. J. Meteorol. Soc. Jpn. 93, 5–48. https://doi.org/10.2151/jmsj.2015-001

Köhler, P., Frankenberg, C., Magney, T.S., Guanter, L., Joiner, J., Landgraf, J., 2018a. Global Retrievals of Solar‐Induced Chlorophyll Fluorescence With TROPOMI: First Results and Intersensor Comparison to OCO‐2. Geophys. Res. Lett. 45. https://doi.org/10.1029/2018GL079031

Köhler, P., Guanter, L., Joiner, J., 2015. A linear method for the retrieval of sun-induced chlorophyll fluorescence from GOME-2 and SCIAMACHY data. Atmospheric Meas. Tech. 8, 2589–2608. https://doi.org/10.5194/amt-8-2589-2015

Köhler, P., Guanter, L., Kobayashi, H., Walther, S., Yang, W., 2018b. Assessing the potential of sun-induced fluorescence and the canopy scattering coefficient to track large-scale vegetation dynamics in Amazon forests. Remote Sens. Environ. 204, 769–785. https://doi.org/10.1016/j.rse.2017.09.025

Kolluru, V., Kolluru, S., Konkathi, P., 2020. Evaluation and integration of reanalysis rainfall products under contrasting climatic conditions in India. ATMOSPHERIC Res. 246. https://doi.org/10.1016/j.atmosres.2020.105121

Konings, A.G., Gentine, P., 2017. Global variations in ecosystem‐scale isohydricity. Glob. Change Biol. 23, 891–905. https://doi.org/10.1111/gcb.13389

Konings, A.G., Saatchi, S.S., Frankenberg, C., Keller, M., Leshyk, V., Anderegg, W.R.L., Humphrey, V., Matheny, A.M., Trugman, A., Sack, L., Agee, E., Barnes, M.L., Binks, O., Cawse‐Nicholson, K., Christoffersen, B.O., Entekhabi, D., Gentine, P., Holtzman, N.M., Katul, G.G., Liu, Y., Longo, M., Martinez‐Vilalta, J., McDowell, N., Meir, P., Mencuccini, M., Mrad, A., Novick, K.A., Oliveira, R.S., Siqueira, P., Steele‐Dunne, S.C., Thompson, D.R., Wang, Y., Wehr, R., Wood, J.D., Xu, X., Zuidema, P.A., 2021. Detecting forest response to droughts with global observations of vegetation water content. Glob. Change Biol. 27, 6005–6024. https://doi.org/10.1111/gcb.15872

Konings, A.G., Williams, A.P., Gentine, P., 2017. Sensitivity of grassland productivity to aridity controlled by stomatal and xylem regulation. Nat. Geosci. 10, 284–288. https://doi.org/10.1038/ngeo2903

Kraft, B., Jung, M., Korner, M., Koirala, S., Reichstein, M., 2022. Towards hybrid modeling of the global hydrological cycle. Hydrol. EARTH Syst. Sci. 26, 1579–1614. https://doi.org/10.5194/hess-26-1579-2022

Kraft, B., Jung, M., Körner, M., Requena Mesa, C., Cortés, J., Reichstein, M., 2019. Identifying Dynamic Memory Effects on Vegetation State Using Recurrent Neural Networks. Front. Big Data 2, 31. https://doi.org/10.3389/fdata.2019.00031

Krich, C., Runge, J., Miralles, D.G., Migliavacca, M., Perez-Priego, O., El-Madany, T., Carrara, A., Mahecha, M.D., 2019. Causal networks of biosphere–atmosphere interactions. Biogeosciences. https://doi.org/10.5194/bg-2019-297

Kroll, J., Denissen, J.M.C., Migliavacca, M., Li, W., Hildebrandt, A., Orth, R., 2022. Spatially varying relevance of hydrometeorological hazards for vegetation productivity extremes. Biogeosciences 19, 477–489. https://doi.org/10.5194/bg-19-477-2022

Kundzewicz, Z.W., Kaczmarek, Z., 2000. Coping with Hydrological Extremes. Water Int. 25, 66–75. https://doi.org/10.1080/02508060008686798

Landerer, F.W., Swenson, S.C., 2012. Accuracy of scaled GRACE terrestrial water storage estimates: ACCURACY OF GRACE-TWS. Water Resour. Res. 48. https://doi.org/10.1029/2011WR011453

Le Quéré, C., Andrew, R.M., Friedlingstein, P., Sitch, S., Hauck, J., Pongratz, J., Pickers, P.A., Korsbakken, J.I., Peters, G.P., Canadell, J.G., Arneth, A., Arora, V.K., Barbero, L., Bastos, A., Bopp, L., Chevallier, F., Chini, L.P., Ciais, P., Doney, S.C., Gkritzalis, T., Goll, D.S., Harris, I., Haverd, V., Hoffman, F.M., Hoppema, M., Houghton, R.A., Hurtt, G., Ilyina, T., Jain, A.K., Johannessen, T., Jones, C.D., Kato, E., Keeling, R.F., Goldewijk, K.K., Landschützer, P., Lefèvre, N., Lienert, S., Liu, Z., Lombardozzi, D., Metzl, N., Munro, D.R., Nabel, J.E.M.S., Nakaoka, S., Neill, C., Olsen, A., Ono, T., Patra, P., Peregon, A., Peters, W., Peylin, P., Pfeil, B., Pierrot, D., Poulter, B., Rehder, G., Resplandy, L., Robertson, E., Rocher, M., Rödenbeck, C., Schuster, U., Schwinger, J., Séférian, R., Skjelvan, I., Steinhoff, T., Sutton, A., Tans, P.P., Tian, H., Tilbrook, B., Tubiello, F.N., van der Laan-Luijkx, I.T., van der Werf, G.R., Viovy, N., Walker, A.P., Wiltshire, A.J., Wright, R., Zaehle, S., Zheng, B., 2018. Global Carbon Budget 2018. Earth Syst. Sci. Data 10, 2141–2194. https://doi.org/10.5194/essd-10-2141-2018

Lewis, S.L., Brando, P.M., Phillips, O.L., van der Heijden, G.M.F., Nepstad, D., 2011. The 2010 Amazon Drought. Science 331, 554–554. https://doi.org/10.1126/science.1200807

Li, M., Wu, P., Ma, Z., 2020. A comprehensive evaluation of soil moisture and soil temperature from third-generation atmospheric and land reanalysis data sets. Int. J. Climatol. 40, 5744–5766. https://doi.org/10.1002/joc.6549

Li, S.-G., Romero-Saltos, H., Tsujimura, M., Sugimoto, A., Sasaki, L., Davaa, G., Oyunbaatar, D., 2007. Plant water sources in the cold semiarid ecosystem of the upper Kherlen River catchment in Mongolia: A stable isotope approach. J. Hydrol. 333, 109–117. https://doi.org/10.1016/j.jhydrol.2006.07.020

Li, W., Migliavacca, M., Forkel, M., Denissen, J.M.C., Reichstein, M., Yang, H., Duveiller, G., Weber, U., Orth, R., 2022. Widespread increasing vegetation sensitivity to soil moisture. Nat. Commun. 13, 3959. https://doi.org/10.1038/s41467-022-31667-9

Li, W., Migliavacca, M., Forkel, M., Walther, S., Reichstein, M., Orth, R., 2021. Revisiting Global Vegetation Controls Using Multi‐Layer Soil Moisture. Geophys. Res. Lett. 48. https://doi.org/10.1029/2021GL092856

Li, X., Xiao, J., 2020. Global climatic controls on interannual variability of ecosystem productivity: Similarities and differences inferred from solar-induced chlorophyll fluorescence and enhanced vegetation index. Agric. For. Meteorol. 288–289, 108018. https://doi.org/10.1016/j.agrformet.2020.108018

Li, X., Xiao, J., He, B., 2018. Higher absorbed solar radiation partly offset the negative effects of water stress on the photosynthesis of Amazon forests during the 2015 drought. Environ. Res. Lett. 13, 044005. https://doi.org/10.1088/1748-9326/aab0b1

Li, Y., Guan, K., Gentine, P., Konings, A.G., Meinzer, F.C., Kimball, J.S., Xu, X., Anderegg, W.R.L., McDowell, N.G., Martinez-Vilalta, J., Long, D.G., Good, S.P., 2017. Estimating Global Ecosystem Isohydry/Anisohydry Using Active and Passive Microwave Satellite Data: ESTIMATE GLOBAL

ECOSYSTEM ISOHYDRY/ANISOHYDRY. J. Geophys. Res. Biogeosciences 122, 3306–3321. https://doi.org/10.1002/2017JG003958

Lian, X., Piao, S., Li, L.Z.X., Li, Y., Huntingford, C., Ciais, P., Cescatti, A., Janssens, I.A., Peñuelas, J., Buermann, W., Chen, A., Li, X., Myneni, R.B., Wang, X., Wang, Y., Yang, Y., Zeng, Z., Zhang, Y., McVicar, T.R., 2020. Summer soil drying exacerbated by earlier spring greening of northern vegetation. Sci. Adv. 6, eaax0255. https://doi.org/10.1126/sciadv.aax0255

Linscheid, N., Estupinan-Suarez, L.M., Brenning, A., Carvalhais, N., Cremer, F., Gans, F., Rammig, A., Reichstein, M., Sierra, C.A., Mahecha, M.D., 2020. Towards a global understanding of vegetation–climate dynamics at multiple timescales. Biogeosciences 17, 945–962. https://doi.org/10.5194/bg-17-945-2020

Liu, J., Zhang, Q., Feng, S., Gu, X., Singh, V.P., Sun, P., 2019. Global Attribution of Runoff Variance Across Multiple Timescales. J. Geophys. Res. Atmospheres 124, 13962–13974. https://doi.org/10.1029/2019JD030539

Liu, L., Zhang, R.H., Zuo, Z.Y., 2014. Intercomparison of spring soil moisture among multiple reanalysis data sets over eastern China. J. Geophys. Res.-Atmospheres 119, 54–64. https://doi.org/10.1002/2013jd020940

Liu, Y., Liu, R., Chen, J.M., 2012. Retrospective retrieval of long-term consistent global leaf area index (1981 -2011) from combined AVHRR and MODIS data: LONG-TERM GLOBAL LEAF AREA INDEX. J. Geophys. Res. Biogeosciences 117, n/a-n/a. https://doi.org/10.1029/2012JG002084

Liu, Y., Xiao, J., Ju, W., Zhu, G., Wu, X., Fan, W., Li, D., Zhou, Y., 2018. Satellite-derived LAI products exhibit large discrepancies and can lead to substantial uncertainty in simulated carbon and water fluxes. REMOTE Sens. Environ. 206, 174–188. https://doi.org/10.1016/j.rse.2017.12.024

Liu, Y.Y., de Jeu, R.A.M., McCabe, M.F., Evans, J.P., van Dijk, A.I.J.M., 2011. Global long-term passive microwave satellite-based retrievals of vegetation optical depth: LONG-TERM VEGETATION OPTICAL DEPTH. Geophys. Res. Lett. 38, n/a-n/a. https://doi.org/10.1029/2011GL048684

Lundberg, S., Lee, S., 2017. A Unified Approach to Interpreting Model Predictions, in: Guyon, I., Luxburg, U., Bengio, S., Wallach, H., Fergus, R., Vishwanathan, S., Garnett, R. (Eds.). Presented at the ADVANCES IN NEURAL INFORMATION PROCESSING SYSTEMS 30 (NIPS 2017).

Lunetta, K.L., Hayward, L.B., Segal, J., Van Eerdewegh, P., 2004. Screening large-scale association study data: Exploiting interactions using random forests. BMC Genet. 5, 32. https://doi.org/10.1186/1471-2156-5-32

Luo, X., Keenan, T.F., 2020. Global evidence for the acclimation of ecosystem photosynthesis to light. Nat. Ecol. Evol. 4, 1351–1357. https://doi.org/10.1038/s41559-020-1258-7

Ma, H., Li, X., Zeng, J., Zhang, X., Dong, J., Chen, N., Fan, L., Sadeghi, M., Frappart, F., Liu, X., Wang, M., Wang, H., Fu, Z., Xing, Z., Ciais, P., Wigneron, J.-P., 2023. An assessment of L-band surface soil moisture

products from SMOS and SMAP in the tropical areas. Remote Sens. Environ. 284, 113344. https://doi.org/10.1016/j.rse.2022.113344

Madani, N., Kimball, J., Jones, L., Parazoo, N., Guan, K., 2017. Global Analysis of Bioclimatic Controls on Ecosystem Productivity Using Satellite Observations of Solar-Induced Chlorophyll Fluorescence. Remote Sens. 9, 530. https://doi.org/10.3390/rs9060530

Magney, T., Bowling, D., Logan, B., Grossmann, K., Stutz, J., Blanken, P., Burns, S., Cheng, R., Garcia, M., Kohler, P., Lopez, S., Parazoo, N., Raczka, B., Schimel, D., Frankenberg, C., 2019. Mechanistic evidence for tracking the seasonality of photosynthesis with solar-induced fluorescence. Proc. Natl. Acad. Sci. U. S. A. 116, 11640–11645. https://doi.org/10.1073/pnas.1900278116

Martens, B., Miralles, D.G., Lievens, H., van der Schalie, R., de Jeu, R.A.M., Fernández-Prieto, D., Beck, H.E., Dorigo, W.A., Verhoest, N.E.C., 2017. GLEAM v3: satellite-based land evaporation and root-zone soil moisture. Geosci. Model Dev. 10, 1903–1925. https://doi.org/10.5194/gmd-10-1903-2017

Martini, D., Sakowska, K., Wohlfahrt, G., Pacheco‐Labrador, J., van der Tol, C., Porcar‐Castell, A., Magney, T.S., Carrara, A., Colombo, R., El‐Madany, T.S., Gonzalez‐Cascon, R., Martín, M.P., Julitta, T., Moreno, G., Rascher, U., Reichstein, M., Rossini, M., Migliavacca, M., 2022. Heatwave breaks down the linearity between sun‐induced fluorescence and gross primary production. New Phytol. 233, 2415–2428. https://doi.org/10.1111/nph.17920

Matheny, A.M., Bohrer, G., Garrity, S.R., Morin, T.H., Howard, C.J., Vogel, C.S., 2015. Observations of stem water storage in trees of opposing hydraulic strategies. Ecosphere 6, 1–13.

McDowell, N., Pockman, W.T., Allen, C.D., Breshears, D.D., Cobb, N., Kolb, T., Plaut, J., Sperry, J., West, A., Williams, D.G., Yepez, E.A., 2008. Mechanisms of plant survival and mortality during drought: why do some plants survive while others succumb to drought? New Phytol. 178, 719–739. https://doi.org/10.1111/j.1469-8137.2008.02436.x

Medina Camarena, K.S., Wübbelmann, T., Förster, K., 2022. What Is the Contribution of Urban Trees to Mitigate Pluvial Flooding? Hydrology 9, 108. https://doi.org/10.3390/hydrology9060108

Medlyn, B., De Kauwe, M., Duursma, R., 2016. New developments in the effort to model ecosystems under water stress. NEW Phytol. 212, 5–7. https://doi.org/10.1111/nph.14082

Medlyn, B.E., Duursma, R.A., Eamus, D., Ellsworth, D.S., Prentice, I.C., Barton, C.V.M., Crous, K.Y., De Angelis, P., Freeman, M., Wingate, L., 2011. Reconciling the optimal and empirical approaches to modelling stomatal conductance: RECONCILING OPTIMAL AND EMPIRICAL STOMATAL MODELS. Glob. Change Biol. 17, 2134–2144. https://doi.org/10.1111/j.1365-2486.2010.02375.x

Merz, B., Blöschl, G., Vorogushyn, S., Dottori, F., Aerts, J.C.J.H., Bates, P., Bertola, M., Kemter, M., Kreibich, H., Lall, U., Macdonald, E., 2021. Causes, impacts and patterns of disastrous river floods. Nat. Rev. Earth Environ. 2, 592–609. https://doi.org/10.1038/s43017-021-00195-3

Merz, R., Blöschl, G., 2003. A process typology of regional floods: PROCESS TYPOLOGY OF REGIONAL FLOODS. Water Resour. Res. 39. https://doi.org/10.1029/2002WR001952

Migliavacca, M., Meroni, M., Manca, G., Matteucci, G., Montagnani, L., Grassi, G., Zenone, T., Teobaldelli, M., Goded, I., Colombo, R., Seufert, G., 2009. Seasonal and interannual patterns of carbon and water fluxes of a poplar plantation under peculiar eco-climatic conditions. Agric. For. Meteorol. 149, 1460–1476. https://doi.org/10.1016/j.agrformet.2009.04.003

Migliavacca, M., Perez‐Priego, O., Rossini, M., El‐Madany, T.S., Moreno, G., van der Tol, C., Rascher, U., Berninger, A., Bessenbacher, V., Burkart, A., Carrara, A., Fava, F., Guan, J., Hammer, T.W., Henkel, K., Juarez‐Alcalde, E., Julitta, T., Kolle, O., Martín, M.P., Musavi, T., Pacheco‐Labrador, J., Pérez‐Burgueño, A., Wutzler, T., Zaehle, S., Reichstein, M., 2017. Plant functional traits and canopy structure control the relationship between photosynthetic CO 2 uptake and far‐red sun‐induced fluorescence in a Mediterranean grassland under different nutrient availability. New Phytol. 214, 1078–1091. https://doi.org/10.1111/nph.14437

Miguez-Macho, G., Fan, Y., 2021. Spatiotemporal origin of soil water taken up by vegetation. Nature 598, 624–628. https://doi.org/10.1038/s41586-021-03958-6

Mildrexler, D.J., Zhao, M., Running, S.W., 2011. A global comparison between station air temperatures and MODIS land surface temperatures reveals the cooling role of forests. J. Geophys. Res. 116, G03025. https://doi.org/10.1029/2010JG001486

Mishra, A.K., Singh, V.P., 2010. A review of drought concepts. J. Hydrol. 391, 202–216. https://doi.org/10.1016/j.jhydrol.2010.07.012

Moesinger, L., Dorigo, W., de Jeu, R., van der Schalie, R., Scanlon, T., Teubner, I., Forkel, M., 2020. The global long-term microwave Vegetation Optical Depth Climate Archive (VODCA). Earth Syst. Sci. Data 12, 177–196. https://doi.org/10.5194/essd-12-177-2020

Molnar, C., 2022. Interpretable machine learning: a guide for making black box models explainable, Second edition. ed. Christoph Molnar, Munich, Germany.

Morton, D.C., Nagol, J., Carabajal, C.C., Rosette, J., Palace, M., Cook, B.D., Vermote, E.F., Harding, D.J., North, P.R.J., 2014. Amazon forests maintain consistent canopy structure and greenness during the dry season. Nature 506, 221–224. https://doi.org/10.1038/nature13006

Mu, M., De Kauwe, M.G., Ukkola, A.M., Pitman, A.J., Guo, W., Hobeichi, S., Briggs, P.R., 2021. Exploring how groundwater buffers the influence of heatwaves on vegetation function during multi-year droughts. Earth Syst. Dyn. 12, 919–938. https://doi.org/10.5194/esd-12-919-2021

Mu, Q., Zhao, M., Running, S.W., 2011. Improvements to a MODIS global terrestrial evapotranspiration algorithm. Remote Sens. Environ. 115, 1781–1800. https://doi.org/10.1016/j.rse.2011.02.019

Muñoz-Sabater, J., Dutra, E., Agustí-Panareda, A., Albergel, C., Arduini, G., Balsamo, G., Boussetta, S., Choulga, M., Harrigan, S., Hersbach, H., Martens, B., Miralles, D.G., Piles, M., Rodríguez-Fernández, N.J., Zsoter, E., Buontempo, C., Thépaut, J.-N., 2021. ERA5-Land: a state-of-the-art global reanalysis dataset for land applications. Earth Syst. Sci. Data 13, 4349–4383. https://doi.org/10.5194/essd-13-4349-2021

Myneni, R.B., Hall, F.G., Sellers, P.J., Marshak, A.L., 1995. The interpretation of spectral vegetation indexes. IEEE Trans. Geosci. Remote Sens. 33, 481–486. https://doi.org/10.1109/36.377948

Naumann, G., Spinoni, J., Vogt, J.V., Barbosa, P., 2015. Assessment of drought damages and their uncertainties in Europe. Environ. Res. Lett. 10, 124013. https://doi.org/10.1088/1748-9326/10/12/124013

Nemani, R.R., Keeling, C.D., Hashimoto, H., Jolly, W.M., Piper, S.C., Tucker, C.J., Myneni, R.B., Running, S.W., 2003. Climate-Driven Increases in Global Terrestrial Net Primary Production from 1982 to 1999. Science 300, 1560–1563. https://doi.org/10.1126/science.1082750

Nicodemus, K.K., 2011. Letter to the Editor: On the stability and ranking of predictors from random forest variable importance measures. Brief. Bioinform. 12, 369–373. https://doi.org/10.1093/bib/bbr016

Nippert, J.B., Holdo, R.M., 2015. Challenging the maximum rooting depth paradigm in grasslands and savannas. Funct. Ecol. 29, 739–745.

Novick, K.A., Ficklin, D.L., Stoy, P.C., Williams, C.A., Bohrer, G., Oishi, A.C., Papuga, S.A., Blanken, P.D., Noormets, A., Sulman, B.N., Scott, R.L., Wang, L., Phillips, R.P., 2016. The increasing importance of atmospheric demand for ecosystem water and carbon fluxes. Nat. Clim. Change 6, 1023–1027. https://doi.org/10.1038/nclimate3114

O, S., Bastos, A., Reichstein, M., Li, W., Denissen, J., Graefen, H., Orth, R., 2022. The Role of Climate and Vegetation in Regulating Drought–Heat Extremes. J. Clim. 35, 5677–5685. https://doi.org/10.1175/JCLI-D-21-0675.1

O., S., Orth, R., 2021. Global soil moisture data derived through machine learning trained with in-situ measurements. Sci. Data 8, 170. https://doi.org/10.1038/s41597-021-00964-1

Ohta, T., Kotani, A., Iijima, Y., Maximov, T.C., Ito, S., Hanamura, M., Kononov, A.V., Maximov, A.P., 2014. Effects of waterlogging on water and carbon dioxide fluxes and environmental variables in a Siberian larch forest, 1998–2011. Agric. For. Meteorol. 188, 64–75. https://doi.org/10.1016/j.agrformet.2013.12.012

Oliphant, T.E., 2006. A guide to NumPy. Trelgol Publishing USA.

Oliveira, R.S., Bezerra, L., Davidson, E.A., Pinto, F., Klink, C.A., Nepstad, D.C., Moreira, A., 2005. Deep root function in soil water dynamics in cerrado savannas of central Brazil. Funct. Ecol. 19, 574–581. https://doi.org/10.1111/j.1365-2435.2005.01003.x

Orth, R., Destouni, G., 2018. Drought reduces blue-water fluxes more strongly than green-water fluxes in Europe. Nat. Commun. 9, 3602. https://doi.org/10.1038/s41467-018-06013-7

Orth, R., O, S., Zscheischler, J., Mahecha, M.D., Reichstein, M., 2022. Contrasting biophysical and societal impacts of hydro-meteorological extremes. Environ. Res. Lett. 17, 014044. https://doi.org/10.1088/1748-9326/ac4139

Orth, R., Seneviratne, S.I., 2013. Propagation of soil moisture memory to streamflow and evapotranspiration in Europe. Hydrol. Earth Syst. Sci. 17, 3895–3911. https://doi.org/10.5194/hess-17-3895-2013

Owens, M.K., Lyons, R.K., Alejandro, C.L., 2006. Rainfall partitioning within semiarid juniper communities: effects of event size and canopy cover. Hydrol. Process. 20, 3179–3189. https://doi.org/10.1002/hyp.6326

Pacheco-Labrador, J., Perez-Priego, O., El-Madany, T.S., Julitta, T., Rossini, M., Guan, J., Moreno, G., Carvalhais, N., Martín, M.P., Gonzalez-Cascon, R., Kolle, O., Reischtein, M., van der Tol, C., Carrara, A., Martini, D., Hammer, T.W., Moossen, H., Migliavacca, M., 2019. Multiple-constraint inversion of SCOPE. Evaluating the potential of GPP and SIF for the retrieval of plant functional traits. Remote Sens. Environ. 234, 111362. https://doi.org/10.1016/j.rse.2019.111362

Page, T., Chappell, N.A., Beven, K.J., Hankin, B., Kretzschmar, A., 2020. Assessing the significance of wet ‐ canopy evaporation from forests during extreme rainfall events for flood mitigation in mountainous regions of the UNITED KINGDOM. Hydrol. Process. 34, 4740–4754. https://doi.org/10.1002/hyp.13895

Pan, J., Sharif, R., Xu, X., Chen, X., 2021. Mechanisms of Waterlogging Tolerance in Plants: Research Progress and Prospects. Front. Plant Sci. 11, 627331. https://doi.org/10.3389/fpls.2020.627331

Panwar, A., Kleidon, A., 2022. Evaluating the Response of Diurnal Variations in Surface and Air Temperature to Evaporative Conditions across Vegetation Types in FLUXNET and ERA5. J. Clim. 35, 2701–2728. https://doi.org/10.1175/JCLI-D-21-0345.1

Panwar, A., Renner, M., Kleidon, A., 2020. Imprints of evaporative conditions and vegetation type in diurnal temperature variations. Hydrol. Earth Syst. Sci. 24, 4923–4942. https://doi.org/10.5194/hess-24-4923-2020

Papale, D., Valentini, R., 2003. A new assessment of European forests carbon exchanges by eddy fluxes and artificial neural network spatialization: A NEW ASSESSMENT OF EUROPEAN FORESTS CARBON. Glob. Change Biol. 9, 525–535. https://doi.org/10.1046/j.1365-2486.2003.00609.x

Paschalis, A., Fatichi, S., Katul, G.G., Ivanov, V.Y., 2015. Cross ‐ scale impact of climate temporal variability on ecosystem water and carbon fluxes. J. Geophys. Res. Biogeosciences 120, 1716–1740. https://doi.org/10.1002/2015JG003002

Pastorello, G. et al., 2021. Author Correction: The FLUXNET2015 dataset and the ONEFlux processing pipeline for eddy covariance data. Sci. Data 8, 72. https://doi.org/10.1038/s41597-021-00851-9

Pearson, R.G., Phillips, S.J., Loranty, M.M., Beck, P.S., Damoulas, T., Knight, S.J., Goetz, S.J., 2013. Shifts in Arctic vegetation and associated feedbacks under climate change. Nat. Clim. Change 3, 673–677.

Pedelty, J., Devadiga, S., Masuoka, E., Brown, M., 2017. Generating a long-term land data record from the AVHRR and MODIS instruments. 2007 IEEE Int. Geosci. Remote Sens. Symp. 1021–1025.

Pedregosa, F., Varoquaux, G., Gramfort, A., Michel, V., Thirion, B., Grisel, O., Blondel, M., Prettenhofer, P., Weiss, R., Dubourg, V., 2011. Scikit-learn: Machine learning in Python. J. Mach. Learn. Res. 12, 2825–2830.

Peel, M.C., Finlayson, B.L., McMahon, T.A., 2007. Updated world map of the Köppen-Geiger climate classification. Hydrol. Earth Syst. Sci. 11, 1633–1644. https://doi.org/10.5194/hess-11-1633-2007

Peters, E., Bier, G., van Lanen, H.A.J., Torfs, P.J.J.F., 2006. Propagation and spatial distribution of drought in a groundwater catchment. J. Hydrol. 321, 257–275. https://doi.org/10.1016/j.jhydrol.2005.08.004

Piao, S., Liu, Z., Wang, T., Peng, S., Ciais, P., Huang, M., Ahlstrom, A., Burkhart, J.F., Chevallier, F., Janssens, I.A., Jeong, S.-J., Lin, X., Mao, J., Miller, J., Mohammat, A., Myneni, R.B., Peñuelas, J., Shi, X., Stohl, A., Yao, Y., Zhu, Z., Tans, P.P., 2017. Weakening temperature control on the interannual variations of spring carbon uptake across northern lands. Nat. Clim. Change 7, 359–363. https://doi.org/10.1038/nclimate3277

Pitman, A.J., 2003. The evolution of, and revolution in, land surface schemes designed for climate models. Int. J. Climatol. 23, 479–510. https://doi.org/10.1002/joc.893

Powell, T.L., Galbraith, D.R., Christoffersen, B.O., Harper, A., Imbuzeiro, H.M.A., Rowland, L., Almeida, S., Brando, P.M., Costa, A.C.L., Costa, M.H., Levine, N.M., Malhi, Y., Saleska, S.R., Sotta, E., Williams, M., Meir, P., Moorcroft, P.R., 2013. Confronting model predictions of carbon fluxes with measurements of Amazon forests subjected to experimental drought. New Phytol. 200, 350–365. https://doi.org/10.1111/nph.12390

Reichstein, M., Bahn, M., Ciais, P., Frank, D., Mahecha, M.D., Seneviratne, S.I., Zscheischler, J., Beer, C., Buchmann, N., Frank, D.C., Papale, D., Rammig, A., Smith, P., Thonicke, K., van der Velde, M., Vicca, S., Walz, A., Wattenbach, M., 2013. Climate extremes and the carbon cycle. Nature 500, 287–295. https://doi.org/10.1038/nature12350

Reichstein, M., Camps-Valls, G., Stevens, B., Jung, M., Denzler, J., Carvalhais, N., Prabhat, 2019. Deep learning and process understanding for data-driven Earth system science. Nature 566, 195–204. https://doi.org/10.1038/s41586-019-0912-1

Reichstein, M., Falge, E., Baldocchi, D., Papale, D., Aubinet, M., Berbigier, P., Bernhofer, C., Buchmann, N., Gilmanov, T., Granier, A., Grunwald, T., Havrankova, K., Ilvesniemi, H., Janous, D., Knohl, A., Laurila, T.,

Lohila, A., Loustau, D., Matteucci, G., Meyers, T., Miglietta, F., Ourcival, J.-M., Pumpanen, J., Rambal, S., Rotenberg, E., Sanz, M., Tenhunen, J., Seufert, G., Vaccari, F., Vesala, T., Yakir, D., Valentini, R., 2005. On the separation of net ecosystem exchange into assimilation and ecosystem respiration: review and improved algorithm. Glob. Change Biol. 11, 1424–1439. https://doi.org/10.1111/j.1365-2486.2005.001002.x

Rene Orth, Seneviratne, S.I., 2015. Introduction of a simple-model-based land surface dataset for Europe. Environ. Res. Lett. 10, 044012. https://doi.org/10.1088/1748-9326/10/4/044012

Reynolds, C.A., Jackson, T.J., Rawls, W.J., 2000. Estimating soil water-holding capacities by linking the Food and Agriculture Organization Soil map of the world with global pedon databases and continuous pedotransfer functions. Water Resour. Res. 36, 3653–3662. https://doi.org/10.1029/2000WR900130

Rogers, A., Medlyn, B.E., Dukes, J.S., Bonan, G., von Caemmerer, S., Dietze, M.C., Kattge, J., Leakey, A.D.B., Mercado, L.M., Niinemets, U., Prentice, I.C., Serbin, S.P., Sitch, S., Way, D.A., Zaehle, S., 2017. A roadmap for improving the representation of photosynthesis in Earth system models. New Phytol. 213, 22–42. https://doi.org/10.1111/nph.14283

Rouse, J.W., Haas, R.H., Schell, J.A., Deering, D.W., 1974. Monitoring vegetationsystemsin theGreat Plains withERTS. NASA. Goddard Space Flight Center 3d ERTS-1 Symposium 1 Sect. A, 309–317.

Sack, L., Scoffoni, C., 2012. Measurement of Leaf Hydraulic Conductance and Stomatal Conductance and Their Responses to Irradiance and Dehydration Using the Evaporative Flux Method (EFM). J. Vis. Exp. 4179. https://doi.org/10.3791/4179

Sadiqi, S.S.J., Hong, E.-M., Nam, W.-H., Kim, T., 2022. Review: An integrated framework for understanding ecological drought and drought resistance. Sci. Total Environ. 846, 157477. https://doi.org/10.1016/j.scitotenv.2022.157477

Sakschewski, B., Von Bloh, W., Boit, A., Poorter, L., Peña-Claros, M., Heinke, J., Joshi, J., Thonicke, K., 2016. Resilience of Amazon forests emerges from plant trait diversity. Nat. Clim. Change 6, 1032–1036.

Sakschewski, B., von Bloh, W., Drüke, M., Sörensson, A.A., Ruscica, R., Langerwisch, F., Billing, M., Bereswill, S., Hirota, M., Oliveira, R.S., Heinke, J., Thonicke, K., 2020. Variable tree rooting strategies improve tropical productivity and evapotranspiration in a dynamic global vegetation model (preprint). Biodiversity and Ecosystem Function: Terrestrial. https://doi.org/10.5194/bg-2020-97

Samanta, A., Ganguly, S., Hashimoto, H., Devadiga, S., Vermote, E., Knyazikhin, Y., Nemani, R.R., Myneni, R.B., 2010. Amazon forests did not green-up during the 2005 drought: AMAZON DROUGHT SENSITIVITY. Geophys. Res. Lett. 37, n/a-n/a. https://doi.org/10.1029/2009GL042154

Schaphoff, S., von Bloh, W., Rammig, A., Thonicke, K., Biemans, H., Forkel, M., Gerten, D., Heinke, J., Jagermeyr, J., Knauer, J., Langerwisch, F., Lucht, W., Muller, C., Rolinski, S., Waha, K., 2018. LPJmL4-a

dynamic global vegetation model with managed land - Part 1: Model description. Geosci. MODEL Dev. 11, 1343–1375. https://doi.org/10.5194/gmd-11-1343-2018

Schenk, H.J., Jackson, R.B., 2009. ISLSCP II Ecosystem Rooting Depths 1.350322 MB. https://doi.org/10.3334/ORNLDAAC/929

Schlaepfer, D.R., Bradford, J.B., Lauenroth, W.K., Munson, S.M., Tietjen, B., Hall, S.A., Wilson, S.D., Duniway, M.C., Jia, G., Pyke, D.A., Lkhagva, A., Jamiyansharav, K., 2017. Climate change reduces extent of temperate drylands and intensifies drought in deep soils. Nat. Commun. 8, 14196. https://doi.org/10.1038/ncomms14196

Schulze, E.-D., Mooney, H.A., Sala, O., Jobbagy, E., Buchmann, N., Bauer, G., Canadell, J., Jackson, R., Loreti, J., Oesterheld, M., 1996. Rooting depth, water availability, and vegetation cover along an aridity gradient in Patagonia. Oecologia 108, 503–511.

Schumacher, D., Keune, Jessica, Dirmeyer, Paul, Miralles, Diego G., 2022. Source code for "Drought self-propagation in drylands due to land–atmosphere feedbacks." https://doi.org/10.5281/ZENODO.5840791

Schumacher, D.L., Keune, J., Dirmeyer, P., Miralles, D.G., 2022. Drought self-propagation in drylands due to land–atmosphere feedbacks. Nat. Geosci. 15, 262–268. https://doi.org/10.1038/s41561-022-00912-7

Seabold, S., Perktold, J., 2010. Statsmodels: Econometric and statistical modeling with python. Presented at the Proceedings of the 9th Python in Science Conference, Austin, TX, p. 61.

Seddon, A.W.R., Macias-Fauria, M., Long, P.R., Benz, D., Willis, K.J., 2016. Sensitivity of global terrestrial ecosystems to climate variability. Nature 531, 229–232. https://doi.org/10.1038/nature16986

Seneviratne, S.I., Corti, T., Davin, E.L., Hirschi, M., Jaeger, E.B., Lehner, I., Orlowsky, B., Teuling, A.J., 2010. Investigating soil moisture–climate interactions in a changing climate: A review. Earth-Sci. Rev. 99, 125–161. https://doi.org/10.1016/j.earscirev.2010.02.004

Seneviratne, S.I., Lehner, I., Gurtz, J., Teuling, A.J., Lang, H., Moser, U., Grebner, D., Menzel, L., Schroff, K., Vitvar, T., Zappa, M., 2012. Swiss prealpine Rietholzbach research catchment and lysimeter: 32 year time series and 2003 drought event: RIETHOLZBACH 32 YEAR SERIES AND 2003 DROUGHT. Water Resour. Res. 48. https://doi.org/10.1029/2011WR011749

Sharma, A., Wasko, C., Lettenmaier, D.P., 2018. If Precipitation Extremes Are Increasing, Why Aren't Floods? Water Resour. Res. 54, 8545–8551. https://doi.org/10.1029/2018WR023749

Siebert, S., Kummu, M., Porkka, M., Doll, P., Ramankutty, N., Scanlon, B., 2015. A global data set of the extent of irrigated land from 1900 to 2005. Hydrol. EARTH Syst. Sci. 19, 1521–1545. https://doi.org/10.5194/hess-19-1521-2015

Sikorska, A.E., Viviroli, D., Seibert, J., 2015. Flood‐type classification in mountainous catchments using crisp and fuzzy decision trees. Water Resour. Res. 51, 7959–7976. https://doi.org/10.1002/2015WR017326

Sitch, S., Friedlingstein, P., Gruber, N., Jones, S.D., Murray-Tortarolo, G., Ahlström, A., Doney, S.C., Graven, H., Heinze, C., Huntingford, C., Levis, S., Levy, P.E., Lomas, M., Poulter, B., Viovy, N., Zaehle, S., Zeng, N., Arneth, A., Bonan, G., Bopp, L., Canadell, J.G., Chevallier, F., Ciais, P., Ellis, R., Gloor, M., Peylin, P., Piao, S.L., Le Quéré, C., Smith, B., Zhu, Z., Myneni, R., 2015. Recent trends and drivers of regional sources and sinks of carbon dioxide. Biogeosciences 12, 653–679. https://doi.org/10.5194/bg-12-653-2015

Smith, W.K., Fox, A.M., MacBean, N., Moore, D.J.P., Parazoo, N.C., 2020. Constraining estimates of terrestrial carbon uptake: new opportunities using long‐term satellite observations and data assimilation. New Phytol. 225, 105–112. https://doi.org/10.1111/nph.16055

Song, S., Wang, W., 2019. Impacts of Antecedent Soil Moisture on the Rainfall-Runoff Transformation Process Based on High-Resolution Observations in Soil Tank Experiments. WATER 11. https://doi.org/10.3390/w11020296

Song, X.P., Hansen, M.C., Stehman, S.V., Potapov, P.V., Tyukavina, A., Vermote, E.F., Townshend, J.R., 2018. Global land change from 1982 to 2016. Nature 560, 639–643. https://doi.org/10.1038/s41586-018-0411-9

Stahl, K., Hisdal, H., Hannaford, J., Tallaksen, L.M., van Lanen, H.A.J., Sauquet, E., Demuth, S., Fendekova, M., Jódar, J., 2010. Streamflow trends in Europe: evidence from a dataset of near-natural catchments. Hydrol. Earth Syst. Sci. 14, 2367–2382. https://doi.org/10.5194/hess-14-2367-2010

Stein, L., Pianosi, F., Woods, R., 2020. Event‐based classification for global study of river flood generating processes. Hydrol. Process. 34, 1514–1529. https://doi.org/10.1002/hyp.13678

Stocker, B.D., Tumber-Dávila, S.J., Konings, A.G., Anderson, M.B., Hain, C., Jackson, R.B., 2021. Global distribution of the rooting zone water storage capacity reflects plant adaptation to the environment (preprint). Ecology. https://doi.org/10.1101/2021.09.17.460332

Stocker, B.D., Wang, H., Smith, N.G., Harrison, S.P., Keenan, T.F., Sandoval, D., Davis, T., Prentice, I.C., 2020. P-model v1.0: an optimality-based light use efficiency model for simulating ecosystem gross primary production. Geosci. Model Dev. 13, 1545–1581. https://doi.org/10.5194/gmd-13-1545-2020

Stocker, B.D., Zscheischler, J., Keenan, T.F., Prentice, I.C., Peñuelas, J., Seneviratne, S.I., 2018. Quantifying soil moisture impacts on light use efficiency across biomes. New Phytol. 218, 1430–1449. https://doi.org/10.1111/nph.15123

Stocker, B.D., Zscheischler, J., Keenan, T.F., Prentice, I.C., Seneviratne, S.I., Peñuelas, J., 2019. Drought impacts on terrestrial primary production underestimated by satellite monitoring. Nat. Geosci. 12, 264–270. https://doi.org/10.1038/s41561-019-0318-6

Sundararajan, M., Najmi, A., 2019. The many Shapley values for model explanation. ArXiv Prepr. ArXiv190808474.

Swenson, S., Wahr, J., 2006. Post-processing removal of correlated errors in GRACE data. Geophys. Res. Lett. 33, L08402. https://doi.org/10.1029/2005GL025285

Tarasova, L., Merz, R., Kiss, A., Basso, S., Blöschl, G., Merz, B., Viglione, A., Plötner, S., Guse, B., Schumann, A., Fischer, S., Ahrens, B., Anwar, F., Bárdossy, A., Bühler, P., Haberlandt, U., Kreibich, H., Krug, A., Lun, D., Müller‐Thomy, H., Pidoto, R., Primo, C., Seidel, J., Vorogushyn, S., Wietzke, L., 2019. Causative classification of river flood events. WIREs Water 6. https://doi.org/10.1002/wat2.1353

Tarek, M., Brissette, F.P., Arsenault, R., 2020. Evaluation of the ERA5 reanalysis as a potential reference dataset for hydrological modelling over North America. Hydrol. Earth Syst. Sci. 24, 2527–2544.

Teuling, A.J., Seneviratne, S.I., Stöckli, R., Reichstein, M., Moors, E., Ciais, P., Luyssaert, S., van den Hurk, B., Ammann, C., Bernhofer, C., Dellwik, E., Gianelle, D., Gielen, B., Grünwald, T., Klumpp, K., Montagnani, L., Moureaux, C., Sottocornola, M., Wohlfahrt, G., 2010. Contrasting response of European forest and grassland energy exchange to heatwaves. Nat. Geosci. 3, 722–727. https://doi.org/10.1038/ngeo950

Teuling, A.J., Van Loon, A.F., Seneviratne, S.I., Lehner, I., Aubinet, M., Heinesch, B., Bernhofer, C., Grünwald, T., Prasse, H., Spank, U., 2013. Evapotranspiration amplifies European summer drought: EVAPOTRANSPIRATION AND SUMMER DROUGHTS DROUGHTS. Geophys. Res. Lett. 40, 2071–2075. https://doi.org/10.1002/grl.50495

Tian, W., Liu, X., Liu, C., Bai, P., 2018. Investigation and simulations of changes in the relationship of precipitation-runoff in drought years. J. Hydrol. 565, 95–105. https://doi.org/10.1016/j.jhydrol.2018.08.015

Tramblay, Y., Villarini, G., Khalki, E.M., Gründemann, G., Hughes, D., 2021. Evaluation of the Drivers Responsible for Flooding in Africa. Water Resour. Res. 57. https://doi.org/10.1029/2021WR029595

Tramontana, G., Jung, M., Schwalm, C.R., Ichii, K., Camps-Valls, G., Ráduly, B., Reichstein, M., Arain, M.A., Cescatti, A., Kiely, G., 2016. Predicting carbon dioxide and energy fluxes across global FLUXNET sites with regression algorithms. Biogeosciences 13, 4291–4313.

Trugman, A.T., Medvigy, D., Mankin, J.S., Anderegg, W.R.L., 2018. Soil Moisture Stress as a Major Driver of Carbon Cycle Uncertainty. Geophys. Res. Lett. 45, 6495–6503. https://doi.org/10.1029/2018GL078131

Tucker, C.J., Pinzon, J.E., Brown, M.E., Slayback, D.A., Pak, E.W., Mahoney, R., Vermote, E.F., El Saleous, N., 2005. An extended AVHRR 8‐km NDVI dataset compatible with MODIS and SPOT vegetation NDVI data. Int. J. Remote Sens. 26, 4485–4498. https://doi.org/10.1080/01431160500168686

Ukkola, A M, De Kauwe, M.G., Pitman, A.J., Best, M.J., Abramowitz, G., Haverd, V., Decker, M., Haughton, N., 2016. Land surface models systematically overestimate the intensity, duration and magnitude of seasonal-scale evaporative droughts. Environ. Res. Lett. 11, 104012. https://doi.org/10.1088/1748-9326/11/10/104012

Ukkola, Anna M., Pitman, A.J., Decker, M., De Kauwe, M.G., Abramowitz, G., Kala, J., Wang, Y.-P., 2016. Modelling evapotranspiration during precipitation deficits: identifying critical processes in a land surface model. Hydrol. Earth Syst. Sci. 20, 2403–2419. https://doi.org/10.5194/hess-20-2403-2016

van der Tol, C., Berry, J.A., Campbell, P.K.E., Rascher, U., 2014. Models of fluorescence and photosynthesis for interpreting measurements of solar‐induced chlorophyll fluorescence. J. Geophys. Res. Biogeosciences 119, 2312–2327. https://doi.org/10.1002/2014JG002713

van Dijk, A.I.J.M., Beck, H.E., Crosbie, R.S., de Jeu, R.A.M., Liu, Y.Y., Podger, G.M., Timbal, B., Viney, N.R., 2013. The Millennium Drought in southeast Australia (2001-2009): Natural and human causes and implications for water resources, ecosystems, economy, and society: CAUSES AND IMPACTS OF AUSTRALIA'S RECORD DROUGHT. Water Resour. Res. 49, 1040–1057. https://doi.org/10.1002/wrcr.20123

Van Loon, A.F., 2015. Hydrological drought explained. WIREs Water 2, 359–392. https://doi.org/10.1002/wat2.1085

Van Loon, F., 2013. On the propagation of drought. How climate and catchment characteristics influence hydrological drought development and recovery. Wageningen University, Wageningen.

Verger, A., Baret, F., Weiss, M., 2020. Algorithm Theoretical Basis Document - GEOV2/AVHRR: Leaf Area Index (LAI), Fraction of Absorbed Photosynthetically Active Radiation (FAPAR) and Fraction of green Vegetation Cover (FCOVER) from LTDR AVHRR.

Vicari, M.B., Pisek, J., Disney, M., 2019. New estimates of leaf angle distribution from terrestrial LiDAR: Comparison with measured and modelled estimates from nine broadleaf tree species. Agric. For. Meteorol. 264, 322–333. https://doi.org/10.1016/j.agrformet.2018.10.021

Wagle, P., Zhang, Y., Jin, C., Xiao, X., 2016. Comparison of solar‐induced chlorophyll fluorescence, light‐use efficiency, and process‐based GPP models in maize. Ecol. Appl. 26, 1211–1222.

Wahr, J., Swenson, S., Zlotnicki, V., Velicogna, I., 2004. Time-variable gravity from GRACE: First results: TIME-VARIABLE GRAVITY FROM GRACE. Geophys. Res. Lett. 31, n/a-n/a. https://doi.org/10.1029/2004GL019779

Walther, S., Duveiller, G., Jung, M., Guanter, L., Cescatti, A., Camps‐Valls, G., 2019. Satellite Observations of the Contrasting Response of Trees and Grasses to Variations in Water Availability. Geophys. Res. Lett. 46, 1429–1440. https://doi.org/10.1029/2018GL080535

Wang, S., Zhang, Y., Ju, W., Chen, J., 2021. Response to Comments on "Recent global decline of CO2 fertilization effects on vegetation photosynthesis." SCIENCE 373, 6562.

Wang, S., Zhang, Y., Ju, W., Chen, J.M., Ciais, P., Cescatti, A., Sardans, J., Janssens, I.A., Wu, M., Berry, J.A., Campbell, E., Fernández-Martínez, M., Alkama, R., Sitch, S., Friedlingstein, P., Smith, W.K., Yuan, W.,

He, W., Lombardozzi, D., Kautz, M., Zhu, D., Lienert, S., Kato, E., Poulter, B., Sanders, T.G.M., Krüger, I., Wang, R. Zeng, N., Tian, H., Vuichard, N., Jain, A.K., Wiltshire, A., Haverd, V., Goll, D.S., Peñuelas, J., 2020. Recent global decline of CO 2 fertilization effects on vegetation photosynthesis. Science 370, 1295–1300. https://doi.org/10.1126/science.abb7772

Wang, S., Zhang, Y., Ju, W., Wu, M., Liu, L., He, W., Peñuelas, J., 2022. Temporally corrected long-term satellite solar-induced fluorescence leads to improved estimation of global trends in vegetation photosynthesis during 1995–2018. ISPRS J. Photogramm. Remote Sens. 194, 222–234. https://doi.org/10.1016/j.isprsjprs.2022.10.018

Wang, W., Ertsen, M.W., Svoboda, M.D., Hafeez, M., 2016. Propagation of Drought: From Meteorological Drought to Agricultural and Hydrological Drought. Adv. Meteorol. 2016, 1–5. https://doi.org/10.1155/2016/6547209

Warren, J.M., Hanson, P.J., Iversen, C.M., Kumar, J., Walker, A.P., Wullschleger, S.D., 2015. Root structural and functional dynamics in terrestrial biosphere models – evaluation and recommendations. New Phytol. 205, 59–78. https://doi.org/10.1111/nph.13034

Wasko, C., Nathan, R., Peel, M.C., 2020. Trends in Global Flood and Streamflow Timing Based on Local Water Year. Water Resour. Res. 56. https://doi.org/10.1029/2020WR027233

Wohlfahrt, G., Gerdel, K., Migliavacca, M., Rotenberg, E., Tatarinov, F., Müller, J., Hammerle, A., Julitta, T., Spielmann, F.M., Yakir, D., 2018. Sun-induced fluorescence and gross primary productivity during a heat wave. Sci. Rep. 8, 14169. https://doi.org/10.1038/s41598-018-32602-z

Wu, C., Peng, J., Ciais, P., Peñuelas, J., Wang, H., Beguería, S., Andrew Black, T., Jassal, R.S., Zhang, X., Yuan, W., Liang, E., Wang, X., Hua, H., Liu, R., Ju, W., Fu, Y.H., Ge, Q., 2022. Increased drought effects on the phenology of autumn leaf senescence. Nat. Clim. Change 12, 943–949. https://doi.org/10.1038/s41558-022-01464-9

Wu, D., Zhao, X., Liang, S., Zhou, T., Huang, K., Tang, B., Zhao, W., 2015. Time-lag effects of global vegetation responses to climate change. Glob. Change Biol. 21, 3520–3531. https://doi.org/10.1111/gcb.12945

Wu, G., Guan, K., Li, Y., Novick, K.A., Feng, X., McDowell, N.G., Konings, A.G., Thompson, S.E., Kimball, J.S., De Kauwe, M.G., Ainsworth, E.A., Jiang, C., 2021. Interannual variability of ecosystem iso/anisohydry is regulated by environmental dryness. New Phytol. 229, 2562–2575. https://doi.org/10.1111/nph.17040

Wu, J., Albert, L.P., Lopes, A.P., Restrepo-Coupe, N., Hayek, M., Wiedemann, K.T., Guan, K., Stark, S.C., Christoffersen, B., Prohaska, N., Tavares, J.V., Marostica, S., Kobayashi, H., Ferreira, M.L., Campos, K.S., da Silva, R., Brando, P.M., Dye, D.G., Huxman, T.E., Huete, A.R., Nelson, B.W., Saleska, S.R., 2016. Leaf development and demography explain photosynthetic seasonality in Amazon evergreen forests. Science 351, 972–976. https://doi.org/10.1126/science.aad5068

Xiao, Z., Liang, S., Wang, J., Xiang, Y., Zhao, X., Song, J., 2016. Long-Time-Series Global Land Surface Satellite Leaf Area Index Product Derived From MODIS and AVHRR Surface Reflectance. IEEE Trans. Geosci. REMOTE Sens. 54, 5301–5318. https://doi.org/10.1109/TGRS.2016.2560522

Yan, H., Wang, S., Huete, A., Shugart, H.H., 2019. Effects of light component and water stress on photosynthesis of Amazon rainforests during the 2015/2016 El Niño drought. J. Geophys. Res. Biogeosciences 124, 1574–1590.

Yan, K., Park, T., Yan, G., Liu, Z., Yang, B., Chen, C., Nemani, R., Knyazikhin, Y., Myneni, R., 2016. Evaluation of MODIS LAI/FPAR Product Collection 6. Part 2: Validation and Intercomparison. Remote Sens. 8, 460. https://doi.org/10.3390/rs8060460

Yang, H., Ciais, P., Wigneron, J.-P., Chave, J., Cartus, O., Chen, X., Fan, L., Green, J.K., Huang, Y., Joetzjer, E., Kay, H., Makowski, D., Maignan, F., Santoro, M., Tao, S., Liu, L., Yao, Y., 2022. Climatic and biotic factors influencing regional declines and recovery of tropical forest biomass from the 2015/16 El Niño. Proc. Natl. Acad. Sci. 119, e2101388119. https://doi.org/10.1073/pnas.2101388119

Yang, J., Tian, H., Pan, S., Chen, G., Zhang, B., Dangal, S., 2018. Amazon drought and forest response: Largely reduced forest photosynthesis but slightly increased canopy greenness during the extreme drought of 2015/2016. Glob. Change Biol. 24, 1919–1934. https://doi.org/10.1111/gcb.14056

Yang, P., van der Tol, C., 2018. Linking canopy scattering of far-red sun-induced chlorophyll fluorescence with reflectance. Remote Sens. Environ. 209, 456–467. https://doi.org/10.1016/j.rse.2018.02.029

Yang, X., Tang, J., Mustard, J.F., Lee, J., Rossini, M., Joiner, J., Munger, J.W., Kornfeld, A., Richardson, A.D., 2015. Solar‐induced chlorophyll fluorescence that correlates with canopy photosynthesis on diurnal and seasonal scales in a temperate deciduous forest. Geophys. Res. Lett. 42, 2977–2987.

Yang, Y., Donohue, R.J., McVicar, T.R., 2016a. Global estimation of effective plant rooting depth: Implications for hydrological modeling. Water Resour. Res. 52, 8260–8276. https://doi.org/10.1002/2016wr019392

Yang, Y., Guan, H., Batelaan, O., McVicar, T.R., Long, D., Piao, S., Liang, W., Liu, B., Jin, Z., Simmons, C.T., 2016b. Contrasting responses of water use efficiency to drought across global terrestrial ecosystems. Sci. Rep. 6, 23284. https://doi.org/10.1038/srep23284

Yu, X., Orth, R., Reichstein, M., Bahn, M., Klosterhalfen, A., Knohl, A., Koebsch, F., Migliavacca, M., Mund, M., Nelson, J.A., Stocker, B.D., Walther, S., Bastos, A., 2022. Contrasting drought legacy effects on gross primary productivity in a mixed versus pure beech forest. Biogeosciences 19, 4315–4329. https://doi.org/10.5194/bg-19-4315-2022

Zeng, Y., Badgley, G., Dechant, B., Ryu, Y., Chen, M., Berry, J., 2019. A practical approach for estimating the escape ratio of near-infrared solar-induced chlorophyll fluorescence. REMOTE Sens. Environ. 232. https://doi.org/10.1016/j.rse.2019.05.028

Zeng, Y., Hao, D., Huete, A., Dechant, B., Berry, J., Chen, J.M., Joiner, J., Frankenberg, C., Bond-Lamberty, B., Ryu, Y., Xiao, J., Asrar, G.R., Chen, M., 2022. Optical vegetation indices for monitoring terrestrial ecosystems globally. Nat. Rev. Earth Environ. 3, 477–493. https://doi.org/10.1038/s43017-022-00298-5

Zhang, F., Yang, X., 2020. Improving land cover classification in an urbanized coastal area by random forests: The role of variable selection. REMOTE Sens. Environ. 251. https://doi.org/10.1016/j.rse.2020.112105

Zhang, Y., Gentine, P., Luo, X., Lian, X., Liu, Y., Zhou, S., Michalak, A.M., Sun, W., Fisher, J.B., Piao, S., Keenan, T.F., 2022. Increasing sensitivity of dryland vegetation greenness to precipitation due to rising atmospheric CO2. Nat. Commun. 13, 4875. https://doi.org/10.1038/s41467-022-32631-3

Zhang, Y., Joiner, J., Alemohammad, S.H., Zhou, S., Gentine, P., 2018. A global spatially contiguous solar-induced fluorescence (CSIF) dataset using neural networks. Biogeosciences 15, 5779–5800. https://doi.org/10.5194/bg-15-5779-2018

Zhang, Y., Parazoo, N., Williams, A., Zhou, S., Gentine, P., 2020. Large and projected strengthening moisture limitation on end-of-season photosynthesis. Proc. Natl. Acad. Sci. U. S. A. 117, 9216–9222. https://doi.org/10.1073/pnas.1914436117

Zhang, Y., Peña-Arancibia, J.L., McVicar, T.R., Chiew, F.H.S., Vaze, J., Liu, C., Lu, X., Zheng, H., Wang, Y., Liu, Y.Y., Miralles, D.G., Pan, M., 2016. Multi-decadal trends in global terrestrial evapotranspiration and its components. Sci. Rep. 6, 19124. https://doi.org/10.1038/srep19124

Zhang, Y., Peng, C., Li, W., Fang, X., Zhang, T., Zhu, Q., Chen, H., Zhao, P., 2013. Monitoring and estimating drought-induced impacts on forest structure, growth, function, and ecosystem services using remote-sensing data: recent progress and future challenges. Environ. Rev. 21, 103–115. https://doi.org/10.1139/er-2013-0006

Zhang, Y., Zhou, S., Gentine, P., Xiao, X., 2019. Can vegetation optical depth reflect changes in leaf water potential during soil moisture dry-down events? Remote Sens. Environ. 234, 111451. https://doi.org/10.1016/j.rse.2019.111451

Zhao, M., A, G., Liu, Y., Konings, A.G., 2022. Evapotranspiration frequently increases during droughts. Nat. Clim. Change 12, 1024–1030. https://doi.org/10.1038/s41558-022-01505-3

Zhou, S., Williams, A.P., Lintner, B.R., Berg, A.M., Zhang, Y., Keenan, T.F., Cook, B.I., Hagemann, S., Seneviratne, S.I., Gentine, P., 2021. Soil moisture–atmosphere feedbacks mitigate declining water availability in drylands. Nat. Clim. Change 11, 38–44. https://doi.org/10.1038/s41558-020-00945-z

Zhou, X., Zhang, Y., Wang, Y., Zhang, H., Vaze, J., Zhang, L., Yang, Y., Zhou, Y., 2012. Benchmarking global land surface models against the observed mean annual runoff from 150 large basins. J. Hydrol. 470–471, 269–279. https://doi.org/10.1016/j.jhydrol.2012.09.002

Zhu, Z., Bi, J., Pan, Y., Ganguly, S., Anav, A., Xu, L., Samanta, A., Piao, S., Nemani, R., Myneni, R., 2013. Global Data Sets of Vegetation Leaf Area Index (LAI)3g and Fraction of Photosynthetically Active Radiation (FPAR)3g Derived from Global Inventory Modeling and Mapping Studies (GIMMS) Normalized Difference Vegetation Index (NDVI3g) for the Period 1981 to 2011. Remote Sens. 5, 927–948. https://doi.org/10.3390/rs5020927

Zimba, H., Kawawa, B., Chabala, A., Phiri, W., Selsam, P., Meinhardt, M., Nyambe, I., 2018. Assessment of trends in inundation extent in the Barotse Floodplain, upper Zambezi River Basin: A remote sensing-based approach. J. Hydrol. Reg. Stud. 15, 149–170. https://doi.org/10.1016/j.ejrh.2018.01.002

Zuromski, L., Bowling, D., Kohler, P., Frankenberg, C., Goulden, M., Blanken, P., Lin, J., 2018. Solar-Induced Fluorescence Detects Interannual Variation in Gross Primary Production of Coniferous Forests in the Western United States. Geophys. Res. Lett. 45, 7184–7193. https://doi.org/10.1029/2018GL077906

Zwillinger, D., Kokoska, S., 1999. CRC standard probability and statistics tables and formulae. CRC Press.

Statement of authorship contributions

The introduction and the synthesis (Chapters 1 and 7) have been written by Wantong Li. Chapters 2-6 have been written by Wantong Li with contributions from all the co-authors. An overview of co-authors and their contributions are summarized below:

AH = Anne Hoek van Dijke (MPI-BGC)
AP = Annu Panwar (MPI-BGC)
BK = Basil Kraft (MPI-BGC)
CF = Christian Frankenberg (Caltech, JPL)
CM = Carla May (MPI-BGC)
CZ = Chunhui Zhan (MPI-BGC)
DM = Diego Miralles (UGhent)
GeDe = Georgia Destouni (SU)
GrDu = Gregory Duveiller (MPI-BGC)
HY = Hui Yang (MPI-BGC)
JD = Jasper Denissen (MPI-BGC)
JP = Javier Pacheco-Labrador (MPI-BGC)
MF = Matthias Forkel (TU Dresden)
ML = Manal Lam'barki (MPI-BGC)
MM = Mirco Migliavacca (JRC)
MR = Markus Reichstein (MPI-BGC)
QZ = Qian Zhang (NJU)
RO = René Orth (MPI-BGC)
SO = Sungmin O (EWU)
SW = Sophia Walther (MPI-BGC)
UW = Ulrich Weber (MPI-BGC)
WL = Wantong Li (MPI-BGC)
WZ = Weijie Zhang (MPI-BGC)

	Concept design	Methods	Materials	Data analysis and visualisation	Drafting	Manuscript revision
Chapter 2	WL, RO, MM	MM, MF, MR	WL, UW	WL	WL	WL, RO, MM, SW, MF, MR
Chapter 3	WL, RO, MF, MM	RO, WL	WL, UW	WL	WL	WL, RO, MM, MF, JD, MR, HY, GrDu, UW
Chapter 4	WL, RO, CF	WL, MF, MR, RO, MM	WL, UW, CF, JP	WL, JP	WL	WL, RO, JP, MM, DM, AH, MR, MF, WZ, CF, QZ, AP
Chapter 5	RO, WL, CM	RO, WL, CM	WL, UW	WL, CM	WL	WL, RO, MR, SO, GeDe, MM, BK, UW
Chapter 6	RO, ML, WL	RO, ML, WL	ML, WL	ML, WL	ML, WL	WL, RO, ML, SO, CZ

Acknowledgements

Time flies so quickly since 2019 I started my PhD in MPI-BGC in Jena. These years in Jena are unique for me, establishing a cornerstone of my career and illuminating me a future. Now I try to remember details of the entire journey and would like to thank many people who support me to reach this point.

I would like to first thank my parents, grandparents, other family members, and all my old friends outside of Jena. I harvest a lot in this journey but only missing in-person interactions with you in the past three years due to covid. My father, Ming Li, and my mother, Guoxiu Han, I gave my special thanks to you. You have accompanied me since I was born, you sent me plenty of happiness, and taught me principles to live and study. Although I always chose to explore adventures for my life which you like to complain, but all my motivations and decisions are on the basis of the haven that you provide. I would also like to deliver my thanks to Weijie who is not my family member yet but staying the longest time with me in Jena and supporting me with everything. Thank you Weijie for your patience to listen to my noisy details about code bugs, about work and life. Because of you I can quickly recover from failures big or small.

Now I start to express my thousands of thanks to my supervisors. René Orth, I could not easily express my full thanks because you need to understand that they are a lot. You respected my ideas no matter if they are naive, and you gave me the right to do any decision, and such trust and flexibility are the best that I can image as my ideal working atmosphere. At the same time, you are the best responsible daily supervisor, and whenever I ask for help you are ready to give suggestion, scientifically or non-scientifically. There are so many memories that I am grateful that I could share with you, every scientific achievement, every group and BGC party, every hiking, our weekly meetings, and HBCI group meetings. By the way, you are really good at encouraging people and you are also a nice example of being confident. I built upon my career confidence by learning from you.

I would also like to thank Mirco Migliavacca who contributes crucially his expertise regarding many aspects such as ecological and remote sensing to advance my PhD projects. Mirco, I appreciate that you took care of me a lot when I just started and tried to follow BAIE group discussions. You encouraged me to present my work in BAIE group. You jumped in my office and drawn a conceptual figure about Permutation importance on the whiteboard; Many times due to your explanation and encouragement on science, I dug into them. All these efforts you gave ultimately contribute to our efficient scientific achievements. You also took care of me in terms of life. I remember the beginning of covid I have to find another place to stay, and you helped me getting a guest house. I appreciate all your supports.

I also thank my remaining two PAC members, Markus Reichstein and Matthias Forkel, for fruitful insights of my scientific and career developments. Markus, I appreciate that you spent time to advance my PhD projects in our monthly meetings in the past year, in my previous BGI seminar talks, PAC meetings and follow-up discussions. All your comments leverage me to carefully review my projects with potential advantages and

disadvantages. Your insistence on SHAP values quite some while ago made sense, because it turned out to be one of the key methods I constantly use throughout projects. Matthias, I would like to deliver my special thanks to you, because in addition to constructive suggestions you gave in our countless meetings and all time you spent for scientific discussions, you also took care of me in registering the university and hosting me two-month research stay. The two months in Dresden I expanded my understanding by benefitting from projects of your group members, and the colloquium every week of your group also updates me your group progress continuously which is a great organisation. I am happy that we targeted similarly in my second project where you helped a lot in terms of land surface modelling. I remember that we last year had a lot of fun in a field work, nope, a BBQ in Dresden. Will you arrange another field work next year?

I would like to thank two BGI groups, HBCI group and BAIE group. I got to know many colleagues in these groups, and many of them became my friends and shared many happy-party memories with me. Ekaterina, Kelley, and Anne, we definitely enjoyed the trip together in Netherland. Jasper and Sungmin, I'm super happy I met you in the group since I started my PhD. You were both experienced colleagues. You made great models to work and you were always there to answer my questions, so that I learnt a lot from you. Prajwal, Manal, Carla, Marisa, Josephin, you are all great graduate students and gave me fun to get along with young people. Sinikka, you are the best officemate, and I enjoyed every chat with you, very relaxed. Relaxation is a gift that you actually gave me to balance the busy work. Melissa, Xin, and Chunhui, I am grateful that we share the same group. You are all talent people with unique aspects, and I love to discuss science with you as well as diving into parties with you. I send special thanks to Chunhui and Hoontaek, and Xin. You guys sometimes really made delicious Asian food for parties. For old BAIE group, I want to thank Yunpeng, Tiana, Qian, Javier, Tarek, Richard, and Jake who sometimes pretended to be the group member. You expanded my understanding for site-level studies, and some of you expanded my knowledge that how many bottles that a person can drink. Not related to these two groups, but I would also like to thank some more colleagues who contributed fruitful discussions after my seminar talks, Nuno, Martin, Hui, Greg, and many other colleagues who were always full of scientific outputs. I also thank Nick for suggestions on my career development.

I thank three more groups: Christian Frankenberg, Alexandra Konings, and Trevor Keenan's groups. Although my research visit was short, but you and many of your group members gave me your best hospitality. I appreciate the great chances that you provided for meaningful scientific exchanges.

Last but not least, I thank Chinese Scholarship Council who funded my living costs, and Mirco and Markus who financially supported my business trips. I thank the IMPRS-gBGC graduate school, Steffi and Stefanie, for supporting my structured PhD program. I thank Uli for numerous data downloading and aggregation. I thank Alice, Sarah, and Linda for many paperwork.

Curriculum Vitae

Basic Information

Name: Wantong Li

Date and place of birth: 20/07/1995, Chuzhou, Anhui, China

Nationality: Chinese

Language: Chinese (native), English (fluent)

Programming: Python (expert)

Interests: Swimming, badminton, traveling, photography

Education

- **11/2019 - Present: PhD candidate at Max Planck Institute for Biogeochemistry, Jena**
- **09/2016 - 07/2019: MSc. in Remote Sensing at Nanjing University, China (GPA: top 10%)**

09/2017 - 08/2018: Exchange MSc. in Environmental Earth Science at Free University of Berlin

MSc. thesis: vegetation productivity and its relationship to meteorology across African ecosystems

- **09/2012 - 07/2016: BSc. in Geographic Information System at Anhui University, China (GPA: 3.52/4, recommended for doing MSc. without the qualification exam)**

BSc. thesis: Evaluating the habitat suitability of waterbird in a wetland ecosystem in China

Awards and societal practice

Internship: Mapping brilliant people for industrial cooperators, Shanghai, Egon Zehnder, MSc.

Internship: data cleaning and software testing in AI Car Navigation Project, Hefei, iFLYTEK, BSc.

Chinese Scholarship Council (11/2019 - Present), PhD Scholarship.

Chinese Scholarship Council (09/2017-08/2018), MSc. Scholarship.

Model Student of Academic Scholarship (2017, 2019), MSc. Scholarship.

Hengxin Scholarship for outstanding students (2013), BSc. Scholarship.

Model Student of Academic Scholarship (2012, 2013, 2014), BSc. Scholarship.

University Summer Social Practice Prize (2013), BSc.

One of the Main Initiators and Organizers of Campus Photography Studio (2015), BSc.

The Second Prize of Campus Dance Competition (2014), BSc.

Scientific publications

Manuscripts for peer review

During PhD

Lam'barki, M.*, **Li, W.***, O, S., Zhan, C., and Orth, R. (2022d). Beyond precipitation: diversity of drivers of high river flows in European near-natural catchments, to be submitted.

Li, W., Reichstein, M., O, S., May, C., Destouni, G., Migliavacca, M., Kraft, B., Weber, U., Orth, R. (2023). Contrasting drought propagation into the terrestrial water cycle between dry and wet regions. Earth's Future, accepted.

Li, W., Pacheco-Labrador, J., Migliavacca, M., Miralles, D., Hoek van Dijke, A., Reichstein, M., Forkel, M., Zhang, W., Frankenberg, C., Panwar, A., Zhang, Q., Weber, U., Orth, R. (2023). Widespread and complex drought effects on vegetation physiology inferred from space. Nature Communications, accepted.

Li, W., Migliavacca, M., Forkel, M., Denissen, J., Reichstein, M., Yang, H., Duveiller, G., Weber, U. & Orth, R. (2022). Widespread increasing vegetation sensitivity to soil moisture. Nature Communications, 13, 3959. https://doi.org/10.1038/s41467-022-31667-9

Li, W., Migliavacca, M., Forkel, M., Walther, S., Reichstein, M. & Orth, R. (2021). Revisiting global vegetation controls using multi-layer soil moisture. Geophysical Research Letters, 48, e2021GL092856. https://doi.org/10.1029/2021GL092856

Denissen, J., Teuling, A.J., Pitman, A.J, Koirala, S., Migliavacca, M., **Li, W.**, Reichstein, M., Winkler, A.J., Zhan, C. & Orth, R. (2022). Widespread shift from ecosystem energy to water limitation with climate change, Nature Climate Change, 12, 677–684. https://doi.org/10.1038/s41558-022-01403-8

O, S., Bastos, A., Reichstein, M., **Li, W.**, Denissen, J., Graefen, H. & Orth, R. (2022). The role of climate and vegetation in regulating drought-heat extremes, Journal of Climate, 1(aop), 1–21. https://doi.org/10.1175/JCLI-D-21-0675.1

Kroll, J.*, Denissen, J.*, Migliavacca, M., **Li, W.**, Hildebrandt, A. & Orth, R. (2022). Spatially varying relevance of hydrometeorological hazards for vegetation productivity extremes, Biogeosciences, 19, 477-489. https://doi.org/10.5194/bg-2021-206

During MSc.

Li, W., Du, J., Li, S., et al (2019). The variation of vegetation productivity and its relationship to temperature and precipitation based on the GLASS-LAI of different African ecosystems from 1982 to 2013. International journal of biometeorology, 2019, 63: 847-860. https://doi.org/10.1007/s00484-019-01698-x

Li, M., Du, J., **Li, W.**, Li, R., Wu, S., Wang, S. Global Vegetation Change and Its Relationship with Precipitation and Temperature Based on GLASS-LAI in 1982-2015. SCIENTIA GEOGRAPHICA SINICA, 2020, 40(5): 823-832. DOI: 10.13249/j.cnki.sgs.2020.05.017 (In Chinese)

During BSc.

Yang, Y., **Li, W.**, Zhou, Z., Li, C. The study on the relationship between wetland landscape pattern and water level in Shengjin Lake. Journal of Biology, 2019, 36(02). DOI: 10.3969/j.issn.2095-1736.2019.02.061 (In Chinese)

Conference abstracts

Li, W., Migliavacca, M., Reichstein, M., Forkel, M., Frankenberg, C., and Orth, R.: Large-scale vegetation physiological responses to drought from multiple satellite-based observations, AGU Fall Meeting 2022, Chicago, 12-17 December 2022, B43F-01, https://agu.confex.com/agu/fm22/meetingapp.cgi/Paper/1120697

Li, W., Migliavacca, M., Forkel, M., Denissen, J., Reichstein, M., Yang, H., Duveiller, G., Weber, U. & Orth, R.: Global vegetation getting more sensitive to short-term soil moisture variability, AGU Fall Meeting 2021, hybrid, 13-17 December 2021, B12B-04, https://ui.adsabs.harvard.edu/abs/2021AGUFM.B12B..04L/abstract

Li, W., Migliavacca, M., Reichstein, M., Forkel, M., Frankenberg, C., and Orth, R.: Revealing the drought response of large-scale vegetation physiology from multiple satellite-based observations, EGU General Assembly 2022, Vienna, Austria, 23–27 May 2022, EGU22-8239, https://doi.org/10.5194/egusphere-egu22-8239, 2022.

Li, W., Forkel, M., Migliavacca, M., Reichstein, M., Walther, S., Denissen, J., and Orth, R.: Changing sensitivity of global vegetation productivity to hydro-climate drivers, EGU General Assembly 2021, online, 19–30 Apr 2021, EGU21-1783, https://doi.org/10.5194/egusphere-egu21-1783, 2021.

Li, W., Migliavacca, M., Luo, Y., and Orth, R.: Which hydro-meteorological variables control large-scale photosynthesis?, EGU General Assembly 2020, Online, 4–8 May 2020, EGU2020-15936, https://doi.org/10.5194/egusphere-egu2020-15936, 2020

IMPRS certificate

IMPRS gBGC
International Max Planck Research School for Global Biogeochemical Cycles

Certificate Supplement

Ms. Wantong Li

born on 20 July, 1995

in Chuzhou, China

At the International Max Planck Research School high potential students have the opportunity to work on their Ph.D. theses in the framework of a structured programme providing excellent research conditions.

She carried out (amongst others) the following curricular activities in the respective categories and earned in total 26.1 credit points (1 CP = 25-30 hours of work ≈ 5-day block course).

	CP
Courses related to global biogeochemical cycles	∑ 3.1
- Biogeochemical cycles in the Earth system - an overview	1.1
- Atmosphere, Ocean and Land	1.0
- Swiss Climate Summer School 2021	1.0
Transferable skill courses	∑ 0.8
- Rules for Good Scientific Practice	0.2
- Academic Writing	0.4
- Career Planning in Science	0.2
Skill & elective courses	∑ 2.2
- Applied Statistics & Data Analysis - Basics & Advanced	1.6
- R - Advanced	0.6
Outreach activities and other scientific activities	∑ 20.0
- Research stays at the Technical University Dresden and at the Heidelberg University	3.0
- Oral presentation at the	5.0
• General Assembly at the European Geosciences Union 2020	
• General Assembly at the European Geosciences Union 2021	
• General Assembly at the European Geosciences Union 2022	
• Fall Meeting of the American Geophysical Union 2021	
• Fall Meeting of the American Geophysical Union 2022	
- Two published, two submitted first-author and three non-first-author publications in peer-reviewed journals	9.0
- Reviewing of three publications for peer-reviewed journals	2.0
- Public outreach	1.0

Max Planck Institute for Biogeochemistry

FRIEDRICH-SCHILLER-UNIVERSITÄT JENA